Bayerische Julius-Maximilians Universität Würzburg

Geographisches Institut
Lehrstuhl für Fernerkundung
Stiftungslehrstuhl in Kooperation mit dem
Deutschen Zentrum für Luft- und Raumfahrt e.V. (DLR)
Prof. Dr. Stefan Dech

Department of Land Information (DLI)
Satellite Remote Sensing Services,
Perth, Western Australia

Measuring Burn Severity in Forests of South-West Western Australia Using MODIS

Diplomarbeit

vorgelegt von
Yvonne Walz

Erstgutachter: Prof. Dr. Stefan Dech

Zweitgutachter: Dr. Stefan Maier, DLI

Perth, November 2004

Summary

Burn severity was measured within the Mediterranean sclerophyll forests of south-west Western Australia (WA) using remote sensing data from the Moderate Resolution Imaging Spectroradiometer (MODIS). The region of south-west WA is considered a high fire prone landscape and is managed by the state government's Department of Conservation and Land Management (CALM). Prescribed fuel reduction burning is used as a management tool in this region. The measurement of burn severity with remote sensing data focused on monitoring the success and impact of prescribed burning and wildfire in this environment. The high temporal resolution of MODIS with twice daily overpasses in this area was considered highly favourable, as opportunities for prescribed burning are temporally limited by climatic conditions.

The Normalised Burn Ratio (NBR) was investigated to measure burn severity in the forested area of south-west WA. This index has its heritage based on data of the Landsat TM/ETM+ sensors and was transferred from Landsat to MODIS data (Key and Benson, 1999 [1],[2]). The measurement principally addresses the biomass consumption due to fire, whereas the change detected between the pre-fire image and the post-fire image is quantified by the ΔNBR.

The NBR and the Normalised Difference Vegetation Index (NDVI) were applied to MODIS and Landsat TM/ETM+ data. The spectral properties and the index values of the remote sensing data were analysed within different burnt areas. The influence of atmospheric and BRDF effects on MODIS data were investigated by comparing analyses of uncorrected top of atmosphere (TOA) reflectance and atmospheric and BRDF corrected (BOANADIR) reflectance. The definition of burn severity classes was established in a field trip to the study area. However, heterogeneous fire behaviour and patchy distribution of different vegetation structure made field classification difficult. Ground truth data were collected in two different types of vegetation structure present in the burnt area. The burn severity measurement of high resolution Landsat data was assessed based on ground truth data. However, field data was not sufficient for rigorous validation of remote sensing data. The ΔNBR index images of both sensors were calibrated based on training areas in the high resolution Landsat image. The burn severity classifications of both sensors were comparable, which demonstrates the feasibility of a burn severity measurement using moderate spatial resolution 250m MODIS data.

The index reduced atmospheric and BRDF effects of the remote sensing data, and thus MODIS TOA data were considered suitable for the burn severity measurement. The ΔNBR could not be uniformly applied, as different structures of vegetation influenced the value range of the index. Furthermore, the index was sensitive to variability in moisture content. However, the study concluded that the ΔNBR on MODIS data is a useful measure of burn severity in the forested area of south-west WA.

I dedicate this work to my parents in appreciation for all their love and support.

Acknowledgements

I would like to thank the following people for their contribution throughout this work.

Prof. Dr. Stefan Dech enabled this excellent opportunity for me to do research in Western Australia. He provided the contact between the Bayerische Julius-Maximilians University Würzburg, Germany and the Department of Land Information in Perth, Western Australia. I am greatful for his support and supervision of this work.

Dr. Richard Smith made it possible for me to join his team at the Department of Land Information - Satellite Remote Sensing Services (DLI-SRSS) and provided an excellent working place for the duration of this project. Furthermore, I am thankful for facilitating the field trip to the study area and reading the work.

My supervisor Dr. Stefan Maier assisted me very skillfully throughout my work at DLI. I would like to thank him for his continuous and patient support during the complete time of research, for his critical input to my draft and for challenging me in this important step of my career.

Furthermore, Belinda Heath from DLI-SRSS was supervising this work. She imparted lots of her skill and experience with fire and remote sensing. I want to thank her greatfully for correcting all of my drafts and for very supportive discussions that encouraged me during the complete time of research.

I want to give special thanks to the Department of Conservation and Land Management (CALM) - Fire Management Services. The cooperation with CALM enabled a broadened insight into the environment and management of the study area. In particular I would like to thank Donna Green, Rod Simmonds and Li Shu for their assistance in the field validation and providing an insight into field fire management.

Thanks to all staff members of DLI-SRSS, who cordially accepted me into their team and were always open for many questions and problems throughout this work. Especially I would like to thank Robert Shaw and Miguel Tovar for their company on the field trip, Sarfraz Khokhar and Matthew Adams for the support in technical questions and Mike Steber for correcting my English.

The German Academic Exchange Service (DAAD) provided a scholarship, which financially supported the realisation of this project.

I am very thankful to my family, in particular my parents Hartmut and Babsy Walz, for providing moral and financial support. They enabled and encouraged my studies and supported all my interests.

I want to thank my partner Alex, who accompanied me throughout the complete time of this work and gave important support and encouragement through good and bad times.

THANK YOU!

Table of Contents

List of Figures

Chapter 6: Methods and Analyses

Chapter 7: Results

Appendix

List of Tables

List of Acronyms

ACRES	Australian Centre of Remote Sensing
ASTER	Advanced Spaceborne Thermal Emission and Reflection
ATSR	Along Track Scanning Radiometer
AVHRR	Advanced Very High Resolution Radiometer
AVIRIS	Airborne Visible / Infrared Imaging Spectrometer
B.P.	Before Present
BOA	Bottom of Atmosphere
BOANADIR	Bottom of Atmosphere and Nadir View Angle
BRDF	Bi-directional Reflectance Distribution Function
BRF	Bi-directional Reflectance Factor
Ca	Calcium
CALM	Department of Conservation and Land Management
DEM	Digital Elevation Model
DLI	Department of Land Information
DN	Digital Number
ΔNBR	Differenced Normalised Burn Ratio
EOS	Earth Observing System
ER Mapper	Earth Ressource Mapper
ERS	European Remote Sensing Satellites
ETM+	Enhanced Thematic Mapper Plus
FAA	Fire Affected Area
GCP	Ground Control Point
GDA94	Geocentric Datum of Australia 1994
GPS	Global Positioning System
H_2O	Water
HDF	Hierarchical Data Format
IBRA	Interim Biogeographic Regions of Australia
IMAPP	International MODIS / AIRS Processing Package
MIR	Middle Infrared
MODIS	Moderate Resolution Imaging Spectroradiometer
MSS	Multi Spectral Scanner
N	Nitrogen
NASA	National Aeronautics and Space Administration
NATMAP	Government Division of National Mapping
NBR	Normalised Burn Ratio
NDVI	Normalised Difference Vegetation Index
NIR	Near Infrared
NOAA	National Oceanic and Atmospheric Administration
O	Oxygen
P	Phosphorus
PCA	Principal Component Analysis
RGB	Red Green Blue
RMS	Root Mean Square Error
SRSS	Satellite Remote Sensing Services
TIR	Thermal Infrared
TM	Thematic Mapper
TOA	Top of Atmosphere
TRMM	Tropical Rainfall Measurement Mission
UTM	Universal Transversal Mercator
VIRS	Visible and Infrared Scanner
VIS	Visible Light
WA	Western Australia
WASTAC	Western Australian Satellite Technology and Applications Consortium
WGS84	World Geodetic System 1984

Chapter 1: Introduction

The aim of this research is to measure burn severity using satellite imagery from the *Moderate Resolution Imaging Spectroradiometer* (MODIS) sensor in the forests of south-west Western Australia (WA). The south-west of WA has been exposed to and shaped by fire for thousands of years and is considered to be one of the most fire prone regions of the world (Abbott and Burrows, 2003). The Mediterranean climate is characterised by long hot and dry periods, resulting in a fire prone environment. Due to a high rate of endemism this region is in the top 25 global biodiversity hotspots (Myers et al., 2000). The sclerophyll vegetation is widespread and rich in essential oil, making it highly flammable. It is also exposed to natural ignition through lightning strikes (Abbot and Burrows, 2003). It is a unique environment, which requires a high level of management to maintain and keep the natural ecosystem intact.

In recent times sustainable fire management has been high on the WA government's agenda. In the forested region of the South West prescribed burning is used as a management tool by land managers from the WA *Department of Conservation and Land Management* (CALM). Their goal is to reduce flammable fuel and avoid naturally ignited, disastrous wildfires. The aims of prescribed burning are to provide protection for human life and property, to conserve the rich biodiversity of the region and to meet future challenges such as climate change (Burrows and Abbott, 2003; Hodgson, 2004).

Sustainable fire management requires continuous monitoring of prescribed burning, wildfires and the environmental effects of fires. Satellite remote sensing has become an important and effective tool in monitoring fire and the environment (Pereira and Setzer, 1993; Turner et al., 1994; White et al., 1996; Patterson and Yool, 1998; Chuvieco, 1999; Key and Benson, 1999; García-Haro et al., 2001; Roy et al., 2002; Justice et al., 2002 [2]; Miller and Yool, 2002; Díaz-Delgado et al., 2003). Satellite imagery with sufficient spatial and temporal resolution can provide a detailed insight into fire detection and the environmental change post-fire. The digital format of the data allows the application of automated classification algorithms to determine burn severity and area statistics. Currently, daily fire hotspots are detected by satellite remote sensing and are available for Australia (http://firewatch.dli.wa.gov.au) and the globe (http://rapidfire.sci.gsfc.nasa.gov) (Justice et al., 2002 [2]).

This research focuses on a quantitative measurement of vegetation change due to fire using MODIS satellite imagery. Satellite images contain both spectral and spatial information. Fire consumes vegetation and alters landscape patterns. These changes have a particular spectral signature, which can be detected by remote sensing. The magnitude of change is expressed as low, moderate or high burn severity. The different structures of vegetation within the study area are considered in burn severity measurement. Data from MODIS sensor, installed on the Terra and Aqua satellites, give twice daily coverage of south-west WA in near-real time with a spatial resolution of 250m to 1km.

The study area is located in the state forest of south-west WA, which is managed by CALM. Fire affected areas (FAAs) from the years 2002 and 2004 were chosen as study sites for several reasons:

- The forested area of south-west WA requires regular prescribed burning and therefore a need for monitoring the success of these burns.
- The comparison of prescribed burns and wildfires are possible as both phenomena are present in the FAAs.
- The cooperation with CALM allowed access to ground truth data for validation.
- The MODIS validation project in the Department of Land Information (DLI) made high resolution Landsat data available for validation.

The image differencing index ΔNBR used on Landsat data was transferred to MODIS data. It is considered an appropriate index for operational daily change detection within the forested area of south-west WA. The major topics addressed in this work are:

- the spectral characteristics of MODIS within a burnt area before and after fire,
- the effects of atmosphere and varying view and illumination angles,
- the effect of burn severity on different vegetation structures within the Mediterranean forests of south-west WA
- and the feasibility of using moderate spatial resolution data to measure burn severity.

This is a preliminary investigation into the process of delivering operational daily information about burn severity in forests of south-west WA. The MODIS data cover the study area twice daily, if clouds permit. Fire managers have limited opportunities for prescribed burning due to climatic conditions. The results of this investigation may assist fire managers to monitor prescribed burning.

Figure 1-1: Fire in Australian vegetation. Fire is a natural phenomenon in the environment of south-west Western Australia. The forests are managed by prescribed fuel reduction burning to avoid disastrous wild-fires. (courtesy of Peter Saint from Fire and Emergency Services (FESA))

Chapter 2: Literature Review

Satellite remote sensing is able to measure electromagnetic energy reflected and emitted from the surface of the earth. Within the defined spatial and spectral resolution of the sensor, energy is detected in the *visible* (VIS), *near infrared* (NIR), *middle infrared* (MIR) and *thermal infrared* (TIR) wavelengths (Lillesand and Kiefer, 2000; Sabins, 1997). For any given surface, the amount of emitted and reflected radiation varies by wavelength. These variations are due to interactive mechanisms of radiation such as scattering, transmission, absorption, reflection and emission at wavelengths on the electromagnetic spectrum. They can be used to establish the spectral signature for each surface (Lillesand and Kiefer, 2000; www1).

Remote sensing is a useful tool for fire detection and monitoring. Various aspects of fire can be sensed, including the energy released by active fires, smoke, char and altered vegetation (Robinson, 1991). Satellite images provide a resource to monitor vast and remote areas at relatively low cost and high temporal frequency. At the same time satellite imagery is able to address various questions about the earth´s surface due to its spatial information in different spectral bands. For monitoring biomass burning, remote sensing methods can be used to measure surface reflectance and thermal properties before, during and post-fire (Sabins, 1997).

Prior fire occurrence, remote sensing can be used for predicting fire danger. The susceptibility to forest fire can be forecast with remote sensing methods through estimation of moisture and fuel. The sensitivity of reflectance to variation in leaf water and dry matter content is greatest in the shorter MIR and NIR, respectively. Indices and models are applied to remote sensing imagery to detect changes in leaf water content and fuel moisture (Zarco-Tejada et al., 2003; Danson and Bowyer, 2004; Koetz et al., 2004; Bowyer and Danson, 2004). Chuvieco et al., 2004 estimated fuel moisture based on a linear regression model with the *Normalised Difference Vegetation Index* (NDVI) and surface temperature as independent variables. Fuel complexes can be mapped as a prediction of fire danger using vegetation indices of Landsat TM imagery in combination with a *Digital Elevation Model* (DEM) (Koutsias and Karteris, 2003). Decreasing leaf water content and high fuel load increases the likelihood of fire ignition. Fire danger prediction can be useful for land managers who use prescribed burning as a tool to reduce fuel load and forecast wildfire danger.

During a fire remote sensing can detect the location of active fire and monitor its movement across the landscape. Active fire detection relies on measuring the thermal emission from the combustion process itself. Various algorithms are investigated and work on the detection of high release of emitted radiation in the TIR and MIR wavelengths between 3μm and 11μm (Dozier, 1981; Matson et al., 1984; Flasse and Ceccato, 1996; Giglio et al., 1999; Stroppiana et al., 2000; Justice et al., 2003 [2]). Daily detection of fire from satellite is available for Australia and the globe. The *Department of Land Information* (DLI) *Satellite Remote Sensing Services* (SRSS) provides fire detection for the Australian continent using data from MODIS and the *National Oceanic and Atmospheric Administration* (NOAA) *Advanced Very High Resolution Radiometer* (AVHRR). It is updated several times a day and is available for public access on the Internet (http://firewatch.dli.wa.gov.au). The *MODIS Rapid Response System* presents a fire detection algorithm applied on MODIS data providing global daily distribution of active fire (Justice et al., 2002 [2]). This product is available within 2 to 4 hours of acquisition at 1km resolution on the Internet (http://rapidfire.sci.gsfc.nasa.gov). The hot spot detection has high dependence on the satellite overpass being at the time when fire occurs.

Post-fire, remote sensing is used for monitoring biomass burning. Burnt areas are characterised by removal and alteration of vegetation as well

as deposit of ash and charcoal. A burnt surface has a fairly distinct spectral signature from bare soil and senescent vegetation when compared to the spectral signature of photosynthetically active vegetation. The mapping of burnt areas using satellite remote sensing is based on spectral changes in surface reflectance due to fire. Fire affected areas are mapped in various environments classified as either burnt or unburnt (Richards, 1984; Pereira and Setzer, 1993; Eva and Lambin, 1998[1],[2]; Chuvieco, 1999; Pereira, 2003). Surface characteristics are generally persistent for a longer period and are therefore less sensitive to temporal limitations compared to hot spot detection. However, when burnt areas become older, the ash is partially cleared by the wind and regrowth commences, which reduces the intensity of the burnt area signal (Eva and Lambin, 1998 [2]; Roy et al., 2002). Mapping fire affected areas is very useful for estimating area burnt, amount of biomass burnt and monitoring the post-fire recovery.

There are a number of satellite remote sensing systems that are suited to fire monitoring. MODIS are modern sensors on the Terra and Aqua satellite platforms that are well designed for fire detection and monitoring biomass burning. These sensors have 36 spectral bands that address both detection of thermal emission of active fire and surface reflectance for post-fire burnt area mapping. Reflective bands within the VIS, NIR and shorter MIR wavelengths have a moderate resolution of 250m or 500m, useful for mapping fire affected areas, and thermal bands with resolution of 1km. MODIS has overpasses each day and is therefore well designed for purpose of monitoring the earth´s surface continuously (Roy et al., 2002; Justice et al., 2002 [1],[2]). NOAA AVHRR has been considerably investigated after the first daily global fire product in the year 1992 (Flasse and Ceccato, 1996; Giglio et al., 1999; Stroppiana et al., 2000; Nielsen et al., 2002). The AVHRR sensor is useful for hot spot detection due to global daily coverage and its spectral bands within MIR and TIR wavelengths (bands 3 to 5). The sensor has a spatial resolution of 1.1km and can detect active fires, while fire scars must be greater than 400ha to be visible (Craig et al., 2000). The *Landsat Multi Spectral Scanner* (MSS), *Thematic Mapper* (TM) and *Enhanced Thematic Mapper plus* (ETM+) sensors have spatial resolution of 80m, 30m and 15m in the reflective bands between VIS and MIR wavelengths. The 30m resolution bands of Landsat TM and ETM+ are most investigated for post-fire study and offer a high level of accuracy, however the temporal resolution is limited to 16 days (Richards, 1984; Pereira and Setzer, 1993; Turner et al., 1994; White et al., 1996; Patterson and Yool, 1998; Chuvieco, 1999; García-Haro et al., 2001; Miller and Yool, 2002; Rogan and Yool, 2001; Díaz-Delgado et al., 2003). The literature presents other suitable sensors for remote sensing of fire. The *Visible and Infrared Scanner* (VIRS) on board the *Tropical Rainfall Measurement Mission* (TRMM) with 5 spectral bands between 0.6μm and 12μm and spatial resolution of 2km was used for remote sensing of fire activity in regions within +/- 40° of the equator (Giglio et al., 2000). The *Along Track Scanning Radiometer* (ATSR) on board the *European Remote-Sensing Satellites* (ERS) has 3 visible, 2 infrared and 2 thermal bands in 1km resolution and has been used to map burnt surfaces (Eva and Lambin, 1998 [1],[2]). The regeneration of vegetation after fire has been assessed using the *Airborne Visible/Infrared Imaging Spectrometer* (AVIRIS), which has 224 spectral bands between 0.38μm and 2.5μm and ground resolution of 20m (Riaño et al., 2002).

Landscape fires are of global significance especially through their effects on climate and biodiversity (Bradstock et al., 2002). Fire releases large amounts of trace gases and aerosols, which modify the chemistry of the atmosphere affecting the regional and global climates (Cary, 2002). Biodiversity can be conserved by applying an adapted fire regime required by certain ecosystems. It varies in terms of frequency, season and intensity (Bond and van Wilgen, 1996). Fire intensity is influenced by type of ecosystem, climate and topography. The productivity of the vegetation determines the rate of fuel accumulation. This explains the maximum possible fire frequency, whereas increasing fuel load is at the same time strengthening impact on fire intensity (Huston, 2003). Some species have an obligate dependence on fire for their reproduction and can decline in the absence of fire. Other species carry woody fruits that need heat impulse or smoke to break dormancy. At certain level of fire intensity the positive effects on plant species can become negative and plants are destroyed by fire. At the same time, unburnt patches are important as areas of retreat for flora and fauna (Burrows and Wardell-Johnson, 2003; Dixen and Barrett, 2003). Burn severity and patchiness of fire is important in assessing the impact of fire on vegetation and on the ecological balance of the ecosystem.

Satellite remote sensing is able to measure different levels of burn severity (Key and Benson, 1999[1],[2]). This is very important when quantifying the ecological and atmospheric impacts of fire (Pereira, 2003). The change in reflectance associated with the conversion of vegetation to burnt vegetation is greatest in NIR

and shorter MIR wavelengths. The magnitude of change can be related to burn severity. The *Normalised Burn Ratio* (NBR) is an index, which provides enhanced information about burn severity. It was successfully validated in needle leaf forest with the *Composite Burn Index* (CBI), a post-burn quantitative assessment of burn severity sampled in the field (Key and Benson, 1999[1],[2]). Preparatory research and further investigation for measuring burn severity with change detection of spectral signature using Landsat TM/ETM+ data have been published by Richards, 1984; Pereira and Setzer, 1993; Turner et al., 1994; White et al., 1996; Patterson and Yool, 1998; Chuvieco, 1999; Rogan and Yool, 2001; Miller and Yool, 2002; Díaz-Delgado et al., 2003. The NDVI, based on red and NIR bands, was often added as it addresses the vitality of vegetation. The image differencing index ΔNBR applied on Landsat TM and ETM+ data is presently assisting the *Burned Area Emergency Response* (BAER) program in the U.S.A. in their post-burn severity assessment (www2, www3).

Further methods for burn severity classification are all related to detection of spectral change of the surface due to fire on multitemporal imagery. The *Principal Component Analysis* (PCA) is used for mapping burn severity based on spectral variances in each band and creates new variables as weighted sums of the different channel readings (Richards, 1984; Patterson and Yool, 1998; García-Haro et al., 2001). The *Kauth-Thomas* or *Tasseled-Cap* transformation, theoretically similar to the PCA, reduces the channels to three composite variables describing brightness, greenness and wetness. Brightness identifies variation in reflectance, greenness is related to the amount of green vegetation present in the scene and wetness correlates with soil and canopy moisture (Kushla and Ripple, 1998; Patterson and Yool, 1998; Rogan and Yool, 2001). The Feature Analyst of ArcView, ArcGIS or ERDAS Imagine is another example used for classifying burn severity. The method is based on a machine learning classifier that uses an inductive learning algorithm and training data to automate the classification of certain geographic features (Levien et al., 1999; Redmond, R.L. and Winne, J.C., 2001).

Investigations into mapping burnt areas with the sensor MODIS are not well represented in the literature. Sá et al., (2003) address the accuracy of MODIS detection of burnt area as a major problem due to the moderate spatial resolution. Individual channels of MODIS imagery were investigated with the aim to map burnt areas with sub-pixel accuracy in woodlands of northern Mozambique. Comparison with ETM+ imagery showed no accurate prediction of sub-pixel burnt area fraction in any of the first seven reflective bands. In a savanna ecosystem, band 7 (2.130μm) followed by band 5 (1.240μm) and 2 (0.858μm) exhibited the strongest spectral contrast between the unburnt and burnt area. Roy et al., (2002) present a burnt area mapping method using multitemporal moderate spatial resolution (500m) data from MODIS. A bi-directional reflectance model together with multi-temporal land surface reflectance observations provided an expectation and uncertainty of subsequent observations through time. The highest burnt-unburnt discrimination using MODIS in primarily open wood and grassland of southern Africa was provided in band 5 (1.240μm), followed by bands 2 (0.858μm) and 6 (1.640μm) and poor discrimination in bands 1 (0.645μm), 3 (0.469μm), 4 (0.555μm) and 7 (2.130μm).

Chapter 3: Study Area

The study area is situated within the South West Botanical Province of WA. It is a biological boundary essentially determined by the isohyet of 300mm rainfall per year and corresponds with the administrative South West Land Division (Beard, 1990). It is an isolated region bordered on its western side by the Indian Ocean, on its southern side by the Southern Ocean, and on its north-eastern border by the transition into arid land. It spans latitudes from 27°S to 35°S and longitudes from 114°E to 124°E. This province is divided into seven biogeographic regions, whereas Jarrah Forest and Warren are representative for the forested region of south-west WA (Figure 3-1). The south-west of WA is considered one of the world's most fire prone regions. The Mediterranean climate together with the essential oil rich sclerophyll vegetation expose the region to fire through ignition by lightning strikes (Abbott and Burrows, 2003).

3.1 Physical Setting

The study area is located in the biogeographic regions of Jarrah Forest and Warren. The land appears as a flat stable low plateau. Due to tectonic inertness it experienced its main levelling during the Permian ice age (270 Million B.P.) (Beard, 1990). It is underlain by the deeply weathered Precambrian granite bedrock of the Yilgarn Block (Beard, 1990; Hopper, 2003). The western border of the study area is topographically set with the escarpment of the Darling Range, which resulted from the north to south running fault dividing the Perth Basin from the Yilgarn Block (Figure 3-2). East and south of the escarpment the forested region extends into an undulating plateau with elevations varying between 200m and 600m above sea level, dependent on the resistance of the bedrock against weathering and erosion (Beard, 1990; McCaw and Hanstrum, 2003).

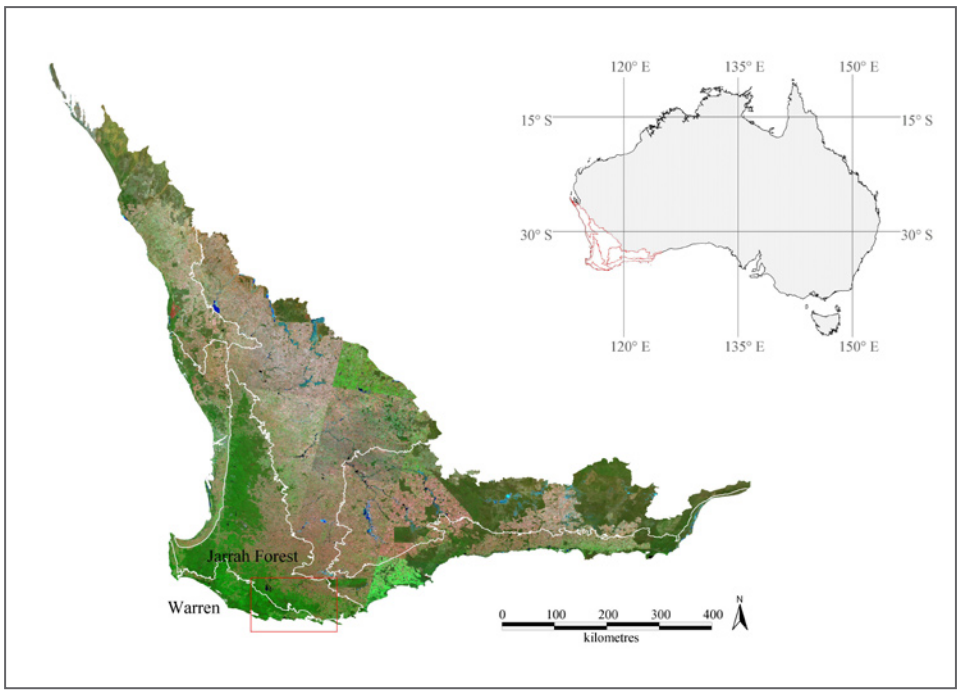

Figure 3-1: The South-West Botanical Province and Biogeographic Regions, Western Australia. The South-West Botanical Province is separated into 7 biogeographic regions, whereas Jarrah Forest and Warren region represent the forested area in this region. The red box borders the location of the study sites investigated in this work. Study sites are situated within Jarrah Forest and Warren region (Image: Landsat ETM+ mosaic in R-G-B as 7-4-2, Nov 01 - Mar 02, Australian Greenhouse Office; SW Botanical Province: Thackway and Cresswell, 1995)

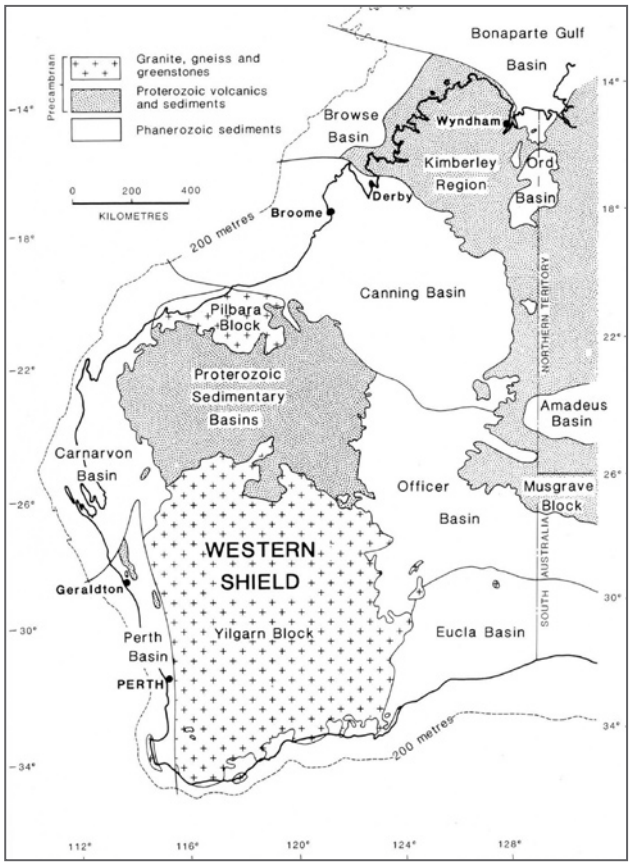

◄ *Figure 3-2: Geological map of south west WA (Beard, 1990)*

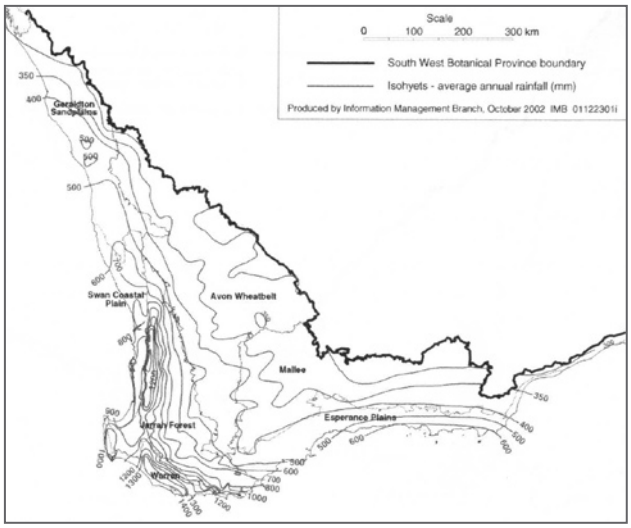

▲ *Figure 3-3: Rainfall for south west WA. The isohyets represent distribution of rainfall per year within the South-West Botanical Province of WA (Abbott and Burrows, 2003)*

Some protruding ranges like the Porungurup and Stirling Ranges have peaks rising over 1000m in elevation. There are also scattered granite bedrock rising to the surface as rocky outcrops (Hopper, 2003). Steep terrain is linked with deeply incised river valleys, where the local difference in elevation between river valley and plateau rarely exceeds 200m (McCaw and Hanstrum, 2003). The drainage system, unorganised after the ice age, was shaped mainly during the geological periods subsequent to the Permian through to the Cretaceous 65 Million B.P. (Beard, 1990). The main streams with a continuous flow that eroded valleys are the Frankland, Kent and Denmark rivers. These rivers all flow southward and terminate at the Southern Ocean.

The climate in south-west WA is typically Mediterranean, characterised by mild winters, a pronounced winter rainfall maximum, and a prolonged seasonal drought during the summer and early autumn period. It is a result of the sub-tropical belt of high pressure migrating north and south across the region with the change of the season (McCaw and Hanstrum, 2003). In the winter months from July to September cold fronts embedded within moist westerly winds on the southern side of the subtropical ridge account for the rainfall over the region. In the summer months, dry continental easterly winds on the northern side of the subtropical ridge lead to high temperatures and very low rainfall. The study area lies within the moderate Mediterranean zone with rainfall of 800mm to 1500mm and 3 to 6 dry months per year (Beard, 1990). The amount of rainfall is highest in Warren region and the escarpment of the Darling Range. It decreases in conjunction with increasing

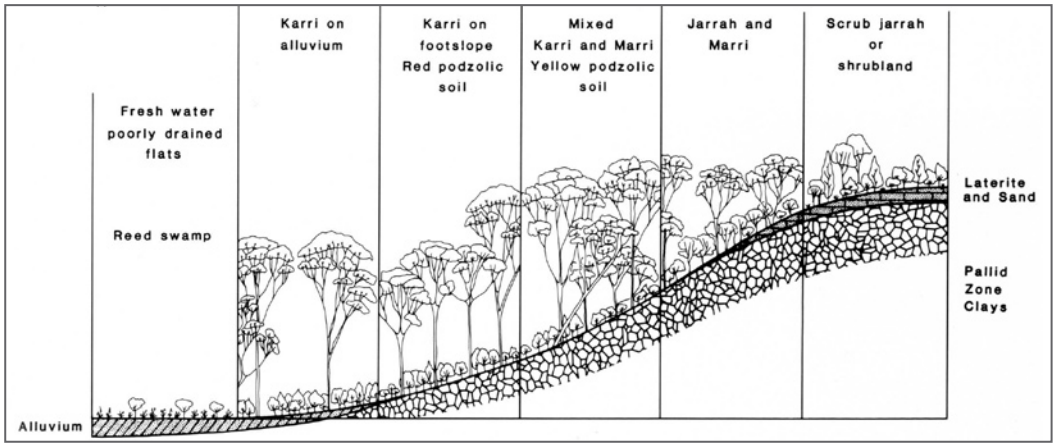

Figure 3-4: Distribution of soil and vegetation across a valley in south-west WA. The distribution of soils correlate with vegetation structure and height (Beard,1990)

dry months towards the interior land (Figure 3-3). As the supply of moisture is of overriding importance for vegetation, the critical factor will be the season and length of the dry period (Beard, 1990). Temperature regime has less impact on the vegetation as the region lies in low latitudes with high oceanic influence and is therefore moderate and excluded from extended frost periods over winter .

The soils in the forested region of south-west WA are deficient in nutrients. The last major soil disturbance occurred through glaciation 250 Million B.P. (Hopper, 2003). Australian rocks have a general deficiency in the essential plant nutrient phosphorus and have undergone deep weathering and leaching. These two factors are largely responsible for the lack of nutrients (Beard, 1990). The inertness of the landscape has left most of this exhausted material in place. The sandy texture provides low capacity in holding soil water, which plants are able to absorb, whereas the deeply weathered pallid zone underneath has a great moisture storage. Plant growth is limited by the process of surface lateritisation, which occurred after the Oligocene period (38 to 26 Million B.P.) and covers vast areas of south-west WA. The lateritic duricrust of hardened ironstone, which caps the higher ground, is a result of high iron content in the soil and the dry and seasonal climate (Beard, 1990). Soil distribution is varying following a catena across a valley and has a narrow correlation to the distribution of vegetation (Figure 3-4). The valley floors are composed of alluvium and exposed pallid clays, which are favourable for tree growth when not averted by backwater. The upland is generally covered with laterite and sand, which promotes lower and more sparse plant growth. The nutrient poor soil is a limitation in an agricultural sense, however, the native flora is well adapted (Beard, 1990).

Vegetation in the study area is generally characterised as evergreen sclerophyll forests with predominantly Eucalyptus species. The optima of temperature and moisture for growth are divided into separate seasons caused by the Mediterranean climate. The native flora in the forested region was shaped over millions of years by nutrient deficient soils, dry and hot summer periods and the natural existence of fire. The hard brittle leaf character can mainly be explained by nutrient deficiency and a physical adaptation to the dry and hot climate. A further strategy to handle infertile soils is symbiosis with mycorrhiza for better nutrient intake by the roots. The limitations to plant growth rate in this environment are dominated by

Figure 3-5: Vegetation structure in the karri forest, jarrah-marri forest and open woodland/shrubland. This structure of vegetation occurs within the study sites (Diagrams: Beard, 1990)

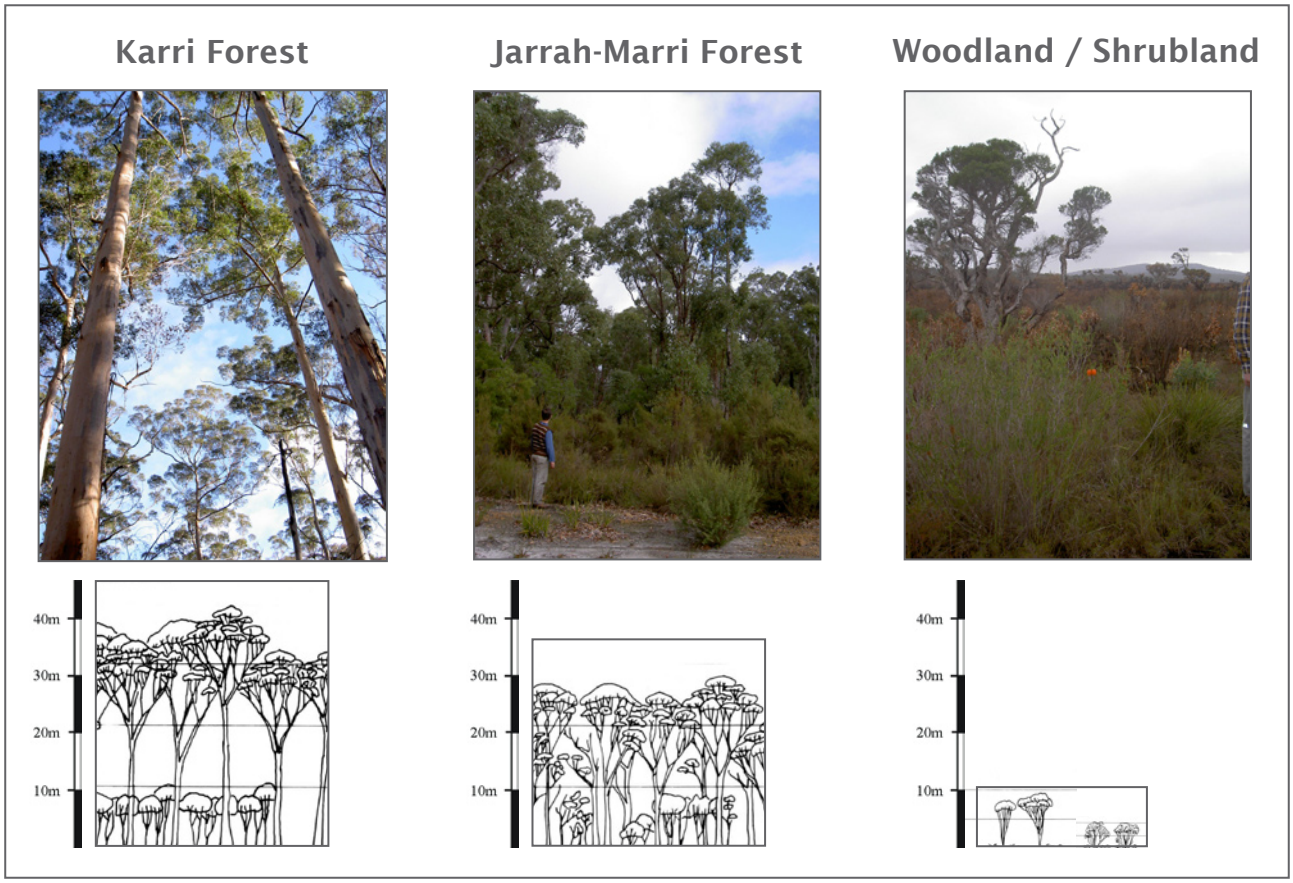

deficient water supply rather than nutrients, light or temperature (Beard, 1990). The structure of vegetation is a key aspect for determining burn severity as the distance between strata, and the amount of strata, influence fire behaviour (Bond and van Wilgen, 1996). There are three general types of vegetation structures occurring within the study area: karri forest, jarrah-marri forest and open shrubland/woodland.

The karri (*Eucalyptus diversicolor*) forest is the tallest forest with a canopy reaching heights between 60m to 80m, mainly occurring in Warren region. There is a sparse upper understorey with widely varying heights around 20m and a more dense lower understorey with an average height of 3m (Beard, 1990) (Figure 3-5). The karri forest is determined by the existence of favourable soil with a reddish-brown loam or sandy loam surface horizon, which gradually changes to red clay at about 50cm depth. Karri forest can handle no more than 3 to 4 months without rainfall (Beard, 1990). These forests are characterised as productive ecosystems with low tree diversity and low spatial heterogeneity (Huston, 2003). The stems of Eucalyptus diversicolor have a very thin bark and are therefore sensitive to fire (Burrows and Wardell-Johnson, 2003).

The jarrah (*Eucalyptus marginata*) and marri (*Eucalyptus calophylla*) mixed forests dominate in the forested ecosystems of south-west WA. The canopy reaches heights of about 20m to 30m with a subordinate tree layer below 10m and an understorey shrub layer 1m to 2m tall (Beard, 1990) (Figure 3-5). Both species have a great capacity to regenerate and survive fire from a seedling stage (Burrows and Wardell-Johnson, 2003). Jarrah forest covers virtually the whole catena from laterite to pallid clay zone. The roots are able to pass the surface duricrust and access water from deeply weathered profiles. Marri is determined by more superficial soil above the duricrust. This mixed forest occurs in rainfall zones with up to 5 or 6 dry months (Beard, 1990). Jarrah-marri forests are less productive compared to karri forests and have their primary plant diversity in the understorey (Huston, 2003). Mature jarrah and marri trees have a thick protective bark. They are vulnerable to intense fire only, when the crown becomes scorched (Burrows and Wardell-Johnson, 2003).

Open shrubland/woodland is summarised as non-forested ecosystem without layered storeys and includes swamps, heaths, shrubs and coastal dunes (Underwood et al, 1991; Beard, 1990). In general they are topographically flat. Vegetation height is about 2m and density varies depending on soil and moisture. Occasionally single trees occur within shrubland turning it into open woodland (Figure 3-5). These ecosystems correlate with poorly drained soils and sandplains where the existence of forest with closed canopy is not possible. There are several swamps existing in the study area. They occur close to the coast where drainage has been obstructed by the coastal dune system (Beard, 1990).

3.2 Fire environment in south-west Western Australia

The environment of south-west WA is considered as one of the world's most fire prone regions (Abbott and Burrows, 2003). Furthermore, this region is among the world's 25 global biodiversity hotspots (Myers et al., 2000). This is due to its endemism rate, where a high proportion of plant species exist only within the south-west of WA. The high value of biodiversity refers mainly to richness in plant species (Beard, 2000). The key biogeographic reason for becoming a global biodiversity hotspot is through the oceanic, climatic and edaphic isolation of the south-west of WA. The species richness can be explained by evolutionary events extending back into the Tertiary (65 Million B.P.)

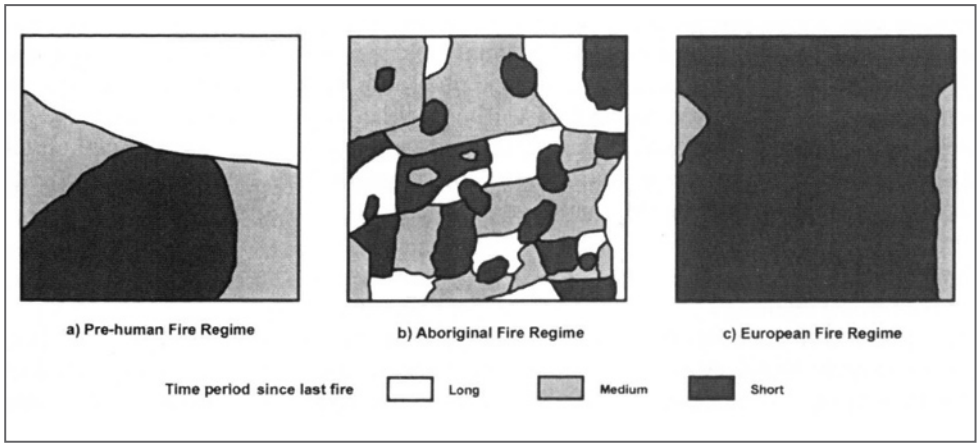

Figure 3-6: Historical burn patterns in south-west WA (Bowman, 2003)

(Hopper, 2003). The government of WA manages fire in this region to conserve biodiversity and to maintain multiple forest resources in a sustainable ecologic and economic manner.

Fire history

Fire, as a natural disturbance, shaped the south-west WA environment evidently from the late Tertiary 10 to 2 Million B.P. (Hassell and Dodson, 2003). A fire history has been reconstructed by sedimentary charcoal and pollen analysis. The earliest dated arrival of the Aborigines was around 40,000 years B.P. (Hassell and Dodson, 2003). Aboriginal people, called Noongars in the South-West, used fire for a variety of reasons, such as cooking, warmth, illumination, ceremony, ritualistic ordeals, clearing camps, facilitating travel, signalling, regenerating senescent vegetation, etc. (Bowman, 2003). The Noongar's main use of fire was for hunting and agriculture, therefore termed fire stick farming. Their fire management was changing the scale and frequency of landscape fires due to their frequent burning of small areas (Bowman, 2003). Fires following European settlement in 1826 had a similar frequency, but burnt larger areas and obliterated the mosaic habitat created by Aboriginal burning (Bowman, 2003) (Figure 3-6).

Fire behaviour

Fire behaviour is highly influenced by the type of ecosystem, climate and topography (Bond and van Wilgen, 1996). The productivity of the ecosystem determines the rate of fuel accumulation which is in turn a function of the soils and climate. The fuel accumulation rate explains the maximum possible fire frequency as well as the increase in potential fire intensity with time between burns (Huston, 2003). Furthermore, the ratio between fuel and air influences fire behaviour which is related to the structure of the ecosystem (Bond and van Wilgen, 1996).

In the study area fire behaves differently in open woodland compared to forest, where different levels of storeys can influence flame height or cause wind breaking. Less distance between storeys, as exists in jarrah forests can more easily cause intense fires compared to huge distances between storeys, as found in tall karri forests (Fox, 2004; Cox, 2004; Simmonds, 2004). The structure of vegetation is an important criteria when measuring burn severity, as scorch of canopy is a major benchmark.

The climate in south-west WA is a major factor for fire proneness of the region due to dry periods and wind regimes. Since 1970 the South-West has experienced a sustained decrease in annual rainfall with extended drought periods over summer. This prolongs the forest fire season into May or early June. On a regular basis strong hot dry northerly winds arise ahead of abrupt cooler south-west winds. This is associated with a pre-frontal trough, which occurs mainly during the summer months over the South-West causing extreme fire weather days. Strong afternoon sea breezes, due to deep troughs inland, can often affect fire behaviour with rapid changes of wind direction and strength. Tropical cyclones, which originate over the Indian Ocean, are an important fire weather factor, as they cause lightning strikes, which are a main ignition source (McCaw and Hanstrum, 2003).

Topography is another important factor in fire behaviour as slope has a direct effect on the fire spread rate. Fire burns upslope faster than downslope (Bond and van Wilgen, 1996). Furthermore, slope and aspect determine soil characteristics, moisture regimes, wind regimes and vegetation structure together with the floristic composition (Bond and van Wilgen, 1996; McCaw and Hanstrum, 2003).

Fire ecology

Within ecosystems in south-west WA, fire is a natural disturbance which results in different responses. On the one hand fire can damage or kill mature plants while on the other hand it stimulates regeneration and rejuvenescence. A post-fire environment is characterised by more light, increasing temperatures, water availability and levels of nutrients, which is favourable for plant growth. More light and high temperature on the ground result from the loss of vegetation and increasing insolation. Higher water availability is a result of the reduction of transpiring leaf surface area and therefore addresses deeper reservoirs of water. Strong insolation can at the same time lead to locally severe conditions of drought on surface due to high evaporation rates (Bond and van Wilgen, 1996; Burrows and Wardell-Johnson, 2003). Plants with deeper root systems or those that penetrate the dry surface have large

Figure 3-7: Banksia woody fruits. Some species are dependent on fire to open and spread seeds.

reservoirs of water available. The effects of fire on the nutrient status of soils depend on the amount and distribution of organic matter on the surface and in the top few centimetres of soil. Despite the loss of nitrogen due to volatilisation, fire generally mobilises nitrogen (N), phosphorus (P), calcium (Ca) and other nutrients. The carbon to nitrogen (C:N) relationship (for example the ratio of non-green to green biomass) increases after fire, releasing high amounts of nitrogen as ash deposition. Nutrients are at the same time released by heating the soil organic matter and increasing rates of biological mineralisation due to changes in soil pH. The result is a nutrient pulse for the first few months post-fire (Adams, 2003; Bond and van Wilgen, 1996; Huston, 2003). In the south-west WA environment it is water and nutrients that set growth limits. This results in a lower plant leaf area and allows relatively large amounts of light to penetrate to the forest floor. The positive effects of increased light have little effect compared to the sudden availability of plant nutrients and increased water resources (Huston, 2003).

Vegetation in south-west WA is considered highly fire prone and carries many pyrophytes that have different strategies to tolerate fire. Some species have an obligate dependence on fire for their reproduction and can decline in the absence of fire. The post-fire environment, with open ground space, increased availability of resources and temporary reduction of seed predators is highly favourable for seedling establishment (Bond and van Wilgen, 1996; Burrows and Wardell-Johnson, 2003). Plant species use a variety of physical and chemical cues from fire. In particular they use the by-products heat and smoke to synchronise germination to the post-burn environment. Thus many plant species are stimulated to reproduce by enhancing flowering post-fire. Some species flower regularly between fires but accumulate high amounts of seeds in seedbanks post-fire (Bond and van Wilgen, 1996; Luepnitz, 1998). Some species carry woody fruits that need a heat impulse or smoke to open the fruits and to break seed dormancy (Bond and van Wilgen, 1996; Dixen and Barrett, 2003) (Figure 3-7). Resprouters have developed a strategy of diverting much of their energy to underground organs such as lignotubers rather than directing it towards above ground biomass and reproduction. Above ground epicormic buds as well as stem and branch shoots are usually protected beneath thick bark from the lethal temperature regimes experienced during a bushfire. This allows resprouting soon after fire (Figure 3-8). Most forest eucalypts such as karri, jarrah and marri take advantage of post-fire conditions such as a suitable seed bed and reduced competition for regeneration and seed establishment (Burrows and Wardell-Johnson, 2003).

Figure 3-8: Epicormic bud of the Zamia. The above ground epicormic bud is protected by a thick bark from lethal heat of fire. Resprouting was observed 6 weeks post-fire.

For conservation of biodiversity it has to be stated that diversity of different types of organisms reaches its maximum in different environments and depend on different fire regimes. Fire regime parameters such as frequency, season and intensity of burning, help maintain the high level of biodiversity through the effect of disturbance. The largest species are prevented from dominating, thus allowing smaller or less competitive species to survive. One of the greatest threats to the diversity of highly disturbed landscapes such as south-west WA is the loss of small areas of resource concentration for retreat and regeneration (Huston, 2003).

Fire management

Fire management and prescribed burning became legal issues in WA following devastating wildfires in the early 1960s (Abbott and Burrows, 2003). In the following decades the state government`s Department of Conservation and Land Management (CALM) was vested with the responsibility of managing fire on public land (Abbott and Burrows, 2003). CALM uses fire as a planned application, where prescribed burning

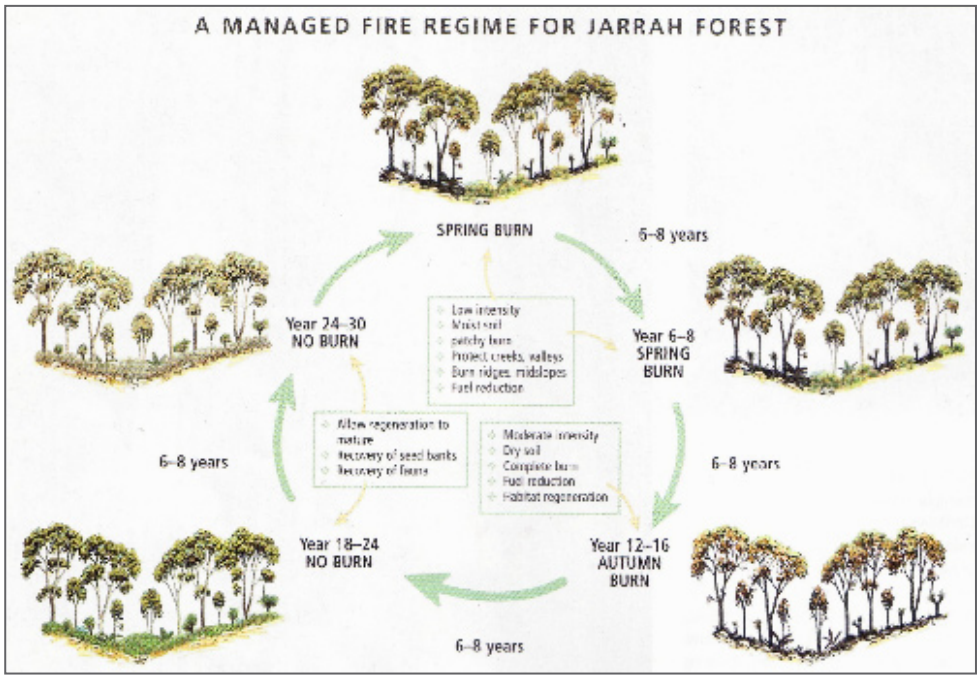

Figure 3-9: A proposed fire regime to manage the jarrah forest. This fire regime contains a variety of seasons of fire and of intervals between fire, which meets protection and biodiversity objectives. (courtesy of Neil Burrows, CALM, in Landscope Magazine, 2004)

is the management tool to achieve specific land management objectives (Hodgson, 2004). The aims are to protect human life, infrastructure and private property and to conserve and protect the biodiversity (Hopper, 2003; Hodgson, 2004). Any applied fire regime, like frequency, season, intensity, patchiness and size depends on the objective of land managers. In order to reduce the risk of uncontrolled wildfires after natural or deliberate ignition the fuel load needs to be diminished. A mild fuel reduction burn of the understorey manages this. To support the germination and advanced regeneration of several species a high intensity fire regime is required. The objective of conserving biodiversity is determined by mosaic burns as a pattern of different fire regimes within a burn envelope (Hodgson, 2004; Fox, 2004; Cox, 2004; Green, 2004). However, there is no fire regime that has been shown to conserve the entire biodiversity of a region. Each ecosystem needs a certain fire cycle to produce the best outcome with respect to conserving biodiversity and managing the forest sustainably. Figure 3-9 represents an appropriate fire regime to manage jarrah forests, which also meets conservation and protection objectives. After 6 to 8 years, a low intensity fire is recommended in spring to reduce fuel. The jarrah forest is burnt again after 6 to 8 years in order to reduce fuel and support habitat regeneration. At this time the prescribed burning is done in autumn, because the intensity of the burn is moderate due to drier conditions. The flora and fauna need the following 12 to 16 years to regenerate.

Prescribed burning can turn into a hazard when environmental aspects are not considered or changed therefore CALM needs to take several precautions. Before igniting a prescribed burn a prediction of fire behaviour is made, guided by the "Forest Fire Behaviour Tables for Western Australia" (Sneeuwjagt and Peet, 1998). This detailed prediction uses sampled factors like surface moisture content, amount and age of fuel, soil dryness, type and structure of ecosystem, climate and weather conditions for predicting fire spread rate and intensity. To protect adjacent properties from fire, the boundary is burnt with the wind towards the burn envelope to set a strategically placed buffer before burning the whole patch. Another important goal is to keep the fuel loads of neighbouring burn envelopes at different ages to set natural firebreaks (Green, 2004). Due to the high risk of fires getting out of control it is illegal to set fires during the period between 15th of December to 15th of March (Abbott, 2003).

Prescribed burning is an ongoing political issue in WA. Smoke pollution and loss of biodiversity are two issues which concern the general public. Fire as a natural disturbance and the understanding of fuel reduction burning to prevent disastrous wildfires are not generally accepted by the society (Bowman, 2003).

3.3 Study Sites

There are three study sites which were subject to both prescribed burns and wildfire between September and December 2002. Another area, affected by prescribed burning in April 2004 was taken into account. It occurred during the progress of this work and provided an opportunity

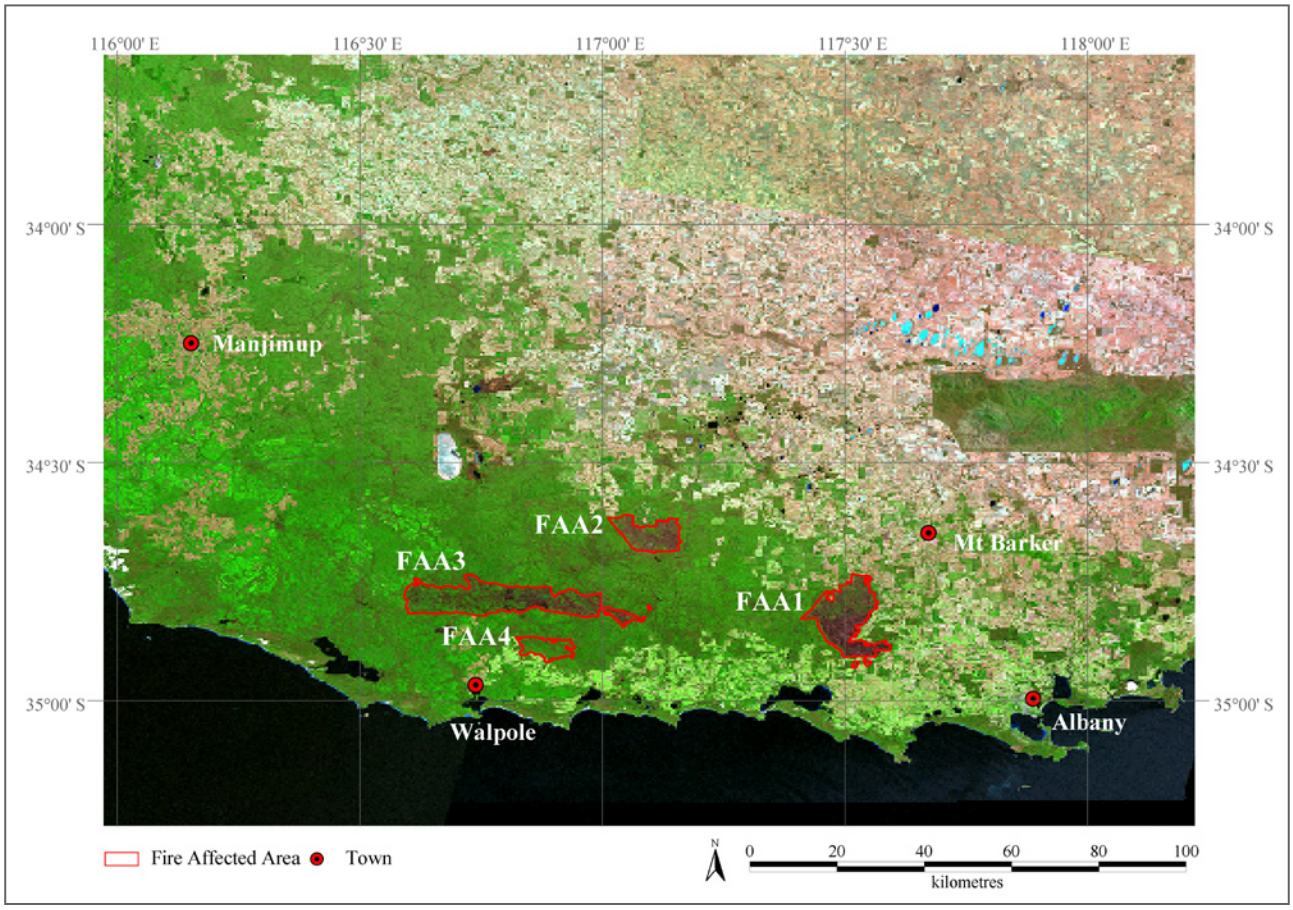

Figure 3-10: Landsat ETM+ image over the study area. Overview of fire affected areas selected as study sites in south-west WA (Image: Landsat ETM+ mosaic in R-G-B as 7-4-2, Nov 02 - Mar 03, Australian Centre of Remote Sensing (ACRES))

to observe burn severity on the ground and collect field data (Figure 3-10).

Fire affected area 1 (FAA1) is situated between 34.73°S to 34.93°S and 117.41°E to 117.60°E. It comprises an area of 153.13 km^2 and is located with the centre about 26km southwest of Mt. Barker. The northern part of the FAA was subject to a prescribed burn while the southern part was exposed to a wildfire. The last day of burning was on 14 November 2002 (Shu, 2004), and the burnt area of the wildfire was visible on 17 November in MODIS imagery. Vegetation in the FAA1 is dominated by medium jarrah-marri forest, which is disconnected by riparian sedge and grassland along the river valleys. There is a small area of low woodland in the south-east corner of the fire affected area and patches of low to medium forest in the south (Figure 3-11).

Fire affected area 2 (FAA2) is located between 34.61°S to 34.69°S and 117.01°E to 117.16°E. It comprises an area of 75.86 km^2 and is located with the centre about 52km west of Mt. Barker. The FAA2 was subject to prescribed burning. The end of the fire was on 21 October 2002 (Shu, 2004). The vegetation within this study site is dominated by low forest and woodland turning into low woodland in the centre. In the north-west and north-east corners there are patches of medium forest. Rocky outcrops are visible in the south and north part of the site (Figure 3-11).

Fire affected area 3 (FAA3) is located between 34.73°S to 34.85°S and 116.58°E to 117.10°E. It comprises an area of 224.56 km^2 and is situated with the centre about 20km north of Walpole. This FAA is a long, narrow area with different patches of prescribed burns and wildfire. It was affected by fire several times over the spring season. The last day of prescribed burning was on 30 November 2002 (Shu, 2004). This FAA3 is composed of a mosaic of low and moderate woodland as well as low, medium and tall forest and rocky outcrops as illustrated in Figure 3-11

Fire affected area 4 (FAA4) is located between 34.86°S to 34.91°S and 116.80°E to 116.94°E. It comprises an area of 41.01 km^2 and is located with the centre about 16km northeast of Walpole. This FAA occurred during the time of this research and was subject to prescribed burning. The end of the fire was on 28 April 2004 (Simmonds, 2004). The vegetation of FAA4 consists of uniform medium forest in the western part and a mosaic of medium forest and low woodland in the eastern part (Figure 3-11).

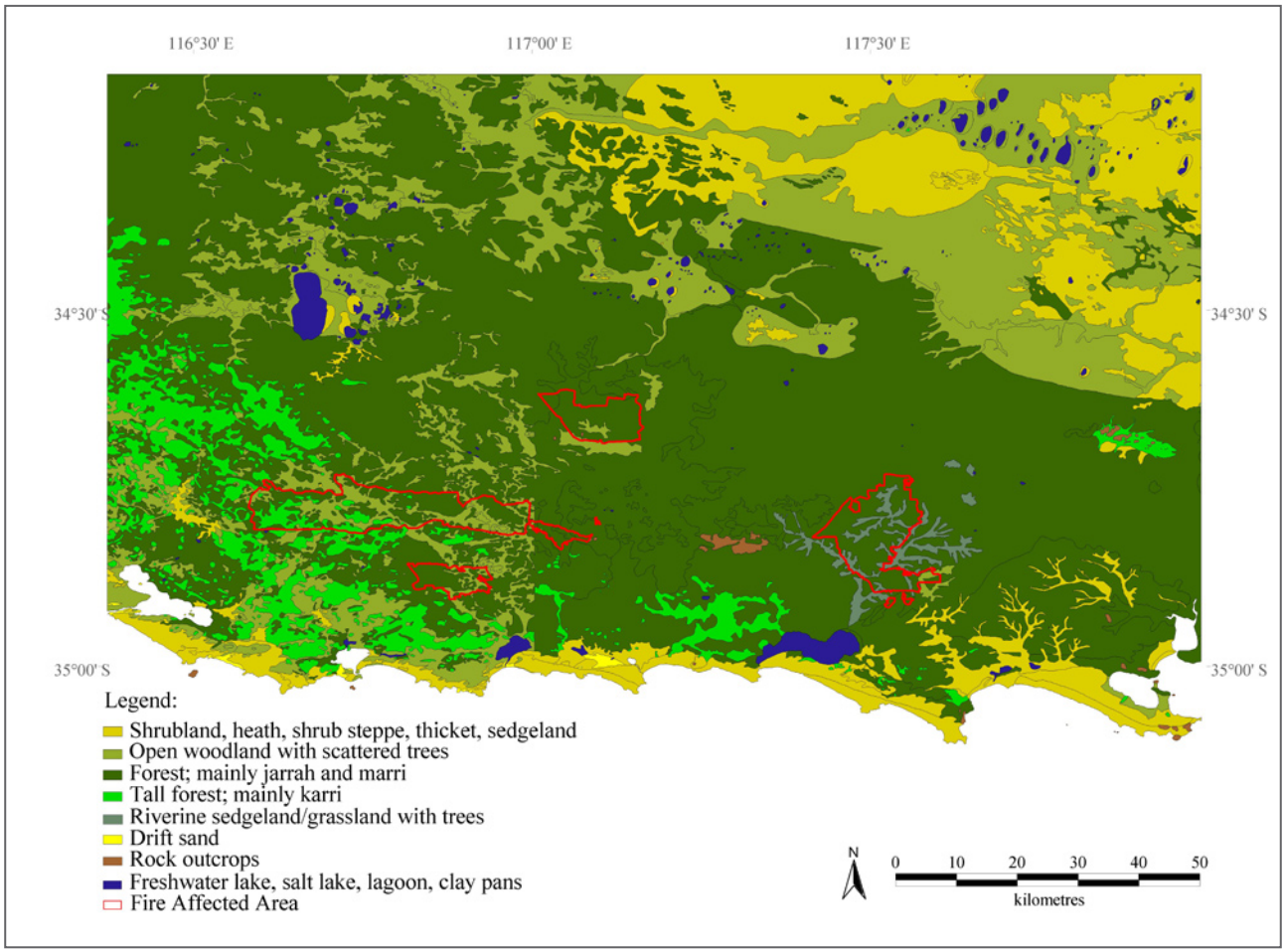

Figure 3-11: Distribution of vegetation structure in the study area. (Department of Agriculture of Western Australia (DAWA))

Chapter 4: Fundamentals of Remote Sensing

Satellite remote sensing provides a useful method for fire detection and monitoring vast and remote areas affected by fire at relatively low cost level and at high frequency. Information is received in different spectral bands and referenced to the earth's surface. This can be used to address various questions about the environment. Fire consumes vegetation and alters the landscape pattern. This is visible in satellite images as the spectral properties of fire affected areas change compared to those measured before fire. Burn severity can be measured by the magnitude of change detected by a sensor.

Remote sensing data are presented as reflectance, which is defined in the first section. The spectral properties of vegetation and soil explain the theoretical fundamentals needed to detect the change of landscape patterns due to fire. The sensors MODIS and Landsat TM/ETM+ are introduced as their data are analysed in this work. The Normalised Difference Vegetation Index (NDVI) and the Normalised Burn Ratio (NBR) were investigated to measure burn severity with satellite remote sensing data.

4.1 Reflectance

Reflectance is the process whereby radiation hits an object at an angle of incidence and rebounds off an object at an angle of reflection. For an ideal specular surface (for example a mirror), the angle of incidence and the angle of reflection are approximately equal (Figure 4-1). Lambert defined a perfectly diffuse Lambertian surface, for which the radiant flux leaving the surface is constant for any angle of reflectance to the surface (Jensen, 2000). However, in practice the surface is generally diffuse and spectral reflectance varies depending on surface properties. The incident and reflected radiation measured by satellite remote sensing are in the same plane.

The reflectance R of a Lambertian surface for a spectral wavelength λ is defined in Equation 4-1 (Schott, 1997):

$$R_\lambda = \frac{\pi * L_\lambda}{E_{0\lambda} * \cos sz} \quad \text{(Equation 4-1)}$$

In Equation 4-1, L represents the spectral radiance measured at the sensor in each spectral wavelength λ with units [W/(m²*sr*μm)]. For a Lambertian surface, the detected radiance reflected from the surface is given by integrating the reflected radiance over the hemisphere, represented by the factor π. $E_{0\lambda}$ is the top of atmosphere irradiance at a certain wavelength, which is normalised by the cosine of the sun zenith angle, sz.

The top of atmosphere irradiance $E_{0\lambda}$ can be derived as defined in Equation 4-2 (Schott, 1997):

$$E_{0\lambda} = \frac{Esun_\lambda}{d^2 [1AE]} \quad \text{(Equation 4-2)}$$

$Esun_\lambda$ stands for the mean solar extraterrestrial irradiance, which is spectrally variable. It is dependent upon the square of the earth-sun distance, d, measured in astronomical units [1AE=1.49598*10¹¹m].

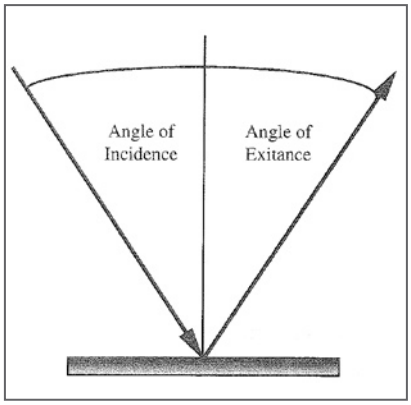

Figure 4-1: Angle of incident radiation and angle of reflectance. The angles are approximately equal when surface is specular (Jensen, 2000)

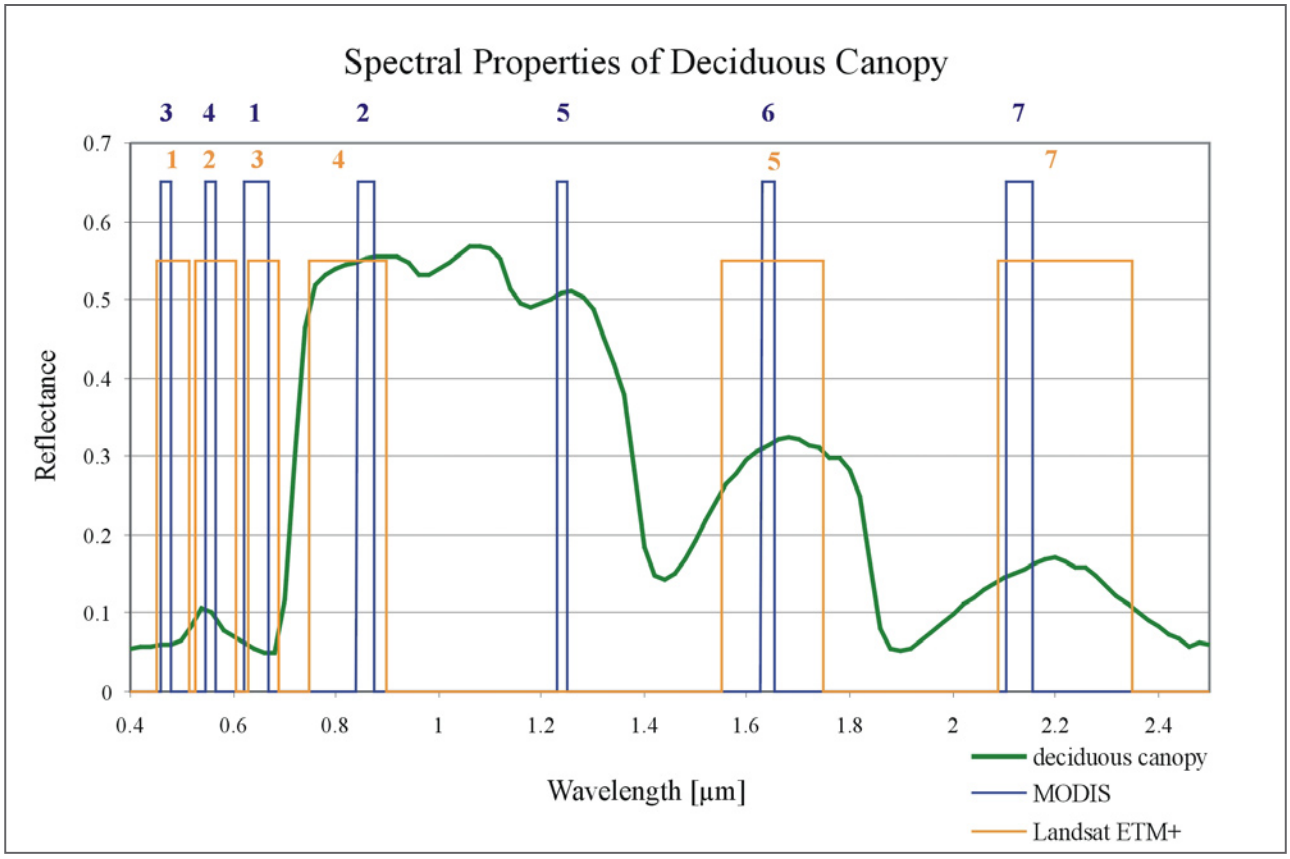

Figure 4-2: Spectral properties of deciduous vegetation. MODIS and Landsat ETM+ bands demonstrate the capacity to detect the signal in the wavelengths between 0.4 and 2.5 µm. (Spectrum: ASTER spectral library, http://speclib.jpl.nasa.gov/Search.htm)

4.2 Spectral Properties of Vegetation and Soil

Basic principles for measuring changes due to fire can be explained by the typical spectral reflectance curves of vegetation and soil.

Figure 4-2 presents a spectrum measured from vegetation, which is composed of deciduous forest. The spectrum of the green vegetation has a typical trend within the wavelength region of 0.4µm to 2.5µm. It shows low reflectance at visible wavelengths (VIS: 0.4µm to 0.7µm), high reflectance in the near infrared wavelengths (NIR: 0.7µm and 1.2µm) and decreasing reflectance in the middle infrared wavelengths (MIR: 1.3µm to 2.5µm). The spectral bands of MODIS and ETM+ demonstrate the ability to measure the spectral signatures.

In the VIS, leaf pigments determine the reflectance properties absorbing the incident solar radiation. Chloroplasts carry the most frequent pigments Chlorophyll a and b absorbing especially the incident blue (0.45-0.52µm) and red (0.63-0.69µm) light energy. Green light around 0.55µm is only partly absorbed by the pigments and thus makes leaves appear green to the human eye. Dependent on leaf structure and amount of pigment, chloroplasts absorb 60% to 80% of incident radiation in the VIS and dominate the spectral properties within this wavelength (Lillesand and Kiefer, 2000; Jensen, 2000; Maier, 2000; Larcher, 2001). Two other groups of pigments, the carotenes and xanthophylls, absorb radiation primarily in the yellow to orange-red spectrum (Maier, 2000). The radiation absorbed between 0.38µm and 0.71µm is used as energy source for photosynthesis and is therefore termed "Photosynthetically Active Radiation" (PAR). A reduction of the chlorophylls due to senescence

Figure 4-3: Influence of leaf water content on spectral properties of vegetation. (Jensen, 2000)

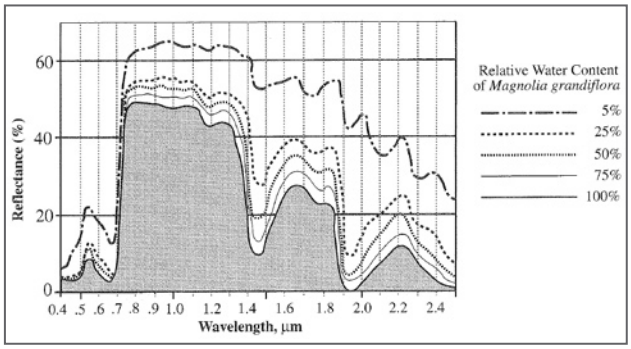

or stress results in dominance of other pigments. Thus leaf colour is changing and photosynthetic activity is reduced (Larcher, 2001; Jensen, 2000).

In the NIR, reflectance of green vegetation has a dramatically increase. The low absorption of vegetation in this wavelength (below 5%) yields to high reflectance between 40% to 60% and high transmittance between 40% to 60%. Transmitted light can be reflected and transmitted again by leaves below. If the canopy is only composed of a single sparse leaf layer, reflectance in the NIR is lower due to absorption of transmitted energy by the ground. Reflectance within this spectrum gives evidence about the amount of biomass (Jensen, 2000). Plant reflectance in this wavelength can be also used to detect plant stress and discriminate species as reflectance largely changes with the internal leaf structure (Lillesand and Kiefer, 2000).

Incident energy in the MIR is either absorbed or reflected by vegetation, whereas transmittance is little or non existant. Water content determines the spectral characteristics of living leaves. Leaf water absorbs incident electromagnetic energy with increasing strength at longer wavelengths. Thus reflectance of vegetation at MIR decreases with increasing leaf moisture content (Lillesand and Kiefer, 2000; Jensen, 2000; Maier, 2000) (Figure 4-3). The dips in reflectance are caused by water absorption bands in the corresponding wavelengths. Dependent on moisture, vegetation reflects between the major water absorption bands at about 1.6µm and 2.2µm (Eiden et al., 1991; Jensen, 2000; Maier, 2000; Zarco-Tejada et al., 2003).

Spectral properties of a vegetation stand are dominated by the leaf area index that indicates the relation of leaf area to ground area. Within a stand the spectrum is modified by the interaction of different species, vertical structure of the stand, the relation of illumination and shadowing effects and the portion of soil reflectance (Eiden et al., 1991; Eiden, 2000).

The spectral properties of a dark to dark brown, sandy soil in the wavelength region between 0.4µm to 2.5µm is presented in Figure 4-4. This example demonstrates that soil has a continuous increase of reflectance from low values in the VIS to higher values in the MIR. The soil spectrum is highly influenced by factors that affect soil reflectance. Some of these factors are for example moisture content, organic content, soil texture, surface roughness and iron oxide (Eiden et al., 1991; Lillesand and Kiefer, 2000). These factors are complex, variable and interrelated. Increasing moisture content of the soil results in decreasing

Figure 4-4: Spectral properties of brown soil. MODIS and Landsat ETM+ bands demonstrate the capacity to detect the signal in the wavelengths between 0.4 and 2.5 µm. (Spectrum: ASTER spectral library, http://speclib.jpl.nasa.gov/Search.htm)

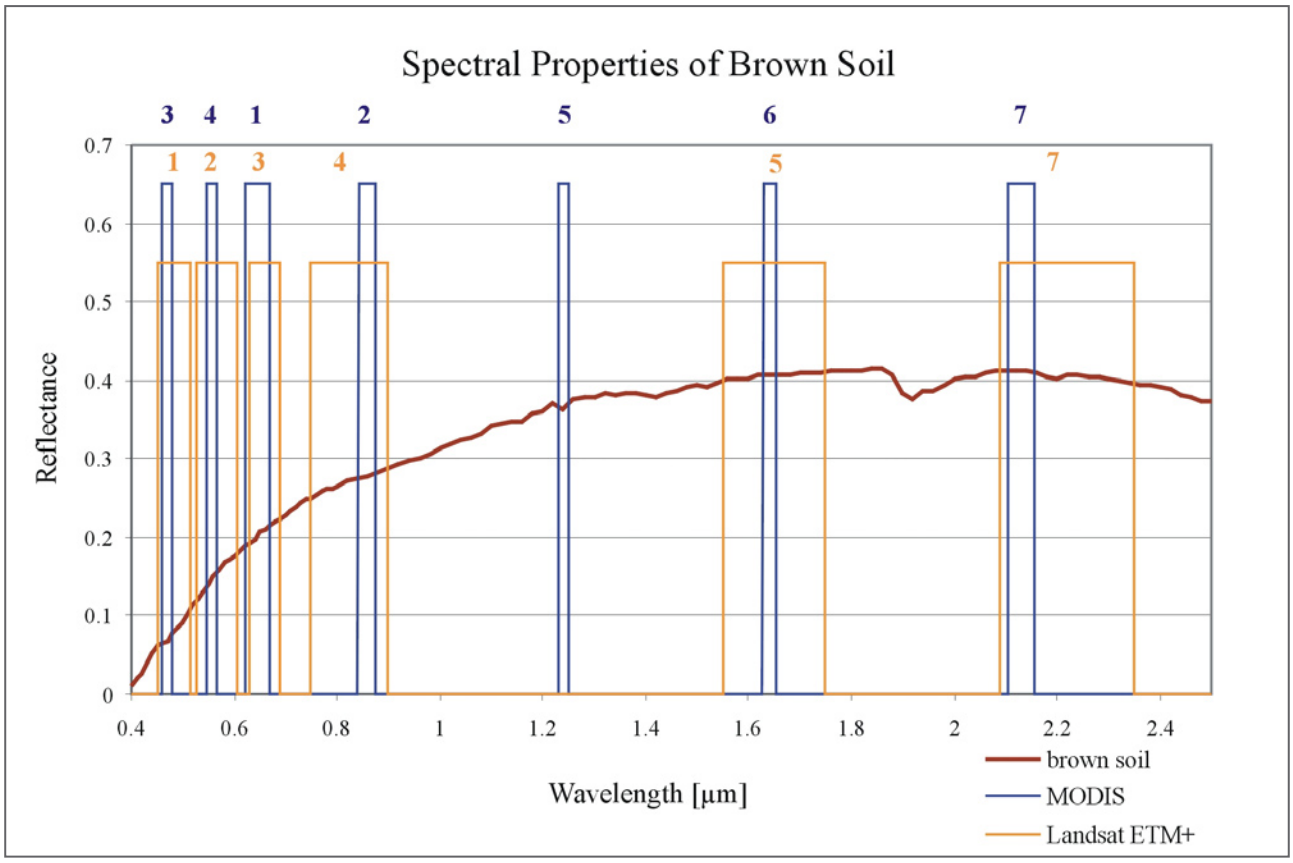

reflectance. Similar to the spectrum of vegetation, this effect is greatest in the water absorption bands (Eiden et al., 1991; Ceccato, 2001). Moisture content is highly influenced by soil texture as this determines moisture holding capacity. Coarse sandy soils that are usually well drained have high reflectance due to low moisture content. It is the reverse with fine-textured soils, which are poorly drained and in which more energy is absorbed by moisture. If water would not be present, the coarse textured soil would reflect less than the fine-textured soil (Eiden et al., 1991; Lillesand and Kiefer, 2000). High content of organic matter in soil reduces reflectance. The same applies to high surface roughness, which reflects less than a finely grained texture (Eiden et al., 1991; Lillesand and Kiefer, 2000). When iron content is high, reflectance is significantly decreased in the VIS green (0.50µm-0.54µm) and increased in the VIS red (0.6µm-0.7µm) (Eiden et al., 1991). The complex interactions between all these factors cause variable patterns of soil reflectance.

4.3 Factors influencing reflectance

Surface reflectance varies for different earth features and at different wavelengths. It is disturbed by two major factors before being detected by the satellite. These factors are the atmosphere and the variations in illumination and viewing directions.

The atmospheric effects on radiation detected by a satellite vary depending on the path length, the atmospheric conditions present and the wavelengths involved. The longer the path length, radiation has to pass through the atmosphere, the stronger it can be influenced by the atmosphere. Aerosols and gases in the atmosphere cause scattering and absorption of radiation, which varies with wavelength (Lillesand and Kiefer, 2000).

Figure 4-5: Atmospheric windows and absorption bands of atmospheric trace gases. (Jensen, 2000)

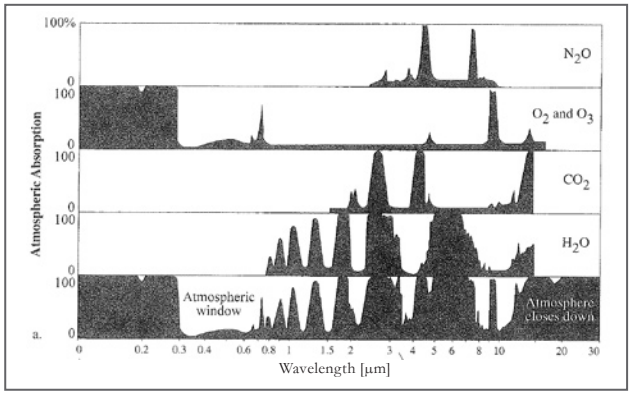

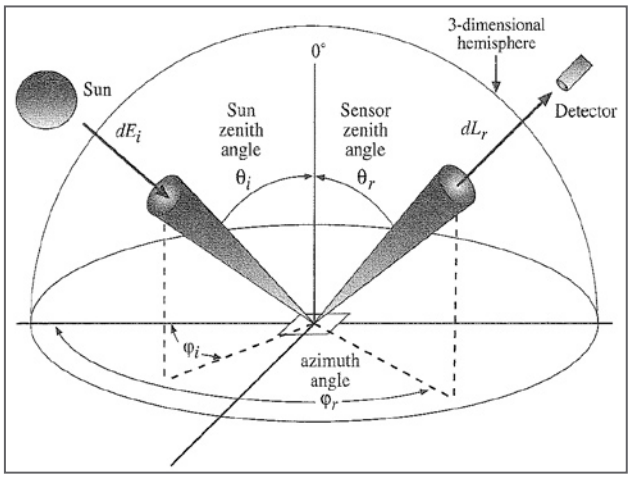

Figure 4-6: Geometry of view and illumination angles. Variation between these angles influences reflectance detected by the sensor (Jensen, 2000)

Atmospheric scattering causes the diffusion of radiation by particles in the atmosphere. Dependent on the size of the particle diameter, the Rayleigh scatter and the Mie scatter are discriminated. Rayleigh scattering results, when radiation interacts with atmospheric molecules that are smaller than the wavelength of the interacting radiation. The molecules oxygen (O_2) and nitrogen (N_2) are examples that cause this scatter. The effect of Rayleigh scattering increases towards shorter wavelengths and dominates in the blue light. Mie scattering occurs when the diameter of atmospheric particles is essentially equal to the wavelength of energy that is sensed. Water vapour and dust predominantly cause this type of scattering. It affects longer wavelengths and has less influence compared to Rayleigh scattering, whereas it is significant in slightly overcast atmospheric conditions. The diameter of particles can also be larger than the wavelength that is being scattered, which is caused for example by water droplets. The resulting scatter is nonselective in respect to wavelength and scatters all VIS, NIR and MIR wavelengths about equally. It is predominantly observable with fog and clouds (Vermote et al., 1997; Lillesand and Kiefer, 2000; Eiden, 2000).

Furthermore, the atmosphere creates an effective loss of energy due to absorption, which is mainly caused by water vapour, carbon dioxide (CO_2) and ozone (O_3). These gases absorb energy in specific wavelength bands (Figure 4-5). Water vapour for example absorbs high amounts of radiation within the NIR resulting in a decrease of reflectance by 3% to 5% (Eiden et al., 1991). There are at least five major absorption bands in the NIR and MIR, where atmospheric water vapour highly absorbs energy. They are centred at 0.97µm, 1.19µm, 1.45µm, 1.94µm and 2.7µm.

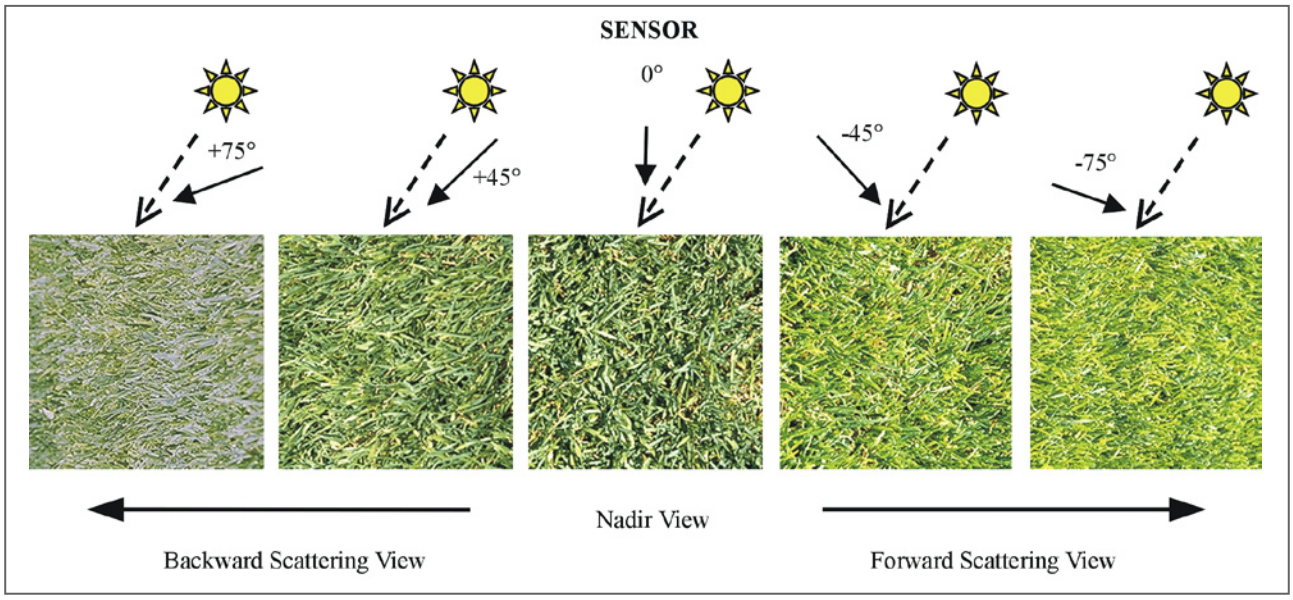

Figure 4-7: BRDF effects observed on grassland. The viewing angles vary between +75°, +45°, 0°, -45° and -75° (black lined arrow) and the sun angle persists in this example (black dashed arrow) (Spectral laboratory University Zuerich: http://www.geo.unizh.ch/rsl/research/SpectroLab/goniometry/brdf_intro.shtml, modified by the author)

The wavelength ranges, in which gases do not absorb energy and the atmosphere is particularly transmissive are referred to as atmospheric windows (Figure 4-5). Acquisition of remote sensing data is limited to these atmospheric windows (Eiden et al., 1991; Lillesand and Kiefer, 2000; Eiden, 2000).

The atmosphere is influencing reflectance differently within the VIS, NIR and MIR wavelengths. Hence, the atmosphere can cause lower or higher reflectance values derived from satellite sensors compared to surface measurements.

The reflectance detected by a sensor is also influenced by its viewing and illumination geometry. Illumination geometry is described by the angle of incidence of solar radiation expressed in sun zenith and sun azimuth angle. The position of the sensor and its scan angle express the viewing geometry noted as view zenith and view azimuth angle. Surface reflectance varies subject to variances of these view and illumination angles (Figure 4-6).

The Bi-directional Reflectance Distribution Function (BRDF) is a function of these four angles and describes the ratio of reflected radiance to incident radiance with units of inverse solid angle [sr^{-1}]. The Bi-directional Reflectance Factor (BRF) is a more practical quantity for relating to measurements as it expresses the BRDF calibrated by a coefficient to determine spectral reflectance. The BRF is unitless (Jensen, 2000; Roy et al., 2002; www4; www5). Figure 4-7 illustrates BRDF effects observed under different viewing angles of a sensor. This is an example, where source of illumination and the target on surface are consistently in the same plane. It demonstrates viewing angles of +75° and +45° in backward scattering view, 0° in nadir view, and -45° and -75° in forward scattering view. When angle of illumination and sensor viewing angle are nearly identical and in the same plane, the back scattered radiation is viewed by the sensor. This increases the brightness of the image and can cause a "hot spot". When illumination and viewing angles are in opposite directions, the forward scattered radiation is observed, which results in reduced brightness detected by the sensor (Jensen, 2000; www6; www7). Hence, vegetation reflectance shows a broad peak in backward scattering direction due to shadow hiding and has a decrease in the forward scattering direction, where higher proportion of shadowed crowns is being viewed (Roy et al., 2002).

All land surfaces exhibit some degree of anisotropy in reflectance. They present non-Lambertian reflectance properties, where incoming radiation is scattered unequally in terms of outgoing direction. Surface properties affect the angular distribution of outgoing radiation. Interactions between surface and radiation also vary in different wavelengths (Jensen, 2000; www4; www5). There are different BRDF models existing that can be used to describe various types of surfaces (www4).

4.4 The sensor MODIS

The Earth Observing System (EOS) was designed by the National Aeronautics and Space Administration (NASA) to provide observation of terrestrial, atmospheric and oceanic phenomenons and processes (JUSTICE ET AL., 2002 [1]). The first Moderate Resolution Imaging Spectroradiometer (MODIS) was integrated on the Terra (EOS AM-1) spacecraft together with four other sensors and was successfully launched on 18th December 1999. A second mission of MODIS was started on 4th May 2002, where the Aqua (EOS PM-1) spacecraft has been launched with MODIS as one of six sensors on board. MODIS data from EOS Terra and EOS Aqua have operational reception. Both platforms have a design life of 6 years (JUSTICE ET AL., 2002 [1]; www8, www9).

The circular orbit of EOS Terra and Aqua is sun-synchronous, near polar at an altitude of 705km with inclination of 98.2°. Mean period to complete an orbit is 98.8 minutes, the repeat cycle is 16 days. Equator crossing time of Terra is 10: 30 a.m. on a descending node. Equator crossing time of Aqua is 1:30 p.m. on an ascending node (GUENTHER ET AL., 2002; WOLFE, 2002; www8, www9).

Bands	Bandwidth [µm]	Spatial Resolution	Primary Use
1	0.620 - 0.670	250m x 250m	Land/Cloud/Aerosols Boundaries
2	0.841 - 0.876	250m x 250m	
3	0.459 - 0.479	500m x 500m	Land/Cloud/Aerosols Properties
4	0.545 - 0.565	500m x 500m	
5	1.230 - 1.250	500m x 500m	
6	1.628 - 1.652	500m x 500m	
7	2.105 - 2.155	500m x 500m	
8	0.405 - 0.420	1km x 1km	Ocean Color/ Phytoplankton/ Biogeochemistry
9	0.438 - 0.448	1km x 1km	
10	0.483 - 0.493	1km x 1km	
11	0.526 - 0.536	1km x 1km	
12	0.546 - 0.556	1km x 1km	
13	0.662 - 0.672	1km x 1km	
14	0.673 - 0.683	1km x 1km	
15	0.743 - 0.753	1km x 1km	
16	0.862 - 0.877	1km x 1km	
17	0.890 - 0.920	1km x 1km	Atmospheric Water Vapour
18	0.931 - 0.941	1km x 1km	
19	0.915 - 0.965	1km x 1km	
20	3.660 - 3.840	1km x 1km	Surface / Cloud Temperature
21	3.929 - 3.989	1km x 1km	
22	3.929 - 3.989	1km x 1km	
23	4.020 - 4.080	1km x 1km	
24	4.433 - 4.498	1km x 1km	Atmospheric Temperature
25	4.482 - 4.549	1km x 1km	
26	1.360 - 1.390	1km x 1km	Cirrus Clouds Water Vapour
27	6.535 - 6.895	1km x 1km	
28	7.175 - 7.475	1km x 1km	
29	8.400 - 8.700	1km x 1km	Cloud Properties
30	9.580 - 9.880	1km x 1km	Ozone
31	10.780 - 11.280	1km x 1km	Surface / Cloud Temperature
32	11.770 - 12.270	1km x 1km	
33	13.185 - 13.485	1km x 1km	Cloud Top Attitude
34	13.485 - 13.785	1km x 1km	
35	13.785 - 14.085	1km x 1km	
36	14.085 - 14.385	1km x 1km	

Table 4-1: Spectral bands and application of the MODIS sensor. (MODIS specified technical description, http://modis.gsfc.nasa.gov/about/specs.html)

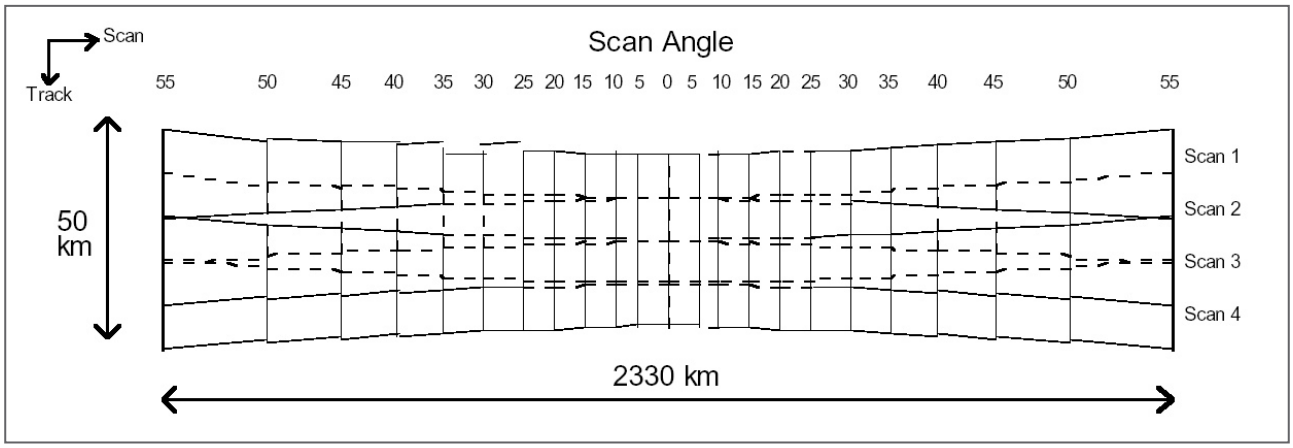

▲ *Figure 4-8: MODIS along track scanning. The adjacent scans show an increasing overlap towards the scan edge in 55° off-nadir. (Wolfe et al, 2002)*

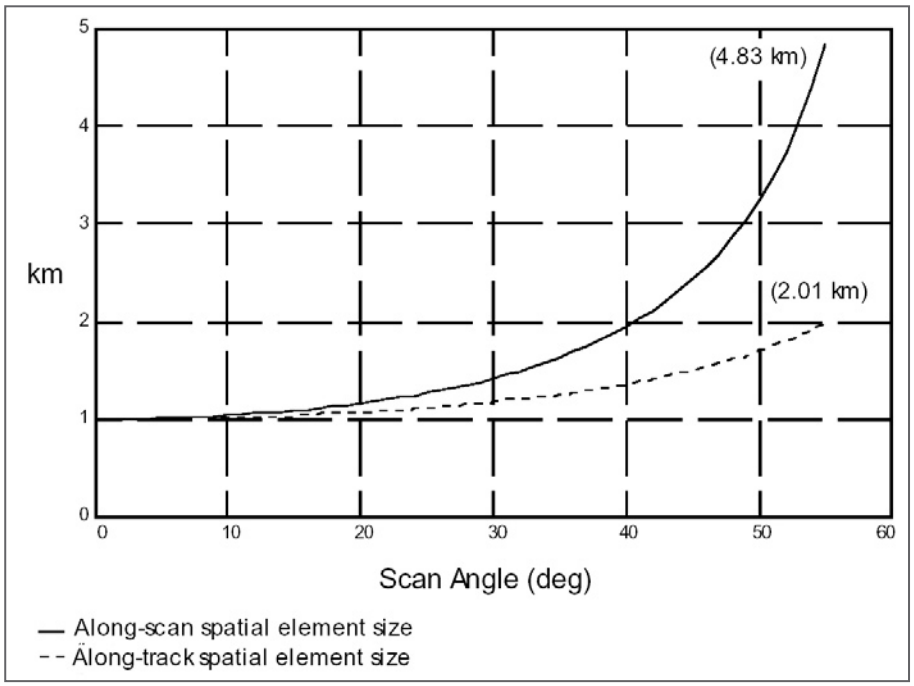

◄ *Figure 4-9: Spatial resolution of MODIS pixel at nadir and off-nadir. A 1km x 1km pixel increases to 4.83km x 2.01km at 55° off-nadir (Nishihama et al., 1997)*

▼ *Figure 4-10: Example of Bowtie artefacts (http://www.eoc.csiro.au/modis/nov02_ws/lecture3.pdf)*

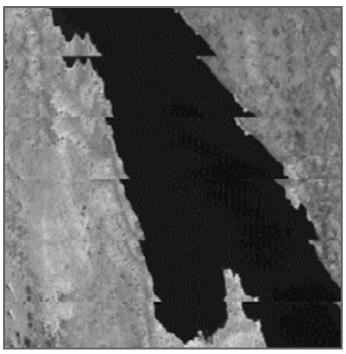

MODIS data has daily global coverage in areas greater than 30° north or south and coverage every second day in lower degrees north or south. The instrument provides high radiometric resolution of 12 bits in 36 spectral bands that range in wavelengths from 0.405µm to 14.385µm. Two bands (1 and 2) have a nominal resolution of 250m at nadir, five bands have 500m (3 to 7) and the remaining 29 bands have 1km. The spectral bands are designed for special applications as listed in Table 4-1 (Guenther et al., 2002; Justice et al., 2002 [1]; Wolfe et al. 2002, www10).

A rotating two-sided scan mirror on board of MODIS produces the across-track scanning motion with a maximum scan angle of 55° off-nadir. The sensor detects within a swath width of 2330km. The along-track scanning is provided by using the forward motion of the satellite. At nadir, the leading edge of one scan abuts the trailing edge of the next scan, while adjacent scans away from nadir begin to overlap. An overlap occurring at scan angles of 24° from nadir is 10% and increasing to a 50% overlap at the scan edge 55° off-nadir (Figure 4-8). At the same time spatial resolution increases from 1km x 1km at nadir to 4.83km x 2.01km at 55° off-nadir (Wolfe et al. 2002, Nishihama et al., 1997; www11) (Figure 4-9). This phenomenon is called the "Bowtie" effect and is explained both by the sensor´s geometry and by the earth´s curvature. It may cause consecutive detection of the same point on earth´s surface up to 3 times at the scan edge (Wolfe et al. 2002). An example of Bowtie artefacts is illustrated in Figure 4-10. The effects can be removed for visualisation purposes by reprojecting the image onto a map. They do not affect science algorithms that run on a pixel-by-pixel basis (www11). Another consequence of high view angle is a decrease in geolocation accuracy (Wolfe et al., 2002).

Sensor	Landsat 5 TM	Landsat 7 ETM+
Spectral Resolution Band: Wavelength [µm]	1: Blue: 0.45 - 0.52 2: Green: 0.52 - 0.60 3: Red: 0.63 - 0.69 4: NIR: 0.76 - 0.90 5: MIR: 1.55 - 1.75 6: TIR: 10.4 - 12.5 7: MIR: 2.08 - 2.35	1: Blue: 0.45 - 0.51 2: Green: 0.52 - 0.60 3: Red: 0.63 - 0.69 4: NIR: 0.75 - 0.90 5: MIR: 1.55 - 1.75 6: TIR: 10.4 - 12.5 7: MIR: 2.08 - 2.35 PAN: 0.52 - 0.90 (VIS - NIR)
Spatial Resolution [m]	Bands 1-5, 7: 30 Band 6: 120	Bands 1-5, 7: 30 Band 6: 60 PAN: 15
Radiometric Resolution [bit]	8	8
Temporal Resolution [days]	16	16
Swath Width [km]	185	185

Table 4-2: Technical specification of the Landsat TM and ETM+ sensors (Jensen, 2000)

Prior to the launch of Aqua, there were several anomalous detectors in MODIS band 6. The performance of MODIS band 6 on Aqua degraded seriously after launch, whereas at present the majority of band 6 detectors are nonfunctional due to focal plane delamination (Guenther et al., 2002; www12).

4.5 The sensors Landsat TM/ ETM+

Landsat is the longest-lasting operational satellite mission with high resolution of 30m. The scientific community and literature show that this satellite has many applications. Thematic Mapper (TM) and Enhanced Thematic Mapper plus (ETM+) are the most recent sensors on Landsat 5 and Landsat 7, respectively. ETM+ is the latest sensor on a Landsat spacecraft and characteristics of TM on Landsat 5 are very similar to the ETM+ (Jensen, 2000; www13; www14) (Table 4-2). Hence, only the latter will be described in details.

Landsat 7 was designed by NASA and was successfully launched on 15th April 1999. The orbit of Landsat 7 is, like MODIS, circular, sun-synchronous, and near polar at a nominal altitude of 705km with inclination of 98.2°. Mean period of the spacecraft to complete an orbit is nearly 99 minutes with a revisit interval of 16 days. Equator

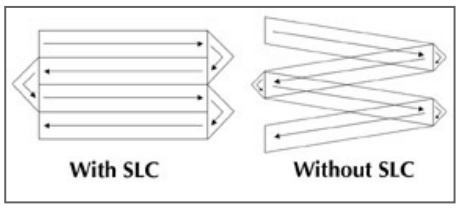

▲ *Figure 4-11: Scan Line Correction Assembly (SLC) of the Landsat ETM+ sensor. The SLC is on left and off right (http://landsat.gsfc.nasa.gov/announcements/program_update.html)*

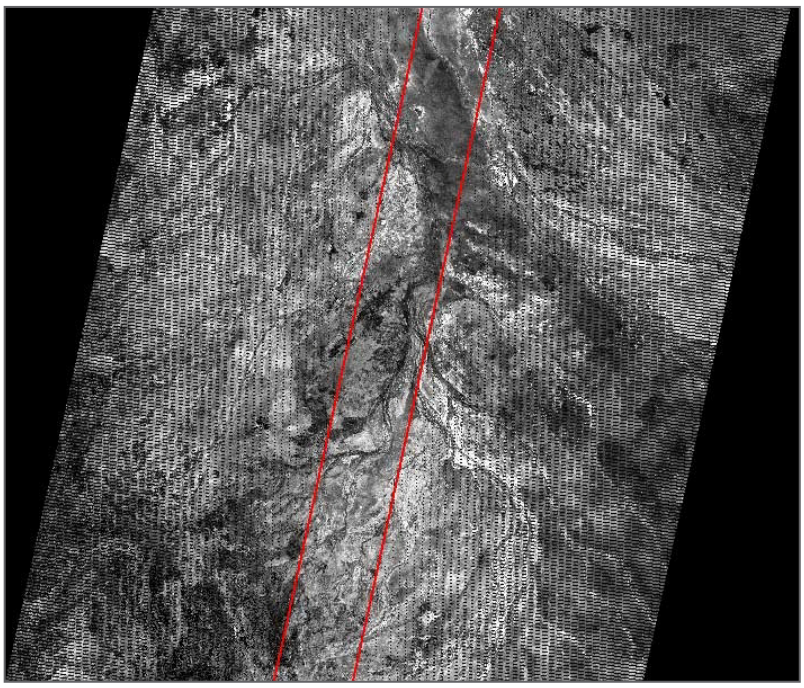

► *Figure 4-12: Impacts of the mal-functioning SLC on Landsat ETM+. The effects are most pronounced along the edge of the scene and gradually diminish toward the centre of the scene (http://www.ga.gov.au/image_cache/GA3426.jpg)*

crossing time of Landsat ETM+ is at 10:00 a.m. +/ -15 minutes on descending orbital node. (Jensen, 2000; www14; www15).

The ETM+ sensor is a single nadir-pointing instrument on-board Landsat 7 and obtains data along the ground track at a fixed swath width of 185km. At the Equator, the adjacent swaths have an overlap of 7.3% at the edges. Moving from the Equator toward either pole, the sidelap increases due to the fixed swath width (Jensen, 2000; www15).

A scene, standardised in the World Reference System as path and row numbers, covers a land area approximately 185km across-track by 180km along-track. The instrument provides a radiometric resolution of 8 bits in 8 spectral bands ranging in wavelengths from 0.45µm to 12.5µm. Bands 1 to 5 and 7 are imaged at a resolution of 30m, Band 6 at 60m, and the panchromatic Band 8 at 15m (Table 4-2) (Jensen, 2000; www15, www16).

Since late May 2003, the Landsat ETM+ sensor has a malfunctioning Scan Line Correction Assembly (SLC). This causes an oblique detection due to the forward motion of the satellite, which has originally been corrected into parallel scanning by the SLC (Figure 4-11). It results in a loss of image data of approximately 25% over any given scene. The impacts are most pronounced along the edge of the scene and gradually diminish towards the centre of the scene. There are only about 22km in the middle of the scene that contain very little duplication or data loss (Figure 4-12) (www17, www18).

4.6 Vegetation Indices

Vegetation indices are designed to enhance information about plant biophysical parameters. They normalise external effects caused by the atmosphere and varying viewing and illumination angles. At the same time internal effects such as canopy background variations, such as topography and soil variations are normalised (Jensen, 2000).

Within this research, the Normalised Difference Vegetation Index (NDVI) and the Normalised Burn Ratio (NBR) are investigated in respect to alteration of vegetation due to fire. Fire alters or consumes green vegetation at various rates of fire intensity. The magnitude of change due to fire is used as an indication of burn severity. The most accurate result of change detection can be gained by using the greatest positive or negative spectral response (Key and Benson, 1999 [1], [2]; van Wagtendonk et al., 2004).

4.6.1 The Normalised Difference Vegetation Index (NDVI)

The NDVI is the most common ratio used for vegetation studies. It responds to change in the amount of green biomass and chlorophyll content (Eiden et al., 1991; Eiden, 2000; Jensen, 2000). Reflectances in the red and NIR wavelengths are used to calculate the NDVI. The red band records the absorption of chlorophyll, whereas lower values indicate higher chlorophyll content. The NIR band detects high values of reflectance, when vegetation is dense and grows vigorously. Hence, many leaves reflect NIR wavelengths due to their internal structure (Sabins, 1996).

The NDVI for MODIS is calculated by subtracting reflectance of red band 1 (R1) from the NIR band 2 (R2) and is normalised by dividing by its sum (Equation 4-3). The NDVI of MODIS provides information in spatial resolution of 250m in both bands.

$$NDVI_{(MODIS)} = \frac{(R2 - R1)}{(R2 + R1)} \quad \text{(Equation 4-3)}$$

The NDVI for Landsat TM/ETM+ is calculated similar to MODIS using reflectance of band 3 in the red (R3) and band 4 in the NIR wavelength (R4) (Equation 4-4). Landsat TM/ETM+ provide the index information in spatial resolution of 30m.

$$NDVI_{(TM/ETM+)} = \frac{(R4 - R3)}{(R4 + R3)} \quad \text{(Equation 4-4)}$$

Results are unitless and can theoretically vary in the range between –1.0 and 1.0. With increasing vegetation density and thus photosynthetic activity, NDVI values are increasing. Thus, high values are expected to characterise healthy unburnt vegetation. Low values correspond to lower vegetation density and thus highly reduced photosynthetic activity. The NDVI is investigated in respect to alteration of vegetation due to fire.

4.6.2 The Normalised Burn Ratio (NBR)

The NBR is an algorithm that integrates the two spectral bands that have the greatest response to landscape change due to fire (Key and Benson, 1999 [1],[2]). These bands are centred in the NIR wavelength between 0.7µm to 0.9µm

and in the MIR wavelength between 2.0µm to 2.4µm. The NIR reflectance provides the highest discrimination for loss of biomass. There are high values reflected from dense vegetation and low values from sparse vegetation. The MIR wavelengths detect low reflectance when the surface is vegetated. Reflectance is increased, when soil is exposed or leaf water content is low (Key and Benson, 1999 [1],[2]; Jensen, 2000).

The index is calculated by subtracting reflectances of band 7 from band 2 of MODIS data. It is scaled by the sum of the two bands to normalise within-scene topographic effects and between-scene solar illumination effects (Key and Benson, 1999 [1], [2]) (Equation 4-5). The NBR derived from MODIS is composed of spatial information in resolution of 250m from band 2 and 500m from band 7.

$$NBR_{(MODIS)} = \frac{(R2 - R7)}{(R2 + R7)} \quad \text{(Equation 4-5)}$$

The NBR has originally been applied to Landsat TM/ETM+ data, where reflectance of band 7 (R7) in the MIR is subtracted from reflectance of band 4 (R4) in the NIR (Equation 4-6) (Key and Benson, 1999 [1], [2]). Ground resolution is 30m.

$$NBR_{(TM/ETM+)} = \frac{(R4 - R7)}{(R4 + R7)} \quad \text{(Equation 4-6)}$$

Results are unitless and vary in the range between –1.0 and 1.0. Due to the spectral properties of vegetation and soil, positive values reflect high amounts of biomass, whereas negative values correspond to predominantly exposed soil and increasing leaf dryness.

In order to quantify the vegetation change due to fire, the image differencing index ΔNBR is calculated. Thus the NBR derived post-fire is subtracted from the NBR calculated from pre-fire data (Key and Benson, 1999 [1], [2]) (Equation 4-7).

$$\Delta NBR = NBR_{prefire} - NBR_{postfire} \quad \text{(Equation 4-7)}$$

Results are unitless and vary between –2.0 and 2.0. The ΔNBR expresses the magnitude of change that fire has caused, whereas high values refer to a higher degree of change within the landscape (Key and Benson, 1999 [1], [2]).

When the NBR was applied to MODIS, another possibility considered was to calculate the index from band 5 instead of band 2. Band 5 is centred at 1.24µm at the edge of the NIR and has a spatial resolution of 500m. This means, that spatial information is reduced compared to 250m resolution of band 2. Band 5 is at the same time located on the edge of liquid water absorption and is therefore highly influenced by variabilities in water content (Zarco-Tejada et al., 2003). The NBR using MODIS bands 5 and 7 was not further investigated in this study, as highest discrimination between biomass and soil exposure is apparent in bands 2 and 7.

Chapter 5: Data and Data Preprocessing

This chapter describes all data used in this study. Satellite remote sensing data from MODIS were assessed for the measurement of burn severity in the study area. Data from the MODIS and Landsat TM/ETM+ sensors were compared to validate the moderate spatial resolution of MODIS. A high correspondence between MODIS and Landsat has been well presented in past scientific research (Liang et al., 2002; Rojas et al., 2002; Price, 2003; Sà et al., 2003). Another compatible sensor for MODIS validation could be the *Advanced Spaceborne Thermal Emission and Reflection* (ASTER) radiometer, which sits on the Terra platform. However, image acquisition is limited as predominantly areas specified by principle investigators of the ASTER science team are taken (Rojas et al., 2002). Ground truth data were collected within a field campaign in the study area to further validate the remote sensing data. Data preprocessing was carried out using ER Mapper 6.4 and ArcView 3.2.

5.1 MODIS Data

MODIS has twice daily coverage in south-west WA from a morning Terra overpass and an afternoon Aqua overpass. Within 24 hours, four images from MODIS are available due to night time acquisitions of Terra and Aqua overpasses. Data are received as direct broadcast in near-real time at the *Western Australian Satellite Technology and Applications Consortium* (WASTAC) station located at Murdoch University, Perth. The raw data is processed with *International MODIS / AIRS Processing Package* (IMAPP) to get radiometric and geometric calibrated Level 1B data. Level 1B data

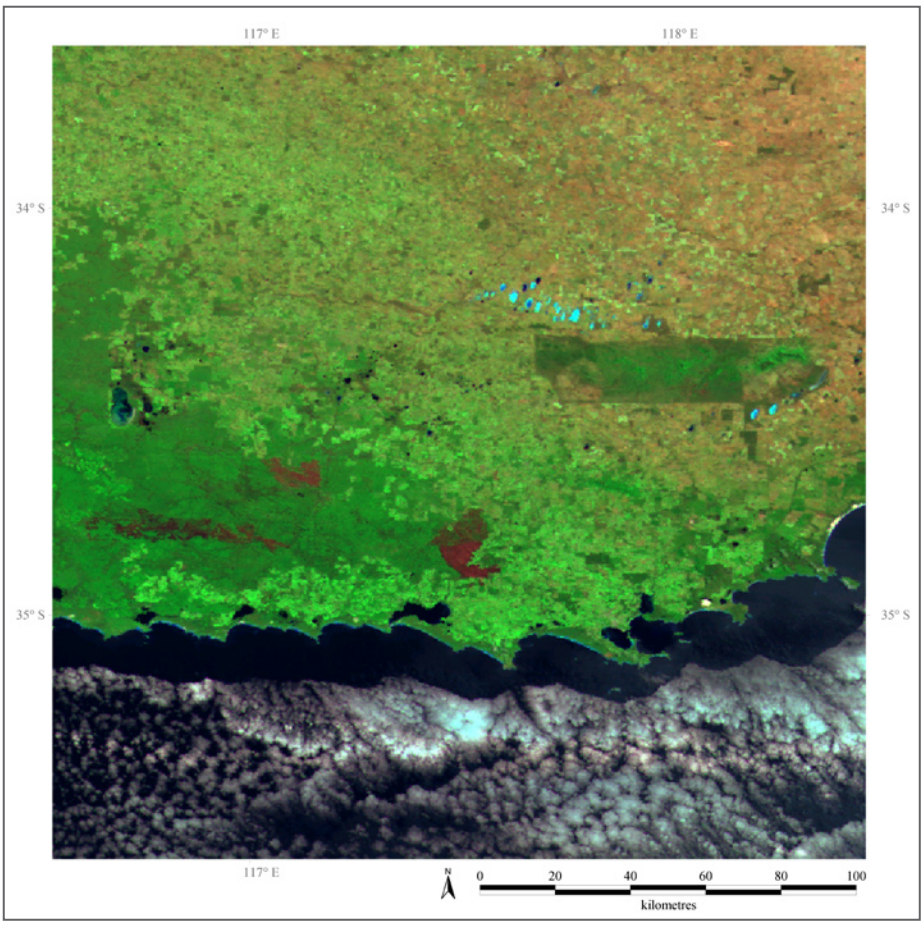

Figure 5-1: MODIS image over study area. It presents a subset of the study area, as all MODIS data was provided in this study (MODIS on Terra, 26th Nov 02, R-G-B as 7-2-4). (Department of Land Information - Satellite Remote Sensing Services)

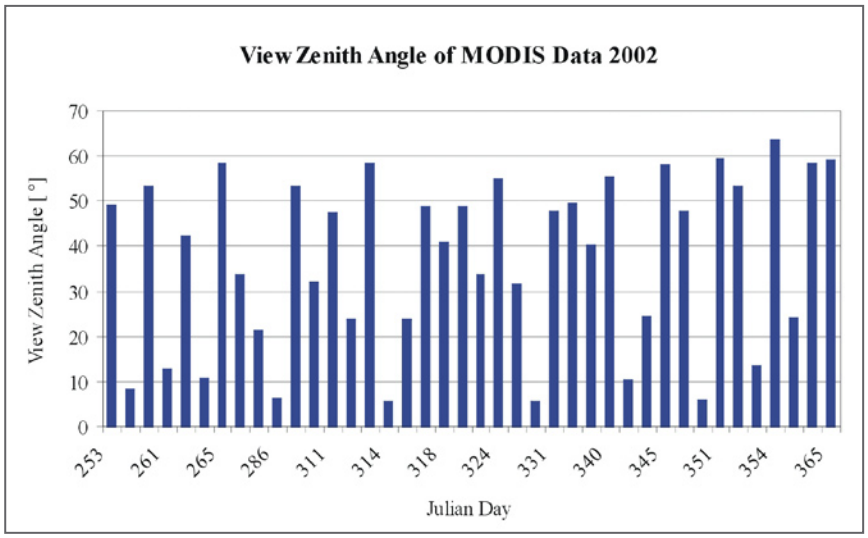

Figure 5-2: View zenith angle of MODIS data used in this study.

were provided by the *Department of Land Information* (DLI) *Satellite Remote Sensing Services* (SRSS) in the *Hierarchical Data Format* (.hdf) Version 4. In this data format additional metadata can be saved.

MODIS data were calibrated into reflectance in order to enable spectral analyses and comparison between sensors. The data calibration into reflectance R of the spectral bandwidth λ is specific for the sensor as defined in Equation 5-1 (NASA, 2000).

$$R_\lambda = \frac{R\_scales_\lambda * (DN_\lambda - R\_offset_\lambda)}{\cos sz} \quad \text{(Equation 5-1)}$$

In equation 5-1, DN refers to the digital number of pixels within each spectral band λ. R_scales and R_offset represent the calibration parameters, which are written as attributes to the reflective bands λ. The sun zenith angle sz is provided in the HDF metadata. All reflectance values were multiplied by 10^4 and stored as signed 16bit Integer with null value –32,767.

MODIS scenes from 1st September to 31st December 2002 and from 1st April to 31st May 2004 were reprocessed from the DLI archive as described above. Data from Aqua and Terra were provided as subsets covering the study area from 116°30'E to 118°30'E and 33°36'S to 35°36'S (Figure 5-1). The data were projected as latitudes/longitudes with World Geodetic System 1984 (WGS84) datum. Each band of the scenes was available in the standard generic binary format with an ER Mapper header file (.ers).

In this study, all MODIS 2002 data were provided as top of atmosphere reflectance (TOA), atmospheric corrected bottom of atmosphere reflectance (BOA) and BRDF corrected nadir reflectance (NADIR). Atmospheric correction of MODIS data was done by using the Simplified Method for Atmospheric Corrections (SMAC) (Rahman, H. and Dedieu, G., 1994). BRDF effects were corrected by using the Ross-Thick/Li-Sparse kernel driven model (Strahler et al., 1999; Maier, 2004). This processing, which is on a pixel-by-pixel basis is only possible, if at least 7 cloud free observations are available within the last 30 days. More detailed description of this data processing is beyond the scope of this work.

MODIS scenes acquired in 2002 were provided as TOA reflectance from bands 1 to 7. The sun zenith, sun azimuth, view zenith and view azimuth angles were included in the data of each acquisition (see Table A1-1, Appendix). For the same dates, atmospheric and BRDF corrected data (BOANADIR) were available with bands 1 to 5, 7 and the view zenith angle (see Table A1-2, Appendix). Data of September could not be corrected for many pixels in the FAAs due to few cloud free information. In order to investigate corrected data pre-fire, September data was additionally provided as BOA reflectance. The BOA scenes contained a subset of bands 1 to 5, 7 and sun zenith, sun azimuth, view zenith and view azimuth angles (see Table A1-3, Appendix).

MODIS data used in this work were inspected for cloud cover on the selected FAAs. The maritime influence of the Southern Ocean favours cloud cover within the study area, especially close to winter between June and September. This reduced the amount of MODIS images useful for this research. The MODIS TOA and BOA data of the year 2002 were cloudmasked to avoid outliers within the analysis. The cloud masking was based on visual identification of clouds in the satellite images. All MODIS scenes used in this study were displayed as real colour composite (R-G-B = 1-4-3). Within the boundaries of FAA1 to 3 clouds were visually detected. They were masked, when reflectance in band 1 was higher than the

corresponding threshold set by the author. The threshold, dependent on the scene, varied between 7.5% (750) and 17% (1700) reflectance (see Tables A1-1 and A1-3, Appendix). Band 1 was used for cloud masking, as it is still highly reflective due to clouds. It provides higher spatial resolution compared to blue band 3, where clouds are generally more highlighted. The scenes with no clouds in FAA1 to 3 were excluded from masking. Each cloud mask was added as a separate layer to the corresponding scene of MODIS data. Thus pixels in all bands were masked when the pixels were included in the cloud mask. The cloud cover of FAA1 to 3 and masking threshold of each image used in the study are presented in the Appendix (Tables A1-1 and A1-3).

The MODIS images have been georeferenced during the processing through IMAPP to Level 1B data. The geolocation accuracy correlates with the scan angle of the instrument, as errors are lowest at nadir view and geolocation becomes less accurate towards off-nadir view angle (Wolfe et al., 2002). There was a third update of the interior orientation parameters of MODIS instruments in March 2001. Since then the geolocation accuracy of MODIS Level 1B data was estimated to approach 50m (Wolfe et al., 2002).

The high swath dimension of MODIS (2330km) results in view angles between –65° and +65°. The reflectance of MODIS TOA and BOA data is not corrected in respect to BRDF effects. The variations of the average view angle between images used in this study are illustrated in Figure 5-2.

5.2 Landsat TM / ETM+ data

Landsat TM and ETM+ data used in this research were bought from the Australian Centre of Remote Sensing (ACRES) as Level 1B data. The scenes with path 111 and row 84 cover the study area. Landsat scenes from five different dates in the years 2002 to 2004 were collected and processed to have data of reference before the fire and data post-fire for each FAA considered within the study area. All images were subset to bands 1 to 5 and 7 (see Table A1-4, Appendix). Landsat imagery was provided in Universal Transversal Mercator (UTM) projection zone MGA50 and Geocentric Datum of Australia 1994 (GDA94). The data were imported into ER Mapper 6.4, where all further data processing was completed. The images were reprojected to latitude/longitude projection with WGS84 datum.

Image values of Landsat data were calibrated into reflectance values in order to analyse and compare their spectral properties with MODIS spectra. The conversion of Landsat Level 1B data into top of atmosphere reflectance values required the definition of radiances as specific for the Landsat TM/ETM+ sensors. The radiance L with unit [W/(m²*sr*μm)] is defined for Landsat TM/ETM+ with bandwidth λ as presented in Equation 5-2 (www1).

$$L_\lambda = (DN_\lambda * gain_\lambda) + offset_\lambda \quad \text{(Equation 5-2)}$$

In Equation 5-2, DN refers to the digital number of pixels within each band λ. The gain and offset for each spectral band per scene were available in the metadata.

Landsat data has been calibrated into reflectance based on Equation 5-3 (www19). This equation is derived for Landsat data based on reflectance as defined in Equations 4-1 and 4-2 (Chapter 4.1).

$$R_\lambda = \frac{\pi * ((DN_\lambda * gain_\lambda) + offset_\lambda) * d^2}{E_{sun\lambda} * \cos sz} \quad \text{(Equation 5-3)}$$

The sun earth distance d [1AE] on day of acquisition and the mean extraterrestrial solar irradiance E_{sun} for each spectral band λ are provided in the Landsat Handbook (www19). The sun zenith angle is derived from the sun elevation angle, which is delivered with the image metadata. The Landsat TM/ETM+ reflectance was stored as 4byte real to avoid loss of information.

Landsat data were provided from the dates 12th February 2002, 26th November 2002 and 12th December 2002 as complete scenes with path 111 and row 84. Data from 23rd December 2003 were available as subset with extension from 116°44'32.78"E to 116°59'12.72"E and 34°35'4.56"S to 34°57'56.01"S. Data from 31st May 2004 were bought as subset with extension from 116°46'4.45"E to 116°57'54.72"E and 34°36'47.55"S to 34°55'12.1"S.

As the study area was free of clouds in all five Landsat scenes, cloud masking was not required. Landsat TM/ETM+ images were provided from ACRES as georeferenced product and resampled with Cubic Convolution method. Images of 12th February 2002, 12th December 2002 and 23rd December 2003 were again rectified with an accuracy assessment based on 100 to 150 GCPs (Wu, 2004). The geometric accuracy of the images from 26th November and 31st of May was assessed based on 5 GCPs. The Root Mean Square errors (RMS) along track and across track are listed for

each data in the Appendix (Table A1-4). The pixel size of Landsat data as measured in ArcView were 25m rather than 30m ground resolution of the sensor configuration.

5.3 Comparison of MODIS and TM/ETM+ data

The moderate resolution MODIS imagery and high resolution Landsat TM/ETM+ imagery are compared in this research for the purpose of validation. It is required, that data are comparable between the sensors. The spectral bands 1 to 7 of MODIS and 1 to 5 and 7 of Landsat are investigated in this work.

The Terra platform and Landsat 7 were launched into identical 705 kilometer, sun-synchronous orbits. Equator crossing time of Landsat 7 is ideally 15 minutes ahead of Terra, as equator crossing time of Landsat 7 is 10.00 am +/- 15 minutes and of Terra is at 10.30 am. Therefore data acquired by MODIS on Terra and Landsat 7 are under nearly identical atmospheric and plant physiological conditions (see Chapter 4.4 and 4.5; www15).

The spectral bands 3, 4, 1, 2, 6 and 7 of MODIS match with the spectral range of Landsat TM/ETM+ bands 1, 2, 3, 4, 5 and 7, respectively. The MODIS and TM/ETM+ bands do not exactly match, as TM/ETM+ bands are generally slightly broader. This is due to energy considerations (Liang et al., 2002; Price, 2003). In this research the red, NIR and MIR bands 1, 2 and 7 of MODIS and 3, 4 and 7 of Landsat are used to construct the NBR and NDVI. The spectral responses of the corresponding bands of MODIS, Landsat TM and ETM+ are compared in Figures 5-3 to 5-5. It is significant that MODIS and Landsat bands do not exactly match. MODIS bands are all integrated in the same wavelength regions compared to the corresponding Landsat spectral bands, whereas in the MIR band 7, deviations between the MODIS band centre and Landsat band centres are most accentuated.

The moderate resolution of MODIS with 250m to 500m reduces the detail of features visible in the MODIS image compared to 30m resolution of Landsat. Due to their spatial resolution, the likelihood that MODIS surface reflectance relates to mixed surface is higher compared to Landsat data (Price, 2003). Data from MODIS are influenced by BRDF effects due to varying view angles, whereas Landsat scanning is only pointing at nadir.

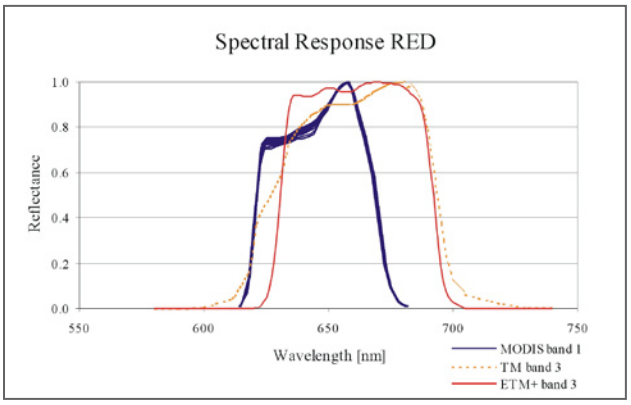

Figure 5-3: Spectral response of MODIS and Landsat TM/ETM+ bands in the red wavelength

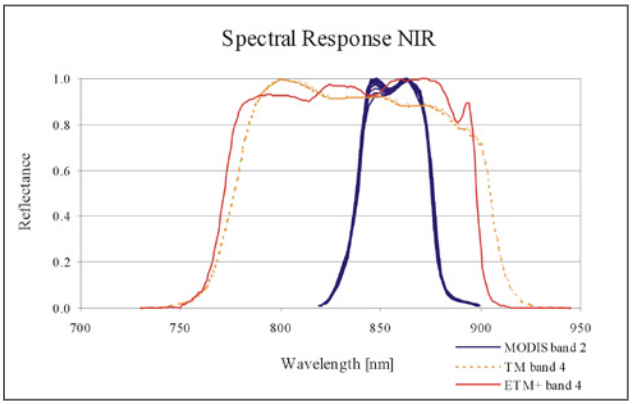

Figure 5-4: Spectral response of MODIS and Landsat TM/ETM+ bands in the near infrared (NIR) wavelength

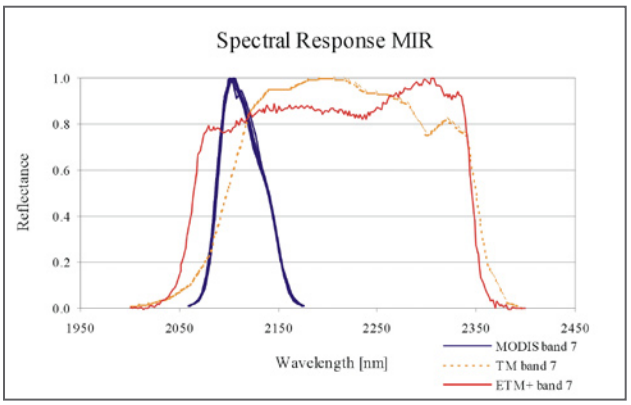

Figure 5-5: Spectral response of MODIS and Landsat TM/ETM+ bands in the middle infrared (MIR) wavelength between 1.9 and 2.5µm
(Spectral response of MODIS on Terra in Figures 5-3 to 5-5: http://www.mcst.ssai.biz/mcstweb; Spectral response of Landsat in Figures 5-3 to 5-5: http://ltpwww.gsfc.nasa.gov/IAS/handbook/handbook_htmls/chapter8/chapter8.html#section8.1.2.1)

5.4 Other data

In this study, various other datasets have been used during the processing and analysis phase. A digital topographic mosaic of Australia with scale 1:250,000 was used creating a subset of the study area. The data were provided by the *Government Division of National Mapping* (NATMAP) in a compressed format (.ecw). The data was projected in latitudes/longitudes with GDA94. A subset of the study area in south-west WA was extracted to a generic binary format and projected in latitudes/longitudes with WGS84. A map of the broad native vegetation types of south-west WA was completed in June 2004 by the *Department of Agriculture of WA* and used as a GIS layer. The mapping was based on a vegetation map scaled 1:250,000. It was provided as ESRI Shapefile Format (.shp) projected in latitudes/longitudes with GDA94. Further the *Interim Biogeographic Regions of Australia* (IBRA) were provided as ESRI Shapefile format in latitudes / longitudes with GDA94 (THACKWAY AND CRESSWELL, 1995). The South-West Botanical Province was extracted from the data set using ArcView.

Field data were acquired from 16th to 18th of June 2004 during a field trip in cooperation with CALM. Information gathered during the field visit provided broad insights into fire behaviour within various structured ecosystems and fire management. Detailed fieldwork focused on the classification of burn severity in the field, which was supported by fire coordinators from CALM. Altogether, 62 GCPs were sampled within different structures of vegetation. The position was defined with a handheld GPS (GARMIN 12XL) with positional accuracy of 15m. 35 GCPs were taken along the boundary of FAA4 for ground truth validation. The area was subject to prescribed burning approximately 6 weeks before the visit and carries the ecosystems of jarrah-marri forest and flat shrubby woodlands. The remaining 27 GCPs were sampled in recently burnt areas outside the coverage of Landsat data. The points were sampled for the purpose of comparing different ecosystems. At most GCP, several digital photos were taken on ground in a 180° view angle.

Chapter 6: Methods and Analyses

In this research, MODIS data were investigated to measure burn severity in the south-western forests of WA. MODIS has moderate spatial resolution and needs to be validated with high spatial resolution satellite data to resolve scaling up issues (Liang et al., 2002; Sá et al., 2003). Landsat imagery is well suited, because the spectral bands between VIS and MIR wavelengths of Landsat are centred in similar wavelengths compared to MODIS. Landsat data has been shown in the literature to be suited to measuring burn severity (see Chapter 2). Ground truth data were collected in the field to validate the Landsat burn severity data.

Initially, the extents of FAAs were mapped. The indices NDVI, NBR and ΔNBR were derived for data of both sensors. The spectral properties and index values of MODIS and Landsat ETM+ data were analysed within fire affected areas. The effects of atmosphere and off-nadir scan angles were considered. Different levels of burn severity were classified using information collected in the field and compared to the remote sensed data.

6.1 Mapping Fire Affected Areas (FAAs)

Fire affected areas can be detected from remote sensing data due to the spectral signals changing from the surrounding vegetation cover (see Chapters 4.1 and 4.2). The extent of a FAA is a fundamental aspect for burn severity measurement. The spatial resolution of the sensor determines the accuracy of mapping the boundary of FAAs. It is important to map burnt areas as soon as possible post-fire, because the "burn signal" becomes progressively weaker as the burnt area ages due to dissipation of charcoal and ash and regrowth of vegetation post-fire (Eva and Lambin, 1998 [2]; Roy et al, 2002).

Landsat TM/ETM+ satellite imagery with 30m accuracy was used to map the boundaries of FAAs . There were two Landsat post-fire images available for mapping FAA1 to 3 in the year 2002 (see Chapter 5.2). The first post-fire image was acquired in November, the second in December.

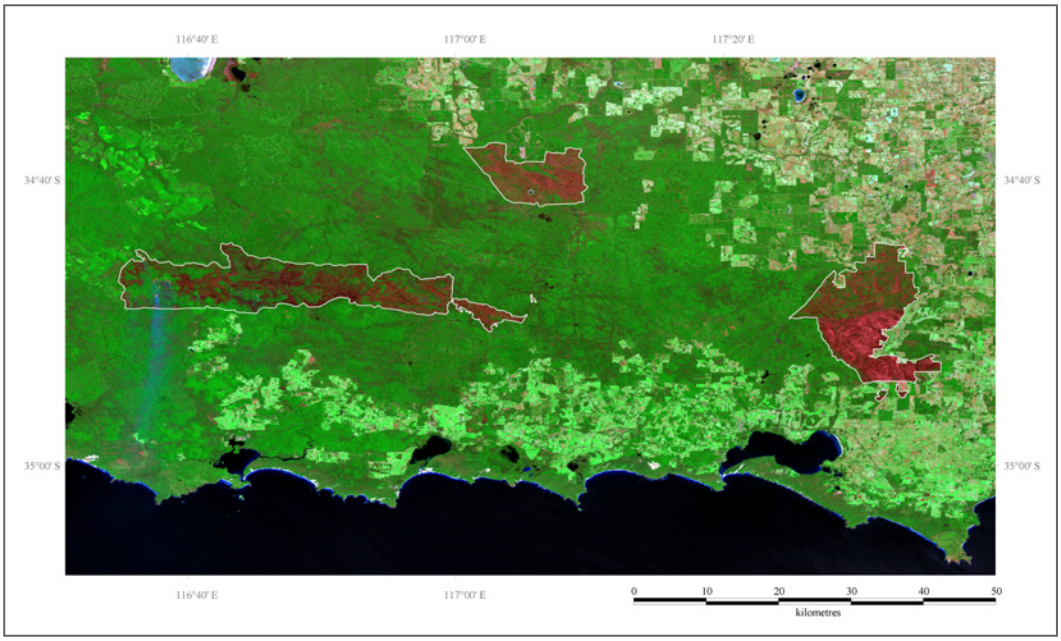

Figure 6-1: Landsat ETM+ image of study area showing mapped fire affected areas of the year 2002. This scene acquired on 12th Dec 02, displayed as R-G-B- as 7-4-2, provided the basis for mapping the fire affected areas 1 to 3, which occured in Oct and Nov 2002 (Image: Australian Centre of Remote Sensing (ACRES))

Images were viewed in true colour composite (bands 3-2-1 as R-G-B) to check for the presence of cloud, smoke and cloud shadow. Both images were cloud free over the FAAs, however there was some smoke visible within FAA3 in the December Landsat scene. Various band combinations of Landsat post-fire images were examined. The display of bands 7-4-2 as R-G-B was considered most suitable for mapping FAAs due to the high visible discrimination between burnt and unburnt areas. Burnt areas are accentuated in this band combination due to high reflectance in the MIR band 7 and low reflectance in the NIR band 4. The Landsat ETM+ image of 12th December 2002 was used to map FAA1 to 3 in order to take the latest extent of burnt areas into account, as fire was still active (Figure 6-1). The boundary of each burnt area within the study area was digitised on-screen. The extent of FAA4 was digitised based on Landsat TM image of 31st May 2004 (7-4-2 as R-G-B). These boundaries describe the whole burn envelope including unburnt patches as they are considered in the burn severity measurement.

The boundaries of all FAAs were saved in the ER Mapper Vector Format (.erv) projected in latitudes and longitudes with WGS84 datum. The vector polygons were converted into an ESRI Shapefile Format (.shp) to enable the handling of boundaries either in ER Mapper or in ArcView, as both software packages were used in this work.

6.2 Derivation of NDVI, NBR and ΔNBR

The first step was to create the NDVI, NBR and ΔNBR indices for the MODIS and Landsat ETM+ data used in this study.

The NDVI and NBR derivation of MODIS reflectances were processed by calling the executable ndvi2.exe based on Equations 4-3 and 4-5 in Chapter 4 (Maier, 2004). Index values were multiplied by 10^3 to store data as signed 16bit Integer with results varying between –1000 and 1000. Hence, multiple NDVI and NBR data with pre-fire and post-fire dates were available. The index imagery was cloud masked with the same mask as the spectral bands of the corresponding datum (see Chapter 5.1). In order to derive the image differencing index ΔNBR, mean values of the NBR pre-fire and NBR post-fire dates were calculated. Mean values were expected to result in higher accuracy for the ΔNBR. The calculation of mean NBR data was derived by processing all input files through the program mean2.exe (Maier, 2004). This program ignores the pixel with cloud masked null values in its mean calculation. The dates included in the input file were adjusted to dates of burn start and burn completeness. The dates were identified in the images displayed as real colour composite (R-G-B = bands 1-4-3).

	Pre Fire Data [Julian Day] 2002	**Post Fire Data** [Julian Day] 2002
ΔNBR_{MODIS}	253, 254, 256, 261, 262, 263, 265, 271, 272, 286, 304	323, 324, 329, 330, 331, 333, 334, 340, 343, 344, 345, 347, 350, 351, 352, 353, 354, 360, 361, 365
ΔNBR_{Nov}	42	330
ΔNBR_{Dec}	42	346

Table 6-1: List of data used to derive the ΔNBRs, which were used to classify MODIS and Landsat imagery for further analyses. The dates to derive the ΔNBR_{MODIS} are based on MODIS data, the dates to derive ΔNBR_{Nov} and ΔNBR_{Dec} refer to Landsat ETM+ data

Analyses of MODIS data focused on FAA1 because it exhibited the most favourable study site due to its clear separation of prescribed low intensity burn and high intensity wildfire. Burning was apparent between 5th November and 17th November 2002 on FAA1. Thus, scenes of September and October 2002 were included in the mean NBR to construct the pre-fire image. The scenes recorded after 17th November 2002 were used to calculate the mean NBR post-fire (Table 6-1). The ΔNBR_{MODIS} was derived from the resulting mean NBR images based on equation 4.6.2.3. Results vary between –2000 and 2000.

The NDVI, NBR and ΔNBR for Landsat TM/ETM+ imagery were derived in ER Mapper. The NDVI and NBR were calculated from reflectance values of bands 3, 4 and 7 of corresponding dates based on Equations 4-4 and 4-6. For each of the five Landsat scenes used in this study, a NDVI and NBR image were available. The resulting values were multiplied by 10^3 to store data as signed 16bit. Resulting values vary in the range between –1000 and 1000. The ΔNBR of Landsat data acquired in the year 2002 was calculated using February as pre-fire image and both November and December data as post-fire image. The ΔNBR of Landsat data was derived for FAA4, as ground truth data was available for validation. The December 2003 image has been used as pre-fire image and data from May 2004 as post-fire image. Processing of the ΔNBR images was accomplished in ER Mapper based on Equation 4-7 with results varying between –2000 and 2000.

6.3 Analysis of MODIS Imagery

The spectral properties and index values of the NDVI and NBR of MODIS data between 1st September and 31st December 2002 were analysed. To consider the influence of atmosphere and BRDF effects within a FAA, analyses were accomplished using both, uncorrected top of atmosphere reflectance (TOA) data corrected for atmospheric and BRDF effects (BOANADIR). The analyses focused on FAA1, because it exhibited the most favourable study site due to its clear separation of prescribed low intensity burn and high intensity wildfire.

Analyses of remote sensing data were based on regions of uniformly classified ΔNBR images. Low values of the ΔNBR indicate less or no change due to fire while high values exhibit change due to fire (Key and Benson, 1999 [1],[2]). The ΔNBR values between 0 and 800 exhibited greatest contrast within the FAA and were classified into 6 different classes of burn severity using thresholds in steps of 200 (Table 6-2). Setting of thresholds is not adjusted to field data, ecosystem and sensor at this stage.

All analyses of MODIS data were based on the classification of the ΔNBR_{MODIS} image, as previously explained. The spectrum of each MODIS scene was investigated for all classes of burn severity within FAA1. This analysis was to represent the spectral characteristics of MODIS data within surfaces of differently altered vegetation. The spectral range between VIS and MIR as shown in the literature is most informative to detect burnt areas. Bands 1 to 7 of all MODIS TOA data were considered in the analyses. Due to high cloud coverage, calculation of BRDF correction was very limited for BOANADIR data in September 2002 (see Table A1-2, Appendix). The gap of missing data in September was filled with cloud masked BOA data. Bands 1 to 5 and 7 of each BOA (September) and BOANADIR (October to December) scene were considered. Band 6 of BOA and BOANADIR data were not provided due to nonfunctional band 6 detectors of MODIS on Aqua. All MODIS bands used in these analyses were cloud masked (see chapter 5.1). Thus pixels with no information of the ground were excluded and outliers avoided. The derivation of the mean spectral signatures for all data within separated classes of burn severity was accomplished in ER Mapper. The resulting reflectance values were further sorted in Microsoft Excel.

The trends of NDVI and NBR values of all available MODIS data were investigated within different classes of burn severity based on the ΔNBR_{MODIS} image. The index values were derived from reflectance values of MODIS as described in the latter section (chapter 6.2). The mean index values of all dates were calculated for each class of FAA1 to investigate their trend through time and their detection of the change due to fire.

Classification of the ΔNBR	
Class Number	**ΔNBR Threshold**
Class 1	< 0
Class 2	0 to < 200
Class 3	200 to < 400
Class 4	400 to < 600
Class 5	600 to < 800
Class 6	> 800

Table 6-2: The classification of the ΔNBR, which provided the fundament for further data analyses. It was uniformly applied to MODIS and Landsat ETM+ data to create regions of burn severity.

To investigate a more detailed analysis of MODIS data within burnt areas, single MODIS pixels with spatial resolution of 250m x 250m were examined. The goal was to examine the variance of spectral signals and index values of the same pixel between different scenes. Five pixels were arbitrarily selected within homogeneous classes of burn severity based on the classification of the ΔNBR_{MODIS} image. The marginal areas within the classes were avoided, as edge pixels are expected to be more heterogeneous. The boundaries of the selected MODIS pixels were digitised on-screen for the analyses. The spectral signatures of all cloud masked MODIS data were derived for a selected pixel for each class. The index values of the NDVI and NBR were calculated from reflectance of bands 1, 2 and 7 of each data within the selected pixels based on Equations 4-3 and 4-5, respectively. The resulting index values were multiplied by 10^3 to compare results with analyses of complete classes of burn severity.

6.4 Analysis of Landsat TM/ ETM+ Imagery

The analysis of Landsat TM/ETM+ imagery focused on the investigation of the spectral signature and index values of the NBR and NDVI. Three scenes from the Landsat ETM+ sensor were analysed from year 2002 (FAA1 to 3). Two more scenes from the Landsat TM sensor with one pre-fire image (Dec 2003) and one post-fire image (May 2004) were collected to be analysed with field data of FAA4.

A pre-fire image was collected in February 2002. There was not a satisfactory cloud free image available closer to the fire event. The reflectance change of evergreen vegetation in south-west WA within the temporal gap of 9 months between February and fire occurrence in November 2002 was estimated within unburnt test areas. The test areas were digitised on screen from the Landsat ETM+ scene of 12th December 2002, displayed with bands 7-4-2 as R-G-B. Four regions comprising about 95,000 pixels were arbitrarily selected in the forested neighbourhood of the fire affected areas, where no change due to fire was visible. The spectral properties of the three Landsat scenes of 2002 were analysed within the test region. To measure changes post-fire, two ETM+ images in November and December 2002 were available.

The classifications of the ΔNBR_{Nov} and ΔNBR_{Dec} images provided the basis for the analyses of all Landsat data. The ΔNBR_{Nov} and ΔNBR_{Dec} images were uniformly classified based on the same thresholds used for classifying the ΔNBR_{MODIS} image (Table 6-2). The mean reflectance of bands 1 to 5 and 7 of each Landsat ETM+ scene were derived for each class of burn severity from both classifications within FAA1 to 3. The trends of mean NDVI and mean NBR values of the three Landsat scenes acquired in 2002 were investigated within different classes of burn severity.

6.5 Field Measurement of Burn Severity

A field trip to the study area was carried out from 16th to 18th June 2004. CALM fire coordinators from the Walpole region accompanied the reasearcher and assisted in defining a field classification of burn severity. Ground truth data were collected to validate the remote sensing measurement of burn severity in FAA4. There were 35 GCPs collected approximately 6 weeks post-fire within open shrubland, open woodland and jarrah-marri forest.

The measurement of burn severity in the field can be assessed using several approaches. It is based on a subjective description which is dependent on the user's focus and objective. Measuring burn severity can follow an ecological approach focusing on plant species that are endangered or more prevalent due to fire. The time vegetation takes to regenerate to the initial point before fire is an essential criterion to measure burn severity. There are certain species used as indicators to observe the regeneration or resprouting process within a burnt area (Fox, 2004; Cox, 2004). A highly severe fire in the study area eliminates species such as *Macrozamia riedlei*, whereas a mild fire stimulates the resprouting of the fire protected bud after several weeks post-fire (Burrows and Wardell-Johnson, 2003; Fox, 2004; Cox, 2004). Two other species useful as indicators within the study area are for example *Xanthorrhoea preissii* (= Grasstree) and *Acacia pentadenia* (Fox, 2004; Cox, 2004). The Grasstree is stimulated to flower by fire, which is visible by sprouting of flower spikes post-fire (Burrows and Wardell-Johnson, 2003). Levels of burn severity can be observed by the regeneration of the green leaves and watching the skirt of dry leaves on the base of the Grasstree (Fox, 2004; Cox, 2004). Acacia pentadenia is a fire sensitive species that has no capacity to resprout from epicormic shoots or lignotubers following crown scorch. This specie however has highly durable seeds stored in the soil layer which sprout post-fire (Burrows and Wardell-Johnson, 2003). The number and density of seedlings post-fire is directly related to the fire severity (Fox, 2004;

Figure 6-2: Biomass reduction and scorch of the tree stems in jarrah-marri forest. The measurement fo burn severity in the field consisted principally in the estimation of biomass reduction and scorch height, which could be related to the sixth of the flame height.

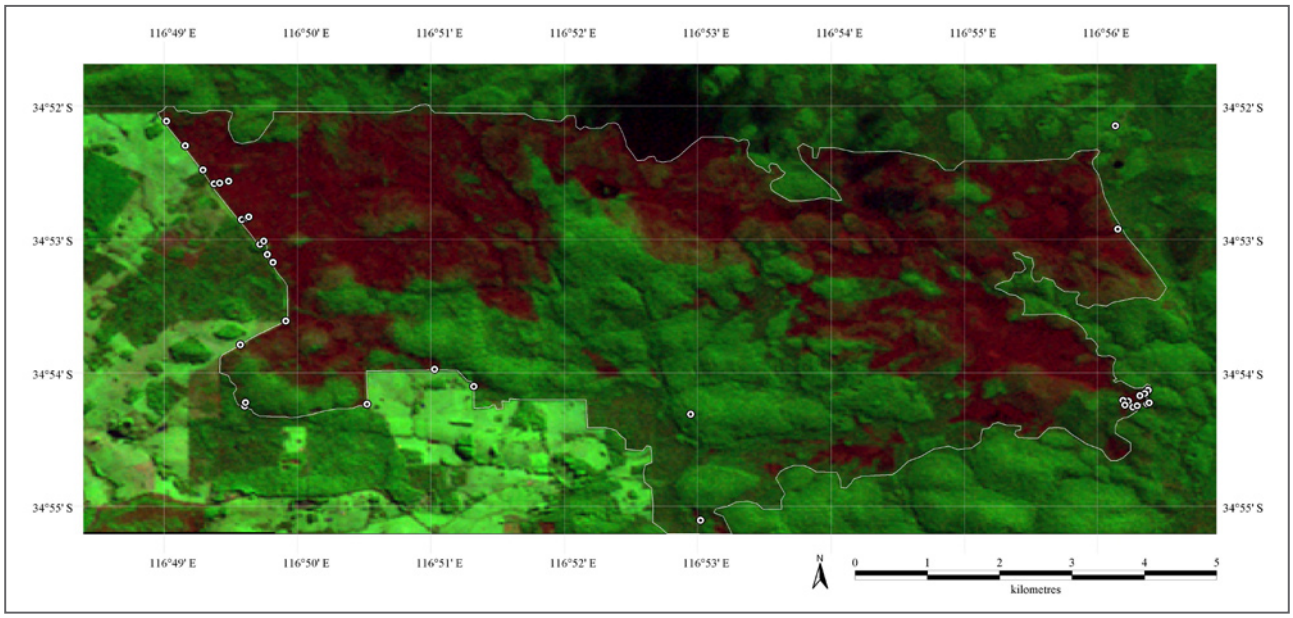

Figure 6-3: Ground Control Points (GCPs) sampled in the field in FAA4. The GCPs are illustrated by the white circles, they were sampled during an excursion to the study area in June 2004. (Image: Landsat TM, 31st May 2004, R-G-B as 7-4-2, Australian Centre of Remote Sensing (ACRES))

Cox, 2004). Measuring burn severity based on the ecological approach is not suited to remote sensing as only the reduction in biomass can be measured from satellite.

Fire coordinators who use prescribed burning as a tool to manage the fire prone environment of south-west WA have certain management objectives that they expect each burn to meet. The predominant objective is to reduce fuel and manage timber resources. In order to reduce fuel and thin out the understorey of a forest, fire is prescribed to be very mild. To rejuvenate a stock of forest, fire is prescribed to be moderately intense in order to support germination. A high intensity fire is purposely lit to initiate regeneration after logging (Green, 2004; Simmonds, 2004).

In this work, burn severity is measured using remote sensing data. Satellite sensors can measure the alteration or consumption of green biomass, the exposure of soil and the leaf dryness in respect to fire. Levels of burn severity were related to reduction of biomass. Hence, burn severity as measured in this work does not express the severity of impact on the ecosystem.

An adjusted measurement of burn severity in the field consisted in measuring scorch height and estimating amount of biomass affected. The scorch height of stems is a useful indicator to measure burn severity as it reflects the flame height (Figure 6-2). In general, scorch height is a sixth of the flame height causing the scorching (Simmonds, 2004). The scorch height itself cannot be measured by the satellite, however a relationship between scorch height and consumption of biomass was observed in the field. To examine alteration of green biomass, the relation between leaves remaining green, leaves scorched and defoliated parts of the trees were estimated. Within the forested ecosystem of south-west WA it was considered reasonable to discriminate four classes of burn severity.

There were 35 GCPs sampled along the boundary of FAA4 thereof a limited number within the burnt area (Figure 6-3). The positions were recorded with a handheld GPS and level of burn severity was estimated for each GCP. The area was subject to prescribed burning approximately 6 weeks before the visit. Photographs were taken at most GCPs. The ecosystems within FAA4 varied between open shrubland, open woodland and jarrah-marri forest. The ground truth data was used to validate the remote sensing data.

6.6 Assessment of Burn Severity with Remote Sensing Data

Remote sensing data and the remotely sensed burn severity measurement are based on detection of spectral characteristics expressed in percentage of reflectance or index values. The ground truth data is sampled to calibrate remote sensing data in order to assess burn severity. The scale mismatch between a Ground Control Point (GCP) and a MODIS pixel with ground resolution of 250m x

250m is large and homogeneity in surface cover is not likely in the south-west WA environment. An intermediate scale can be provided by high-resolution remote sensing imagery. Landsat TM/ETM+ data is considered useful for the intermediate step in the upscaling method (Liang et al., 2002; Sá et al., 2003). Data sampled in the field did not provide a comprehensive data set for validation, as numbers of GCPs were insufficient as well as being located on the boundary rather than scattered through FAA4. The available material was used to compare ground truth and high resolution Landsat data. In a second step, Landsat data was compared to MODIS data focusing on the moderate spatial resolution of MODIS.

6.6.1 Assessment of Burn Severity Using Ground Truth Data

High resolution Landsat TM data were compared with field sampled ground truth data in order to assess burn severity with remote sensing techniques. The burn severity estimated for GCPs was compared to the spectral properties and index values of Landsat pre-fire image and post-fire image.

Landsat TM scenes from 23rd December 2003 and 31st May 2004 were exported from ER Mapper as ESRI BIL format (.bil). The data were imported into ArcView and each band separately converted into a Grid using the Spatial Analyst extension of ArcView. This enabled the read out of values of all bands within the pixel. The GCPs sampled in the field were downloaded from the GPS and imported as ESRI Shapefile (.shp) into ArcView.

There were 14 GCPs taken into account for ground truth validation. GCPs sampled on the path along the boundary of FAA4 were not considered due to mixed surface reflectance. Based on the ΔNBR image of 23rd December 2003 and 31st May 2004, each pixel containing a GCP was digitised as a polygon theme of ArcView. This image was taken to average the offset between the two scenes. The spectral signatures of TM scenes were tabulated for each region. The results were further sorted in Microsoft Excel, where index values of bands 4 and 3 for the NDVI and 4 and 7 for the NBR were calculated for the selected GCPs (Equations 4-4 and 4-6). The change detected by both indices was calculated for each GCP. The differenced indices ΔNBR and ΔNDVI were derived from Equation 4-7.

The spectra and index values identified in remote sensing imagery were compared with the burn severity estimated at the selected GCPs. Hence, biomass affected by fire was estimated and the structure of the ecosystem considered for each plot, as described in the latter section.

6.6.2 Comparison of MODIS and Landsat ETM+ Data

A major goal of this work is to define the feasibility of using moderate spatial resolution MODIS data to measure burn severity. The method consisted in a direct comparison of Landsat and MODIS index imagery. In a preparatory step, classes of burn severity were adjusted to the field data and separated into four classes ranging from unburnt to high burn severity. Landsat ΔNBR_{Nov} image was calibrated with thresholds calculated from training areas. Each class of the calibrated ΔNBR_{Nov} image was converted into vector data. The class regions provided fundamental information for calibrating MODIS thresholds. The resulting classes were directly compared, whereas only FAA1 was considered. This study site performed the most favourable study site for this comparison due to the well known and clear separation between a mild prescribed burn in the northern part and the severe wildfire in the southern part.

The training areas to calibrate the ΔNBR_{Nov} image were manually digitised based on ETM+ reflectance of band 4 (11th February and 26th November). Band 4 reflectance gave the highest change in respect to vegetation alteration. Band 4 of the pre-fire image was displayed in RED and band 4 of the post-fire image in GREEN as R-G-B composite. Areas appearing green indicated high reflectance in both images and were identified as unburnt vegetation. Areas appearing red indicated high reflectance in the pre-fire image and low reflectance in the post-fire image and were identified as highly severe burnt areas. The result was in agreement with fire coordinators from CALM (Green, 2004; Simmonds, 2004), that the selected training areas were unburnt and severely burnt, as indicated in the image.

Defined areas to train detection of unburnt vegetation were selected inside the FAA1 and in the adjacent areas. Training areas for severe burnt vegetation were selected within the southern part of FAA1, which was subject to the wildfire. The definition of training areas for the intermediate classes of low and moderate burn severity from the displayed images would have been very subjective. The thresholds to discriminate classes of burn severity were calculated from mean value and standard deviation of training areas from the Landsat ΔNBR_{Nov} image. The threshold to discriminate the classes unburnt and low burn

severity was calculated by the mean value of the unburnt training area plus the standard deviation. The threshold to discriminate moderate and high burn severity was calculated by subtracting the standard deviation from the mean value of the high burnt training area. The calculation considering the standard deviation was justified by expecting higher accuracy for the corresponding classes. The threshold to separate the intermediate classes of low and moderate burn severity were calculated from the latter thresholds as mean. The ΔNBR_{Nov} image was classified with calibrated values for burn severity classes in ER Mapper.

The defined classes 1 to 4 of the calibrated ΔNBR_{Nov} image were displayed separately. Each class was displayed in one colour, whereas highest contrast between class and background for example black and white was important for a successful raster to vector conversion. Each class was exported as GeoTIFF image (.tif) and displayed in ArcView. The Spatial Analyst of ArcView provides a raster to vector conversion tool, in which vector boundaries for each class of the Landsat ΔNBR_{Nov} image were compiled.

Subsequently, a definition of reasonable thresholds for classifying $\Delta NBR_{MOD26-11}$ images was required. The $\Delta NBR_{MOD26-11}$ image of MODIS was derived from pre-fire mean NBR (September and October data) and post-fire NBR of 26th November to match the post-fire data to Landsat ETM+ data based on Equation 4-7. The $\Delta NBR_{MOD26-11}$ image was exported in ESRI BIL format (.bil) and displayed as Grid in ArcView. MODIS resolution of 250m x 250m was resampled with Cubic Convolution to Landsat cell size of 25m x 25m, as measured in the Landsat image when displayed in ArcView. This was accomplished using the Grid Pig Tool extension of ArcView. The resulting image provided spectral information of MODIS data in spatial resolution approximately equal to Landsat data. Classes of burn severity for the MODIS $\Delta NBR_{MOD26-11}$ image were defined by rounding the resulting mean values received for unburnt and highly severe burnt of this image. These mean values were considered as closest match between thresholds of both the Landsat ETM+ and MODIS classification. Moderate spatial resolution and a general low accuracy due to the use of mean values were justifying rounding values. The $\Delta NBR_{MOD26-11}$ was calibrated into four classes of burn severity based on the resulting thresholds. The classification was completed in ER Mapper and classes separately displayed. The $\Delta NBR_{MOD26-11}$ classes were exported as GeoTIFF image (.tif) and converted into vector data for each class.

The vector data of burn severity classes measured with MODIS and Landsat ETM+ enabled a direct comparison between MODIS and Landsat ETM+ coverage of burn severity classes. This comparison is to assess the feasibility of using moderate spatial resolution MODIS data compared to high resolution Landsat ETM+ data within the example of FAA1.

Chapter 7: Results

The results gathered from analysis of remote sensing and field data are described and represented in various charts. The measurement of burn severity during a field trip established classes of burn severity within the study area. Burn severity was assessed with remote sensing data based on several Ground Control Points (GCPs) sampled in the field. The results of high resolution Landsat TM data and moderate resolution MODIS data were compared to see if spatial resolution of MODIS data is suitable for measuring burn severity in the forests of south-west WA.

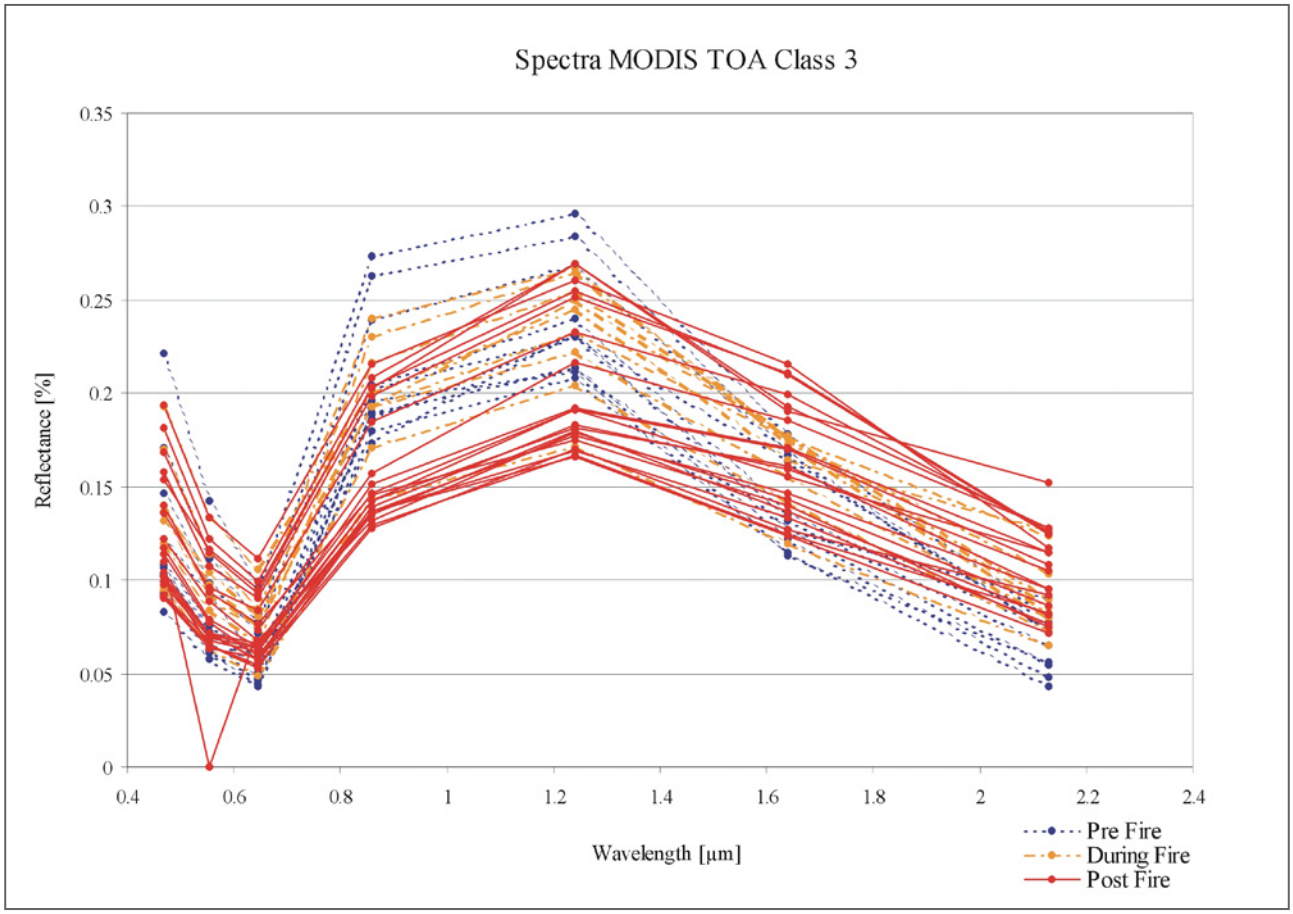

Figure 7-1: Spectral properties detected from bands 1 to 7 of MODIS top of atmosphere (TOA) reflectance in class 3. MODIS data was recorded between September and December 2002. The class 3 from the ΔNBR_{MODIS} image represents a mild burnt area. For all MODIS spectra presented in Figures 7-1 to 7-4 and 7-9 to 7-12, the blue dotted lines refer to data recorded pre-fire, the orange dashed lines refer to data during fire and the red lines refer to post-fire data. For all charts in this chapter, the detected value is illustrated by the filled dots, whereas lines are connceting the recorded data in order to facilitate inspection of results.

7.1 Results of Remote Sensing Data Analyses

Spectral properties of remote sensing data and characteristics of the indices NBR and NDVI were analysed within regions of differently burnt surfaces. MODIS data were analysed within classes of burn severity derived by classifying the ΔNBR_{MODIS} image as described in chapter 6.3. Landsat ETM+ data were analysed within classes derived from ΔNBR_{Nov} and ΔNBR_{Dec} images as described in chapter 6.4. The results will focus on classes 3 and 6 of FAA1, which represent a lower and higher severe burnt surface, respectively. The trends of remote sensing data within classes 1 to 6 are listed in the Appendix. MODIS TOA and BOANADIR data were analysed within equal regions, thus results of MODIS data are directly comparable.

Results of Class Region

The mean reflectance spectra of MODIS TOA data of class 3 are illustrated in Figure 7-1 for each date. The entire spectrum shows a characteristic trend: Reflectance in the blue light (0.469µm; band 3) varies in the range between 0.1 to 0.2 and is decreasing towards the red light (0.645µm; band 1) between 0.05 to 0.12. An outlier with invalid reflectance of 0 in the green light (0.555µm; band 4) is recorded on Julian day 350. The NIR reflectance increases and varies between 0.13 to 0.27 (0.859µm; band 2) and 0.16 to 0.29 (1.24µm; band 5). Towards the MIR, reflectance decreases showing variances between 0.12 to 0.22 (1.64µm; band 6) and 0.04 to 0.15 (2.13µm; band 7). Comparing the TOA spectra recorded pre-fire and post-fire, reflectance of all data varies in a similar manner in blue and green light. There is low discrimination between spectra in the red light due to a minor increase of reflectance post-fire. In the NIR bands 2 and 5, the pre-fire dates show higher reflectance compared to a decreasing reflectance of dates post-fire. This phenomenon is changing towards the MIR bands. The pre-fire dates have generally lower reflectance in bands 6 and 7, whereas post-fire dates show noticeably higher reflectance within these wavelengths. The spectra of class 3 illustrate the trend that reflectance between pre-fire and post-fire dates have greatest change in bands 2 and 7.

Figure 7-2: Spectral properties detected from bands 1 to 7 of MODIS top of atmosphere (TOA) reflectance in class 6. The class 6 from the ΔNBR_{MODIS} image represents a severe burnt area.

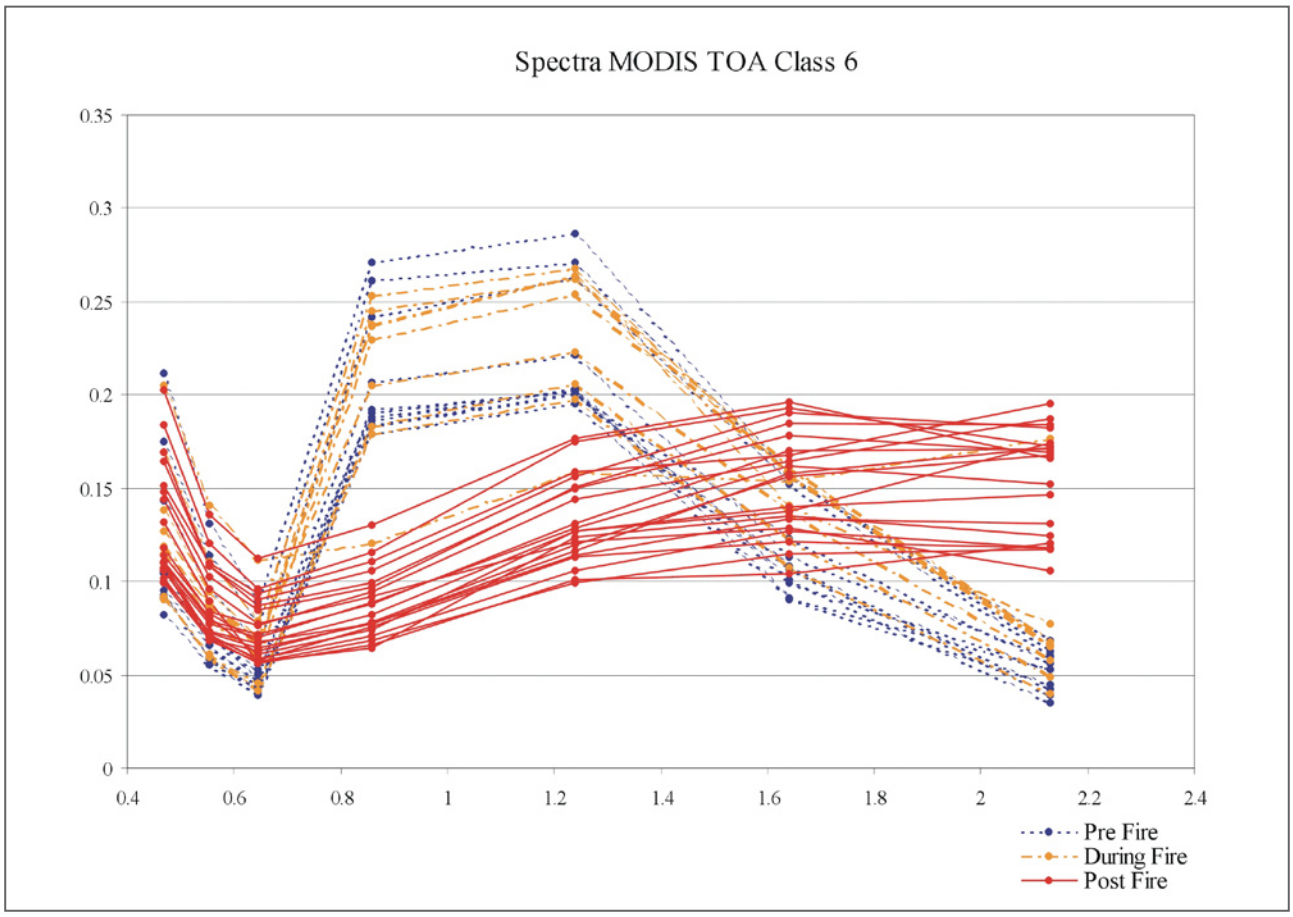

The spectra of TOA data within a more intense burnt surface of class 6 places emphasis on the latter result (Figure 7-2). Compared to the spectra of class 3, the class 6 spectra show a similar trend in the blue and green light. Reflectance of the red band 1 shows similar variance between 0.04 to 0.12, whereas dates recorded pre-fire have significantly lower reflectance than dates post-fire. The increasing reflectance of post-fire dates within this wavelength show high variance ranging between 0.06 to 0.12. Reflectance of NIR bands 2 and 5 highlight the magnitude of change. The pre-fire data of class 6 show similar reflectance compared to pre-fire data of class 3, whereas reflectance of post-fire scenes shows a markedly reduced reflectance in the NIR. The reflectance of post-fire data in NIR wavelengths of 0.859µm (band 2) and 1.24µm (band 5) varies between 0.06 to 0.13 and 0.1 to 0.18, respectively. The MIR reflectance illustrates the change of reflectance between pre-fire and post-fire dates towards longer wavelengths. Reflectance at 1.64µm (band 6) varies between 0.08 to 0.19, whereas pre-fire reflectance is generally lower than post-fire reflectance. At 2.13µm (band 7), the low reflectance of pre-fire dates is similar to pre-fire reflectance of class 3, whereas post-fire reflectance of class 6 shows a prolonged increase at this wavelength with variances ranging between 0.11 to 0.19. The greatest change of reflectance pre and post-fire was detected at 0.859µm and 2.13µm. Comparing class 3 and class 6 spectra of TOA data, the change of reflectance between differently burnt areas is most accentuated in MODIS bands 2 and 7.

The spectra of the same classes were derived from MODIS BOA and BOANADIR data. The mean reflectance spectra of class 3 are illustrated in Figure 7-3 for each date. In comparison to MODIS TOA class 3 spectrum, reflectance within the VIS bands is markedly reduced in BOANADIR data. The reflectance ranges between 0.01 to 0.08 in the blue light (band 3) and has a decreasing variance between 0.03 to 0.06 in the red light (band 1). There are two outliers with reflectance of 0 in the green light (band 4) recorded on Julian days 350 and 354. There is low discrimination between pre-fire dates and post-fire dates in the VIS wavelengths. Within the NIR and MIR wavelengths the spectral signature of class 3 BOANADIR shows a similar trend to

Figure 7-3: Spectral properties detected from bands 1 to 5 and 7 of MODIS bottom of atmosphere and BRDF corrected (BOANADIR) reflectance in class 3. MODIS BOANADIR data are the same dates recorded between September and December 2002. The class 3 of BOANADIR represents the same region as TOA data were analysed in Figure 7-1.

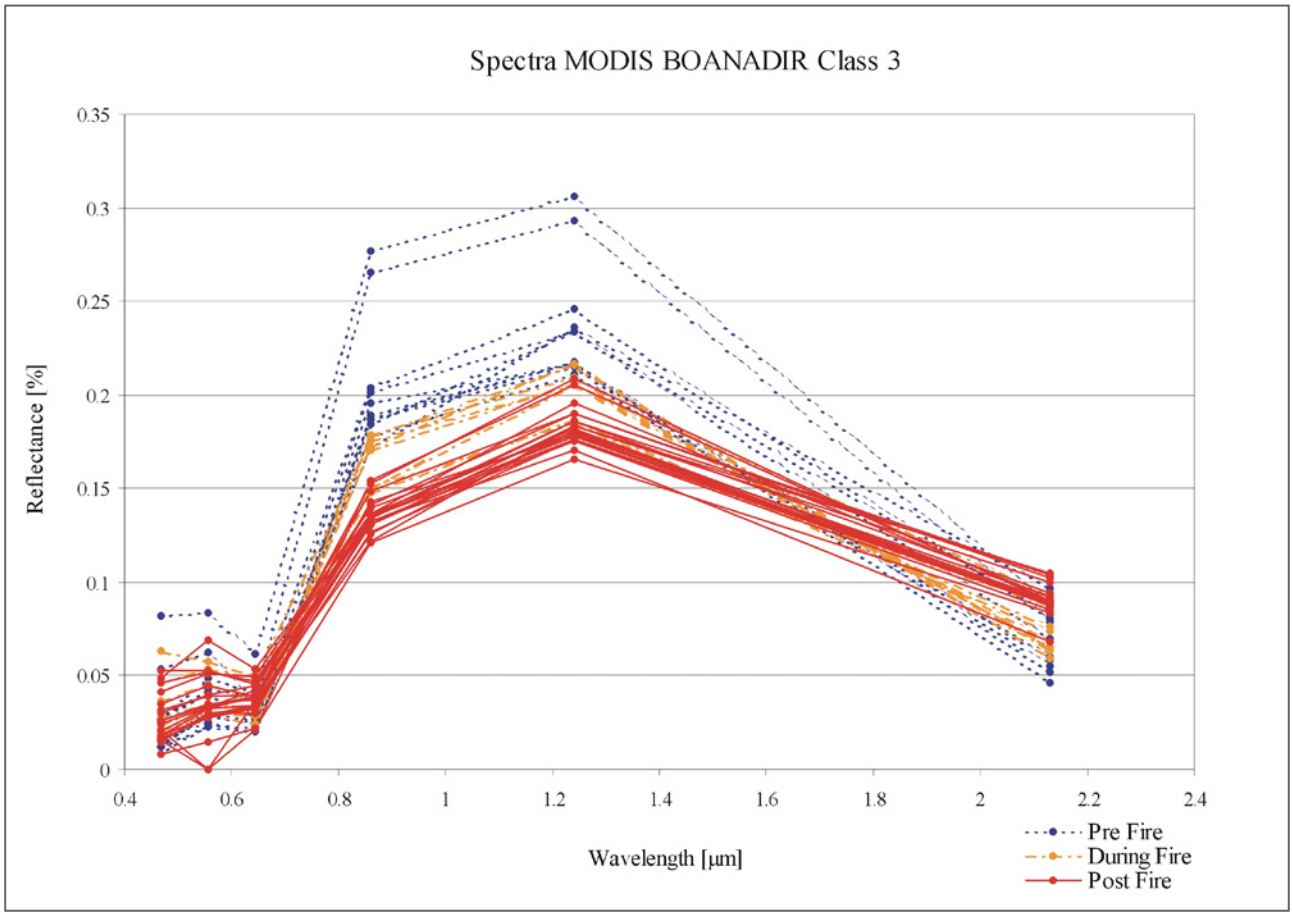

the class 3 TOA spectra. The dates recorded pre-fire have higher reflectance in the NIR and lower reflectance in the MIR compared to dates post-fire. The BOANADIR data show a marked decrease of variances between spectra of different dates. There are two outliers of pre-fire data recorded on Julian days 256 and 265, which show markedly higher reflectance in all bands compared to all pre-fire data. Reflectance of dates pre-fire range between 0.17 to 0.2 in NIR wavelength at 0.859µm (band 2) and between 0.21 to 0.25 at 1.24µm (band 5), the outliers were not considered. Dates post-fire have lower reflectance between 0.13 to 0.16 (band 2) and 0.16 to 0.21 (band 5). Towards the MIR, spectra of BOANADIR data show a similar change of reflectance between pre and post-fire data. Reflectance pre-fire is decreasing between 0.05 to 0.08 at 2.13µm (band 7), whereas post-fire reflectance is higher between 0.07 to 0.11 (band 7). The spectra show highest change between pre-fire and post-fire reflectance in bands 2, 5 and 7.

The mean reflectance spectra of BOANADIR data in class 6 are represented in Figure 7-4. Reflectance in the VIS wavelength shows reduced values compared to TOA class 6 reflectance. The spectral properties in the VIS are similar to class 3 of BOANADIR, whereas discrimination between lower pre-fire reflectance and increased post-fire reflectance is recognisable at 0.645µm (band 1). There is an outlier due to negative reflectance in the VIS wavelength on Julian day 353. The spectra within the NIR and MIR wavelengths put emphasis on the change between dates pre and post-fire. The pre-fire reflectance is similar to reflectance in class 3 of BOANADIR pre-fire dates. The post-fire reflectance shows a noticeable decrease of reflectance in the NIR ranging between 0.05 to 0.1 at 0.859µm (band 2) and between 0.09 and 0.14 at 1.24µm (band 5). Reflectance of post-fire dates increases towards the MIR varying between 0.1 and 0.17 at 2.13µm (band 7). The higher degree of burn severity is again markedly reflected in the spectra. Similar to results of TOA data, the greatest change between burnt and unburnt surface is recognisable in bands 2 and 7 of MODIS data, whereas variance within the BOANADIR spectrum is highly reduced.

The dates during the fire (orange dashed lines) represent a transition between spectra of pre-fire and post-fire dates. The spectral properties are

Figure 7-4: Spectral properties detected from bands 1 to 5 and 7 of MODIS bottom of atmosphere and BRDF corrected (BOANADIR) reflectance in class 6. The class 6 of BOANADIR represents the same region as TOA data were analysed in Figure 7-2.

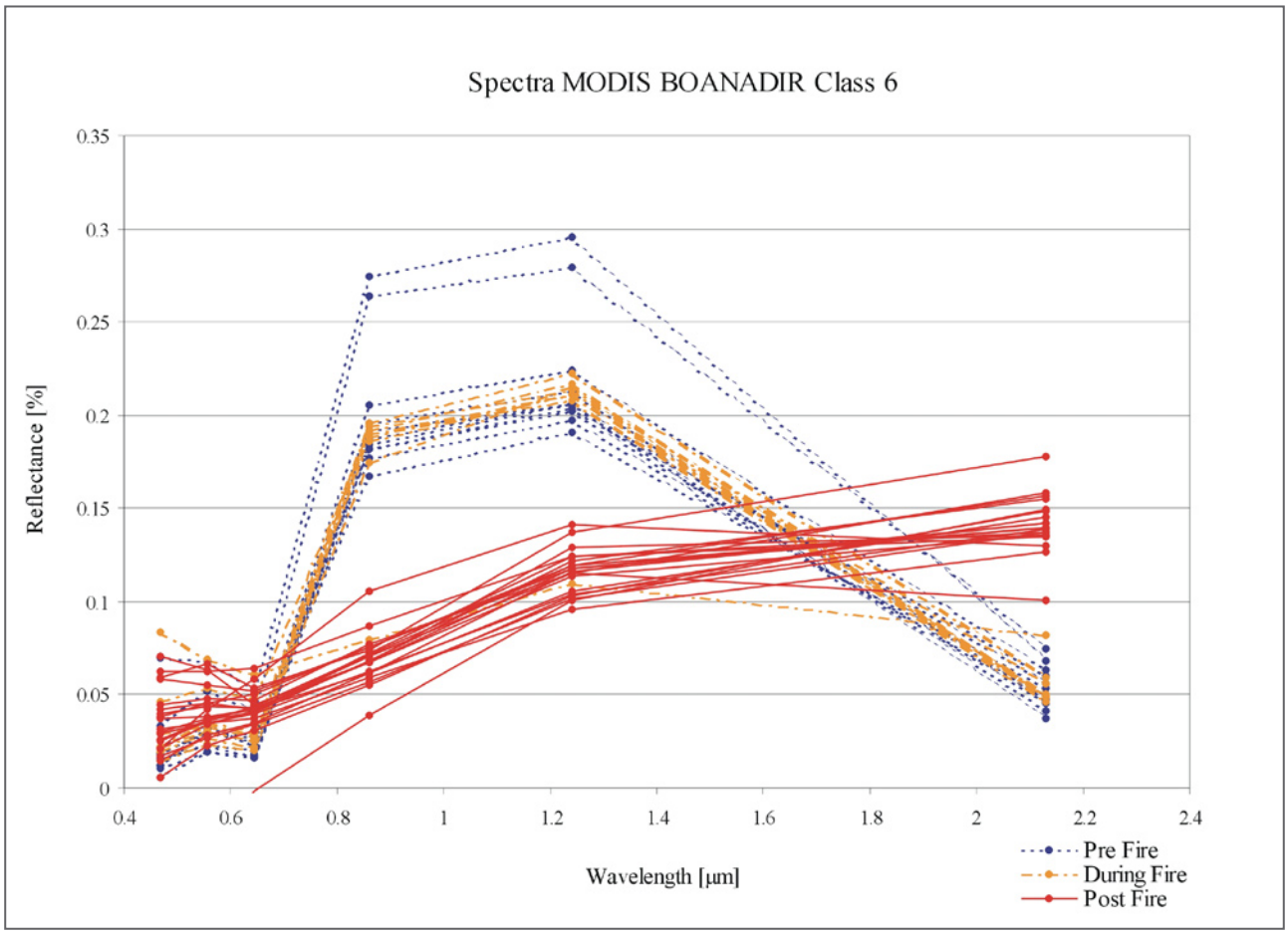

predominantly coming along with the spectra of pre-fire dates. All spectra of classes 1 to 6 of FAA1 derived from TOA and BOANADIR data are represented in the Appendix (Figures A1-1 to A1-6 and A2-1 to A2-6).

The indices NBR and NDVI within classes 3 and 6 of both MODIS TOA and BOANADIR data are illustrated in Figures 7-5 to 7-8. The results of indices in classes 1 to 6 from TOA and BOANADIR data are represented in the Appendix (Figures A3-1 to A3-6 and A4-1 to A4-6)

Figure 7-5 represents the lapse of mean NBR values and mean NDVI values of TOA data within class 3 versus time (Julian days 253-365). Fire occurred within FAA1 between Julian days 305 and 321. The mean NBR of class 3 from dates pre-fire have values around 500, there are two outliers visible on Julian days 254 and 263. The spectra of the outlier data have merely low contrast between reflectance in NIR and MIR bands 2 and 7, whereas values itself show no obvious outliers within the spectra. The mean NBR values decrease in the stage during fire and vary between 100 and 300 within post-fire data. There is a minor increase of NBR values towards Julian day 365. The mean NDVI values of class 3 pre-fire develop slightly higher values and show a minor variance with values between 500 and 600 compared to the mean NBR values. There is an outlier at Julian day 263 for the NDVI due to low contrast of reflectance in the corresponding wavelengths, but no obvious outliers within the pre-fire spectra. Post-fire, the NDVI has a minor reduction of values compared to the NBR, which vary between 300 and 400. During fire, both indices show a highly variable decrease of values. The NDVI has a smooth curve through time compared to the NBR, whereas signal contrast between pre-fire dates and post-fire dates is more enhanced by the NBR.

The trend of indices within class 6 of MODIS TOA data is shown in Figure 7-6. Values of both indices recorded before the fire are around 600. There is a marked decrease in both index values post-fire. The NBR values calculated from post-fire data vary between –400 and –100. Values show a minor increase during the development of post-fire environment towards Julian day 365. Hence, the maximum decrease of the NBR is visible soon after fire. The NDVI values show a

Figure 7-5: The trend of the NBR and NDVI through time in class 3, derived from MODIS top of atmosphere (TOA) reflectance. For all MODIS index analyses presented in Figures 7-5 to 7-8 and 7-13 to 7-14, the blue lines refer to the NBR and the orange dashed lines refer to the NDVI. Measured values are represented by the filled square, whereas connecting lines are to facilitate inspection.

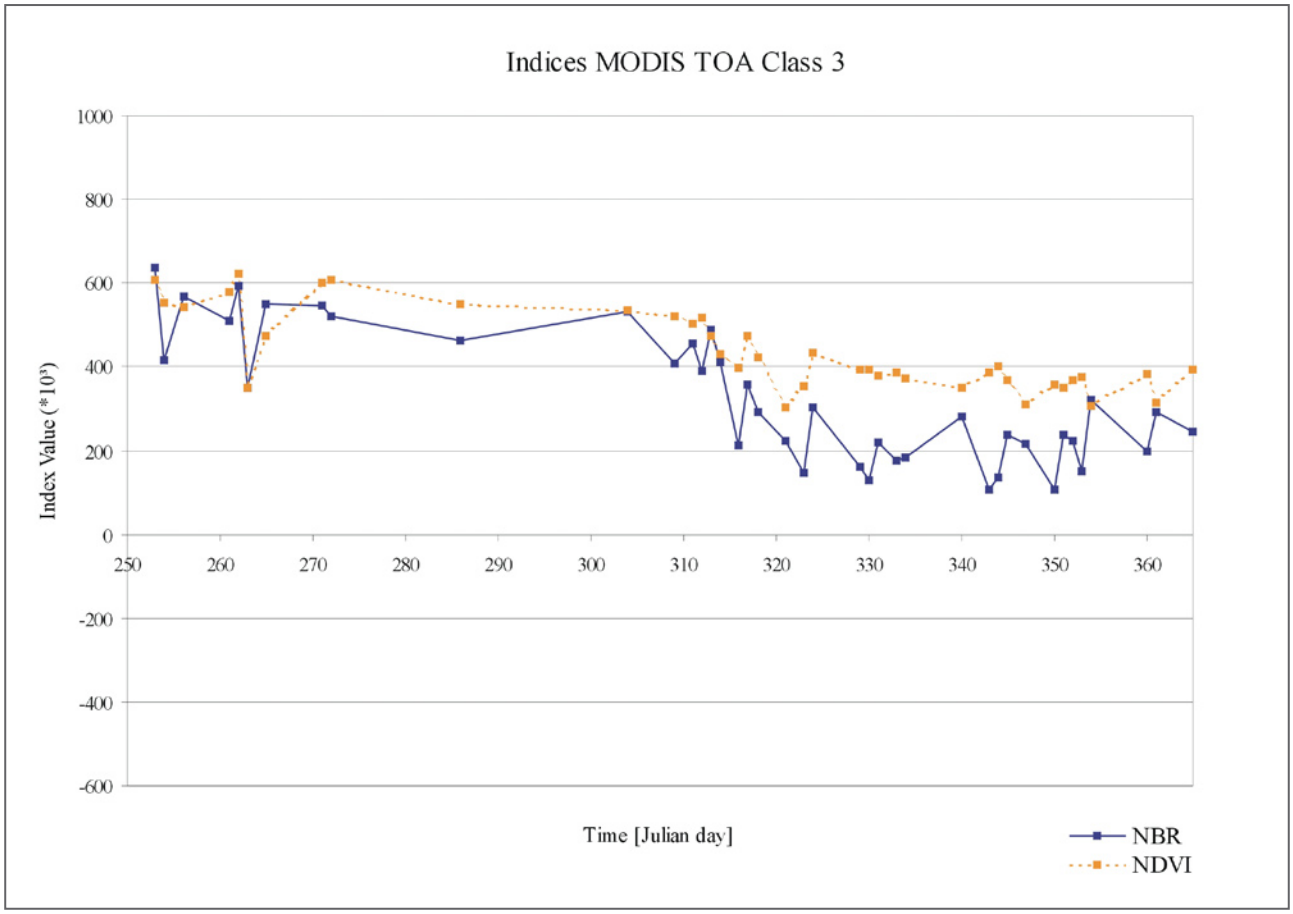

smooth trend around 100 in post-fire data. The change between dates recorded before the fire and post-fire are well detected by both indices, however the NBR provides higher signal in comparison to the NDVI.

The influences of atmosphere and various scan and illumination angles of MODIS data were investigated in respect to the NBR and NDVI. Figure 7-7 shows both indices calculated from BOANADIR data in class 3. The mean NBR values of class 3 derived from BOANADIR pre-fire data have values between 400 and 600 and show similar outliers compared to TOA data. Index values of post-fire dates decrease and vary between 100 and 300. They show a similar compared to TOA data, whereas the noise was not significantly reduced. The NDVI values calculated from dates before fire vary between 600 and 800 and are therefore higher compared to the NDVI of TOA data. There is still an obvious outlier at Julian day 263 due to low values. The NDVI of post-fire dates varies between 400 and 600 and is comparable to TOA data. The outlier recorded at Julian day 329 showing NDVI value greater 1000, spectral analyses did not show a conspicuous outlier at this date, but cloud coverage was high, which could explain the outlier. The NDVI of class 3 calculated from BOANADIR data shows a minor signature change between pre-fire and post-fire data and higher variance within the values compared to the NBR.

Index values of class 6 calculated from BOANADIR data are illustrated in Figure 7-8. The NBR shows values around 600 pre-fire. The marked decrease post-fire is similar to TOA data, however values are slightly lower ranging between –500 and –300 in the BOANADIR data. Increasing values of the NBR towards Julian day 365 are similar to results of TOA data in class 6. The mean NDVI values of BOANADIR data in class 6 are generally higher compared to the NDVI TOA data. Index values of pre-fire data vary between 700 and 800 and show the outlier recorded at Julian day 263. This was similarly observed by comparing the latter class 3 data. The post-fire NDVI has values around 200, whereas an obvious outlier is recorded on Julian day 329 similar to NDVI of class 3 BOANADIR. The BOANADIR data result in an increase of NDVI values, whereas the change detected by indices is barely influenced by atmospheric and BRDF effects.

Figure 7-6: The trend of the NBR and NDVI through time in class 6, derived from MODIS top of atmosphere (TOA) reflectance.

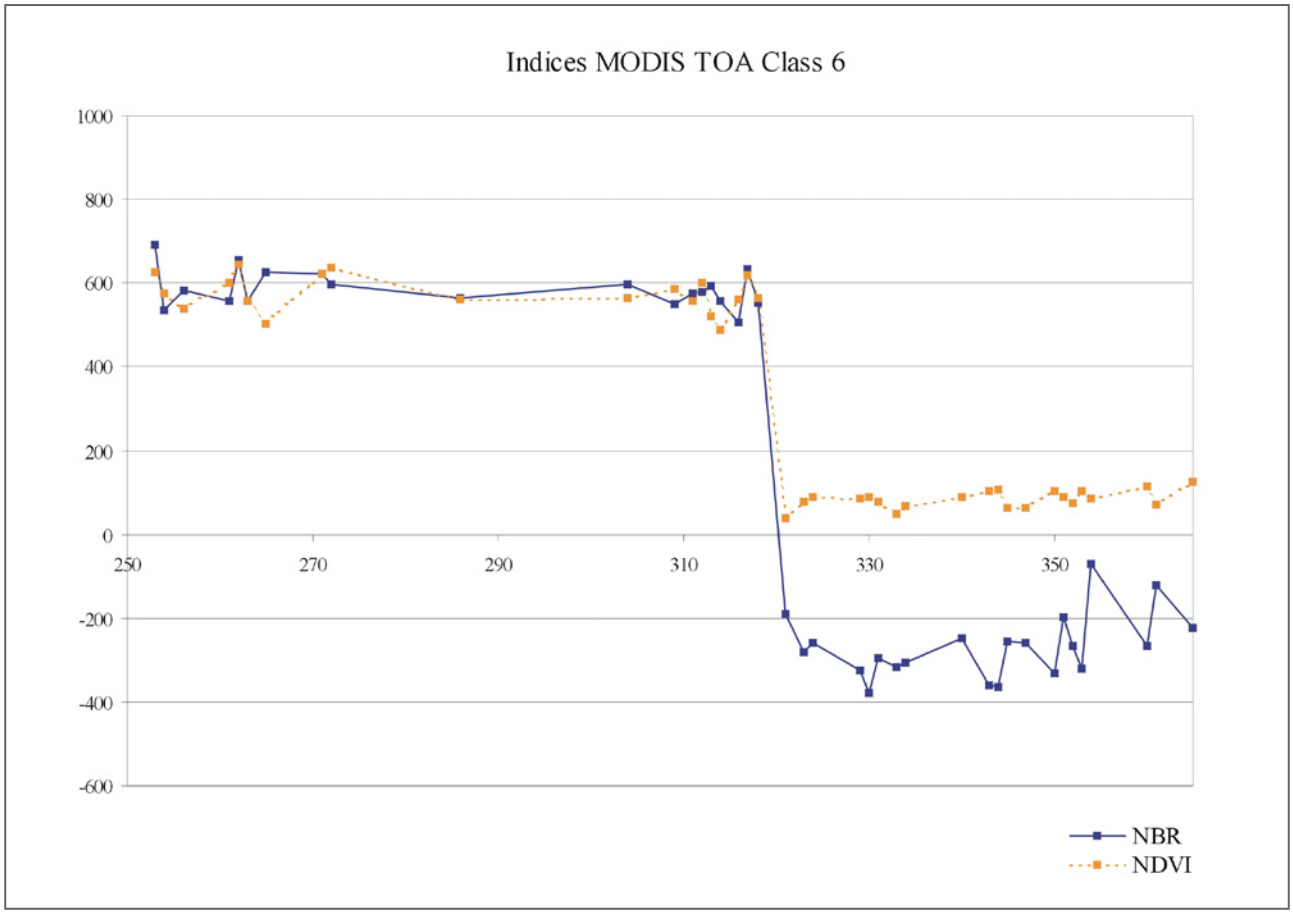

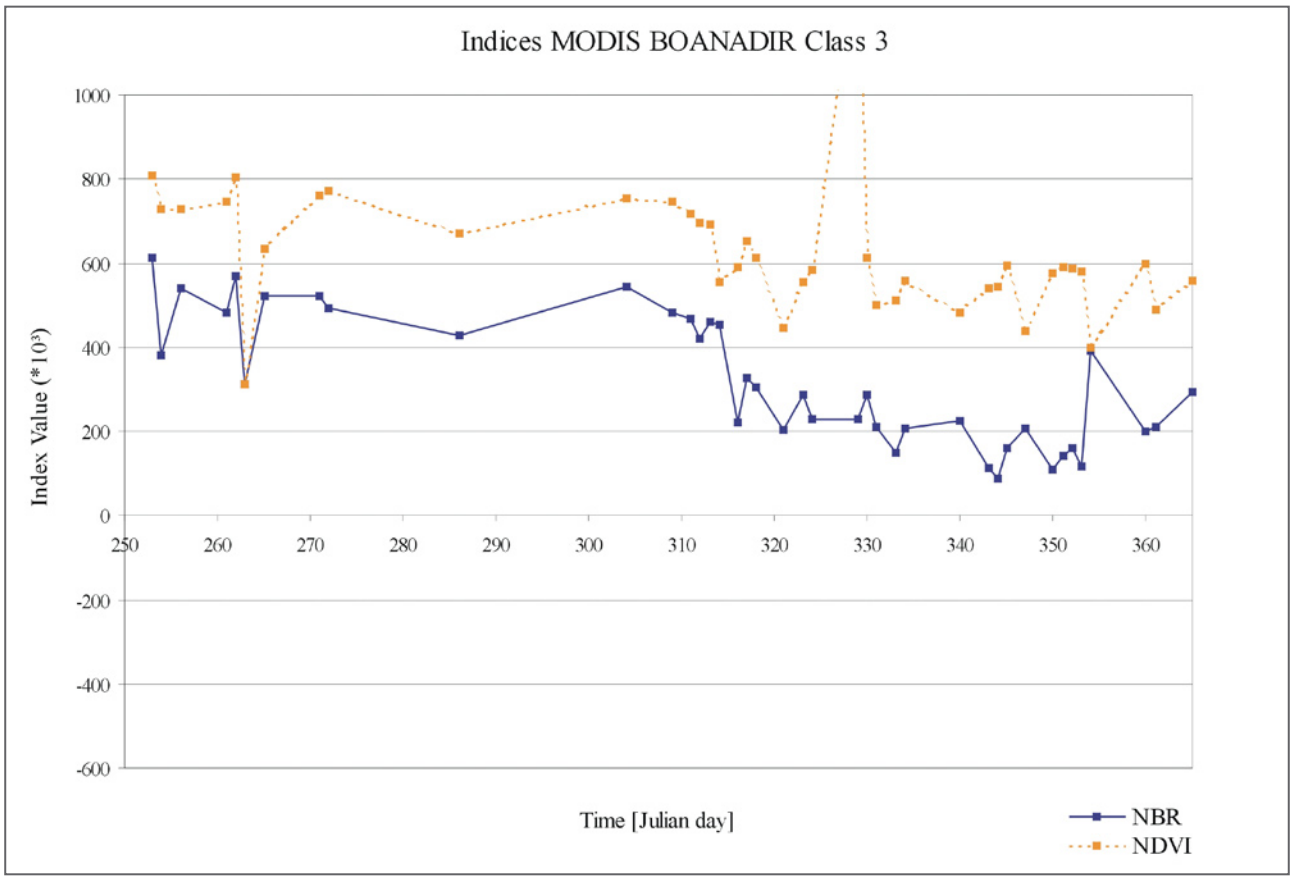

▲ *Figure 7-7: The trend of the NBR and NDVI through time in class 3, derived from MODIS bottom of atmosphere and BRDF corrected (BOANADIR) reflectance.*

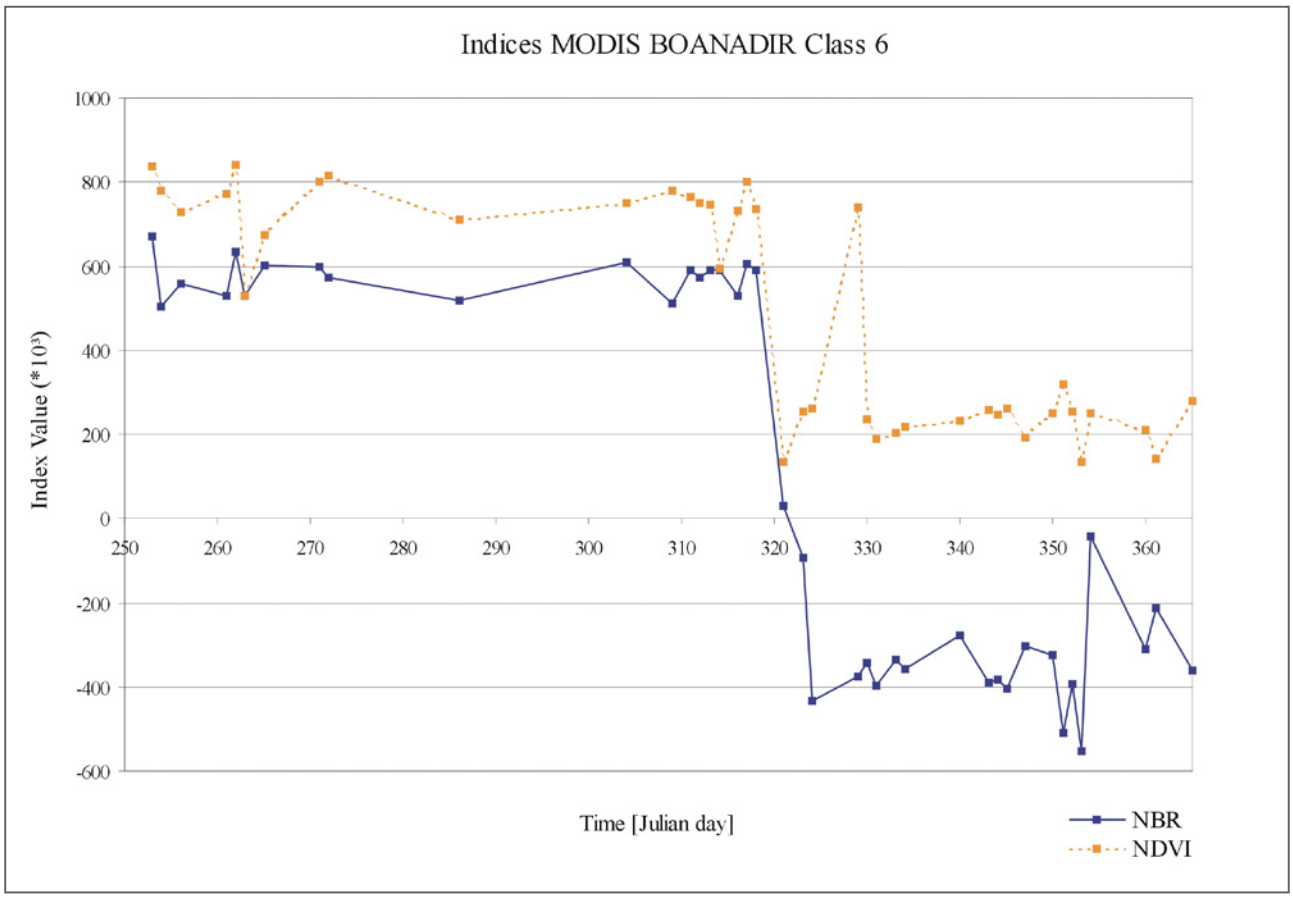

▼ *Figure 7-8: The trend of the NBR and NDVI through time in class 6, derived from MODIS bottom of atmosphere and BRDF corrected (BOANADIR) reflectance.*

Results of Pixels in Class Region

Results are gathered from single MODIS pixels to investigate variability within pixels in respect to spectral and index properties. Figures 7-9 to 7-12 illustrate the resulting spectra of TOA and BOANADIR scenes. The results of one class 3 and one class 6 pixel are presented, the same pixels were used for analysing both, TOA and BOANADIR data. The spectral properties of pixels in classes 1 to 6 are represented in the Appendix (Figures A5-1 to A5-6 and A6-1 to A6-6).

The spectrum of MODIS TOA data class 3 pixel is shown in Figure 7-9. The spectral properties of TOA data class 3 pixel are comparable to the spectral characteristics within the entire class 3. Reflectance of dates post-fire have a similar trend compared to the post-fire spectrum of class 3. It is significant, that reflectance of dates recorded pre-fire have higher variances in the pixel than in the entire class. The deviation is most significant between 0.15 to 0.24 at 0.859µm (band 2) and between 0.2 to 0.32 at 1.24µm (band 5). Despite this, bands 2, 5 and 7 reflect the most significant change between unburnt and burnt surfaces.

Figure 7-10 shows the spectrum of TOA data within a class 6 pixel. The spectral development of data pre-fire and post-fire in the class 6 pixel is comparable to the spectrum of the entire class. There are two outliers visible due to high reflectance in band 6 within the class 6 pixel recorded on Julian days 343 and 351.

The spectral properties within the same pixel of class 3 and 6 are investigated further using MODIS BOANADIR data. Figure 7-11 illustrates the resulting spectra within the class 3 pixel. The trends of the spectra are comparable to the spectra of entire class 3 BOANADIR. But there is a significantly higher variance in the spectral properties of dates recorded pre-fire. There are outliers that are accentuated due to conspicuously high reflectance in the NIR between 0.2 to 0.3 at 0.859µm (band 2) and 0.22 to 0.33 at 1.24µm (band 5). The outliers refer to data acquired on Julian days 254, 256, 265 and 271, which refers to BOA that was not corrected for BRDF effects and used as pre-fire data in September. Another outlier is recorded on Julian day 330 post-fire with negative reflectance in the VIS bands 3 and 1 and the MIR band 7. Not considering the outliers, the noise within the BOANADIR spectrum is reduced compared to the TOA class 3 spectrum. This is further emphasised in the spectral properties of data recorded post-fire, as more data were available.

The spectra of BOANADIR data within the class 6 pixel have a comparable trend to the spectra of entire class 6 (Figure 7-12). It is noticeable, that the noise within the spectra of the selected pixel is higher than within the entire class. An outlier is recorded on Julian day 265 with significantly high reflectance at 0.859µm (0.29) and at 1.24µm (0.3). Furthermore, reflectance detected on Julian day 354 is significantly high at 0.469µm (0.13) and at 0.555µm (0.14).

The indices NBR and NDVI were calculated for each of the 5 selected pixels per class. The results represent the deviation of indices within pixels of similar burnt surfaces. The index values calculated from TOA data are illustrated in Figures 7-13 to 7-14. The results received from indices of classes 3 and 6 based on BOANADIR data are presented in the Appendix together with results of all further classes of TOA and BOANADIR indices (Figures A7-1 to A7-6 and A8-1 to A8-6. Due to huge gaps of missing data and significant outliers within the existent data, the content of information was highly reduced in BOANADIR data.

The NBR and NDVI values calculated from TOA data within the selected pixels of class 3 are represented in Figure 7-13. The trends of both indices are comparable to the mean NBR and NDVI calculated for the entire class 3. Values before fire vary between 400 and 600 without considering an outlier close to 0 recorded on Julian day 254. NBR values derived from post-fire dates have variances between 0 and 400, whereas results of same dates within different pixels deviate in a value range between 200 to 300. The trend of the NDVI is similar to the NBR with less decreasing values and less variance in the dates recorded post-fire.

The same indices of selected class 6 pixels are illustrated in Figure 7-14. The trends of both indices are comparable to the NBR and NDVI calculated for the entire class 6. The NBR values of different pixels in class 6 vary between 500 and 700 in the pre-fire data and between -600 and -200 in the post-fire data. Deviations between different pixels within the same date are in a value range of 200 to 300. The NBR values increase towards Julian day 365 varying between –300 and 0. The NDVIs of TOA data in class 6 pixels show minor variances compared to the NBR. The values vary between 500 and 700 in dates recorded before fire and between 0 and 200 in dates post-fire. Variances between different pixels of the same date are in a value range of 100. Index values have a noticeable variance between similarly burnt surfaces within the same date, whereas deviation from the mean trend is less from NDVI than from NBR.

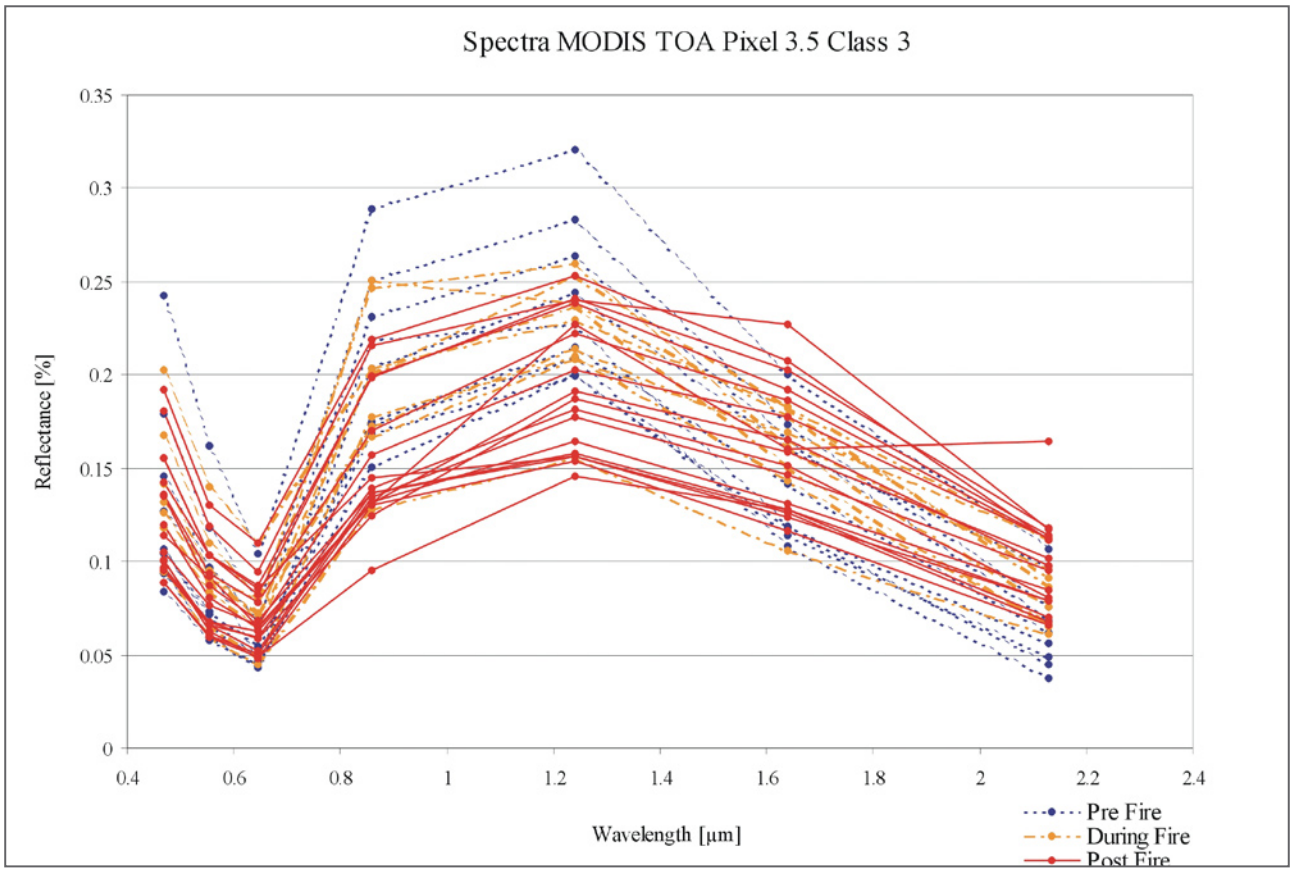

▲ *Figure 7-9: Spectral properties detected from bands 1 to 7 of MODIS (TOA) within one pixel (3.5) selected in class 3.*

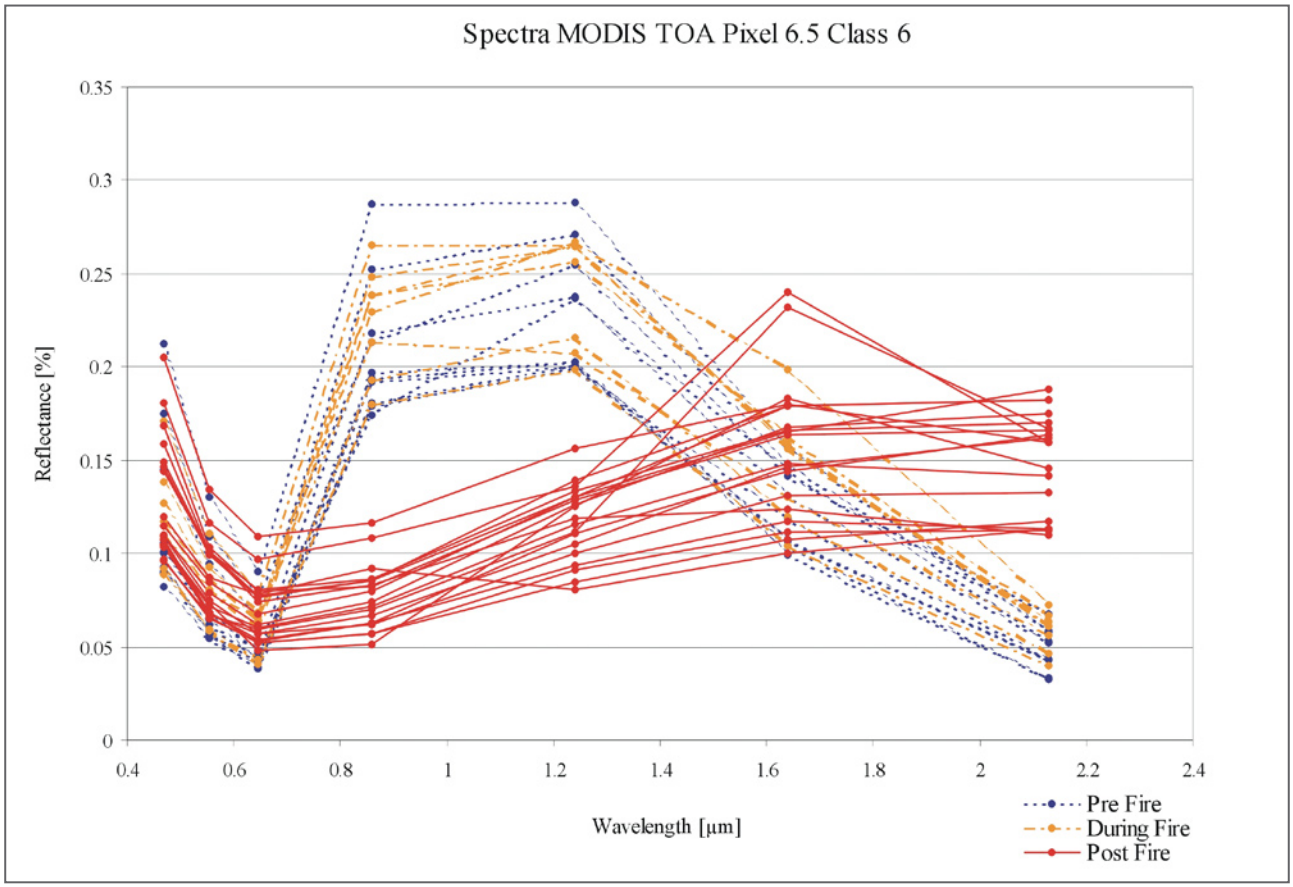

▼ *Figure 7-10: Spectral properties detected from bands 1 to 7 of MODIS (TOA) within one pixel (6.5) selected in class 6.*

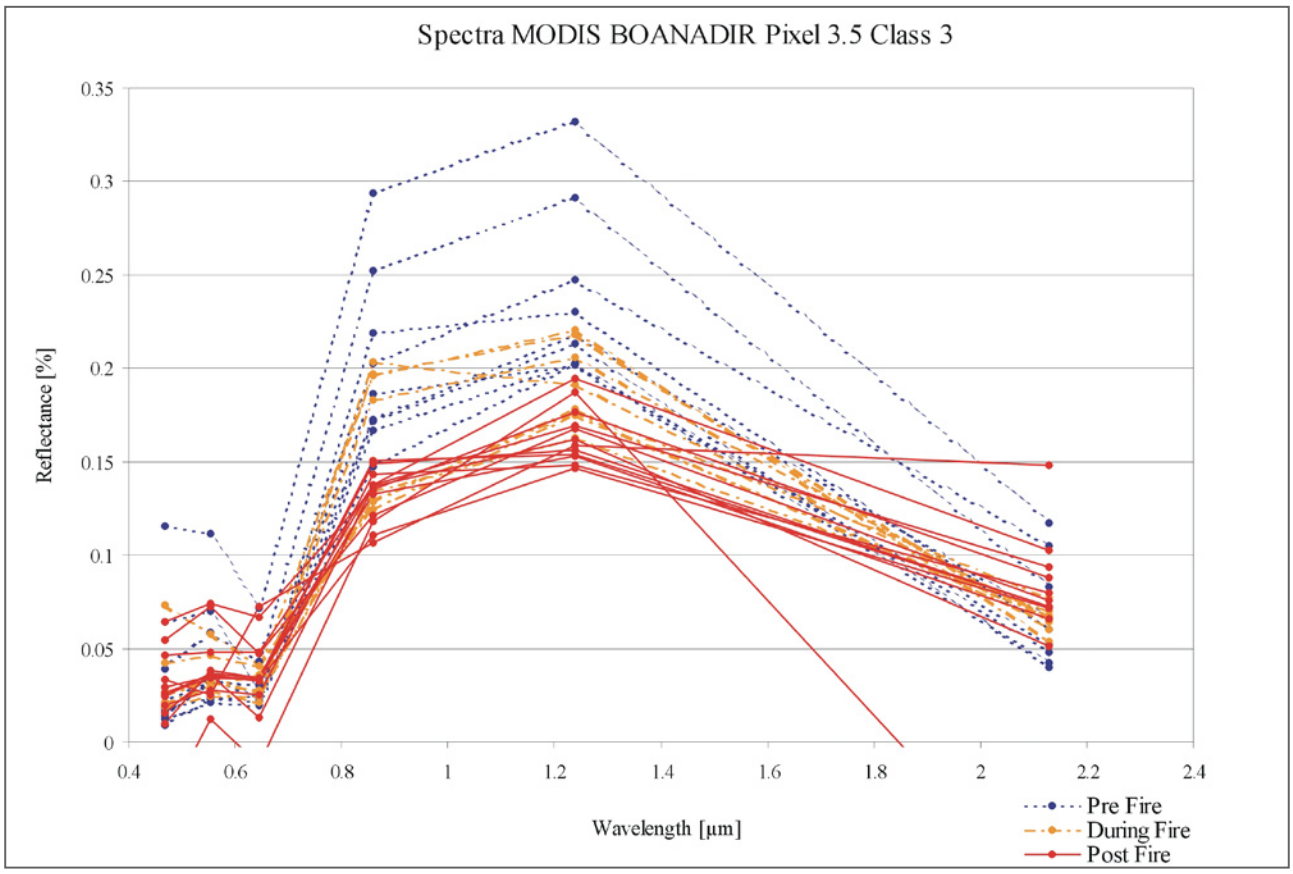

▲ *Figure 7-11: Spectral properties detected from bands 1 to 5 and 7 of MODIS (BOANADIR) within one pixel (3.5) selected in class 3.*

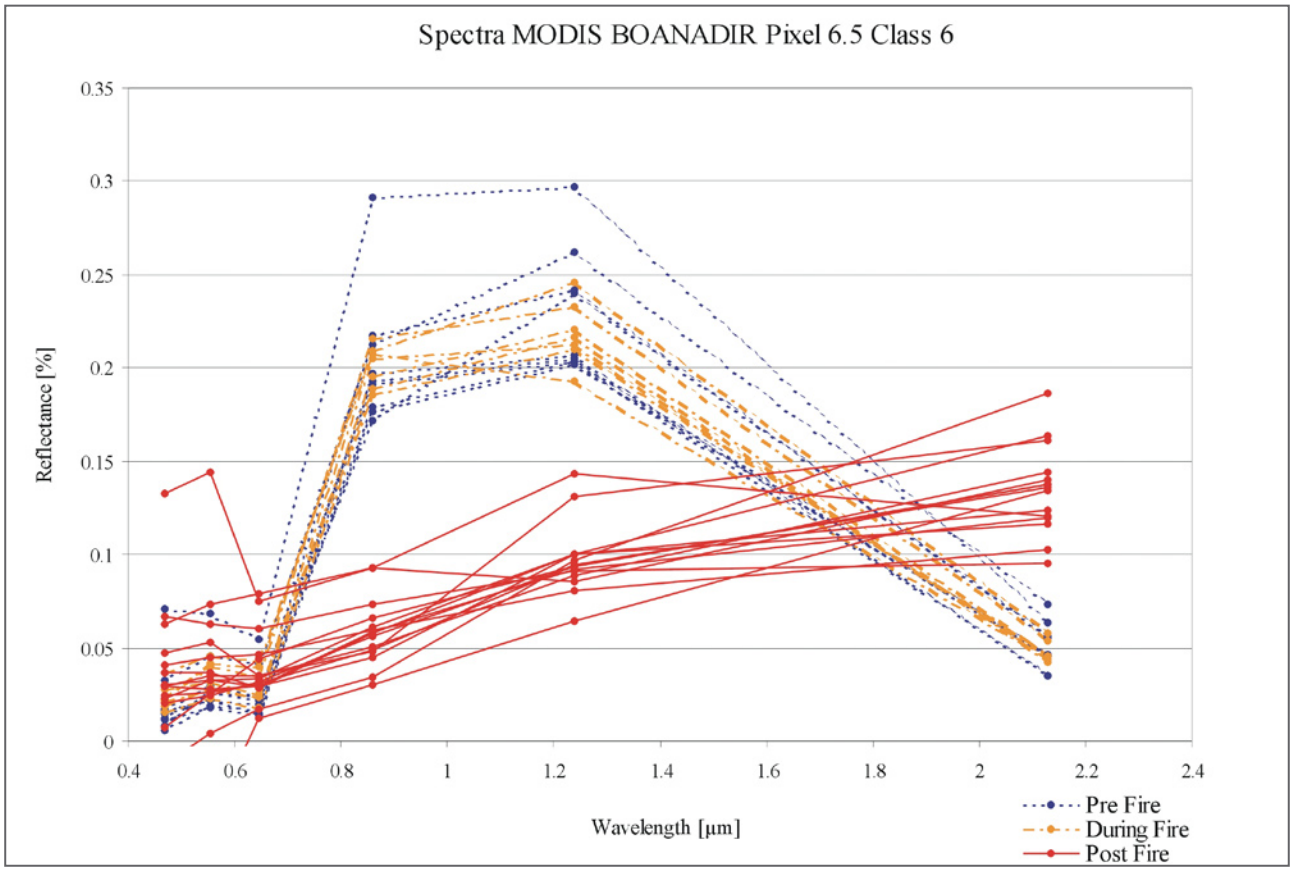

▼ *Figure 7-12: Spectral properties detected from bands 1 to 5 and 7 of MODIS (BOANADIR) within one pixel (6.5) selected in class 6.*

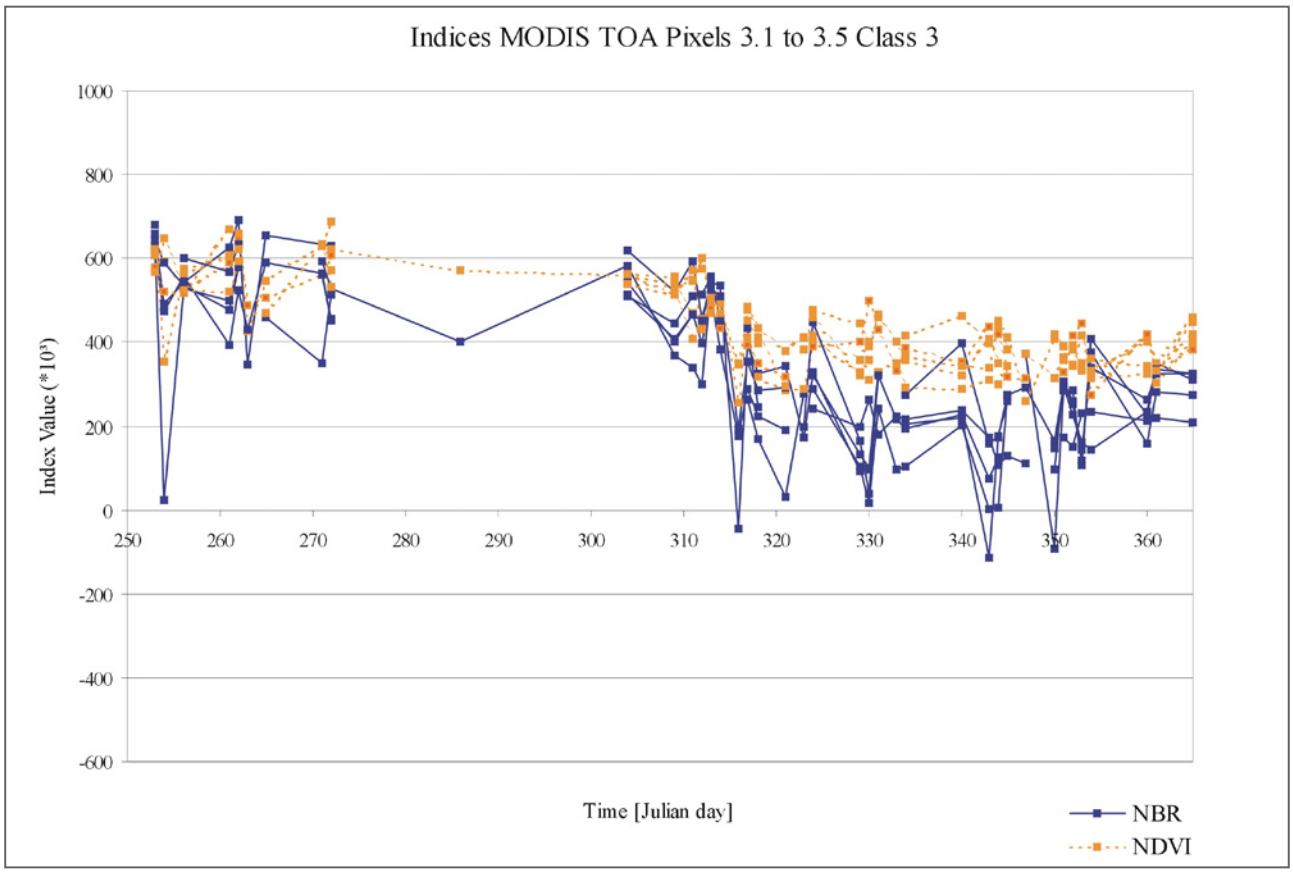

▲ *Figure 7-13: NBR and NDVI values derived from MODIS (TOA) data within 5 pixels (3.1 to 3.5) selected in class 3.*

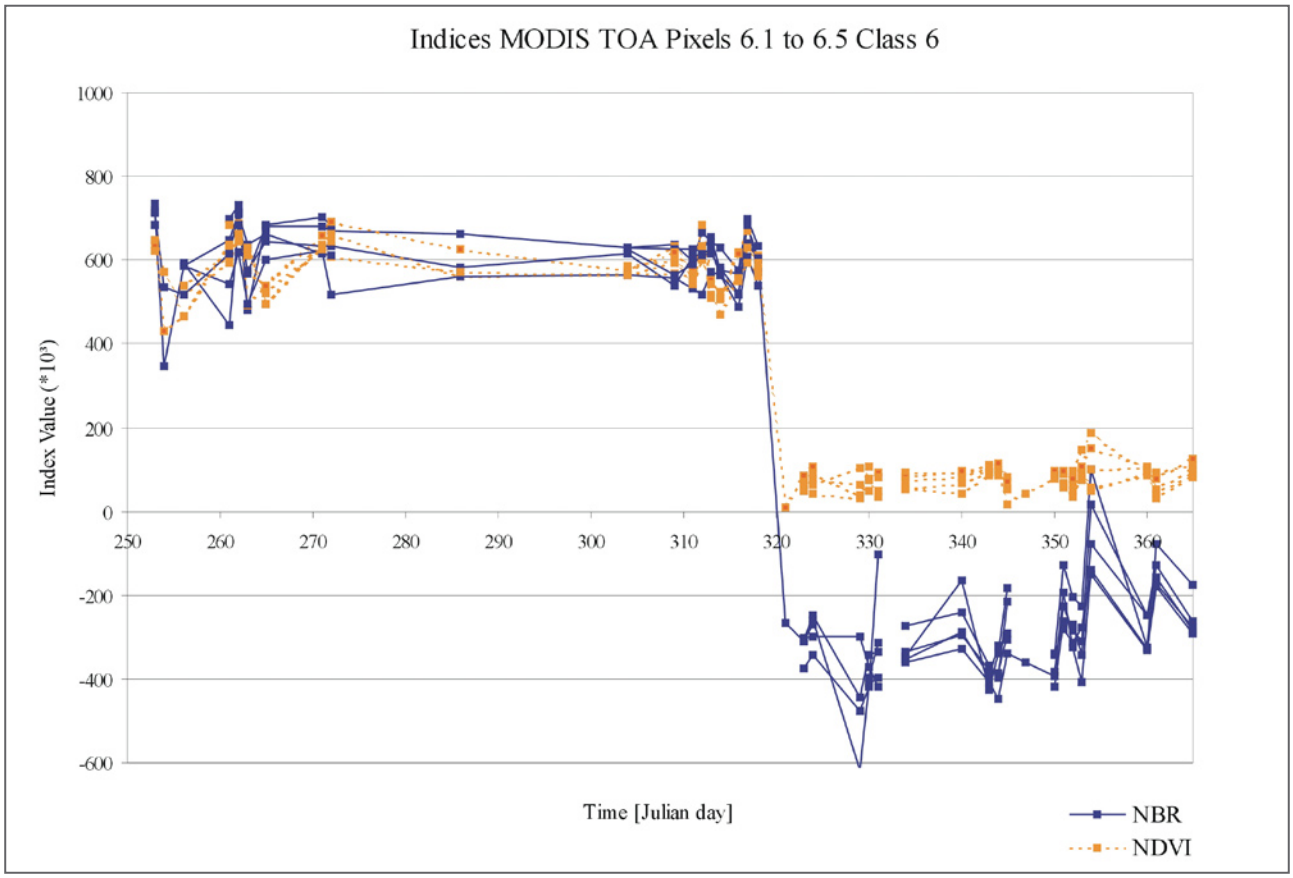

▼ *Figure 7-14: NBR and NDVI values derived from MODIS (TOA) data within 5 pixels (6.1 to 6.5) selected in class 6.*

Results from Landsat ETM+ Data

Data from the Landsat ETM+ sensor were analysed within burnt surfaces of FAA1 to 3 based on three scenes from year 2002. Firstly, the reflectance change due to variations of phenology between pre-fire and post-fire data were analysed, as pre-fire image was recorded 9 months before fire.

The spectral properties of Landsat ETM+ data of the year 2002 within selected training areas with ~95,000 pixels are presented in Figure 7-15. The spectra represent the reflectance change of phenological variation between different scenes of February, November and December. The variance within bands 3, 4 and 7 are focused as those where used to derive the indices. At 0.66µm (band 3) reflectance detected in February image is centred between lower reflectance (0.02) in December and higher reflectance (0.045) in November. At 0.84µm (band 4) reflectance shows a marked decrease in post-fire data, despite the area not being affected by fire. Band 4 reflectance of February within training area is 0.235. It decreases in November to 0.205 and in December to 0.189. In band 7 at 2.22µm November reflectance is higher with 0.046 compared to reflectance in February (0.024) and December (0.019). The results of classes 3 and 6 of FAA1 are presented in Figures 7-16 and 7-17. The trends of data within all classes 1 to 6 and the results from FAA 2 and 3 are listed in the Appendix (Figures A9-1 to A9-6, A10-1 to A10-6 and A11-1 to A11-6).

The spectra of ETM+ data in class 3 are illustrated in Figure 7-16. Results of either class 3, derived by classifying ΔNBR_{Nov} image and ΔNBR_{Dec} image are presented. In the VIS wavelengths, reflectance is low with 0.1 in the blue band 1 (0.485µm), between 0.03 and 0.07 in the green band 2 (0.57µm) and between 0.4 and 0.06 in the red band 3 (0.66µm). There is an increase of reflectance in NIR band 4 (0.84µm) with high deviation between 0.11 to 0.24. The mean pre-fire reflectance is 0.22 and markedly higher compared to the mean post-fire reflectance, which varies between 0.13 to 0.17. Towards the MIR, reflectance varies between 0.1 to 0.17 at 1.65µm (band 5), whereas pre-fire reflectance and post-fire reflectance are similar. At 2.22µm (band 7), reflectance varies between 0.02 to 0.13 with predominantly higher reflectance of post-fire data compared to low reflectance of pre-fire data (0.02 to 0.03). The change between pre-fire and post-fire reflectance is most accentuated at 0.84µm (band 4) and at 2.22µm (band 7), whereas standard deviation is highest at these wavelengths at the same time. Pre-fire reflectance is similar based on both classifications. Reflectance of post-fire data has a trend at 2.22µm (band 7), where

Figure 7-15: Spectral properties of 3 Landsat ETM+ scenes from bands 1 to 5 and 7. The data are investigated within the same test regions of unburnt vegetation in the study area. The chart demonstrates variation of reflectance within the temporal gap of ten months between February and Decemeber.

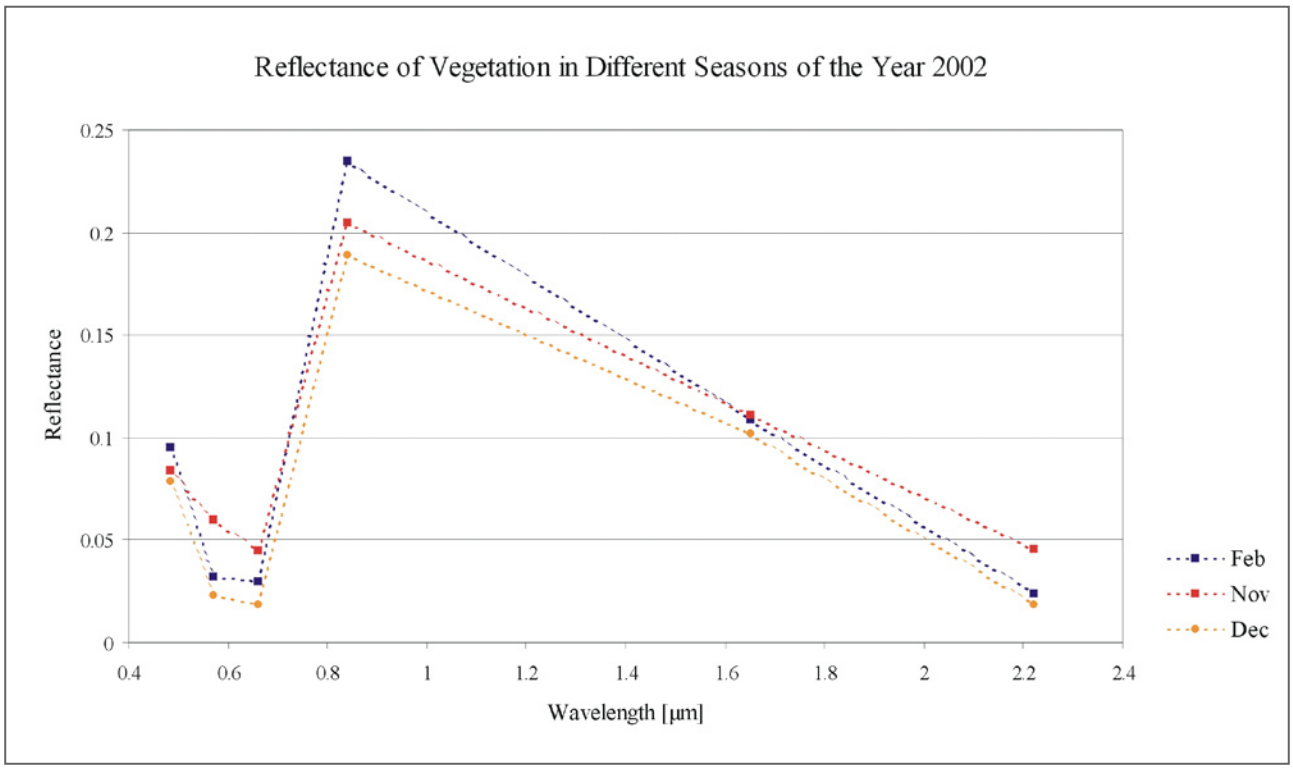

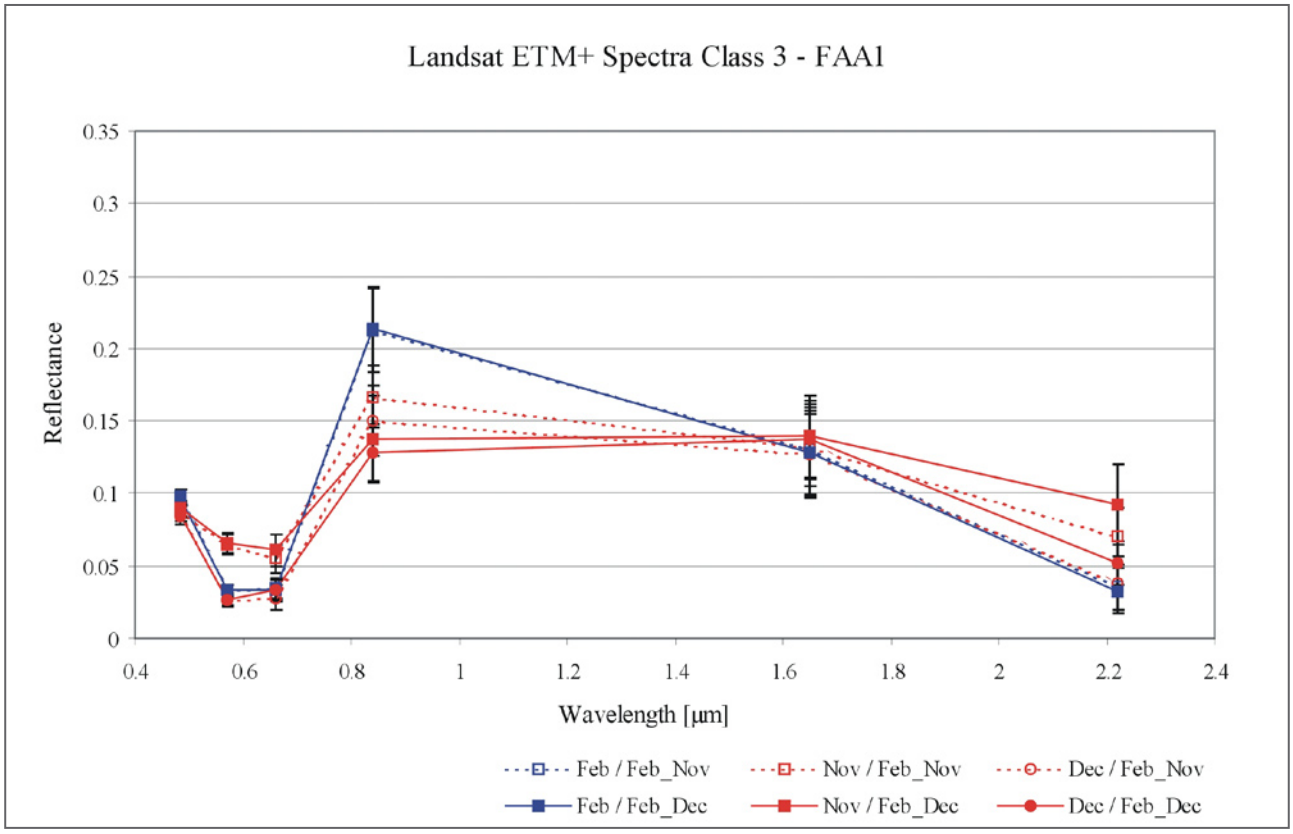

▲ *Figure 7-16: Spectral properties detected from bands 1 to 5 and 7 of Landsat ETM+ within class 3 of FAA1. The results are derived within class 3 from both the ΔNBR_{Nov} image and the ΔNBR_{Dec} image. The blue line refers to February data, which was 9 months before fire, the red lines refer to post-fire data recorded in November and December.*

▼ *Figure 7-17: Spectral properties detected from bands 1 to 5 and 7 of Landsat ETM+ within class 6 of FAA1. The results are derived within class 6 from both the ΔNBR_{Nov} image and the ΔNBR_{Dec} image.*

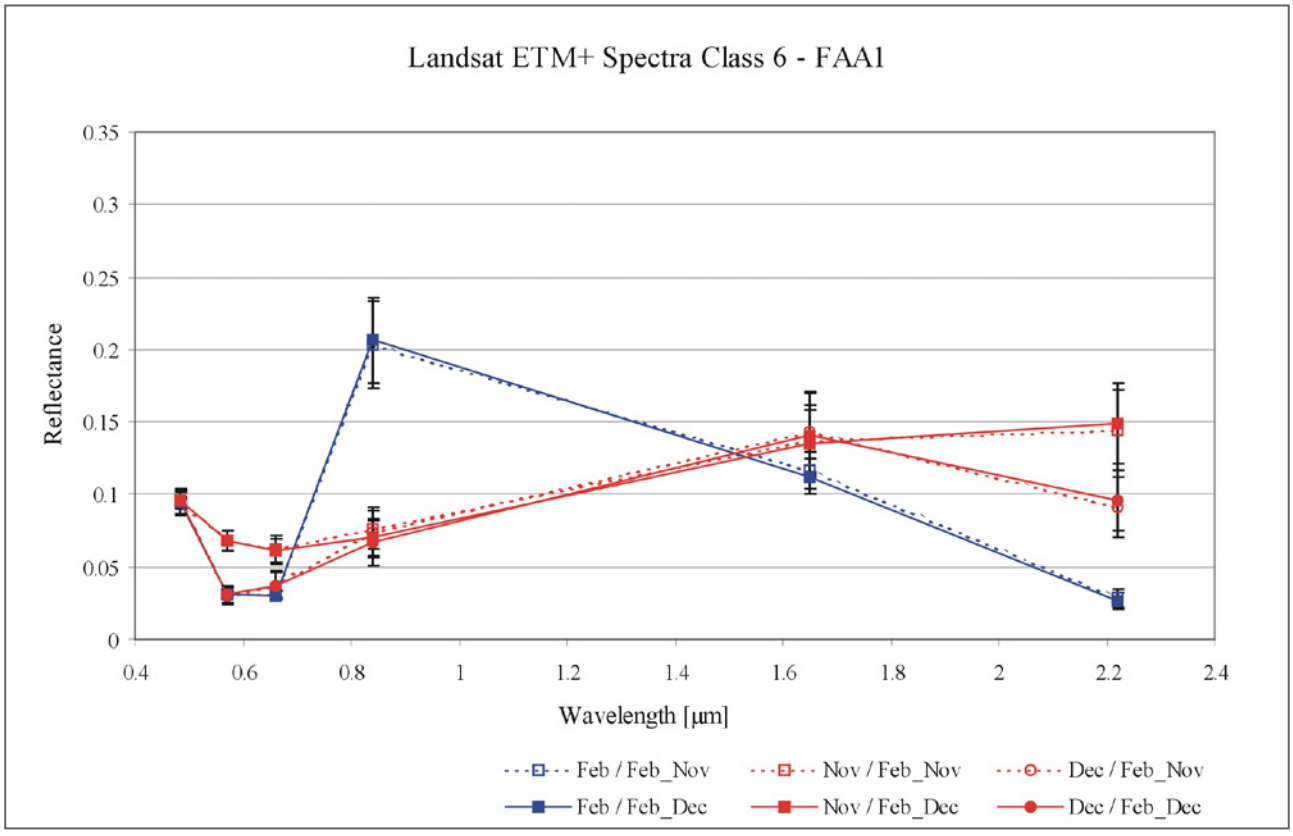

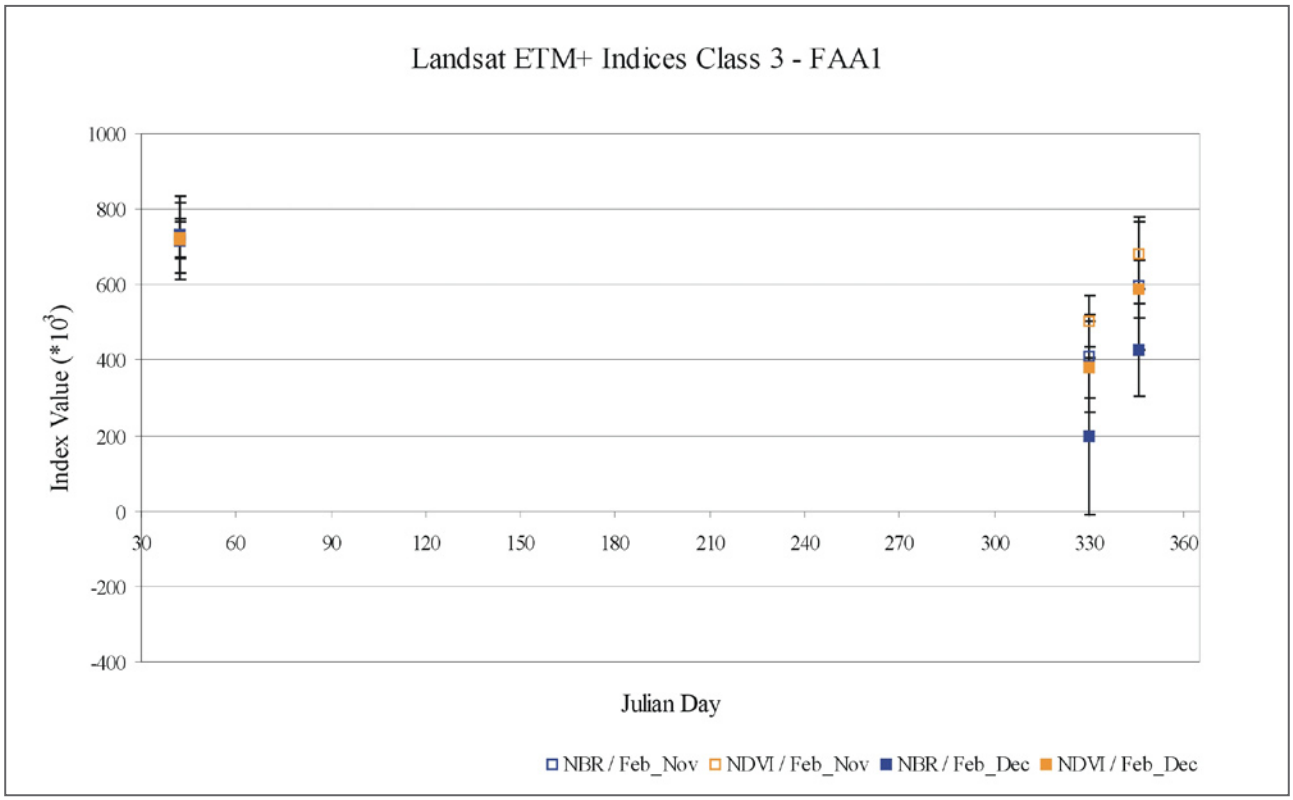

▲ *Figure 7-18: NBR and NDVI values derived from Landsat ETM+ data within class 3 of FAA1. The results are derived within class 3 from both the ΔNBR_{Nov} image and the ΔNBR_{Dec} image.*

▼ *Figure 7-19: NBR and NDVI values derived from Landsat ETM+ data within class 6 of FAA1. The results are derived within class 3 from both the ΔNBR_{Nov} image and the ΔNBR_{Dec} image.*

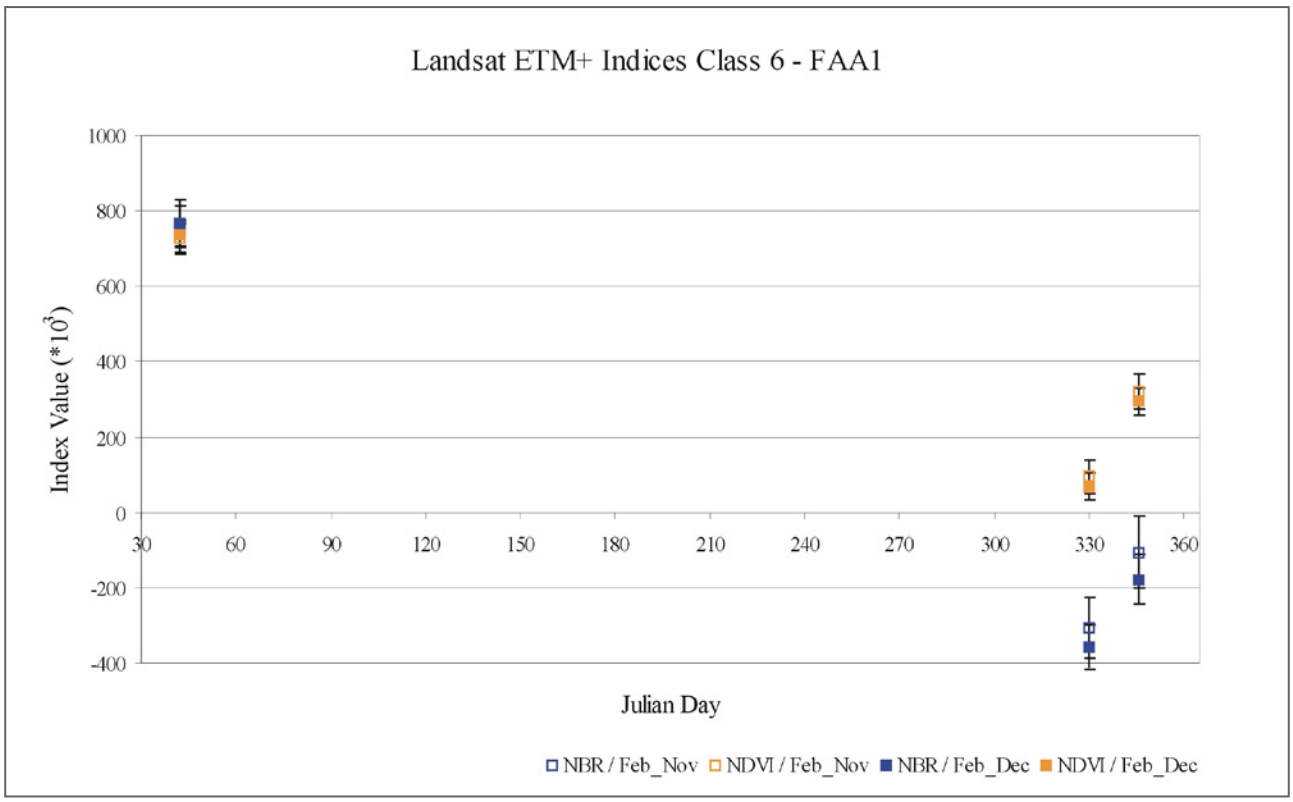

higher values were derived from November data compared to December data.

The spectra derived from ETM+ images of either class 6 accentuate the detection of change between unburnt and burnt surface (Figure 7-17). Results received from all data within the VIS wavelengths are comparable to reflectance values within classes 3. Reflectance of pre-fire data in the NIR band 4 is 0.21 with standard deviation of 0.03, which is similar to the result of class 3. The data post-fire show a marked decline of reflectance varying between 0.05 to 0.08. At 1.65µm (band 5) reflectance is marginally lower in pre-fire data compared to post-fire data varying between 0.1 to 0.17. The pre-fire reflectance at 2.22µm (band 7) is low with values between 0.02 to 0.03, whereas post-fire reflectance shows a marked increase at this wavelength. It is significant that November data has a more accentuated increase compared to December data in band 7, which can be related to the aging of the fire affected area. The greatest difference of reflectance is in bands 4 and 7 of Landsat ETM+, whereas the change signal is more accentuated in class 6 compared to class 3.

Values of the NBR and NDVI were calculated from three Landsat ETM+ scenes of year 2002 in classes 1 to 6 based on uniform classifications of the ΔNBR_{Nov} and ΔNBR_{Dec} images. The results of classes 3 and 6 within FAA1 are presented in Figure 7-18 and Figure 7-19. Further results of indices from FAA 1 to 3 of all classes are presented in the Appendix (Figures A12-1 to A12-6, A13-1 to A13-6 and A14-1 to A14-6).

Figure 7-18 represents the index values derived within class 3 versus time in Julian days. The NBR has values around 700 with standard deviation around 100 within both class 3 regions before fire (Julian day 42). These index values show a decrease in post-fire data, whereas the decline of values is more significant more recent post-fire at Julian day 330 compared to Julian day 346. The NBR mean values vary between 200 (Feb_Dec) and 400 (Feb_Nov) at Julian day 330 and increase between 400 (Feb_Dec) and 600 (Feb_Nov) at Julian day 346. The NDVI has similar values in the pre-fire image, whereas the decline of these index values post-fire is less when compared to the NBR. NDVI mean values vary between 400 (Feb_Dec) and 550 (Feb_Nov) at Julian day 330 and increase between 600 (Feb_Dec) and 700 (Feb_Nov) at Julian day 346. The signal of the burnt surface is more enhanced soon after fire and weakens with age.

The index values derived within class 6 are illustrated in Figure 7-19. The change detected by the indices between unburnt and burnt surfaces is marked. The index values at Julian day 42 before fire vary between 700 and 820. The decline of values post-fire is significant, whereas the NBR shows a greater change than the NDVI. Values of the NBR vary between –400 and –200 at Julian day 330 and increase between –200 and 0 at Julian day 346. The NDVI has values between 50 and 150 at Julian day 330 and increase between 250 and 350 at Julian day 346. The contrast between index values derived from classes of the ΔNBR_{Nov} and ΔNBR_{Dec} images are reduced in class 6 compared to class 3. The weakening signal with increasing age of the burnt area is accentuated by the images through time.

7.2 Field Classification of Burn Severity

The aim of the field trip was to establish a relationship between loss of biomass viewed in the satellite images and the loss of biomass viewed on the ground. The different levels of burn severity relating to loss of biomass have no linear context to ecological effects within different ecosystems. Due to the structure of the vegetation, 4 classes of burn severity were discriminated. The resulting classes were unburnt, low burn severity, moderate burn severity and high burn severity. The strata affected by fire were a major benchmark, as this reflects the flame height and correlates with fire intensity.

Figure 7-20 represents a plot in open shrubland that was visited in the field trip. The image clearly illustrates that distinct borders between total burnt and unburnt plots were visible in the field, where the fire suddenly went out. This resulted in different levels of burn severity within a footstep. A high level of heterogeneity in fire behaviour was frequently observed in the field, as further represented in Figure 7-21. The image illustrates, that this plot in jarrah-marri forest showed lower and higher trees in direct neighbourhood affected by fire, whereas severity of fire impact varied strongly between the adjacent trees. The heterogeneous behaviour of fire made classification of burn severity in this nature very difficult.

Furthermore, various structures of vegetation complicated a uniform classification of burn severity in respect to biomass reduction. At present there are three prevailing structures of vegetation in the study sites, which are described by karri forest, jarrah-marri forest and open shrubland or open woodland (see chapter 3.2). It was recognisable in the field that the structure of vegetation had a significant influence on fire behaviour and resulting burn severity. A burnt area of open shrubland was either burnt or unburnt, as there was no second stratum existing above ground. Burnt shrubland despite being totally burnt showed regeneration of vegetation 6 weeks post-fire, as resprouters are visible in Figure

▲ *Figure 7-21: Heterogeneous burn pattern observed in a burnt area of jarrah-marri forest. Burnt and unburnt trees were in direct neighbourhood within a burnt area.*

◄ *Figure 7-20: Distinct border between burnt and unburnt vegetation observed in a burnt area of open shrubland.*

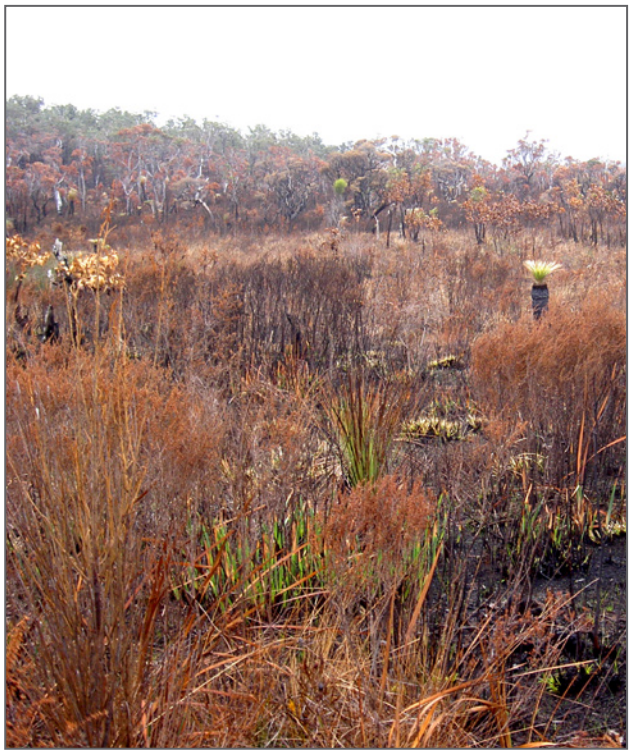

▲ *Figure 7-22: Burnt area in open shrubland. Fire behaved very uniform in shrubland due to a single stratum covering the ground. The vegetation in open shrubland is generally either consumed by fire or remains unburnt. Discrimination of levels of burn severity was therefore limited in this type of vegetation structure. Regeneration due to resprouters was observed 6 weeks post-fire.*

7-22. However, burn severity was classified as high due to complete consumption of the vegetation by fire.

Within open woodland, it was possible to discriminate levels of burn severity. Figure 7-23 illustrates an area in woodland that was considered to be affected by a milder fire because the canopy of trees was unburnt. Due to the consistent burn of the ground layer, burn severity was considered moderate, when the canopy of trees in open woodland was unburnt or partly burnt and green biomasses was remaining. A complete burnt tree canopy in open woodland was considered as high burn severity.

The structure of karri forests influence fire behaviour in the way that different strata within the forest are clearly separated. The distance between the upper understorey and the canopy is often a limit to the flame height, as fuel is not sufficient to spread fire. The term fuel addresses live fuel on trees in this context. The karri forests are rarely affected by high burn severity, because the canopy is rarely affected by fire. Burn severity in karri forests was low, when only the understorey at around 3m height was affected by fire (Figure 7-24). It was moderate, when the upper understorey was also burnt, whereas the canopy of this stratum has to be burnt completely. Karri forest, which was affected moderate or high severely by fire, was not present in the field trip.

The jarrah-marri forests is the vegetation structure that dominates in the study area. It demonstrated a distinct structure composed of 3 strata, whereas the green biomass is similarly distributed between different storeys. It therefore represents the clearest classification of burn severity in respect to biomass reduction due to fire. The resulting classification describes 4 classes of burn severity. Class 1 characterises unburnt vegetation. It was included in the burn severity measurement as areas of retreat for flora and fauna are a major goal of prescribed burning to meet the objective of conservation. Class 2 describes low burn severity, where only the understorey is affected by fire. Class 3 refers to moderate burn severity, where understorey and upper understorey are affected by fire. Class 4 specifies high burn severity, where the canopy is affected by fire.

Figure 7-25 represents a jarrah-marri forest, which characterises low burn severity in class 2. The litter on the forest floor is consumed by fire, whereas heavy fuels like branches were predominantly scorched. The herbs and low shrubs of the understorey were either consumed

▼ *Figure 7-23: Moderately burnt area in open woodland. The canopy of the trees remained green, whereas lower parts of the trees were scorched. The shrub layer was completely burnt. Different levels of burn severity could be discriminated in open woodland benchmarked by the the tree layer of woodland.*

▲ *Figure 7-24: Karri forest affected by low burn severity. The understorey of the forest, which is approximately 3m high, has been completely burnt. The upper understorey and the canopy were not affected by fire. The discrimination of different levels of burn severity was benchmarked by the 3 different strata within the forest. A huge gap between the upper understorey and the canopy caused inhomogeneous distribution of biomass within the forest that highly limits crown fires.*

or scorched, whereas scorched leaves fall off subsequently. Vegetation of the upper understorey and canopy remained green. Flame height causing low burn severity in jarrah-marri forest was around 50cm, which was measured by scorch height up to 3m. Resprouters were visible on the forest floor 6 weeks post-fire.

A jarrah-marri forest was characterised as moderately burnt in class 3, when the understory and the upper understorey were affected by fire (see image in Figure 7-35). Litter, herbs and low shrubs of the forest floor and understorey were consumed, whereas heavy fuels have been deeply charred. Soil was exposed except for scorched leaves falling off the affected trees. The lower trees of the upper understorey were predominantly scorched, but not defoliated. The canopy of the forest remained green or was fractionally scorched. Moderate burn severity in jarrah-marri forests was caused by flame height around 1.5m to 2m with scorch height up to 12m. Regeneration was not visible on the forest floor 6 weeks post-fire.

The jarrah-marri forest was classified as high burn severity in class 4, when all strata of the forest were affected by fire (see image in Figure 7-36). Bare soil is exposed on the forest floor except for some scorched leaves falling off the canopy. The understorey is completely consumed by fire. The trees that form the intermediate stratum of the forest are predominantly defoliated. The stems are frequently charred and blackened. The canopy is scorched or partly defoliated. No green leaves are remaining. Fire with flame height over 2m to 3m caused severe burn conditions. Scorch height on the stems varied between 12m up to the canopy at about 30m. Process of regeneration was not observable 6 weeks post-fire.

This classification defined in the field is at the same time describing the change in the amount of biomass, which is measurable with satellite remote sensing. The results that are gathered from remote sensing data have to be verified in respect to the field measurements. The resulting data from satellite have to be calibrated equivalently to the ground truth data.

▼ *Figure 7-25: Jarrah-marri forest affected by low burn severity. Only the understorey of the forest was affected by fire. The discrimination of different levels of burn severity was benchmarked by the 3 different strata within the forest. The jarrah-marri forest presents a homogeneous distribution of biomass within the forest, which may more easily cause crown fires compared to karri forest.*

7.3 Assessment of Burn Severity with Remote Sensing Data

In order to assess burn severity using satellite remote sensing the data needs to be calibrated with ground truth data. A first approach to validate remote sensing data consisted in the comparison of ground truth data and high resolution Landsat TM data. As the final result of this study, the remotely sensed measurement of burn severity was calibrated based on the ΔNBR index imagery of Landsat and MODIS data. The calibration was related to the field classification of burn severity.

Burn Severity Assessment of Landsat Data based on Ground Truth Data

There were 14 GCPs, which were compared to results received from Landsat TM data in the corresponding area. Five GCPs are presented in a detailed comparison between field data and remote sensing data within this section, whereas results of the others are listed in the Appendix (Figures A15-1 to A15-9). The five GCPs represent different structures of vegetation and different classes of burn severity. The spectra of each sample derived pre-fire and post-fire illustrate the result of Landsat TM data for each plot. The pre-fire Landsat TM image was from December 2003 and the post-fire Landsat TM image was from May 2004, which was recorded 4 weeks post-fire. Bands 3, 4 and 7 are focused as indices are calculated from those bands. The results of index values are listed in tables within the adequate GCP plot. The corresponding photos were taken in the field and added to the results in order to avoid a single subjective interpretation by the author.

The selected GCP 1 was sampled in jarrah-marri forest with moderate burn severity of class 3 (Figure 7-26). The understorey was completely consumed. The soil was exposed, but partly covered by scorched leaves fallen off the upper trees. The intermediate stratum was completely scorched, whereas the major part of the canopy remained green. Resprouters were visible on the ground 4 weeks post-fire. The post-fire spectrum illustrates the greatest change in bands 4 and 7 compared to the pre-fire spectrum. The pre-fire spectrum had reflectance of 0.05 at 0.66µm (band 3), rose to 0.2 at 0.84µm (band 4) and declined to 0.05 at 2.22µm (band 7). The post-fire spectrum had higher reflectance in band 3 with 0.07, increased to 0.1 in band 4 and decreased to 0.08 in band 7. The pre-fire NBR was minorly lower compared to the pre-fire NDVI with values of 601 and 628, respectively. The post-fire NBR was noticeable lower compared to the post-fire NDVI with values of 108 and 232,

Figure 7-26: GCP 1 sampled in jarrah-marri forest, where burn severity was measured as moderate in class 3. The spectral properties and index values within the Landsat pixel of the GCP are illustrated in the Table and Chart of GCP 1, whereas the filled square refers to the measured reflectance and connecting lines are to facilitate inspection. The pre-fire Landsat TM data was aquired in December 2003 and the Landsat post-fire data was aquired in May 2004, approximately 1 month post-fire.

GCP 1	NBR	NDVI	ΔNBR	ΔNDVI
Pre Fire	601	628		
Post Fire	108	232	493	396

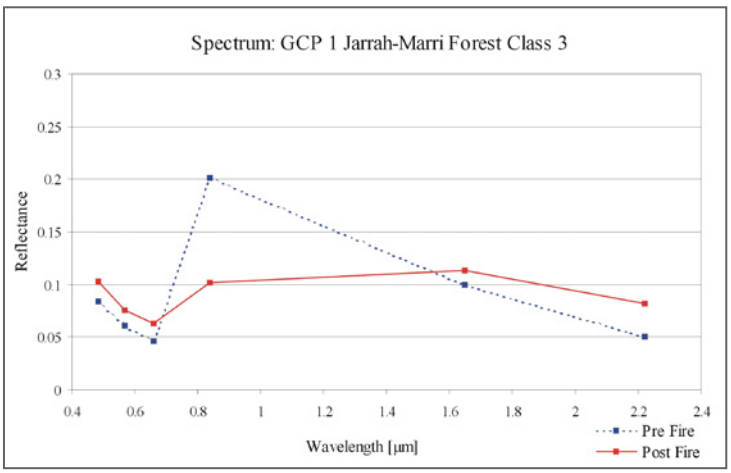

GCP 2	NBR	NDVI	ΔNBR	ΔNDVI
Pre Fire	524	567		
Post Fire	614	392	-90	175

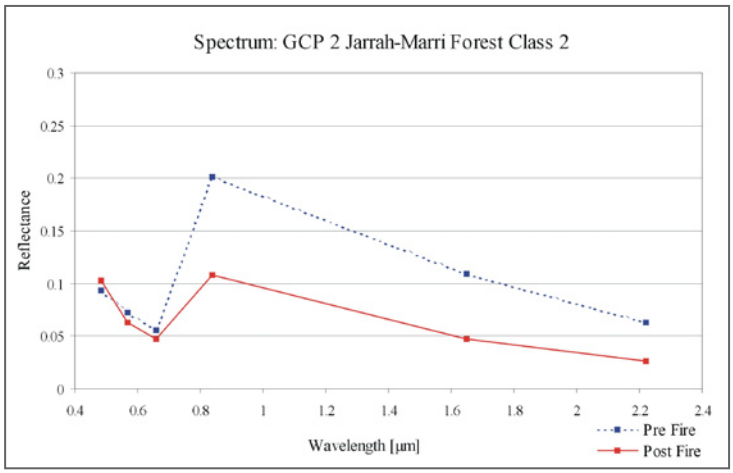

▲ *Figure 7-27: GCP 2 sampled in jarrah-marri forest, where burn severity was measured as low in class 2. The spectral properties and index values within the Landsat pixel of the GCP are compared with the field measurement of burn severity.*

▼ *Figure 7-28: GCP 3 sampled in jarrah-marri forest, which was not affected by fire. An unburnt pixel in pre-fire and post-fire data demonstrates reflectance change between Landsat data recorded in December 2003 and May 2004.*

GCP 3	NBR	NDVI	ΔNBR	ΔNDVI
Pre Fire	615	626		
Post Fire	684	537	-69	89

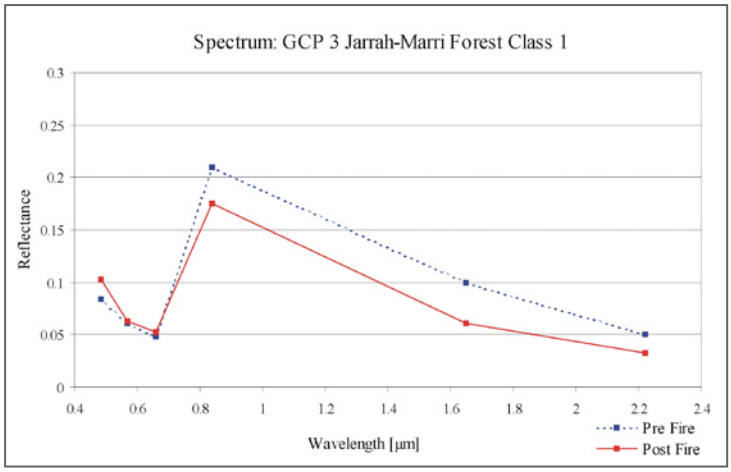

GCP 4	NBR	NDVI	ΔNBR	ΔNDVI
Pre Fire	365	490		
Post Fire	-140	79	505	411

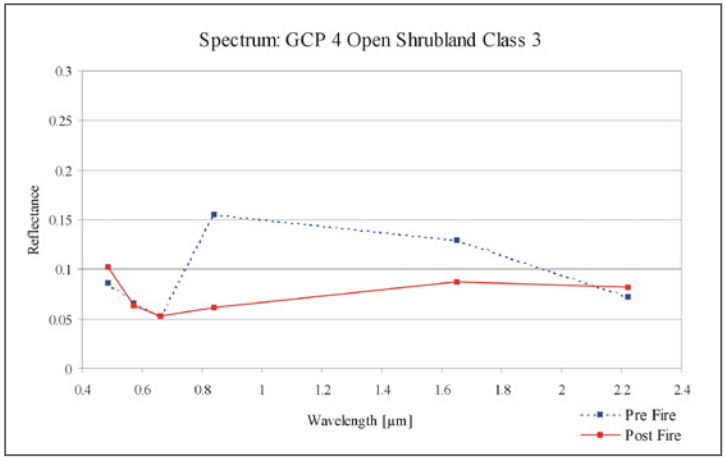

◄ *Figure 7-29: GCP 4 sampled in open woodland, where burn severity was measured as moderate in class 3. The spectral properties and index values within the Landsat pixel of the GCP are compared with the field measurement of burn severity.*

GCP 5	NBR	NDVI	ΔNBR	ΔNDVI
Pre Fire	396	483		
Post Fire	10	75	386	408

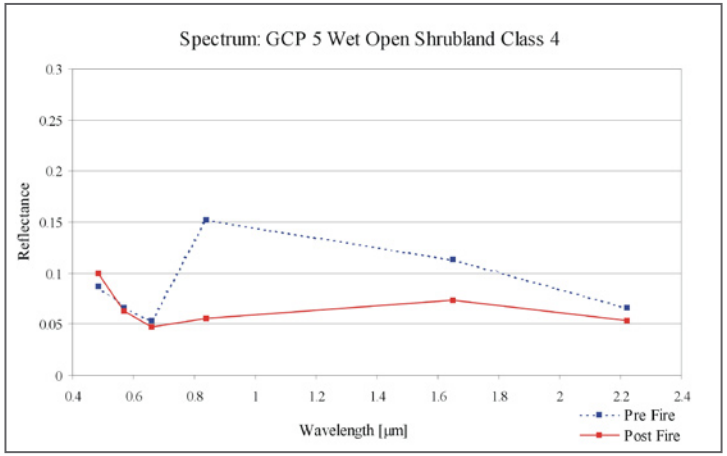

◄ *Figure 7-30: GCP 5 sampled in wet open shrubland, where burn severity was measured as high in class 4. The spectral properties and index values within the Landsat pixel of the GCP are compared with the field measurement of burn severity.*

respectively. The change signal between pre and post-fire indices resulted higher from the ΔNBR with 493 compared to the ΔNDVI with 396.

GCP A2 was selected in jarrah-marri forest as well, whereas this plot was estimated to be low burnt and classified into class 2 (Figure 7-27). The understorey was partly burnt, but green leaves remained in the shrub layer. Fire has affected this area as a mosaic between burnt spots with consumption of the understorey and unburnt herbs and shrubs covering the ground. The signal detected by Landsat in December has reflectance of 0.6 in band 3, 0.2 in band 4 and decreases to 0.7 in band 7. Reflectance measured in May post-fire was 0.05 in band 3, 0.11 in band 4 and showed a significant decline to 0.03 in band 7. The pre-fire NBR was minorly lower compared to the pre-fire NDVI with values of 524 and 567, respectively. The post-fire NBR was significant higher compared to the post-fire NDVI with values of 614 and 392, respectively. The change signal between pre and post-fire indices resulted in this case very low from the ΔNBR with -90 compared to the ΔNDVI with 175. The change due to fire was more accentuated by the NDVI in this example.

The GCP 3 of unburnt jarrah-marri forest was investigated to compare the change between imagery recorded in December and imagery recorded in May (Figure 7-28). The photo illustrates a jarrah-marri forest not affected by fire. as found out in conversation with fire managers, the area did not burn within the last 5 years. The spectrum of GCP 3 detected in December shows reflectance of 0.05 in band 3, 0.21 in band 4 and 0.05 in band 7. The spectrum derived from the May image has reflectance values of 0.06 in band 3, 0.18 in band 4 and 0.03 in band 7. In the infrared wavelengths reflectance in May is lower between 0.02 and 0.04 compared to December, whereas it is insignificantly higher in band 3. The NBR in December was minorly lower compared to the NDVI with values of 615 and 626, respectively. The NBR in May was higher compared to the NDVI with values of 684 and 537, respectively. The change signal between December and May indices resulted lower from the ΔNBR with -69 compared to the ΔNDVI with 89. The ΔNBR value of the unburnt GCP is in a similar range to the signal in low burnt jarrah-marri forest of GCP 2.

The results received from comparing GCP 4 with the corresponding Landsat pixel is illustrated in Figure 7-29. The GCP 4 was sampled in open shrubland and described a moderately burnt area in class 3. There were some green leaves that remained on higher levels of the single stratum, whereas the lower parts were completely scorched. The spectrum of Landsat data before fire has reflectance of 0.15 at 0.84μm (band 4) and a decrease of reflectance to 0.07 at 2.22μm (band 7). Reflectance declines to 0.06 in band 4 and is 0.08 in band 7. Reflectance in band 3 shows little change with values around 0.05 in both images. The pre-fire NBR was significantly lower compared to the pre-fire NDVI with values of 365 and 490, respectively. The post-fire NBR was lower compared to the post-fire NDVI with values of -140 and 79, respectively. The change signal between pre and post-fire indices resulted higher from the ΔNBR with 505 compared to the ΔNDVI with 411.

The GCP 5 was sampled in wet open shrubland, where burn severity was characterised as high in class 4 (Figure 7-30). The green vegetation has been completely consumed by fire and bare soil was exposed, whereas resprouters were visible 6 weeks post-fire. It is evident in the image, that the soil is partly covered by backwater. The spectrum of the TM image recorded pre-fire within GCP 5 has a very similar trend compared to the pre-fire spectrum of GCP 4. The spectrum of GCP 5 derived post-fire had low reflectance in band 4 with 0.06 and presented similar low reflectance around 0.06 in band 7. There was no considerable change in reflectance of band 3 between pre and post-fire. The pre-fire NBR was significantly lower compared to the pre-fire NDVI with values of 396 and 483, respectively. The post-fire NBR was lower compared to the post-fire NDVI with values of 10 and 75, respectively. The change signal between pre and post-fire indices resulted lower from the ΔNBR with 386 compared to the ΔNDVI with 408. This was a further example, where the change due to fire was more accentuated by the NDVI. Furthermore, the value of the ΔNBR at GCP 5 is lower than the ΔNBR at GCP 4, despite burn severity was measured more severe at GCP 5 than at GCP 4.

Pixel of Training Area	Mean of Landsat ΔNBR	Standard Deviation	Class of Burn Severity	Threshold of Landsat ΔNBR
18159	241.40	61.34	1	<= 300
——	—	——	2	> 300 to <= 650
——	—	——	3	> 650 to <= 1000
5655	1092.74	89.89	4	> 1000

Table 7-1: Thresholds for image calibration of the ΔNBR Landsat ETM+ image (pre-fire Feb 02, post-fire Nov 02) based on training areas of unburnt and severe burnt vegetation in and around FAA1.

Classes of Burn Severity

The classes of burn severity as measured with remote sensing data and the classes of burn severity as measured in the field are presented in Figures 7-33 to 7-36 to summarise the final result of this study. The remotely sensed images from Landsat and MODIS were calibrated based on training areas selected in Landsat data of February and November 2002. Altogether 18,159 pixels were selected for training unburnt vegetation and 5,655 pixels were selected within a highly severe burnt surface. The calibrated thresholds, which were used to classify the Landsat ΔNBR_{Nov} image are listed in Table 7-1. The Landsat ΔNBR_{Nov} image was derived from pre-fire NBR of February and post-fire NBR from November. These thresholds to classify burn severity were specifically adjusted for the ΔNBR_{Nov} image, as training areas were selected within these images. The resulting image classification of burn severity is presented in Figure 7-31.

The thresholds to classify the MODIS $\Delta NBR_{MOD26\text{-}11}$ image were based on the calibrated classification of the Landsat ΔNBR_{Nov} image to achieve comparability between the two data sets. Pre-fire data of this index image resulted from mean value of the NBRs derived between September and October and post-fire data from 26th of November. The mean values and standard

Figure 7-31: Calibrated Classification of the ΔNBR Landsat ETM+ for FAA1. The thresholds, which were used to classify the index are listed in Table 7-1.The ΔNBR image was derived from data of Feb 02 as pre-fire and Nov 02 as post-fire. The classification of four classes of burn severity ist based on the field classification of burn severity.

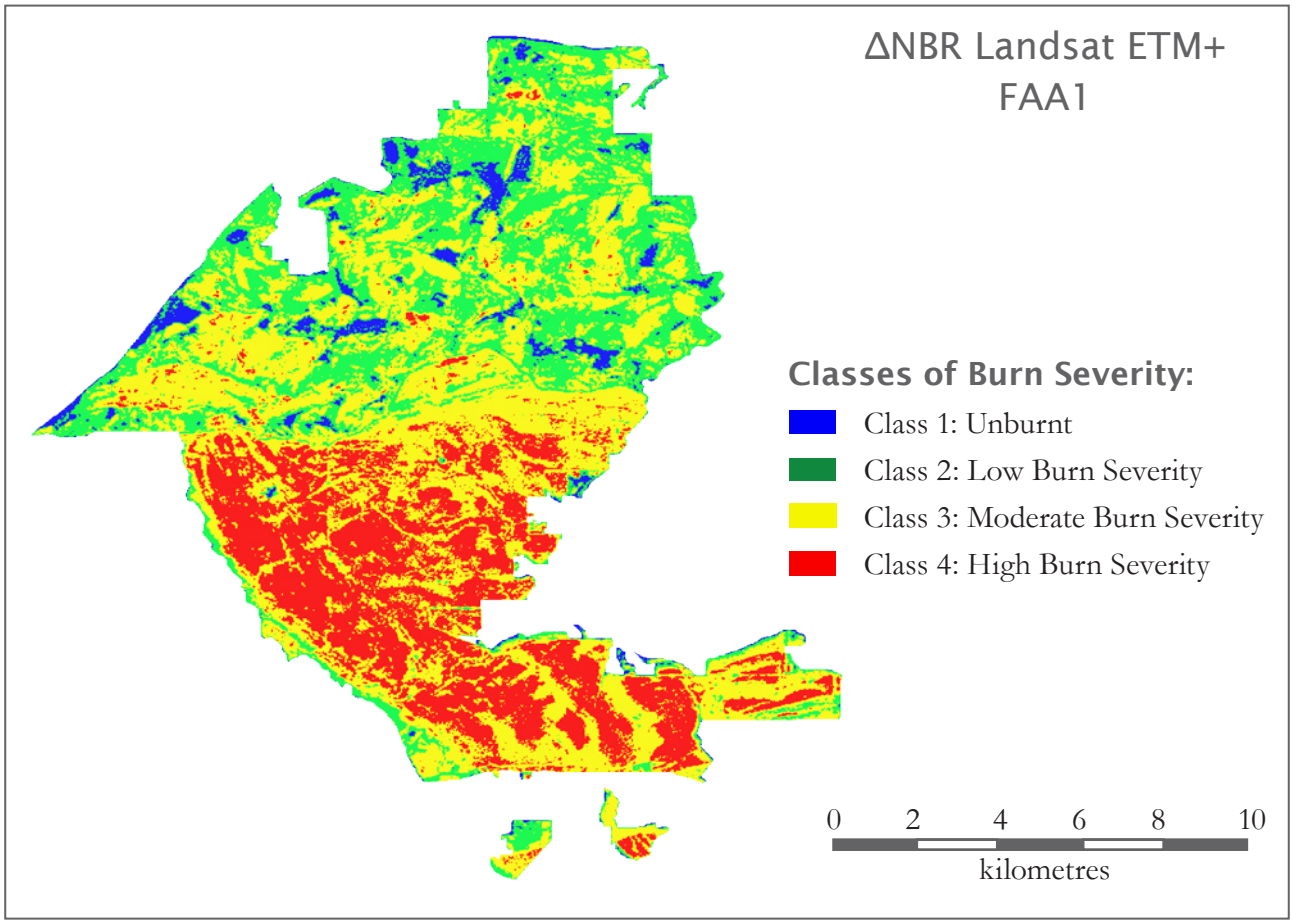

Mean of MODIS ΔNBR	Standard Deviation	Class of Burn Severity	Threshold of MODIS ΔNBR
329.94	166.52	1	<= 330
445.77	167.92	2	> 330 to <= 635
693.12	220.54	3	> 635 to <= 940
940.60	136.65	4	> 940

Table 7-1: Thresholds for image calibration of the ΔNBR Landsat ETM+ image (pre-fire Feb 02, post-fire Nov 02) based on training areas of unburnt and severe burnt vegetation in and around FAA1.

deviations received for each class as well as the thresholds to separate classes are listed in Table 7-2. The standard deviation was significantly high between 135 and 220. The MODIS $\Delta NBR_{MOD26\text{-}11}$ image was calibrated based on these thresholds into 4 classes of burn severity, whereas thresholds are specifically for this image (Figure 7-32).

Figures 7-33 to 7-36 represent the resulting MODIS and Landsat ETM+ classes 1 to 4 of FAA 1 as separate patterns together with the result of field measurement. The results of the field measurement were described in the latter section 7.2. The remotely sensed classification was directly compared between the sensors focusing the moderate spatial resolution of MODIS.

In Figure 7-33, the unburnt areas of MODIS and Landsat ETM+ class 1 are illustrated. MODIS detected the unburnt areas at the edge of the FAA more easily than within the FAA. There is an underestimation of burn severity visible at marginal areas, where MODIS detected larger unburnt areas compared to Landsat. The unburnt areas within the FAA closely match to the detection of the Landsat image, when the patch is large enough. The unburnt areas smaller than a MODIS pixel were not detected by MODIS as unburnt.

Class 2 of MODIS and Landsat classifications are presented in Figure 7-34. The classes show a similar pattern of low burn severity in the northern part of FAA 1, which was subject to prescribed burning. There are some low burnt areas detected by Landsat, which MODIS included into the unburnt class 1. This is especially observable in the

Figure 7-32: Calibrated Classification of the ΔNBR MODIS for FAA1. The thresholds, which were used to classify the index are listed in Table 7-2. The ΔNBR image was derived from MODIS (TOA) mean NBR Sep/Oct 02 as pre-fire and 26th November 2002 as post-fire. The classification of four classes of burn severity ist based on the field classification of burn severity.

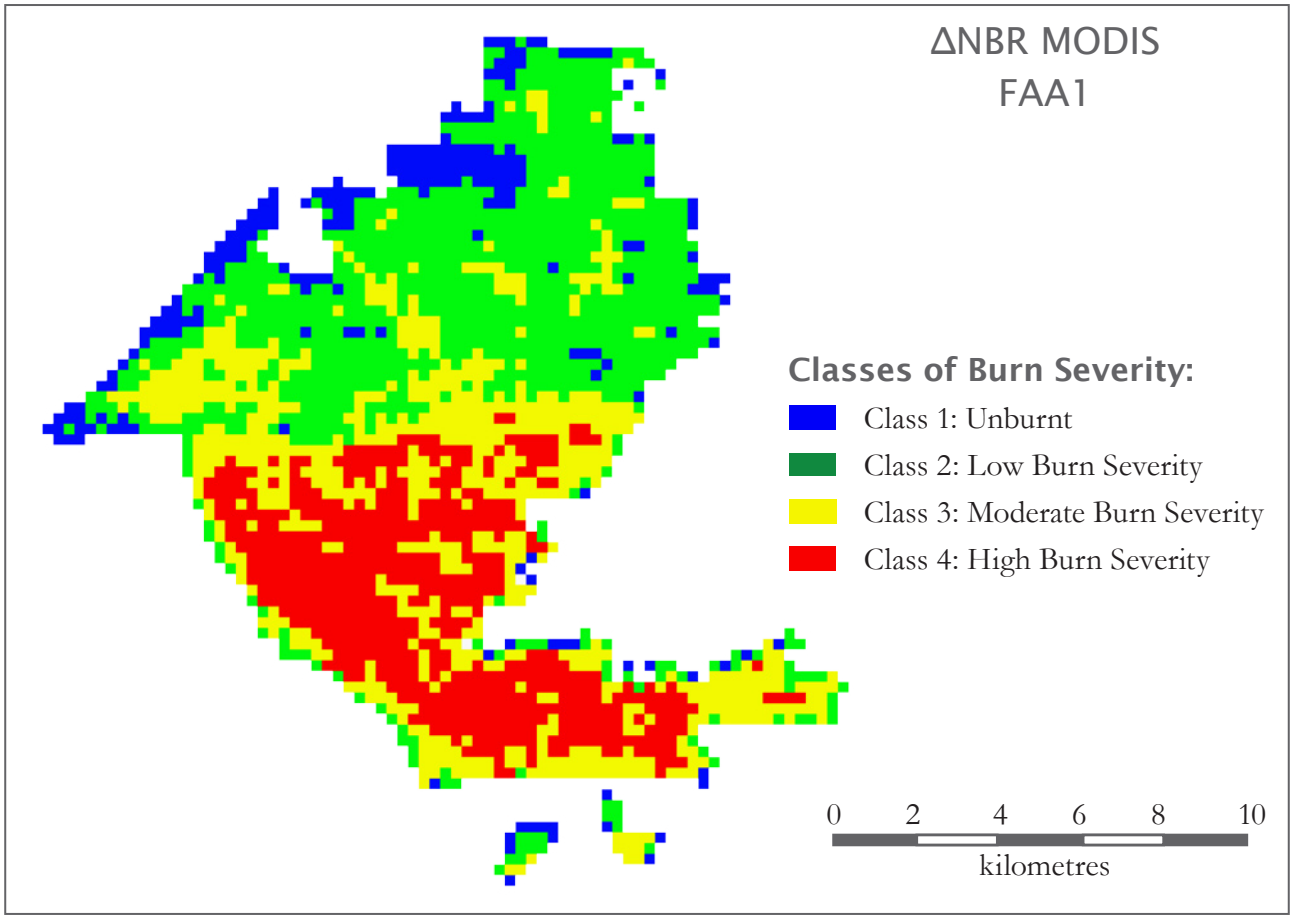

northern corner of the FAA. The unburnt areas classified by Landsat, which were not detected as unburnt by MODIS in the latter Figure, were detected as low burnt class 2 by MODIS.

Figure 7-35 shows class 3 of MODIS and Landsat ETM+. Landsat ETM+ shows a very patchy distribution of class 3 pixels, whereas MODIS was only detecting the larger areas as class 3. The conformity between class 3 of the two images is very low in areas, where Landsat detected very high patchiness. The very patchy areas of Landsat class 3 were predominantly detected as low burnt class 2 by MODIS. The size of not detected class 3 areas by Landsat ETM+ was in some areas smaller and in some areas greater than a MODIS pixel.

Class 4 of MODIS and class 4 of Landsat show high agreement between the detected pattern (Figure 7-36). Both sensors similarly detected a large surface of high burn severity in the south of FAA1, where the wildfire occurred. There are little areas detected by Landsat as severly burnt in the northern part of the FAA, which were not detected by the classification of MODIS. These areas were predominantly smaller than a MODIS pixel. Areas of Landsat ETM+ class 4, which were not detected by MODIS class 4, fell into MODIS class 3.

In summary, there was a very similar pattern between the burn severity classification of MODIS and Landsat observed. The moderate spatial resolution of the MODIS sensor provided limitation for higher conformity, when burn severity was in the intermediate class 3 and for some unburnt areas. However, in this example results between the sensors highly agreed in classes of low burn severity and high burn severity.

Burn Severity Class 1: Unburnt

Unburnt Jarrah-Marri Forest

Class 1 of Landsat ETM+

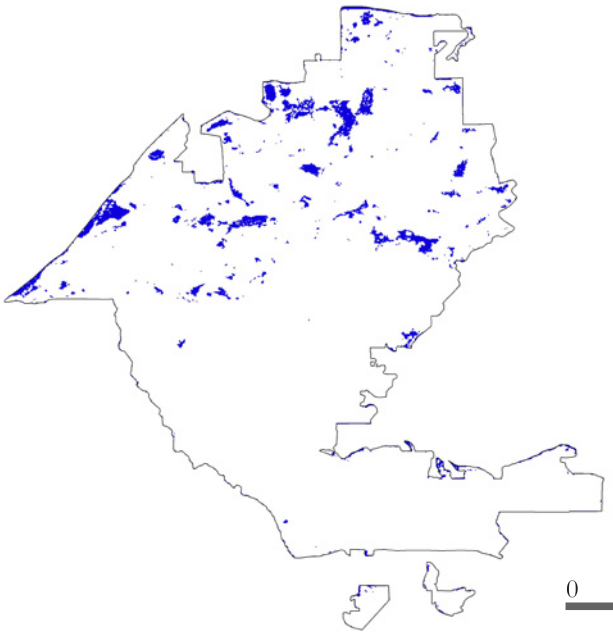

Class 1 of MODIS

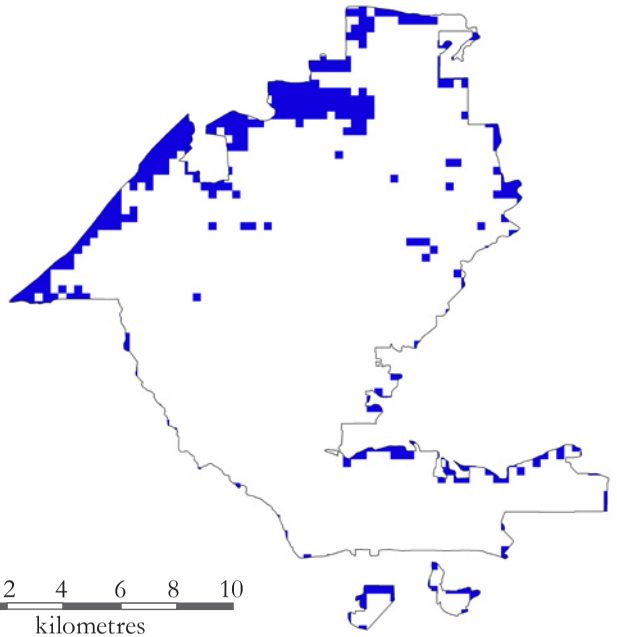

Figure 7-33: Class 1 from field measurement and the remotely sensed measurement of burn severity. The photo on the left side illustrates a jarrah-marri forest, which has not been affected by fire. The pattern of class 1 as detected from Landsat ETM+ sensor is illustrated in the middle and from MODIS on the right side. The remotely sensed class 1 of both sensor is based on the calibrated images from the latter results (Figure 7-31 & 7-32).

Burn Severity Class 2: Low Burn Severity

Low Burnt Jarrah-Marri Forest

Class 2 of Landsat ETM+

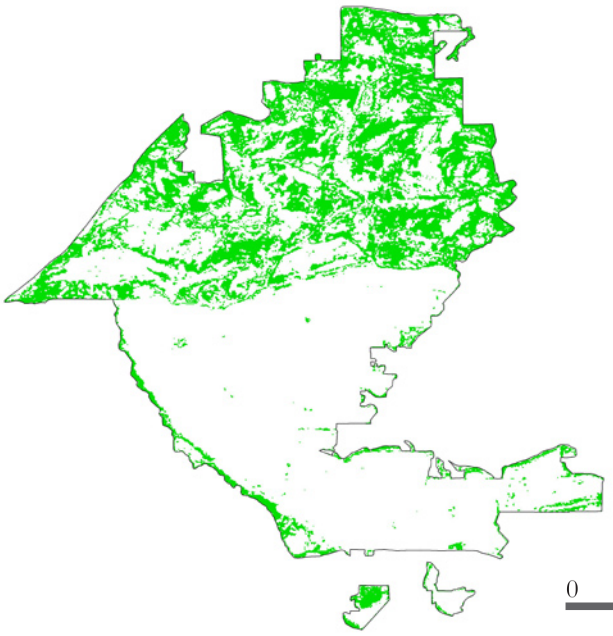

Class 2 of MODIS

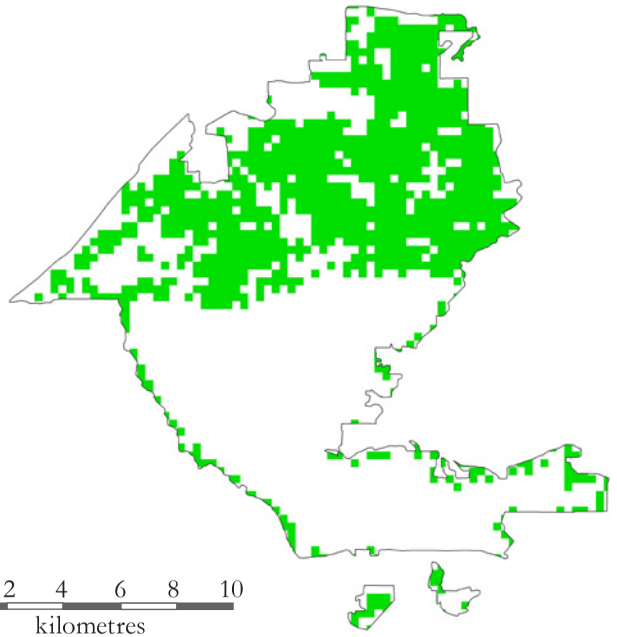

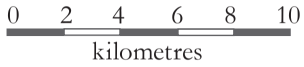

Figure 7-34: Class 2 from field measurement and the remotely sensed measurement of burn severity. The photo on the left side illustrates a jarrah-marri forest, where only the understorey has been affected by fire. The pattern of class 2 as detected from Landsat ETM+ sensor is illustrated in the middle and from MODIS on the right side. The remotely sensed class 2 of both sensor is based on the calibrated images from the latter results (Figure 7-31 & 7-32).

Burn Severity Class 3: Moderate Burn Severity

Moderately Burnt
Jarrah-Marri Forest

Class 3 of Landsat ETM+

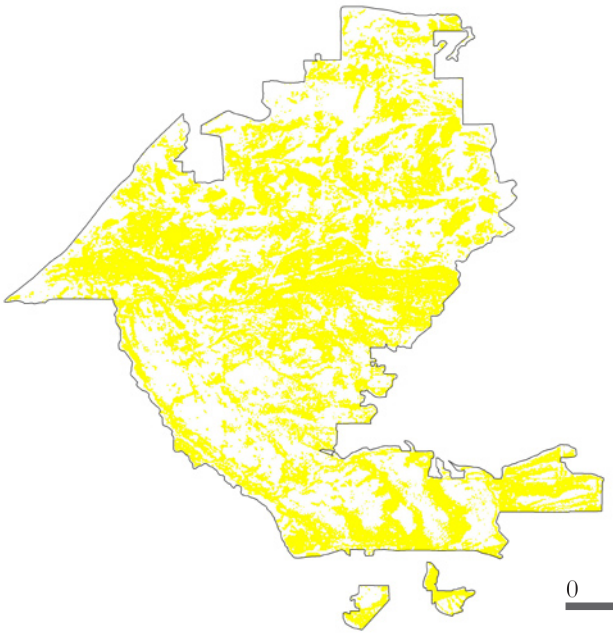

Class 3 of MODIS

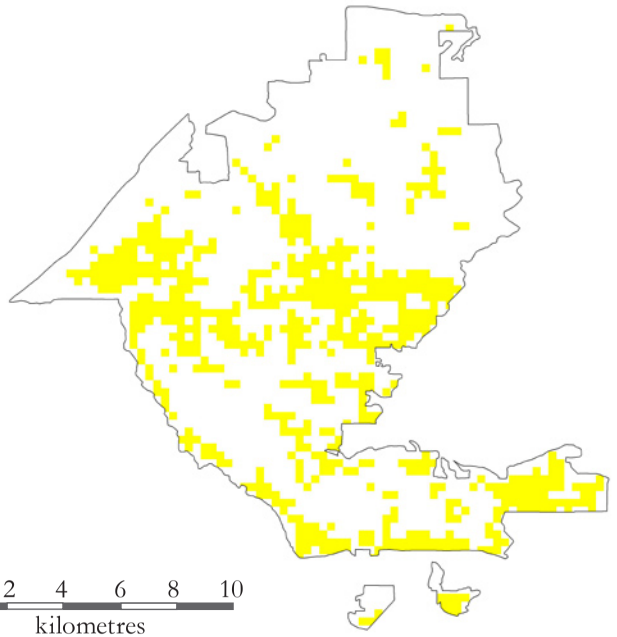

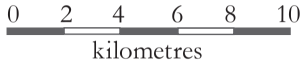

Figure 7-35: Class 3 from field measurement and the remotely sensed measurement of burn severity. The photo on the left side illustrates a jarrah-marri forest, where the understorey and the upper understorey has been affected by fire. The pattern of class 3 as detected from Landsat ETM+ sensor is illustrated in the middle and from MODIS on the right side. The remotely sensed class 3 of both sensor is based on the calibrated images from the latter results (Figure 7-31 & 7-32).

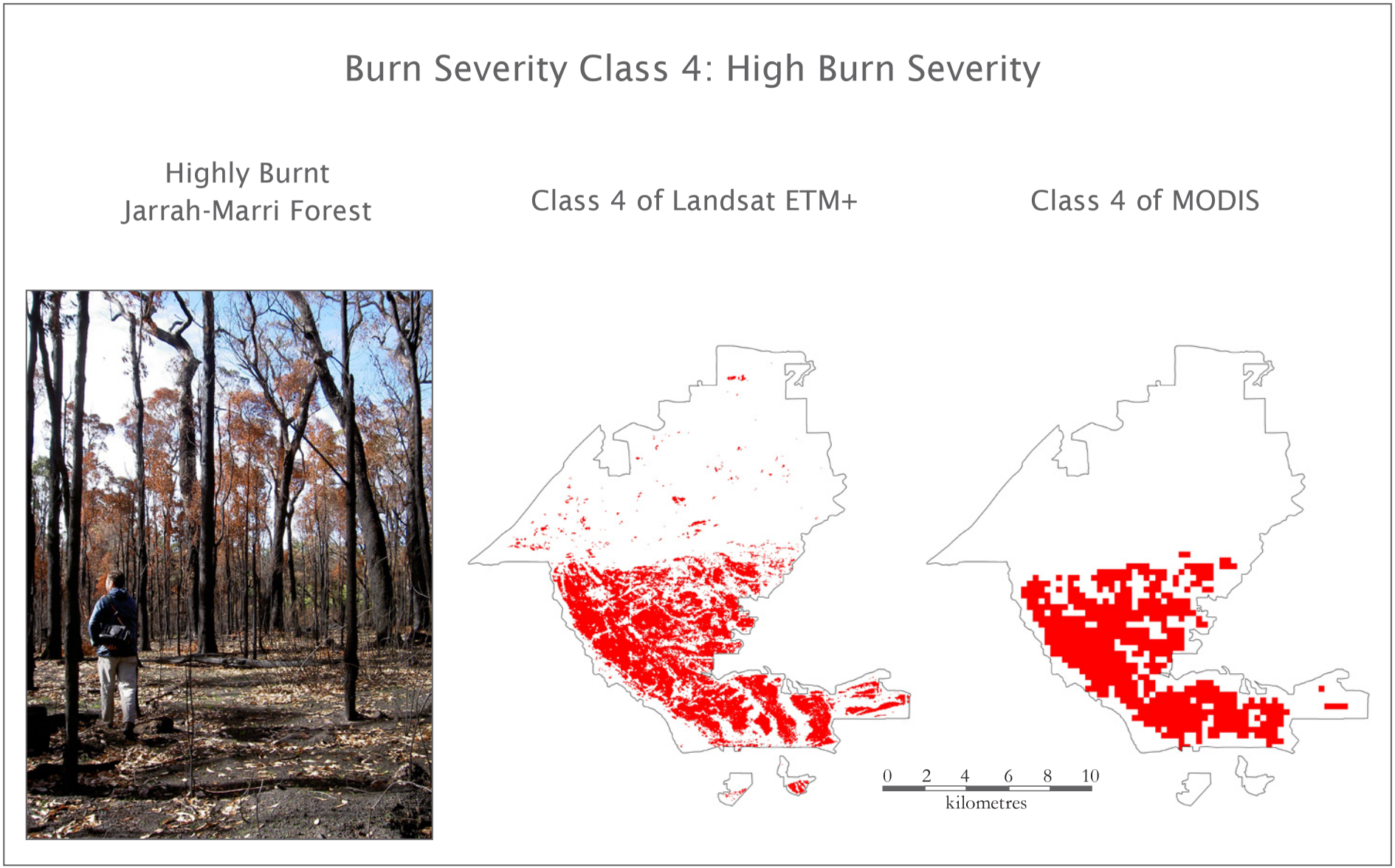

Figure 7-36: Class 4 from field measurement and the remotely sensed measurement of burn severity. The photo on the left side illustrates a jarrah-marri forest, where all strata of the forest have been affected by fire. The pattern of class 4 as detected from Landsat ETM+ sensor is illustrated in the middle and from MODIS on the right side. The remotely sensed class 4 of both sensor is based on the calibrated images from the latter results (Figure 7-31 & 7-32).

Chapter 8: Discussion

This study investigates MODIS data to measure burn severity in the forests of south-west WA using the ΔNBR. The results of this work are discussed in this chapter considering the data basis and the methodology. The measure of remote sensing and field data, the validation and the resulting maps of burn severity are discussed in separate sections.

8.1 Remotely Sensed Measurement of Burn Severity

The measurement of burn severity with MODIS data is defined in this study as a quantitative measure of biomass consumption due to fire. The spectral properties of MODIS data give the highest discrimination between burnt and unburnt surfaces in the NIR band 2 and the MIR band 7 (Figures 7-1 to 7-4). The literature similarly shows Landsat ETM+ bands 4 and 7 as being the best discriminators between burnt and unburnt (White et al., 1996; Key and Benson; 1999 [1],[2]; van Wagtendonk et al., 2004). The major decrease in reflectance in band 2 is correlated to reduction of biomass as a result of fire. Fire consumes vegetation and therefore less energy is reflected by leaves in this wavelength. The reflectance in the NIR shows a strong decrease in signal within the severe burnt area, when little biomass is left post-fire. It should be noted, that the quantitative measure of biomass based on reflectance is not validated in this study. The major increase of reflectance in band 7 is correlated to increasing soil exposure post-fire, which has higher reflectance than vegetation containing moisture in this wavelength region (Figures 4-2 to 4-4). As a result of biomass loss, soil is proportionally more exposed. This explains the lower increase of reflectance in milder burnt areas in comparison to severe burnt areas. It must be stated, that these infrared wavelengths are highly influenced by water absorption, which increases the post-fire signal, when leafs are dried out post-fire. The influence of water absorption is noticeable in the post-fire signal in this band, where for example post-fire rainfall increases surface moisture content.

The high variability of TOA data between single dates of acquisition is caused by atmospheric influences and BRDF effects. This is evident as the difference between scenes is highly reduced in corrected BOANADIR data (Figures 7-1 to 7-4). The varying view angles of MODIS influence the spectral bands similarly in all wavelengths as it is mainly a geometric variation and thus less dependent on wavelength. BRDF effects are considered to be the major cause for broad deviations in all wavelengths between scenes. In contrast, atmospheric effects are varying with wavelength. The high reflectance in the blue band 3 of MODIS TOA data could be explained by high influence of atmospheric scattering, as reflectance in band 3 of corrected data is highly reduced. The decreasing reflectance in the VIS wavelength towards the red band 1 of TOA data illustrates that atmospheric influence is decreasing towards longer wavelengths. This is further confirmed by the reduced deviation between TOA reflectance and corrected BOANADIR reflectance in longer wavelengths. The high variance of reflectance due to varied view angles and atmospheric effects between single acquisitions results in low discrimination between unburnt and burnt surface reflectance (Figure 7-1). The discrimination between unburnt and burnt is enhanced, when the surface was affected by a more severe burn (Figure 7-2). However, top of atmosphere reflectance itself is not considered useful for a quantitative measurement of burn severity, because deviation between scenes of TOA data is still higher compared to the discrimination between burnt and unburnt.

The corrected data present better discrimination between burnt and unburnt, as the noise between scenes is highly reduced by the data correction. This is therefore considered more favourable for a quantitative measurement of burn severity based on reflectance values. In general, the data correction does not represent a perfect result, as deviation of reflectance between scenes is still around 5%. A reason for insufficient atmospheric correction is given by the constant parameters used for data correction in the current operational system, whereas atmospheric parameters are highly variable between the single acquisition days.

The two outliers of BOANADIR data in classes 3 and 6 with high reflectance in all bands refer to BOA data that were not corrected for BRDF effects (Figures 7-3 and 7-4). Both scenes were acquired with view zenith angles greater 50° off-nadir. A possible reason for the noticeably higher reflectance in the NIR bands 4 and 5 is that the detected reflectance from vegetation is supposed to be less reduced by soil reflectance when view angle of the sensor is off-nadir compared to the vertical nadir view. Furthermore, there are more mixed pixel resulting from the greater pixel size towards off-nadir view angle. The negative reflectance in the VIS wavelength recorded on Julian day 353 from BOANADIR data must be a result from insufficient atmospheric correction, because no outlier is visible in the uncorrected TOA data within the same area. If cloud, cloud shadow or smoke would have caused the outlier, it should have been represented in TOA reflectance as well.

The indices NDVI and NBR highly enhance the signal change between unburnt and burnt compared to spectral band reflectance (Figures 7-5 to 7-8). The NDVI shows less contrast between the burnt and unburnt surface, the increase of reflectance is less in the red than in the MIR wavelength post-fire. This could be explained by the dominance of reflectance from post-fire soil exposure, which is generally lower in the red band and increasing towards longer wavelengths (Figure 4-4). The NDVI decreases post-fire because biomass is consumed and burnt vegetation has reduced chlorophyll absorption. The NBR signal is more enhanced, because this index includes the bands that most correspond to surface reflectance change due to fire in this ecosystem. The reflectance change indicates biomass reduction and proportionally increasing soil exposure, which is detected by this index. The ΔNBR is considered a useful measurement for quantifying biomass consumption due to fire. The change between pre-fire and post-fire signal shows greatest change, whereas the magnitude of change is less in milder burnt area and higher in severe burnt area. However, index values are sensor specific as variation in the spectral response and spatial resolution between MODIS and Landsat sensors influence the detected signal. A valid relationship between the consumed biomass and index values needs further validation based on comprehensive ground truth data to set thresholds in the appropriate range considering the ecosystem and sensor.

The derivation of normalised indices highly reduces atmospheric and BRDF effects (Jensen, 2000). This is shown in this study as trends through time and deviation between scenes of both the NDVI and NBR are very similar in TOA and BOANADIR data (Figures 7-5 to 7-8). Only the value range of the NDVI is generally slightly higher in corrected BOANADIR data compared to TOA data. This indicates that atmospheric effects are less reduced by the index derivation than BRDF effects. The NDVI includes the VIS band 1, which is more influenced by the atmosphere than infrared bands. The NBR is therefore in a similar value range in TOA and BOANADIR, because the NIR and MIR bands are less influenced by the atmosphere. The BRDF effects are highly reduced through normalisation, because all spectral bands are similarly affected as already demonstrated by the deviations within the spectral properties. The high value of the NDVI detected on Julian day 329 could result from insufficient atmospheric correction, as it is only occurs in corrected BOANADIR data. However, the spectral analyses showed no significant outlier in the mean reflectance of this date in BOANADIR data. This image was cloud masked and insufficient masking could possibly cause the outlier. A noticeably high NBR value detected on Julian day 354 is explained by the view zenith angle of the scene, which was greater than 60° off-nadir. Similar to observation of high reflectance in the NIR of BOA data, the increasing index value could result from higher amount of unburnt vegetation detected in the larger pixel area off-nadir. The NBR value on this day of acquisition was observed as high in both TOA and BOANADIR data compared to index value before or after that date. This is a counterargument for the error source due to the off-nadir view angle or indicates that BRDF correction was not successful in this case.

There are no observable changes between analyses within averaged classes or a single pixel of burnt area. In general more outliers are visible in the pixel analyses compared to the class analyses. This is explained as single pixels are not averaged and errors therefore highlighted. However, pixel based analyses and class analyses provide similar opportunities for a quantitative measurement of

burn severity. There are several reasons for outliers, which result either from data error or factors that influence reflectance. Outliers observed in band 6 of TOA data are explained by data error due to nonfunctional band 6 detectors as known from MODIS on Aqua (Figure 7-10). Further outliers are detected by corrected BOANADIR data only, which could be explained by insufficient atmospheric correction of atmospheric or BRDF effects. The outliers are predominantly within the VIS wavelength, where the atmosphere has most influence on the signal (Figures 7-11 and 7-12). An insufficient atmospheric correction of BOANADIR data was independently observed by MAIER, 2004.

The NBR measured with Landsat ETM+ data shows a significant increase between the more recent post-fire image in November and the subsequent image in December (Figures 7-18 and 7-19). The reduced burn signal is due to lower reflectance in the later post-fire image as demonstrated by spectral properties of band 7 (Figure 7-17). According to the literature, possible reasons are dissipation of ash and charcoal or vegetation regrowth post-fire, both od which weaken the signal when burnt areas age (Roy et al. 2002). Furthermore, variable moisture content due to rainfall between acquisition dates could reduce the burn signal post-fire, due to water absorption in the MIR wavelength. Atmospheric influences are considered too weak in the infrared wavelengths to explain the lower burn signal. The frequent observations with MODIS data present a similar trend of increasing values in the post-fire NBR, as the burnt area ages. The continual trend of the weakening burn signal indicates ash dissipation rather than certain rainfall events.

The change detected between vegetation reflectance from February to December further demonstrates temporal sensitivity for change detection. The ecosystem of south-west WA consists of evergreen Mediterranean forests, lower NIR reflectance in spring season (Nov/Dec) compared to higher NIR reflectance in summer (Feb) indicates more dense vegetation in summer seasons (Figure 7-15). Therefore phenological change could cause a more intense change signal for Landsat ETM+ data as NIR reflectance in summer season pre-fire is higher than in the actual spring season, when the fire occurred.

The twice daily overpasses of MODIS compared to Landsat overpasses every 16 days are considered as the major benefit of MODIS to measure burn severity in the study area. The phenological change, single rainfall events or rather the weakening burn signal post-fire are modifying the change detection in respect to burn severity. This modification could be highly reduced or rather monitored by high temporal resolution of the sensor. Furthermore, high temporal resolution would support the monitoring of the regeneration process post-fire. Cloud coverage is a notable disturbing factor in the study area due to its atmospheric conditions close to the sea. This greatly reduces the amount of useful Landsat data in this study, whereas MODIS still provides 40 scenes within 4 months, whereas Landsat data offers 3 scenes within 10 months. The cloud mask applied to the MODIS data augments available scenes for data analyses. Despite a subjective application of the mask for each single scene, masking appears successful, as outliers within the analyses are highly reduced in TOA data.

8.2 Field Measurement of Burn Severity

The field trip helped to establish a quantitative measure of biomass consumption to derive a relationship between the remotely sensed measurement and the ground. It is evident, that fire is a very heterogeneous phenomenon in the natural environment. Fire is a regular phenomenon in the study area, which resulted in clear separation between totally burnt and unburnt vegetation within the visited fire scar. Possible reasons for the fire suddenly cutting off could have been a sudden change of wind direction, less fuel load underneath the unburnt vegetation or an increase in fuel moisture content. The patchiness in burn was especially high at the marginal areas close to the road, which is where fire is generally ignited and either spreads or goes out. A variable wind regime favours high patchiness especially in open shrubland due to the large surface exposed to the wind. The variable distribution and moisture of fuel predominantly explains the patchy distribution of different levels of burn severity within the forests. High patchiness is considered to limit the accuracy of the remote sensing measurement, as surface reflectance results from differently burnt surfaces at either spatial resolution. However, high patchiness is a major goal of the forest manager to meet a successful outcome of the burn, because areas of retreat for flora and fauna are conserved.

Heterogeneous fire behaviour provides further difficulties in respect to different vegetation structures in the study area. The burn severity classification of this study addresses 4 classes between unburnt and severely burnt, whereas the consumption of biomass is benchmarked with the single strata of the forests and correlated to the flame height. For a uniform classification, the amount of biomass needs to be homogeneously

distributed between the strata. This is observed in the structure of jarrah-marri forest and therefore provides the principle measure for the field classification. The height distribution of biomass within the jarrah-marri and karri forest is varied due to the high canopy of karri forests. However, the amount of biomass per stratum of the forest is still similar. Therefore, the classification is considered as useful for both, the jarrah-marri and the karri forest. Within the shrubland it is difficult to measure burn severity due to the single stratum, which burns in a uniform manner. This shrubland burning results in horizontal rather than vertical biomass reduction, When biomass is reduced in a horizontal manner the complete vegetation layer is consumed, whereas vertical burning varies within multiple layers of vegetation.

The measurement of scorch height was a useful measure for the flame height, as scorch height reflects about a sixth of the flame height (Simmonds, 2004). However, the scorch height is variable between the different vegetation structures. Flame height thus is not a uniform indicator for the burn severity measurement in the study area in respect to different vegetation structures.

The closeness of the canopy is critical for the detection of vertical biomass reduction by satellite remote sensing. The detection of biomass consumption in the understorey is limited, when the green canopy covers the sensor's view. However, the native forest in the study area exhibits a natural growth, where the closeness of canopy is relatively low.

Burn severity when measured by reduction of biomass is not directly related with ecological impact of the fire event. The ecological impact is highly variable between the vegetation types. The stems of Eucalyptus diversicolor (karri) for example have thin bark, which is less protective to fire than the thick bark of jarrah trees. Karri forests are therefore more fire sensitive than jarrah forests. A mild understorey burn measured as low burn severity in karri forest could have severe ecologically implications. However, the more detailed ecological impact of burn severity is beyond the scope of this work.

The discussion of field measurement illustrates that a uniform classification of burn severity in the study area is highly limited. The limitations are caused by the different structures of ecosystems, as well as the high patchiness due to heterogeneous fire behaviour. The classification into 4 classes of burn severity based on the structure of jarrah-marri forest is still considered the most reasonable for this study. The jarrah-marri forest is most dominant in the study area and presents a relatively homogeneous distribution of biomass between the different strata. Furthermore, the canopy closeness is relatively low, which enhances the satellite detection of the biomass reduction in lower strata of the forest.

8.3 Ground Truth Validation of Remote Sensing Data

The ground truth data is not sufficient to completely validate either Landsat or MODIS data. Furthermore, the high patchiness of the burnt areas highly limits a rigorous validation, as homogeneous surface reflectance within a 30m by 30m area of the Landsat pixel was rarely present in the field. However, this is interpreted rather as a general problem of remote sensing validation than specific in the study area. The large area of burn made it difficult to sample sufficient ground control points for a significant result in this heterogeneous landscape. Nevertheless, the measurement of high resolution Landsat data is assessed based on 14 GCPs. The results of this assessment are considered useful, because the data were collected within a more homogeneous surface. Furthermore, the main goal is a broad scale severity map useful for the fire management, which focuses on the patchiness within a burnt area rather than the patchiness within the area of a Landsat pixel.

The NBR and NDVI values of pre-fire images show generally higher values in jarrah-marri forest compared to shrubland. Higher values of both indices are measured when amount of biomass is dense, shrubland consists of less vegetation per area compared to the forest with three strata. The differences in amount of biomass before fire could influence the change signal, because the detected loss of biomass is measured as change between pre and post-fire biomass. The ΔNBR is therefore variable when the pre-fire biomass density varies. The varying value range of similar classes of burn severity between different ecosystems represents a limit of a uniform application of the ΔNBR. This indicates that the structure of the ecosystem needs to be considered separately when measuring burn severity in the study area.

The GCPs 2 and 5 represent examples where the measurement of the ΔNBR is not successful, as index values are obviously low in respect to the measured burn severity in the field (Figures 7-27 and 7-30). The low ΔNBR values preliminary result from low reflectance in band 7, as post-fire spectra from both GCPs represent the expected decreasing reflectance in the NIR band 4. The possible reason why post-fire reflectance did not increase in the MIR band 7 is related to water

absorption. The high moisture content at GCP 5 was visibly obvious due to backwater covering the soil (see image Figure 7-30). However a further reason could be that the sensor detected biomass reduction, but closeness of canopy could have impeded detection of soil reflectance. This would be more likely in forests where multiple canopy layers are present. This reason is rather unlikely in the example of GCP 2, because post-fire reflectance in band 7 decreased further when compared to pre-fire reflectance. There is a high indication that water caused energy absorption in this band. The example of GCP 5 further approves the suggestion that the burn severity measurement with the ΔNBR is highly sensitive to variability in moisture content. However, the ΔNDVI responds more positive in this case. The literature approves that water absorption is high in the MIR band 7 as similarly observed within the data analyses (Lillesand and Kiefer, 2000; Jensen, 2000; Ceccato et al., 2001).

The significance of index values is further limited as Landsat data present a temporal gap of 5 months between pre-fire and post-fire data. The reflectance in the infrared wavelengths is reduced in post-fire data, which could be explained by a phenological change between summer season in December and late autumn season in May (Figure 7-28). However, reduced reflectance in the MIR is more likely due to increasing moisture in the autumn months. Furthermore, atmospheric effects within pre-fire and post-fire data are not corrected. This is considered negligible as the atmosphere preliminary affects the VIS wavelength and influences are further reduced by the index.

The relation between the field and the burn severity measurements are presented in some examples (Figures 7-1 and 7-4). However, the assessment exhibits major limitations, as the burn severity measurement based on the ΔNBR cannot be uniformly applied within different ecosystems and that water highly influenced the change detection.

4.4 Burn Severity Maps

The classes 1 to 4 of burn severity maps (Figures 7-33 to 7-36) represent the final results for this study. The results of the remotely sensed burn severity classification are associated with the burn severity measured in the field. The feasibility of measuring burn severity with MODIS in respect to the moderate spatial resolution is the initial focus.

The underestimated burn severity at the marginal area of the MODIS class 1 is thought to result from the averaged surface reflectance within the moderate spatial resolution of the MODIS sensor. As prescribed burning is preliminary ignited from the roads at the border of the burn envelope, the underestimated burn severity of MODIS might reflect, that ignition was not successful in this area. This is further suggested, as the unburnt area is not detected in the southern part of the burnt area, which was subject to wildfire. It was similarly observed in the field trip that ignition points showed locally severe burnt areas, but fire was not carried by the ecosystem and therefore extinguished. In this case, the amount of unburnt vegetation would be proportionally high within the larger area covered by the MODIS pixel compared to the smaller areas of the Landsat pixel. However, there is no ground truth data available from this burnt area, as it occurred prior to this study, and no field data were sampled. The MODIS class 1 covers the larger unburnt areas detected by Landsat, whereas the smaller areas are classified as low burnt due to the averaged reflectance within the larger MODIS pixel.

The similar pattern of class 2 from MODIS and Landsat could be explained by very high patchiness or rather a uniform understorey burn within the forests. Very high patchiness between burnt and unburnt over the area covered by the MODIS pixel could cause averaged surface reflectance similar for the spatial resolution of both sensors. It is expected to be similar, when a uniform understorey burn over this area present a similar signal of surface reflectance. The similar pattern between Landsat and MODIS would therefore indicate a successful outcome of the mild prescribed burn. The applicability of MODIS resolution is further observed in the class 2 pattern of MODIS and Landsat along the marginal area in the south of FAA1. Landsat presents this area, which covers hardly the single pixel size of MODIS. However, it is similarly classified by MODIS as class 2. This could indicate a high conformity of surface reflectance over the area covered by the MODIS pixel. MODIS is considered as highly useful as this example presents high conformity between Landsat and MODIS for this scale of burn severity measurement.

The class 3 detection of MODIS is rather limited when compared to the Landsat coverage, where the major part of the missed class 3 detection of MODIS is detected as class 2. The moderate spatial resolution of MODIS generally limits the separate display of areas smaller than 250m by 250m. This could explain that the smaller areas

of class 3 detected by Landsat are not covered by MODIS, whereas large areas for example in the south-west corner of the northern part of the FAA are similarly detected from Landsat and MODIS. However, the burn severity signal of Landsat class 3 not detected by MODIS falls preliminary in class 2 of MODIS. The possible reason for the lower burn severity signal of MODIS is referred to mixed surface reflectance that is averaged for the size of a MODIS pixel. It is suggested that unburnt or lower burnt area within the pixel reduce the signal, whereas Landsat detects moderate burn severity due to the more uniform surface that is covered by the pixel.

The class 4 results from Landsat and MODIS are similar. It was confirmed by CALM fire managers from Walpole that this area was subject to a severe wildfire in 2002 (Green, 2004; Simmonds, 2004). The results therefore demonstrate a successful burn severity measurement with MODIS data. The high conformity between Landsat and MODIS could be explained by a rather homogeneous surface cover over a large area. The moderate spatial resolution of MODIS exhibits hardly any limitations in this case.

The results present a rather successful detection of burn severity, however this classification could not be validated. The relationship between the field measurement and the remotely sensed measurement is therefore estimated rather than a significant result. The calibration of the ΔNBR images of Landsat and MODIS are specifically for the corresponding data, as they are calibrated based on image information of high resolution Landsat rather than ground truth data. It is considered critical to directly compare the index imagery of Landsat and MODIS as the pre-fire data is only available from different dates. However, as index values are calibrated separately for both data, they are specific for each sensor.

The measurement of burn severity with MODIS data is considered as useful for the fire management in south-west WA, due to broad scale burn severity mapping being sufficient to estimate the outcome of the prescribed burn. MODIS could provide monitoring within the same day, if clouds permit. The burn severity measurement could be used to assess wether a burn line has successfully been achieved to protect neighbouring property soon after the fire event. This enables managers to revisit and reignite the prescribed burn whilst weather conditions are suitable.

Chapter 9: Conclusion and Future Research

This study provides a burn severity assessment based on the Normalised Burn Ratio (NBR) using MODIS data within the forested area of south-west WA. The twice daily overpasses of the MODIS sensor in this area exhibited a great resource for monitoring this fire prone environment. The daily burn severity assessment with MODIS has proven useful to monitor the impact and success of prescribed burning.

The ΔNBR is a validated measurement of burn severity for several ecosystems based on Landsat data. It was transferred to MODIS data to measure burn severity in the forests of south-west of WA. The NBR responds to the proportion of biomass and soil exposure on the surface. Burn severity was correlated to the reduction of biomass, which is a result of fire. The ΔNBR quantified this change between the pre-fire image and the post-fire image.

The spectral properties of MODIS exhibited highest discrimination between burnt and unburnt in the NIR band 2 and in the MIR band 7. However, uncorrected top of atmosphere (TOA) data exhibited high deviation between scenes due to atmospheric and BRDF effects. Therefore, discrimination between burnt and unburnt was highly reduced in TOA reflectance. The atmospheric and BRDF corrected (BOANADIR) reflectance reduced noise between scenes and provided higher discrimination between burnt and unburnt.

The NBR and the NDVI were applied on MODIS data and both indices presented high discrimination between burnt and unburnt. However, the signal gathered from the NBR showed higher response within the burnt areas compared to the NDVI. Influences of atmospheric and BRDF effects were highly reduced when indices were applied and TOA and BOANADIR data were comparable. MODIS TOA data, thus was considered sufficient for measuring burn severity using the ΔNBR. The post-fire signal of the NBR became slightly weaker with age of the burnt area.

Heterogeneous fire behaviour in the study area caused very high patchiness in fire scars. Furthermore, the patchy distribution of different structures of vegetation made field classification of burn severity difficult. However, high patchiness was a major goal of prescribed burning to conserve areas of retreat for flora and fauna.

The classification of burn severity in the field resulted in four classes, which were benchmarked by the separated strata within the forest. In relation to flame height and fire intensity, the biomass of a forest is reduced in vertical dircetion between several strata. The biomass reduction of different strata in the forest was correlated with levels of burn severity. The classification is initially useful for the forested area, where biomass is more homogeneously distributed between different strata. In open shrubland and woodland, vegetation consisted of one single stratum that was either burnt or unburnt. In this vegetation, biomass reduction and burn severity is related to patchiness of the burn, which reflects the proportion between burnt and unburnt surfaces in a horizontal manner.

Comparing the remotely sensed burn severity assessment with ground truth data, the ΔNBR did respond to the biomass reduction measured in the field. However, it resulted that a uniform application of the ΔNBR was limited in the study area, because different structures of vegetation influenced the value range of the ΔNBR. Furthermore, the ΔNBR was sensitive to variability in moisture content. Where water influenced the change signal of the ΔNBR, the ΔNDVI responded more positively to the biomass reduction due to a higher burn signal. However, ground truth data were not sufficient for a rigorous validation of remote sensing data.

The 250m spatial resolution of MODIS data was considered sufficient for a burn severity assessment, when sub-pixel accuracy is not required. The burn signal of a patchy or mild burnt area was similarly detected by the high resolution Landsat data and the moderate resolution MODIS data. Both sensors gave comparable results in the region high burn severity. However, detection of the intermediate class of moderate burn severity by the MODIS sensor was limited, where Landsat classification detected a patchy mosaic. The benefit of daily temporal resolution of MODIS for the monitoring of burn severity in the forested area of south-west WA outweighs the spatial limitations as suitable burning conditions for the fire managers are limited and areas vast and remote.

This study demonstrates a successful application and feasibility for a burn severity assessment in the forested area of south-west WA. However, validation was not completed and the burn severity measurement of the ΔNBR could not be uniformly applied in the environment of south-west WA. It therefore encourages further research. The relationship between the NBR and the different structures of vegetation is a major task for further research. This is an important consideration to apply the measurement for the south-west WA environment. The value range of the ΔNBR might be correlated with parameters adjusted to the structure of vegetation. This would require the information of present vegetation within the pixel, which could be provided by GIS analyses. Furthermore, a combination of information gathered from both indices, the NBR and the NDVI might reduce the sensitivity of the burn severity measurement in respect to moisture.

A more comprehensive field data set is required to establish a valid assessment of burn severity in the forests of south-west WA. The field measurement needs to be sampled in all types of vegetation and for all classes of burn severity in a sufficient amount to obtain a statistically significant result. Furthermore, high resolution remote sensing data needs to cover ground truth data sampled for all structures of vegetation.

The transfer of the burn severity assessment to other ecosystems is a major task for monitoring fire prone regions in the future. The tropical savannas of Australia for example are more fire prone and prescribed burning is applied over large areas.

The measurement of burn severity provides a quantitative information of biomass consumption due to fire. This establishes further detailed information of fire impact beside the fire hot spot detection and the mapping of burnt area.

This preliminary study has shown positive results for daily burn severity assessment. With further research this method could be implemented into the daily operational fire system and would support fire management in south-west WA.

References:

Abbott, I. (2003). Aboriginal fire regimes in south-west Western Australia: evidence from historical documents. In Fire in Ecosystems of South-West Western Australia: Impacts and Management. Abbott, I. and Burrows, N. (eds.), Backhuys Publishers, Leiden, Netherlands, pp. 119-146

Abbott, I. and Burrows, N. (2003). Foreword – The genesis of this book. In Fire in Ecosystems of South-West Western Australia: Impacts and Management. Abbott, I. and Burrows, N. (eds.), Backhuys Publishers, Leiden, Netherlands, pp. vii-xiii

Adams, M.A., Grierson, P.F. and Burrows, C. (2003). Fire, soils and plant nutrition in forests of south-west Western Australia: a focus on spatial and temporal variability. In Fire in Ecosystems of South-West Western Australia: Impacts and Management. Abbott, I. and Burrows, N. (eds.), Backhuys Publishers, Leiden, Netherlands, pp. 189-203

Beard, J.S., Chapman, A.R. and Gioia, P. (2000). Species richness and endemism in the Western Australian flora. Journal of Biogeography, Vol 27, pp. 1257-1268

Beard, J.S. (1990). Plant life of Western Australia. Kangaroo Press, Kenthurst, NSW, pp. 320

Bond, W.J. and van Wilgen, B.W. (1996). Fire and plants. Chapman & Hall, London, UK

Bowman, D.M.J.S. (2003). Australian landscape burning: a continental and evolutionary perspective. In Fire in Ecosystems of South-West Western Australia: Impacts and Management. Abbott, I. and Burrows, N. (eds.), Backhuys Publishers, Leiden, Netherlands, pp. 107-118

Bowyer, P. and Danson, F.M. (2004). Sensitivity of spectral reflectance to variation in live fuel moisture content at leaf and canopy level. Remote Sensing of Environment 92, pp. 297-308

Bradstock, R.A., Williams, J.E. and Gill, M.A. (2002). Flammable Australia – The fire regimes and biodiversity of a continent. Cambridge University Press, Tasmania, pp. 462

Burrows, N. and Abbott, I. (2003). Fire in south-west Western Australia: synthesis of current knowledge, management implications and new research directions In Fire in Ecosystems of South-West Western Australia: Impacts and Management. Abbott, I. and Burrows, N. (eds.), Backhuys Publishers, Leiden, Netherlands, pp. 437-452

Burrows, N. and Wardell-Johnston, G. (2003). Fire and plant interactions in forested ecosystems of south-west Western Australia. In Fire in Ecosystems of South-West Western Australia: Impacts and Management. Abbott, I. and Burrows, N. (eds.), Backhuys Publishers, Leiden, Netherlands, pp. 225-268

Cary, G.J. (2002). Importance of a changing climate for fire regimes in Australia. In Flammable Australia – The fire regimes and biodiversity of a continent. Bradstock, R.A., Williams, J.E. and Gill, M.A. (eds.), Cambridge University Press, Tasmania, pp. 26-46

Ceccato, P., Flasse, S., Tarantola, S., Jacquemoud, S. and Grégoire, J-M. (2001). Detecting vegetation leaf water content using reflectance in the optical domain. Remote Sensing of Environment 77, pp. 22-33

Chuvieco, E. (1999). Measuring changes in landscape pattern from satellite images: short-term effects of fire on spatial diversity. International Journal of Remote Sensing 20/12, pp. 2331-2346

Chuvieco, E., Cocero, D., Riaño, D., Martin, P., Martínez-Vega, J., de la Riva, J. and Pérez, F. (2004). Combining NDVI and surface temperature for the estimation of live fuel moisture content in forest fire danger rating. Remote Sensing of Environment 92, pp. 322-331

Cox, C. (2004). Mulgar Research Centre, School of Environmental Biology, Curtin University, Perth, W.A., personal communication

Craig, R., Heath, B., Raisbeck-Brown, N., Steber, M., Marsden, J. and Smith, R. (2000). Assessing fire patterns and their environmental impacts. Department of Land Administration, Perth, W.A., pp. 76

Danson, F.M. and Bowyer, P. (2004). Estimating live fuel moisture content from remotely sensed reflectance. Remote Sensing of Environment 92, pp. 309-321

Díaz-Delgado, R., Lloret, F. and Pons, X. (2003). Influence of fire severity on plant regeneration by means of remote sensing imagery. International Journal of Remote Sensing 24/8, pp. 1751-1763

Dixon, K. and Barrett, R. (2003). Defining the role of fire in south-west Western Australian plants. In Fire in Ecosystems of South-West Western Australia: Impacts and Management. Abbott, I. and Burrows, N. (eds.), Backhuys Publishers, Leiden, Netherlands, pp. 205-223

Dozier, J. (1981). A method for satellite identification of surface temperature fields of subpixel resolution. Remote Sensing of Environment 11, pp. 221-229

Eiden, G., Dreiser, C., Gesell, G. and König, T. (1991). Large scale monitoring of rangeland vegetation using NOAA/11 AVHRR LAC Data. In Range Management Handbook of Kenya Vol. 3/4. Ministry of Livestock Development, Nairobi, Kenya and German Aerospace Research Establishment (DLR), Oberpfaffenhofen, Germany, pp. 92

Eiden, G. (2000). Charakterisierung der raum-zeitlichen Vegetationsdynamik von dürre- und desertifikatio nsgefährdeten, ariden und semi-ariden Regionen.

In Materialien zur Ostafrikaforschung, Heft 22. Geographische Gesellschaft Trier, Germany, pp. 223

Eva, H.D. and Lambin, E.F. (1998) [1]. Remote sensing of biomass burning in tropical regions: sampling issues and multisensor approach. Remote Sensing of Environment 64, pp. 292-315

Eva, H.D. and Lambin, E.F. (1998) [2]. Burnt area mapping in Central Africa using ATSR data. International Journal of Remote Sensing 19/18, pp. 3473-3497

Flasse, S.P. and Ceccato, P. (1996). A contextual algorithm for AVHRR fire detection. International Journal of Remote Sensing 17/2, pp. 419-424

Fox, J.E.D. (2004). Mulgar Research Centre, School of Environmental Biology, Curtin University, Perth, W.A., personal communication

Gao, F., Schaaf, C.B., Strahler, A.H., Jin, Y. and Li, X. (2003). Detecting vegetation structure using a kernel-based BRDF model. Remote Sensing of Environment 86, pp. 198-205

García-Haro, F.J., Gilabert, M.A. and Meliá, J. (2001). Monitoring fire-affected areas using Thematic Mapper data. International Journal of Remote Sensing 22/4, pp. 533-549

Giglio, L., Kendall, J.D. and Justice, C.O. (1999). Evaluation of global fire detection algorithms using simulated AVHRR infrared data. International Journal of Remote Sensing 20/10, pp. 1947-1985

Giglio, L., Kendall, J.D. and Tucker, C.J. (2000). Remote sensing of fires with the TRMM VIRS. International Journal of Remote Sensing 21/1, pp. 203-207

Green, D. (2004). Fire coordinator of Department of Conservation and Land Management (CALM), Walpole, W.A., personal communication

Guenther, B., Xiong, X., Salomonson, V.V., Barnes, W.L. and Young, J. (2002). On-orbit performance of the Earth Observing System Moderate Resolution Imaging Spectroradiometer; first year of data. Remote Sensing of Environment 83, pp. 16-30

Hassell, C.W. and Dodson, J.R. (2003). The fire history of south-west Western Australia prior to European settlement in 1826-1829. In Fire in Ecosystems of South-West Western Australia: Impacts and Management. Abbott, I. and Burrows, N. (eds.), Backhuys Publishers, Leiden, Netherlands, pp. 71-85

Hodgson, A. (2004): Conservation and Land Management's (CALM) fire management policies and practices. Environmental Protection Authority (EPA), Perth, W.A. http://www.epa.wa.gov.au/docs/1845_CALM_FireReview_ConsultantReport.pdf (accessed 20th September 2004)

Hopper, S.D. (2003). An evolutionary perspective on south-west Western Australian landscapes, biodiversity and fire: a review and management implications. In Fire in Ecosystems of South-West Western Australia: Impacts and Management. Abbott, I. and Burrows, N. (eds.), Backhuys Publishers, Leiden, Netherlands, pp. 9-35

Huston, M. (2003). Understanding the effects of fire and other mortality-causing disturbances on species diversity. In Fire in Ecosystems of South-West Western Australia: Impacts and Management. Abbott, I. and Burrows, N. (eds.), Backhuys Publishers, Leiden, Netherlands, pp. 37-70

Jensen, J.R. (2000). Remote Sensing of the environment: an earth resource perspective. Prentice-Hall, Inc., Upper Saddle River, New Jersey, U.S.A., pp. 544

Justice, C.O., Townshend, J.R.G., Vermote, E.F., Masuoka, E., Wolfe, R.E., Saleous, N., Roy, D.P. and Morisette, J.T. (2002) [1]. An overview of MODIS Land data processing and product status. Remote Sensing of Environment 83, pp. 3-15

Justice, C.O., Giglio, L., Korontzi, S., Owens, J., Morisette, J.T., Roy, D., Descloitres, J., Alleaume, S., Petitcolin, F. and Kaufmann, Y. (2002) [2]. The MODIS fire products. Remote Sensing of Environment 83, pp. 244-262

Key, C., and Benson, N.C. (1999) [1]. The Normalized Burn Ratio (NBR): a Landsat TM radiometric measure of burn severity. United States Geological Survey (USGS). http://nrmsc.usgs.gov/research/ndbr.htm (accessed 5th March 2004)

Key, C., and Benson, N.C. (1999) [2]. Fire effects monitoring and inventory protocol – landscape assessment. United States Geological Survey (USGS). http://www.fire.org/firemon/lc.htm (accessed 5th March 2004)

Koetz, B., Schaepman, M., Morsdorf, F., Bowyer, P., Itten, K. and Allgoewer, B. (2004). Radiative transfer modeling within a heterogeneous canopy for estimation of forest fire fuel properties. Remote Sensing of Environment 92, pp. 332-344

Koutsias, N. and Karteris, M. (2003). Classification analyses of vegetation for delineating forest fire fuel complexes in a Mediterranean test site using satellite remote sensing and GIS. International Journal of Remote Sensing 24/15, pp. 3093-3104

Kushla, J.D. and Ripple, W.J. (1998). Assessing wildfire effects with Landsat Thematic Mapper data. International Journal of Remote Sensing 19/13, pp. 2493-2507

Lamont, B.B., Ward, D.J., Eldridge, J., Korczynskyj, D., Colangelo, W.I., Fordham, C., Clements, E. and Wittkuhn, R. (2003). Believing the Balga: a new method for gauging the fire history of vegetation using grasstrees. In Fire in Ecosystems of South-West Western Australia: Impacts and Management. Abbott, I. and Burrows, N. (eds.), Backhuys Publishers, Leiden, Netherlands, pp. 147-169

Larcher, W. (2001). Ökophysiologie der Pflanzen: Leben, Leistung und Stressbewältigung der Pflanzen in ihrer Umwelt. Verlag Eugen Ulmer GmbH & Co., Stuttgart, Germany, 6th edition, pp. 408

Levien, L.M., Roffers, P., Maurizi, B., Suero, J., Fischer, C. and Huang, X. (1999). A machine-learning approach to change detection using multi-scale imagery. http://www.krisweb.com/biblio/gen_usfs_cdf_levienet_al_changescene.pdf (accessed 3rd July 2004)

Liang, S., Fang, H., Chen, M., Shuey, C.J., Walthall, C., Daughtry, C., Morisette, J., Schaaf, C. and Strahler, A. (2002). Validating MODIS land surface reflectance and albedo products: methods and preliminary results. Remote Sensing of Environment 83, pp. 149-162

Lillesand, T.M. and Kiefer, R.W. (2000). Remote sensing and image interpretation. John Wiley & Sons, Inc., U.S.A., 4th edition

Luepnitz, D. (1998). Gondwana – die Pflanzenwelt von Australien und ihr Ursprung. Sonderheft 28 des Palmengartens der Stadt Frankfurt am Main. Stadt Frankfurt am Main, Germany, pp. 120

Maier, S.W. (2000). Modeling the radiative transfer in leaves in the 300nm to 2.5µm wavelength region taking into consideration chlorophyll fluorescence: the leaf model SLOPE. Ph. D. diss. Technische Universitaet Muenchen, Germany, pp. 115

Maier, S.W. (2004). Senior Research Officer, Department of Land Information (DLI) Satellite Remote Sensing Services, Perth, W.A., personal communication

Matson, M., Schneider, S.R., Aldridge, B. and Satchwell, B. (1984). Fire detection using the NOAA-series

satellites. NOAA Technical Report NESDIS 7, National Oceanic and Atmospheric Administration, Washington, D.C., U.S.A.

McCaw, L. and Hanstrum, B. (2003). Fire environment of Mediterranean south-west Western Australia. In Fire in Ecosystems of South-West Western Australia: Impacts and Management. Abbott, I. and Burrows, N. (eds.), Backhuys Publishers, Leiden, Netherlands, pp. 87-106

Miller, J.D. and Yool, S.R. (2002). Mapping forest post-fire canopy consumption in several overstorey types using multi-temporal Landsat TM and ETM+ data. Remote Sensing of Environment 82, pp. 481-496

Myers, N., Mittermeier, R.A., Mittermeier, C.G., da Fonseca, G.A.B. and Kent, J. (2000). Biodiversity hotspots for conservation priorities. NATURE 403, pp. 853-858

NASA (2000). MODIS Level 1B product user's guide, National Aeronautics Space Agency (NASA) / Goddard Spaceflight Centre, Greenbelt, U.S.A., MD 20771, MCST Document#MCM-PUG-01-U-DNCN

Nielsen, T.T., Mbow, C. and Kane, R. (2002). A statistical methodology for burned area estimation using multitemporal AVHRR data. International Journal of Remote Sensing 23/6, pp. 1181-1196

Nishihama, M., Wolfe, R., Solomon, D., Patt, F., Blanchette, J., Fleig, A. and Masuoka, E. (1997). MODIS Level 1A Earth Location: Algorithm Theoretical Basis Document Version 3.0, NASA / Goddard Spaceflight Centre, U.S.A., http://modis.gsfc.nasa.gov/data/atbd/atbd_mod28_v3.pdf (accessed: 12th October 2004)

Patterson, M.W. and Yool, S.R. (1998). Mapping fire-induced vegetation mortality using Landsat Thematic Mapper data: a comparison of linear transformation techniques. Remote Sensing of Environment 65, pp. 132-142

Pereira, J.M.C. (2003). Remote sensing of burned areas in tropical savannas. International Journal of Wildland Fire 12/3 & 4, pp. 259-270

Pereira, M.C. and Setzer, A.W. (1993). Spectral characteristics of fire scars in Landsat-5 TM images of Amazonia. International Journal of Remote Sensing 14/11, pp. 2061-2078

Price, J.C. (2003). Comparing MODIS and ETM+ data for regional and global land classification. Remote Sensing of Environment 86, pp. 491-499

Rahman, H. and Dedieu, G. (1994). SMAC: a simplified method for the atmospheric correction of satellite measurements in the solar spectrum. International Journal of Remote Sensing 15/1, pp. 123-143

Redmond, R.L. and Winne, J.C. (2001). Classifying and mapping wildfire severity. Imaging Notes Sept/Oct 2001. Visual Learning Systems http://www.featureanalyst.com/downloads/publications/FeatureAnalystFire.pdf (accessed: 12th October 2004)

Riaño, D., Chuvieco, E., Ustin, S., Zomer, R., Dennison, P., Roberts, D. and Salas, J. (2002). Assessment of vegetation regeneration after fire through multitemporal analysis of AVIRIS images in the Santa Monica Mountains. Remote Sensing of Environment 79, pp. 60-71

Richards, J.A. (1984). Thematic Mapping from Multitemporal Image Data Using the Principle Component Transformation. Remote Sensing of Environment 16, pp. 35-46

Robinson, J.M. (1991). Fire from space: Global fire evaluation using infrared remote sensing. International Journal of Remote Sensing 12/1, pp. 3-24

Rogan, J. and Yool, S.R. (2001). Mapping fire-induced vegetation depletion in the Peloncillo Mountains, Arizona and New Mexico. International Journal of Remote Sensing 22/16, pp. 3101-3121

Rojas, F., Schowengerdt, R.A., Biggar, S.F. (2002). Early results on the characterization of the Terra MODIS spatial response. Remote Sensing of Environment 83, pp. 50-61

Roy, D.P., Lewis, P.E. and Justice, C.O. (2002). Burned area mapping using multi-temporal moderate spatial resolution data – a bi-directional reflectance model based expectation approach. Remote Sensing of Environment 83, pp. 263-286

Sá, A.C.L., Pereira, J.M.C., Vasconcelos, M.J.P., Silva, J.M.N., Ribeiro, N. and Awasse, A. (2003). Assessing the feasibility of sub-pixel burned area mapping in miombo woodlands of northern Mozambique using MODIS imagery. International Journal of Remote Sensing 24/8, pp. 1783-1796

Sabins, F.F. (1997). Remote sensing principles and interpretation. W.H. Freeman and company, New York, U.S.A., 3rd edition, pp. 494

Schott, J.R. (1997). Remote Sensing: the image chain approach. Oxford University Press, New York, U.S.A.

Shu, Li (2004). Remote Sensing Scientist of Department of Conservation and Land Management (CALM), Perth, W.A., personal communication

Simmonds, R. (2004). Fire coordinator of Department of Conservation and Land Management (CALM), Walpole, W.A., personal communication

Sneeuwjagt, R.J. and Peet, G.B. (1998). Forest fire behaviour tables for Western Australia. Department of Conservation and Land Management (CALM)

Strahler, A.H., Muller, W., Lucht, W., Schaaf, C.B., Tsang, T., Gao, F., Li, X., Lewis, P., and Barnsley, M.J. (1999). MODIS BRDF / Albedo Product: Algorithm Theoretical Basis Document Version 5.0, NASA / Goddard Spaceflight Centre, U.S.A., http://modis.gsfc.nasa.gov/data/atbd/atbd_mod09.pdf (accessed: 12th October 2004)

Stroppiana, D., Pinnock, S. and Gregoire, J.-M. (2000). The Global Fire Product: daily fire occurrence from April 1992 to December 1993 derived from NOAA AVHRR data. International Journal of Remote Sensing 21/6, pp. 1279-1288

Thackway, R. and Cresswell, I.D., (1995). An interim biogeographic regionalisation for Australia: a framework for establishing the National System of Reserves. Version 4.0. Australian Nature Conservation Agency, Canberra

Turner, M.G., Hargrove, W.W., Gardner, R.H. and Romme, W.H. (1994). Effects of fire on landscape heterogeneity in Yellowstone National Park, Wyoming. Journal of Vegetation Science 5, pp. 731-742

Underwood, R.J., Walker, A.W., Schuster, C., Sands, A. and Lush, A. (1991). The karri forest, Western Australia. In Forest Management in Australia. McKinnell, F.H., Hopkins, E.R. and Fox, J.E.D. (eds.), Surrey Beatty & sons, pp. 22-37

van Wagtendonk, J.W., Root, R.R. and Key, C.H. (2004). Comparison of AVIRIS and Landsat ETM+ detection capabilities for burn severity. Remote Sensing of Environment 92, pp. 397-408

Vermote, E.F., Tanré, D., Deuzé, J.L., Herman, M. and Morcrette, J.J. (1997). Second Simulation of the Satellite Signal in the Solar Spectrum, 6S: An Overview. IEEE Transactions on Geoscience and Remote Sensing 35/3. pp. 675-686

White, J.D., Ryan, K.C., Key, C.C. and Running, S.W. (1996). Remote sensing of forest fire severity and vegetation recovery. International Journal of Wildland Fire 6(3), pp. 125-136

Wolfe, R. (2002). MODIS land product flow, formats, projections and geolocation. NASA GSFC Code 922, Raytheon ITSS, http://geography.bu.edu/brdf/modis_land_prod_bu_rwolfe_v3.pdf (accessed: 16th October 2004)

Wolfe, R.E., Nishihama, M., Fleig, A.J., Kuyper, J.A., Roy, D.P., Storey, J.C. and Patt, F.S. (2002). Achieving sub-pixel geolocation accuracy in support of MODIS land science. Remote Sensing of Environment 83, pp. 31-49

Wu, X. (2004). Research Officer at Commonwealth Scientific and Industrial Research Organisation (CSIRO), Perth, W.A., personal communication

Zarco-Tejada, P.J., Rueda, C.A. and Ustin, S.L. (2003). Water content estimation in vegetation with MODIS reflectance data and model inversion methods. Remote Sensing of Environment 85, pp. 109-124

Internet (last accessed: October 2004)

www1: http://ltpwww.gsfc.nasa.gov/IAS/handbook/handbook_htmls/chapter6/chapter6.html
www2: http://earthobservatory.nasa.gov/Study/BAER/baer2.html
www3: http://www.biscuitfire.com/burn_severity.htm
www4: http://www.iriacenter.org/tutorial/guide.frm.html
www5: http://www.geocities.com/RainForest/Canopy/1805/BRDF.html
www6: http://www.geo.unizh.ch/rsl/research/SpectroLab/goniometry/brdf_intro.shtml
www7: http://geography.bu.edu/brdf/brdfexpl.html
www8: http://eosdatainfo.gsfc.nasa.gov/eosdata/terra/platform.html
www9: http://eosdatainfo.gsfc.nasa.gov/eosdata/aqua/platform.html
www10: http://modis.gsfc.nasa.gov/about/specs.html
www11: http://www.eoc.csiro.au/modis/nov02_ws/lecture3.pdf
www12: http://www.mcst.ssai.biz/mcstweb/performance/aqua/aqua-nonfunct-dets.html
www13: http://www.engesat.com.br/satelites/landsat5.htm
www14: http://geo.arc.nasa.gov/sge/landsat/l7.html
www15: http://ltpwww.gsfc.nasa.gov/IAS/handbook/handbook_htmls/chapter5/chapter5.html
www16: http://ltpwww.gsfc.nasa.gov/IAS/handbook/handbook_htmls/chapter6/chapter6.html
www17: http://www.ga.gov.au/acres/referenc/slcoff_descrip.jsp
www18: http://landsat.gsfc.nasa.gov/announcements/program_update.html
www19: http://ltpwww.gsfc.nasa.gov/IAS/handbook/handbook_htmls/chapter11/chapter11.html

Appendix:

This appendix contains the figures and tables of secondary significance for the understanding of this study. In the text, these figures and tables are referenced with an "A" and a consecutive number for Figures and Tables, respectively.

MODIS Data: TOA 2002									
Date of Acquisition	**Julian Day**	**Platform**	**Spectral Bands**	**Projection**	**Datum**	**View Zenith Angle**		**Cloudstate of FAA1 to FAA3**	**Cloudmask**
						Min [Degree]	**Max [Degree]**		**($R_{(1/TOA)}$ > var1)**
10. September 2002	253	Terra	1 2 3 4 5 6 7	LAT/LONG	WGS84	44.34	53.99	Significant clouds NOT present	——
11. September 2002	254	Aqua	1 2 3 4 5 6 7	LAT/LONG	WGS84	5.00	11.20	Significant clouds WERE present	var = 700
13. September 2002	256	Terra	1 2 3 4 5 6 7	LAT/LONG	WGS84	48.37	58.01	Significant clouds WERE present (FAA3)	var = 1200
18. September 2002	261	Aqua	1 2 3 4 5 6 7	LAT/LONG	WGS84	2.86	22.41	Mixed clouds present on a pixel	var = 1100
19. September 2002	262	Terra	1 2 3 4 5 6 7	LAT/LONG	WGS84	36.43	48.12	Mixed clouds present on a pixel	var = 1000
20. September 2002	263	Aqua	1 2 3 4 5 6 7	LAT/LONG	WGS84	1.14	20.45	Significant clouds WERE present	var = 1000
22. September 2002	265	Terra	1 2 3 4 5 6 7	LAT/LONG	WGS84	54.02	62.33	Significant clouds WERE present (FAA2)	var = 1200
28. September 2002	271	Terra	1 2 3 4 5 6 7	LAT/LONG	WGS84	26.60	40.84	Mixed clouds present on a pixel	var = 950
29. September 2002	272	Aqua	1 2 3 4 5 6 7	LAT/LONG	WGS84	12.61	29.96	Significant clouds NOT present	——
13. October 2002	286	Aqua	1 2 3 4 5 6 7	LAT/LONG	WGS84	0.04	12.02	Significant clouds WERE present (FAA3)	var = 750
31. October 2002	304	Terra	1 2 3 4 5 6 7	LAT/LONG	WGS84	48.46	58.12	Significant clouds WERE present (FAA3)	var = 880
5. November 2002	309	Terra	1 2 3 4 5 6 7	LAT/LONG	WGS84	24.06	39.91	Significant clouds NOT present	——
7. November 2002	311	Terra	1 2 3 4 5 6 7	LAT/LONG	WGS84	41.84	53.18	Significant clouds WERE present (FAA3)	var = 930
8. November 2002	312	Terra	1 2 3 4 5 6 7	LAT/LONG	WGS84	15.16	32.10	Significant clouds NOT present	——
9. November 2002	313	Terra	1 2 3 4 5 6 7	LAT/LONG	WGS84	54.23	62.45	Mixed clouds present on a pixel	var = 980
10. November 2002	314	Terra	1 2 3 4 5 6 7	LAT/LONG	WGS84	0.03	10.62	Thin clouds WERE present (FAA3)	var = 900
12. November 2002	316	Aqua	1 2 3 4 5 6 7	LAT/LONG	WGS84	14.65	32.50	Mixed clouds present on a pixel	var = 1050
13. November 2002	317	Terra	1 2 3 4 5 6 7	LAT/LONG	WGS84	43.85	53.66	Significant clouds NOT present	——
14. November 2002	318	Terra	1 2 3 4 5 6 7	LAT/LONG	WGS84	34.10	47.45	Significant clouds NOT present	——
17. November 2002	321	Aqua	1 2 3 4 5 6 7	LAT/LONG	WGS84	43.12	54.13	Significant clouds WERE present (FAA2+3)	var = 1200
19. November 2002	323	Aqua	1 2 3 4 5 6 7	LAT/LONG	WGS84	26.00	41.37	Mixed clouds present on a pixel	var = 1700
20. November 2002	324	Terra	1 2 3 4 5 6 7	LAT/LONG	WGS84	50.85	58.75	Significant clouds NOT present	——
25. November 2002	329	Aqua	1 2 3 4 5 6 7	LAT/LONG	WGS84	24.19	38.99	Mixed clouds present on a pixel	var = 900
26. November 2002	330	Terra	1 2 3 4 5 6 7	LAT/LONG	WGS84	0.03	11.07	Significant clouds NOT present	——
27. November 2002	331	Aqua	1 2 3 4 5 6 7	LAT/LONG	WGS84	42.56	52.70	Mixed clouds present on a pixel	var = 850
29. November 2002	333	Terra	1 2 3 4 5 6 7	LAT/LONG	WGS84	44.44	54.09	Mixed clouds present on a pixel	var = 750
30. November 2002	334	Terra	1 2 3 4 5 6 7	LAT/LONG	WGS84	33.35	46.86	Mixed clouds present on a pixel	var = 1100
6. December 2002	340	Terra	1 2 3 4 5 6 7	LAT/LONG	WGS84	51.26	59.08	Significant clouds WERE present (FAA1)	var = 1100
9. December 2002	343	Aqua	1 2 3 4 5 6 7	LAT/LONG	WGS84	0.65	19.97	Significant clouds NOT present	——
10. December 2002	344	Terra	1 2 3 4 5 6 7	LAT/LONG	WGS84	15.98	32.76	Significant clouds NOT present	——
11. December 2002	345	Terra	1 2 3 4 5 6 7	LAT/LONG	WGS84	53.82	62.21	Significant clouds WERE present (FAA1)	var = 1200
13. December 2002	347	Aqua	1 2 3 4 5 6 7	LAT/LONG	WGS84	42.76	52.81	Significant clouds WERE present (FAA1+3)	var = 900
16. December 2002	350	Aqua	1 2 3 4 5 6 7	LAT/LONG	WGS84	0.03	11.75	Mixed clouds present on a pixel	var = 1000
17. December 2002	351	Aqua	1 2 3 4 5 6 7	LAT/LONG	WGS84	55.31	63.30	Mixed clouds present on a pixel	var = 1200
18. December 2002	352	Terra	1 2 3 4 5 6 7	LAT/LONG	WGS84	48.16	57.89	Mixed clouds present on a pixel	var = 1200
19. December 2002	353	Terra	1 2 3 4 5 6 7	LAT/LONG	WGS84	3.83	22.75	Mixed clouds present on a pixel	var = 900
20. December 2002	354	Terra	1 2 3 4 5 6 7	LAT/LONG	WGS84	61.45	65.56	Mixed clouds present on a pixel	var = 1100
26. December 2002	360	Terra	1 2 3 4 5 6 7	LAT/LONG	WGS84	15.61	32.47	Mixed clouds present on a pixel	var = 900
27. December 2002	361	Terra	1 2 3 4 5 6 7	LAT/LONG	WGS84	54.02	62.33	Significant clouds WERE present (FAA2+3)	var = 1300
31. December 2002	365	Aqua	1 2 3 4 5 6 7	LAT/LONG	WGS84	55.44	62.28	Significant clouds WERE present (FAA3)	var = 900

Table A1-1: Overview of MODIS Top of Atmosphere (TOA) data available in this study

MODIS Data: BOANADIR 2002						
Date of Acquisition	**Julian Day**	**Platform**	**Spectral Bands**	**Projection**	**Datum**	**Available Coverage FAA1 to 3**
10. September 2002	253	Terra	1 2 3 4 5 7	LAT/LONG	WGS84	no data available
11. September 2002	254	Aqua	1 2 3 4 5 7	LAT/LONG	WGS84	no data available
13. September 2002	256	Terra	1 2 3 4 5 7	LAT/LONG	WGS84	no data available
18. September 2002	261	Aqua	1 2 3 4 5 7	LAT/LONG	WGS84	no data available
19. September 2002	262	Terra	1 2 3 4 5 7	LAT/LONG	WGS84	no data available
20. September 2002	263	Aqua	1 2 3 4 5 7	LAT/LONG	WGS84	single pixel available
22. September 2002	265	Terra	1 2 3 4 5 7	LAT/LONG	WGS84	single pixel available
28. September 2002	271	Terra	1 2 3 4 5 7	LAT/LONG	WGS84	single pixel available
29. September 2002	272	Aqua	1 2 3 4 5 7	LAT/LONG	WGS84	single pixel available
13. October 2002	286	Aqua	1 2 3 4 5 7	LAT/LONG	WGS84	single pixel available
31. October 2002	304	Terra	1 2 3 4 5 7	LAT/LONG	WGS84	single pixel available
5. November 2002	309	Terra	1 2 3 4 5 7	LAT/LONG	WGS84	single pixel available
7. November 2002	311	Terra	1 2 3 4 5 7	LAT/LONG	WGS84	partly covered FAA1 to 2 / single pixel available FAA3
8. November 2002	312	Terra	1 2 3 4 5 7	LAT/LONG	WGS84	partly covered FAA1 to 2 / single pixel available FAA3
9. November 2002	313	Terra	1 2 3 4 5 7	LAT/LONG	WGS84	covered FAA1 to 2 / partly covered FAA3
10. November 2002	314	Terra	1 2 3 4 5 7	LAT/LONG	WGS84	partly covered FAA1 to 3
12. November 2002	316	Aqua	1 2 3 4 5 7	LAT/LONG	WGS84	partly covered FAA1 to 3
13. November 2002	317	Terra	1 2 3 4 5 7	LAT/LONG	WGS84	covered FAA1 to 2 / partly covered FAA3
14. November 2002	318	Terra	1 2 3 4 5 7	LAT/LONG	WGS84	partly covered FAA1 to 3
17. November 2002	321	Aqua	1 2 3 4 5 7	LAT/LONG	WGS84	partly covered FAA1 to 3
19. November 2002	323	Aqua	1 2 3 4 5 7	LAT/LONG	WGS84	partly covered FAA1 to 3
20. November 2002	324	Terra	1 2 3 4 5 7	LAT/LONG	WGS84	partly covered FAA1 to 3
25. November 2002	329	Aqua	1 2 3 4 5 7	LAT/LONG	WGS84	partly covered FAA1 to 3
26. November 2002	330	Terra	1 2 3 4 5 7	LAT/LONG	WGS84	partly covered FAA1 to 3
27. November 2002	331	Aqua	1 2 3 4 5 7	LAT/LONG	WGS84	partly covered FAA1 to 3
29. November 2002	333	Terra	1 2 3 4 5 7	LAT/LONG	WGS84	partly covered FAA1 to 3
30. November 2002	334	Terra	1 2 3 4 5 7	LAT/LONG	WGS84	partly covered FAA1 to 3
6. December 2002	340	Terra	1 2 3 4 5 7	LAT/LONG	WGS84	partly covered FAA1 to 3
9. December 2002	343	Aqua	1 2 3 4 5 7	LAT/LONG	WGS84	partly covered FAA1 to 3
10. December 2002	344	Terra	1 2 3 4 5 7	LAT/LONG	WGS84	partly covered FAA1 to 3
11. December 2002	345	Terra	1 2 3 4 5 7	LAT/LONG	WGS84	partly covered FAA1 to 3
13. December 2002	347	Aqua	1 2 3 4 5 7	LAT/LONG	WGS84	partly covered FAA1 to 2 / single pixel available FAA3
16. December 2002	350	Aqua	1 2 3 4 5 7	LAT/LONG	WGS84	partly covered FAA1 to 3
17. December 2002	351	Aqua	1 2 3 4 5 7	LAT/LONG	WGS84	partly covered FAA1 to 3
18. December 2002	352	Terra	1 2 3 4 5 7	LAT/LONG	WGS84	partly covered FAA1 to 3
19. December 2002	353	Terra	1 2 3 4 5 7	LAT/LONG	WGS84	partly covered FAA1 to 3
20. December 2002	354	Terra	1 2 3 4 5 7	LAT/LONG	WGS84	partly covered FAA1 to 3
26. December 2002	360	Terra	1 2 3 4 5 7	LAT/LONG	WGS84	partly covered FAA1 to 3
27. December 2002	361	Terra	1 2 3 4 5 7	LAT/LONG	WGS84	partly covered FAA1 and 3 / single pixel available FAA2
31. December 2002	365	Aqua	1 2 3 4 5 7	LAT/LONG	WGS84	partly covered FAA1 to 3

Table A1-2: Overview of MODIS Bottom of Atmosphere and BRDF corrected (BOANADIR) data available in this study

MODIS Data: BOA 2002									
Date of Acquisition	**Julian Day**	**Platform**	**Spectral Bands**	**Projection**	**Datum**	**View Zenith Angle**		**Cloudstate of FAA1 to FAA3**	**Cloudmask**
						Min [Degree]	**Max [Degree]**		**($R_{(1/TOA)}$ > var1)**
10. September 2002	253	Terra	1 2 3 4 5 7	LAT/LONG	WGS84	44.34	53.99	Significant clouds NOT present	——
11. September 2002	254	Aqua	1 2 3 4 5 7	LAT/LONG	WGS84	0.05	11.02	Significant clouds WERE present (ALL)	var = 700
13. September 2002	256	Terra	1 2 3 4 5 7	LAT/LONG	WGS84	48.37	58.01	Significant clouds WERE present (FAA3)	var = 1200
18. September 2002	261	Aqua	1 2 3 4 5 7	LAT/LONG	WGS84	2.86	22.41	Mixed clouds present on a pixel	var = 1100
19. September 2002	262	Terra	1 2 3 4 5 7	LAT/LONG	WGS84	36.43	48.12	Mixed clouds present on a pixel	var = 1000
20. September 2002	263	Aqua	1 2 3 4 5 7	LAT/LONG	WGS84	1.14	20.45	Significant clouds WERE present (ALL)	var = 1000
22. September 2002	265	Terra	1 2 3 4 5 7	LAT/LONG	WGS84	54.02	62.33	Significant clouds WERE present (FAA2)	var = 1200
28. September 2002	271	Terra	1 2 3 4 5 7	LAT/LONG	WGS84	26.60	40.84	Mixed clouds present on a pixel	var = 950
29. September 2002	272	Aqua	1 2 3 4 5 7	LAT/LONG	WGS84	12.61	29.96	Significant clouds NOT present	——

Table A1-3: Overview of MODIS Bottom of Atmosphere (BOA) data available in this study

Landsat TM/ETM+ Data:								
Date of Acquisition	**Julian Day**	**Sensor**	**Path/Row**	**Spectral Bands**	**Projection**	**Datum**	**RMS-error (m)** Along-Track	**RMS-error (m)** Across-Track
11. February 2002	42	ETM+	111/84	1 2 3 4 5 7	LAT/LONG	WGS84	9.70	9.30
26. November 2002	330	ETM+	111/84	1 2 3 4 5 7	LAT/LONG	WGS84	5.65	5.13
12. December 2002	346	ETM+	111/84	1 2 3 4 5 7	LAT/LONG	WGS84	8.90	10.00
23. December 2003	357	TM	111/84	1 2 3 4 5 7	LAT/LONG	WGS84	6.00	8.90
31. May 2004	152	TM	111/84	1 2 3 4 5 7	LAT/LONG	WGS84	8.18	9.83

Table A1-4: Overview of Landsat TM/ETM+ data available in this study

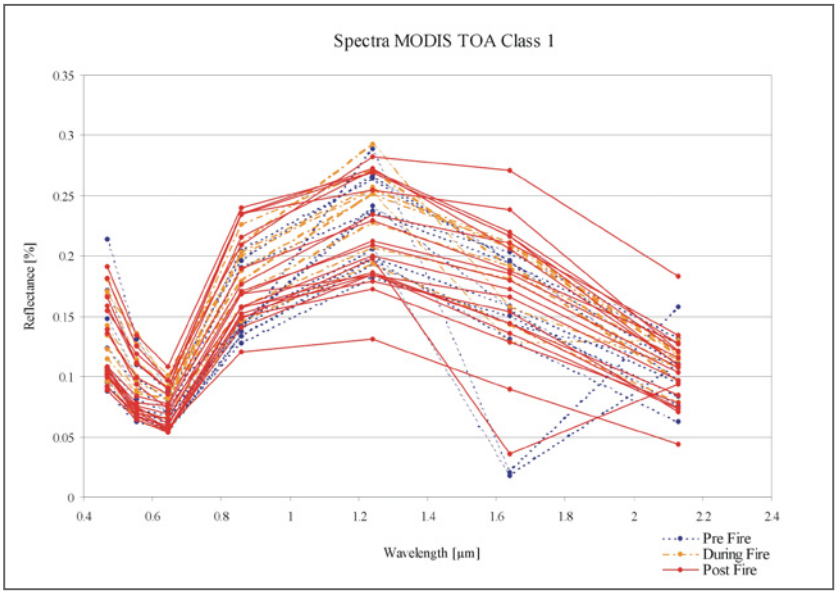

Figure A1-1: Spectral properties detected from bands 1 to 7 of MODIS top of atmosphere (TOA) reflectance in class 1.

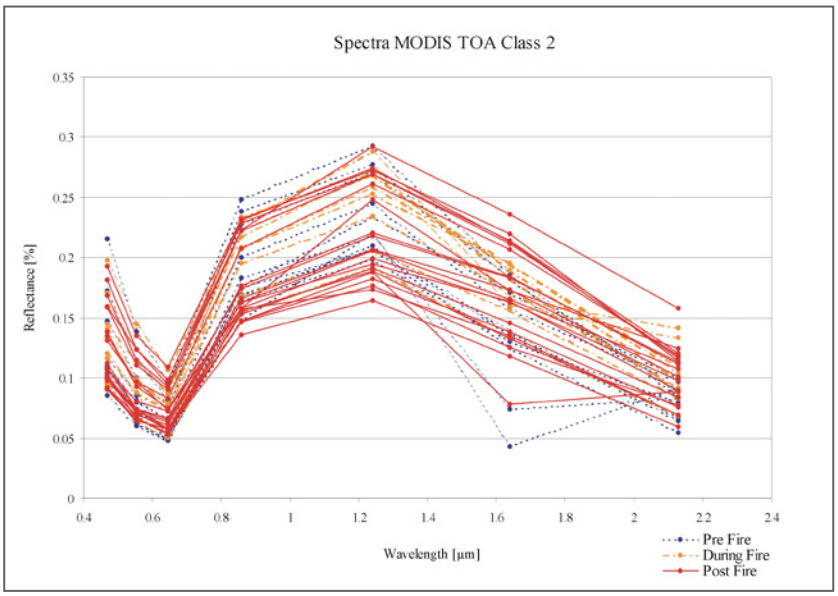

Figure A1-2: Spectral properties detected from bands 1 to 7 of MODIS top of atmosphere (TOA) reflectance in class 2.

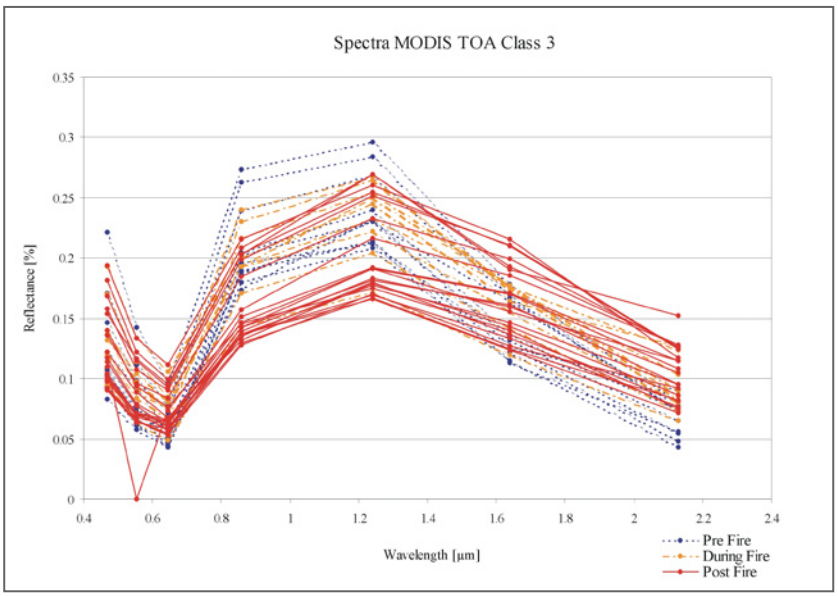

Figure A1-3: Spectral properties detected from bands 1 to 7 of MODIS top of atmosphere (TOA) reflectance in class 3.

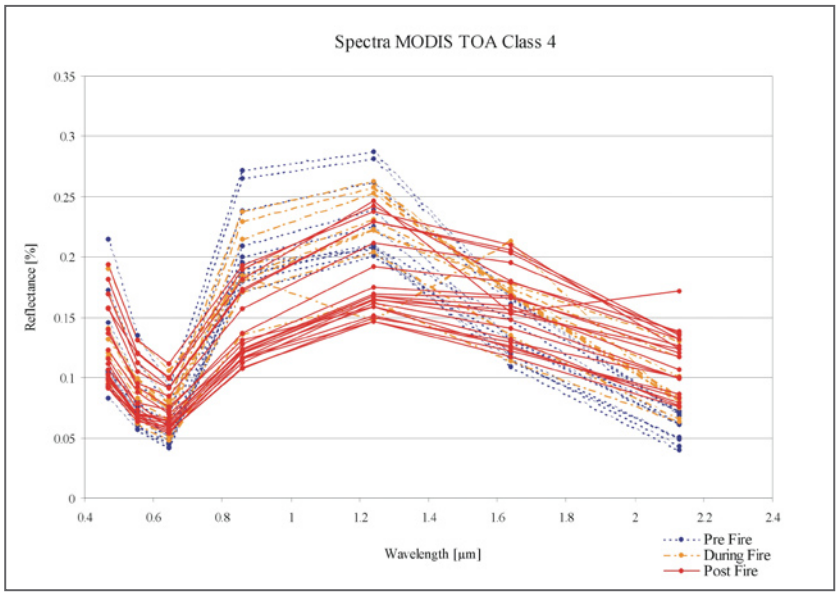

Figure A1-4: Spectral properties detected from bands 1 to 7 of MODIS top of atmosphere (TOA) reflectance in class 4.

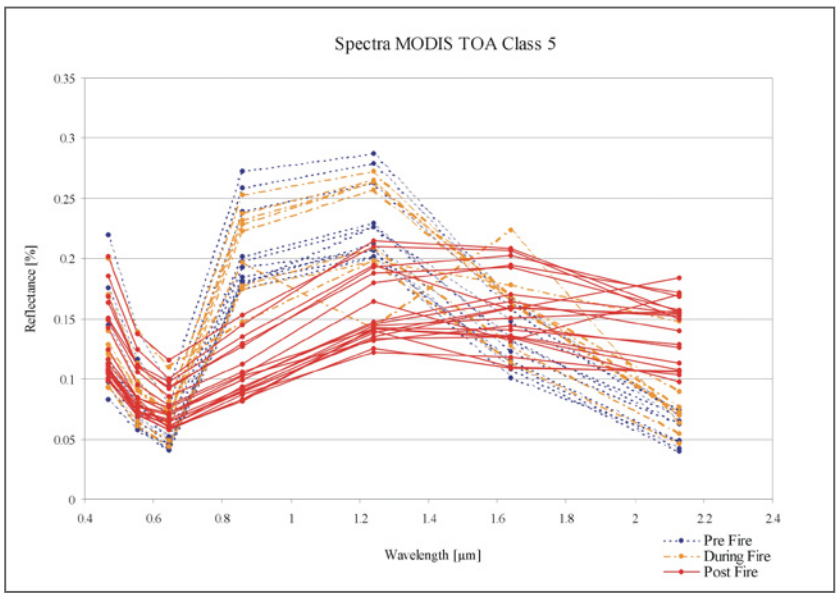

Figure A1-5: Spectral properties detected from bands 1 to 7 of MODIS top of atmosphere (TOA) reflectance in class 5.

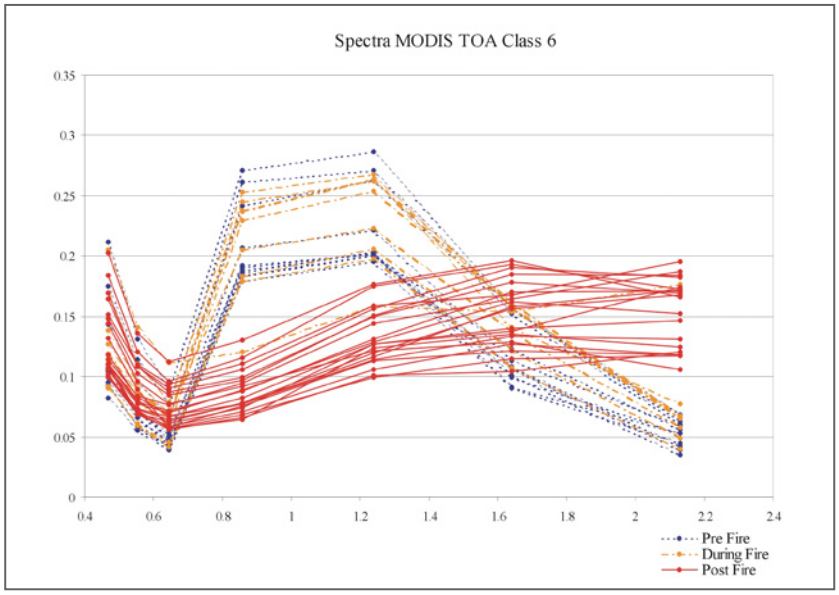

Figure A1-6: Spectral properties detected from bands 1 to 7 of MODIS top of atmosphere (TOA) reflectance in class 6.

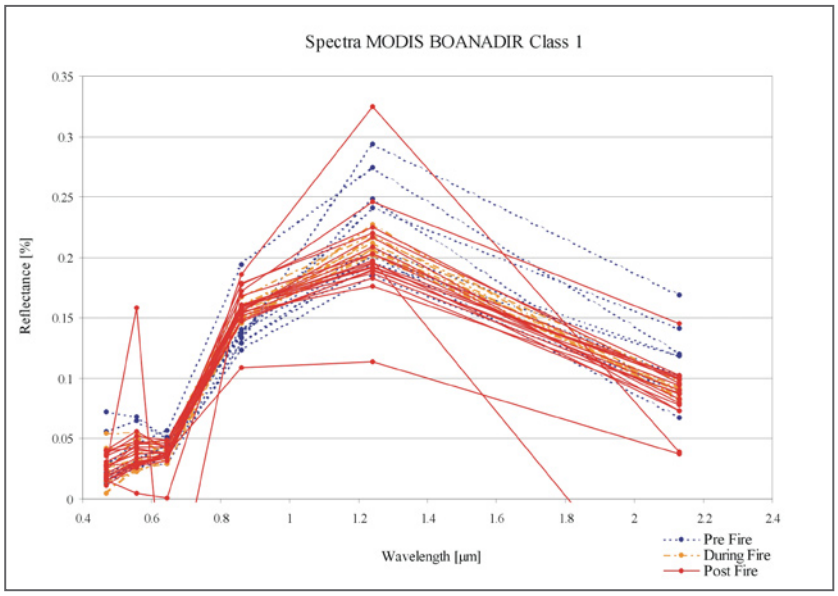

Figure A2-1: Spectral properties detected from bands 1 to 5 and 7 of MODIS bottom of atmosphere and BRDF corrected (BOANADIR) reflectance in class 1.

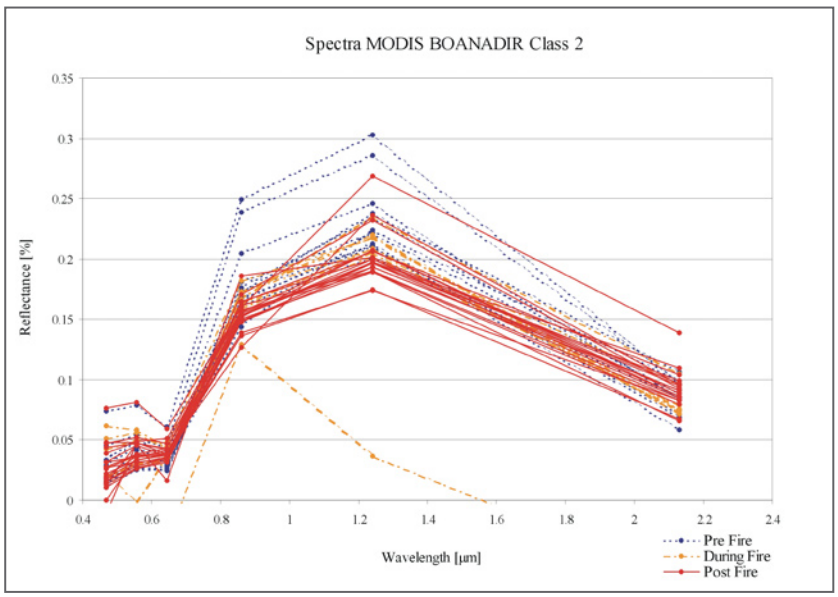

Figure A2-2: Spectral properties detected from bands 1 to 5 and 7 of MODIS bottom of atmosphere and BRDF corrected (BOANADIR) reflectance in class 2.

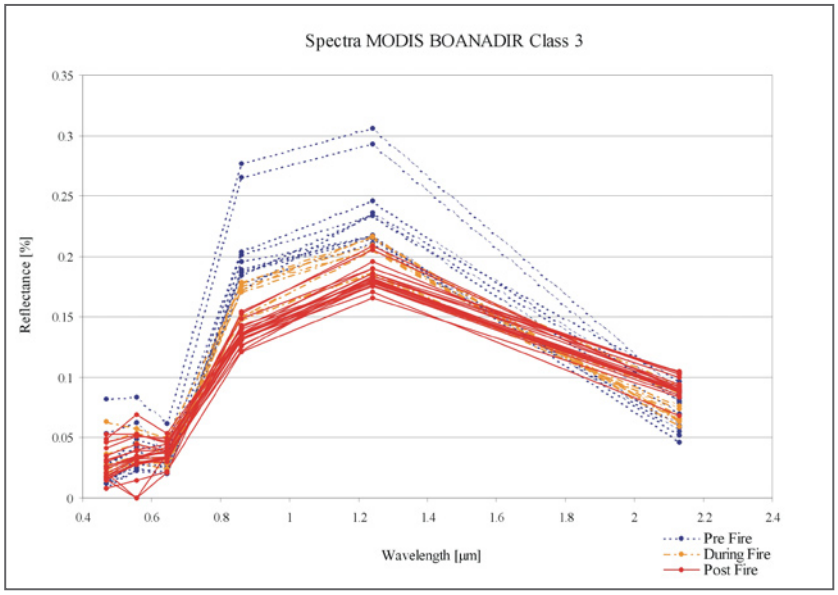

Figure A2-3: Spectral properties detected from bands 1 to 5 and 7 of MODIS bottom of atmosphere and BRDF corrected (BOANADIR) reflectance in class 3.

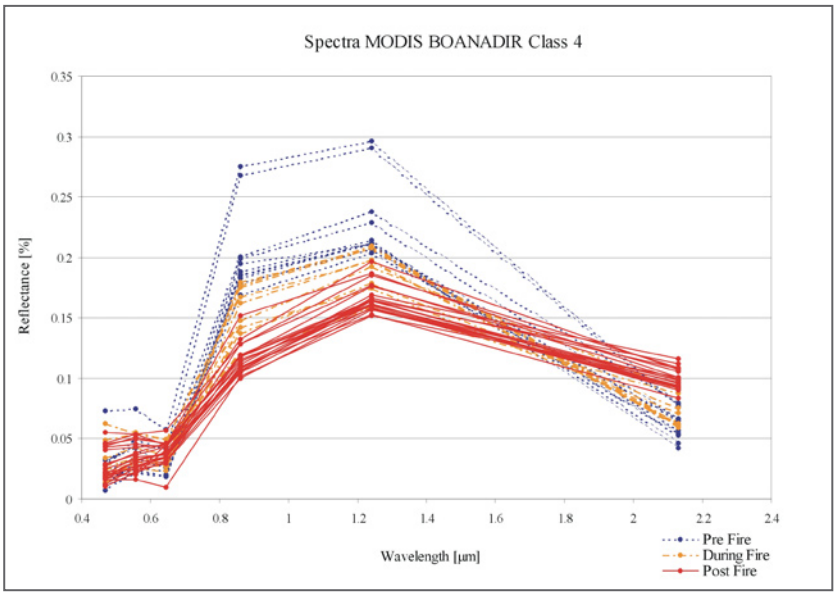

Figure A2-4: Spectral properties detected from bands 1 to 5 and 7 of MODIS bottom of atmosphere and BRDF corrected (BOANADIR) reflectance in class 4.

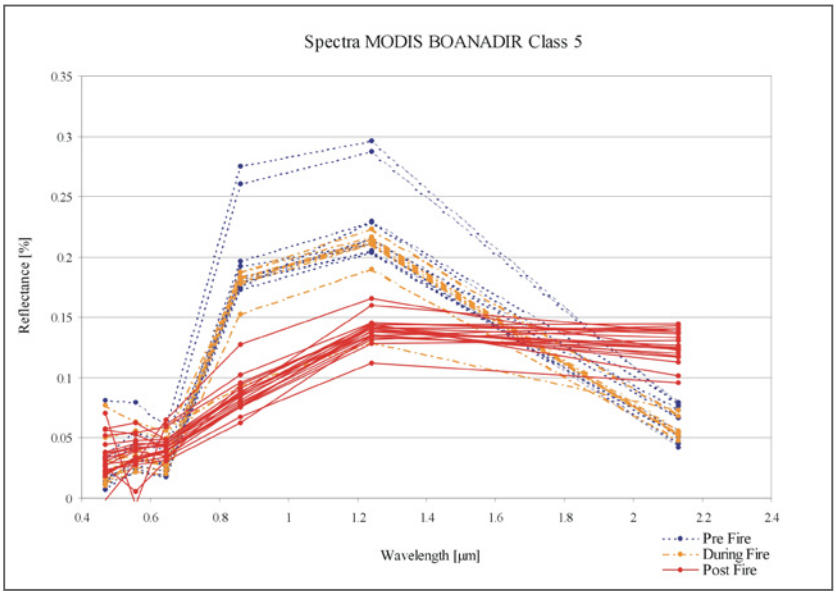

Figure A2-5: Spectral properties detected from bands 1 to 5 and 7 of MODIS bottom of atmosphere and BRDF corrected (BOANADIR) reflectance in class 5.

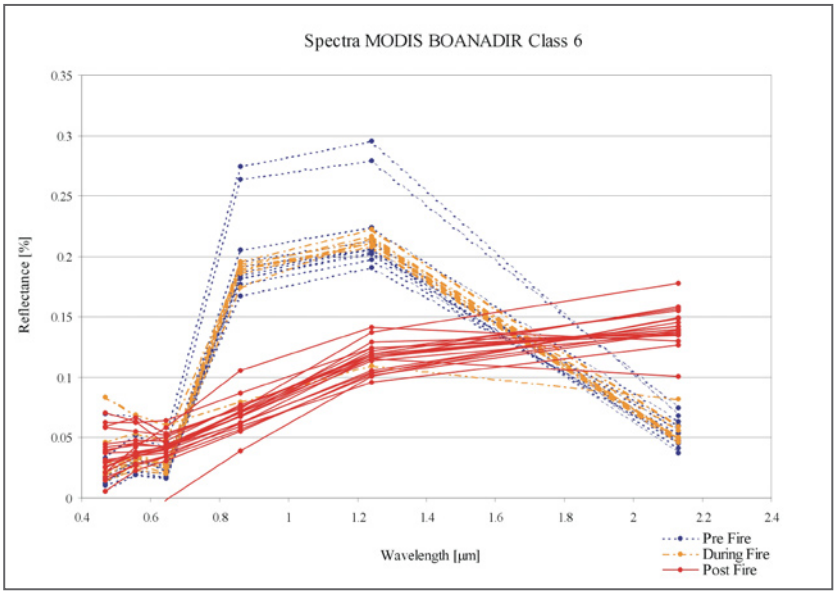

Figure A2-6: Spectral properties detected from bands 1 to 5 and 7 of MODIS bottom of atmosphere and BRDF corrected (BOANADIR) reflectance in class 6.

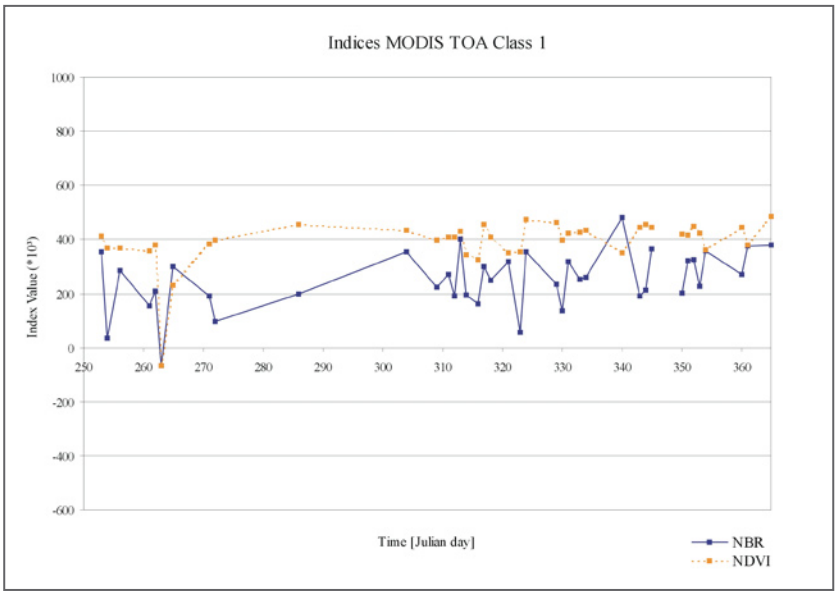

Figure A3-1: The trend of the NBR and NDVI through time in class 1, derived from MODIS top of atmosphere (TOA) reflectance.

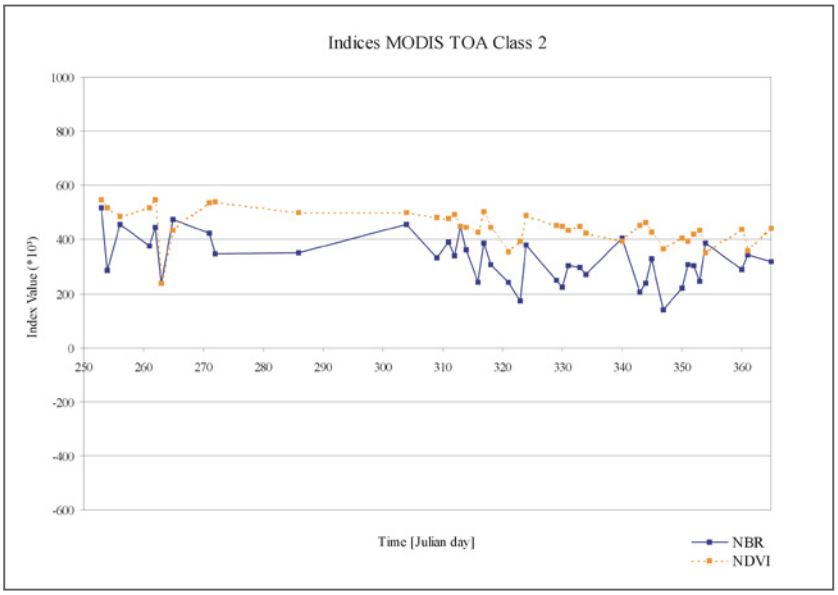

Figure A3-2: The trend of the NBR and NDVI through time in class 2, derived from MODIS top of atmosphere (TOA) reflectance.

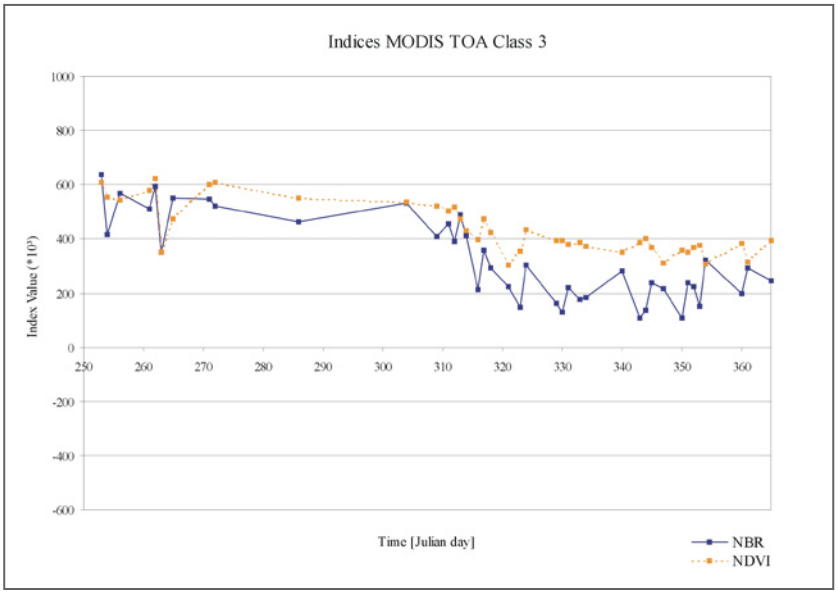

Figure A3-3: The trend of the NBR and NDVI through time in class 3, derived from MODIS top of atmosphere (TOA) reflectance.

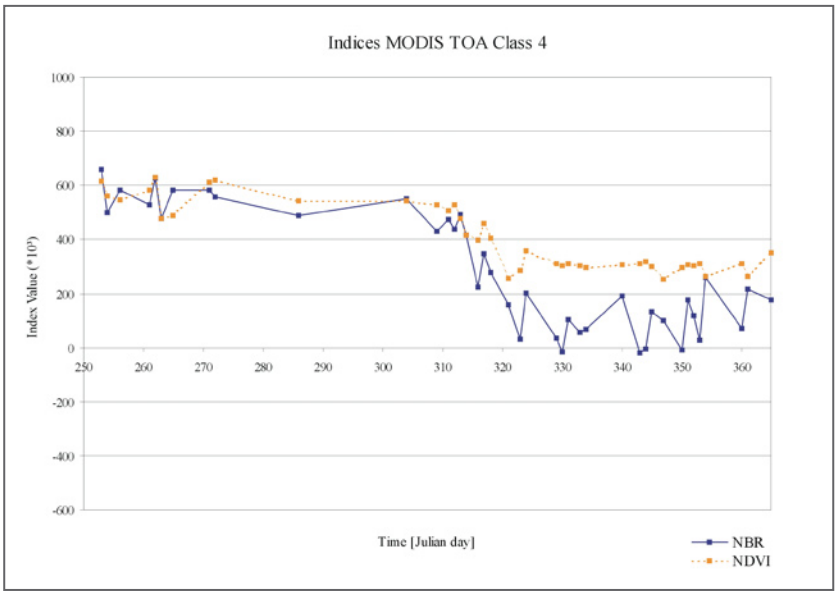

Figure A3-4: The trend of the NBR and NDVI through time in class 4, derived from MODIS top of atmosphere (TOA) reflectance.

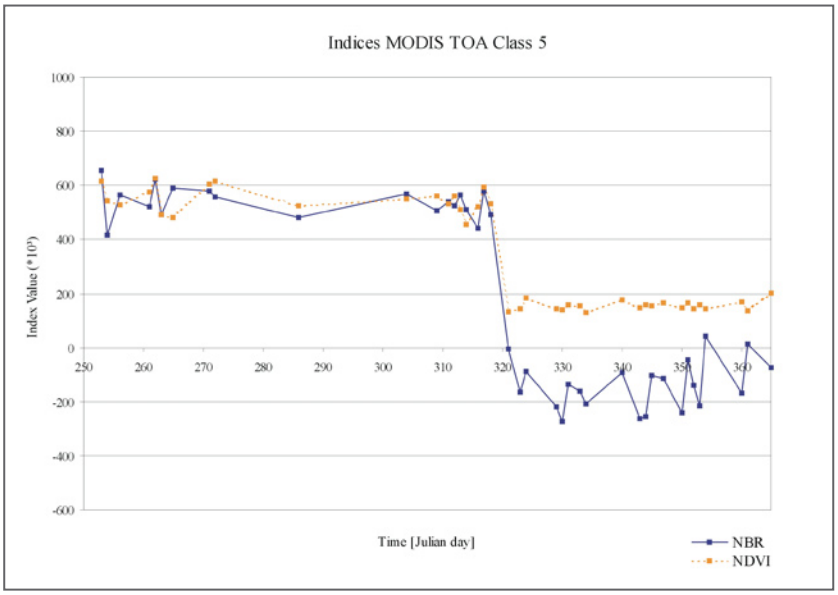

Figure A3-5: The trend of the NBR and NDVI through time in class 5, derived from MODIS top of atmosphere (TOA) reflectance.

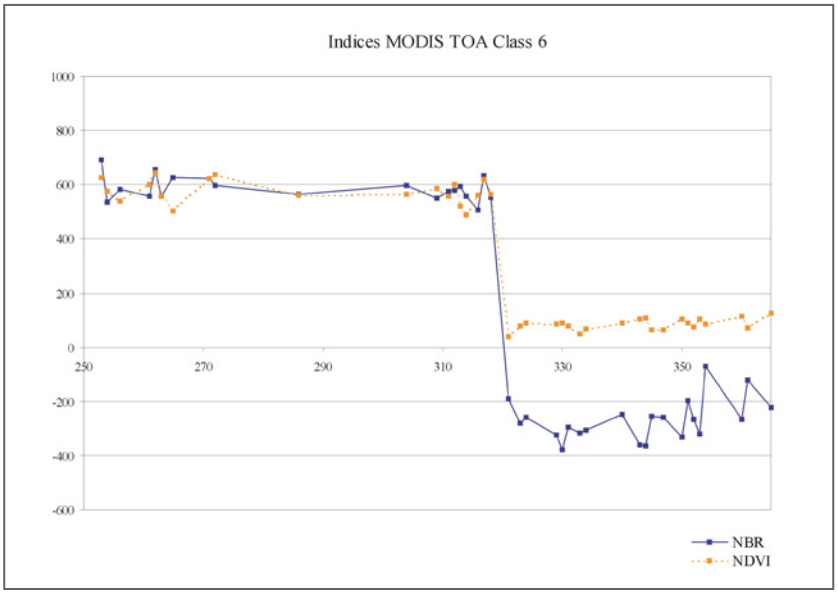

Figure A3-6: The trend of the NBR and NDVI through time in class 6, derived from MODIS top of atmosphere (TOA) reflectance.

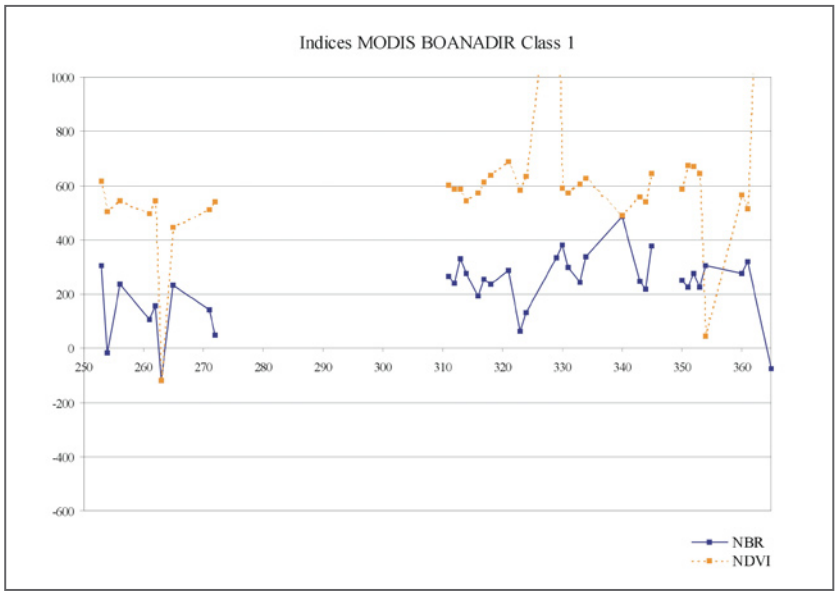

Figure A4-1: The trend of the NBR and NDVI through time in class 1, derived from MODIS bottom of atmosphere and BRDF corrected (BOANADIR) reflectance.

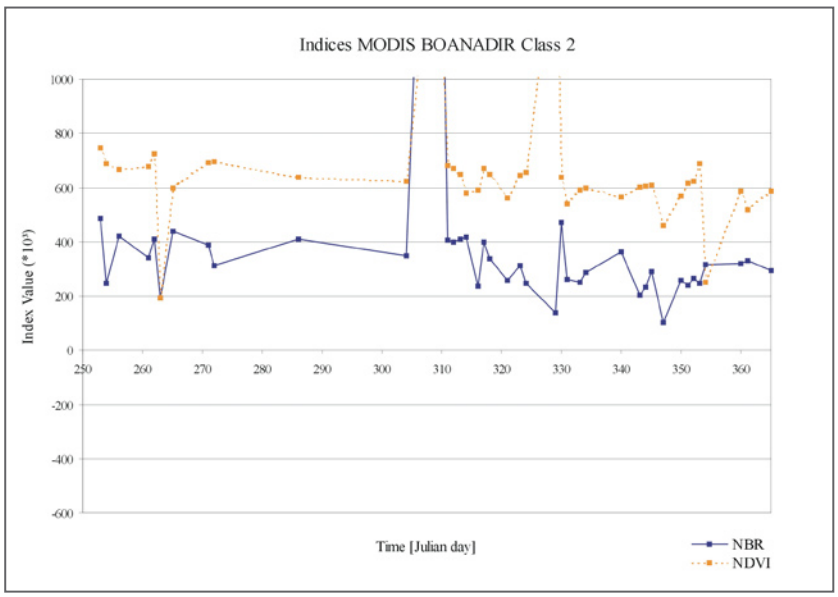

Figure A4-2: The trend of the NBR and NDVI through time in class 2, derived from MODIS bottom of atmosphere and BRDF corrected (BOANADIR) reflectance.

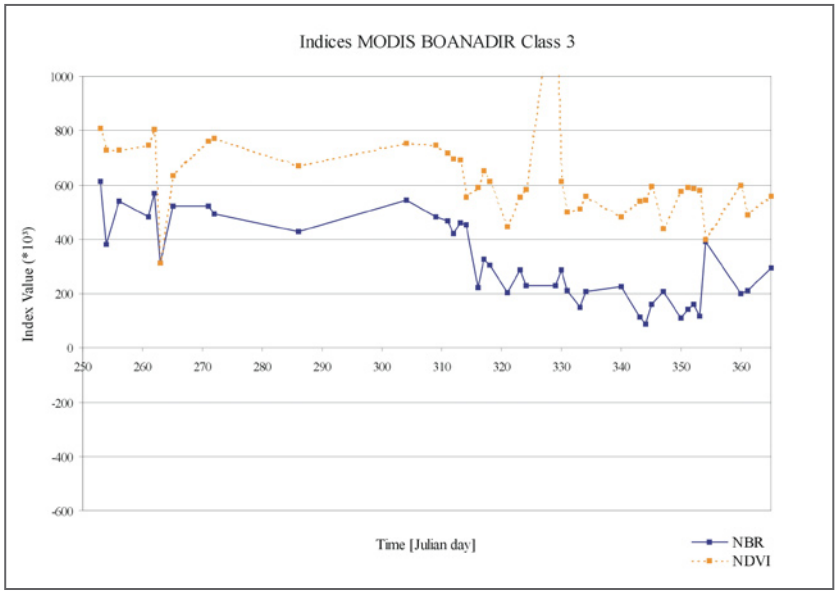

Figure A4-3: The trend of the NBR and NDVI through time in class 3, derived from MODIS bottom of atmosphere and BRDF corrected (BOANADIR) reflectance.

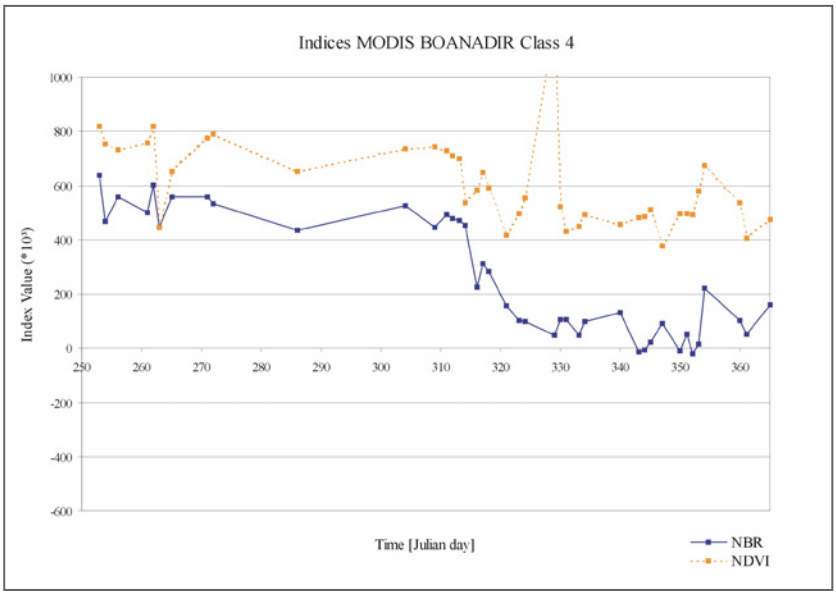

Figure A4-4: The trend of the NBR and NDVI through time in class 4, derived from MODIS bottom of atmosphere and BRDF corrected (BOANADIR) reflectance.

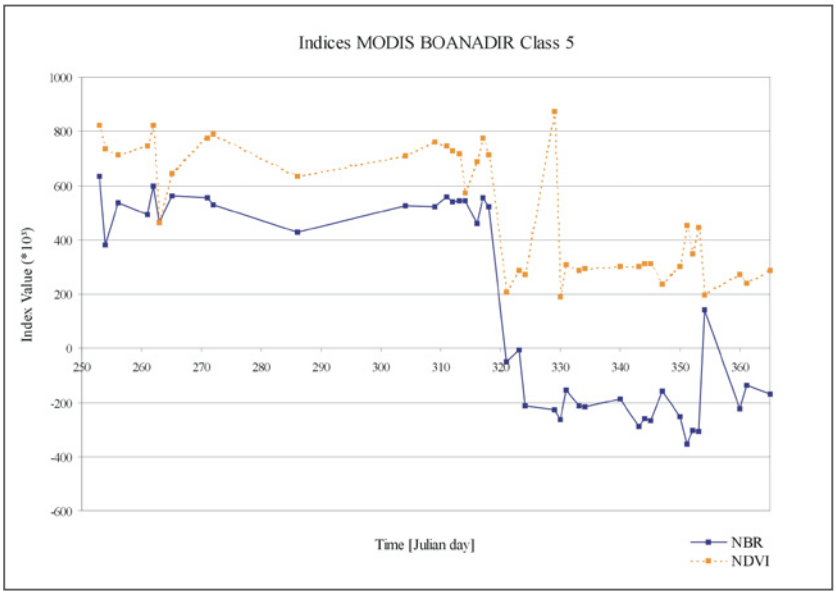

Figure A4-5: The trend of the NBR and NDVI through time in class 5, derived from MODIS bottom of atmosphere and BRDF corrected (BOANADIR) reflectance.

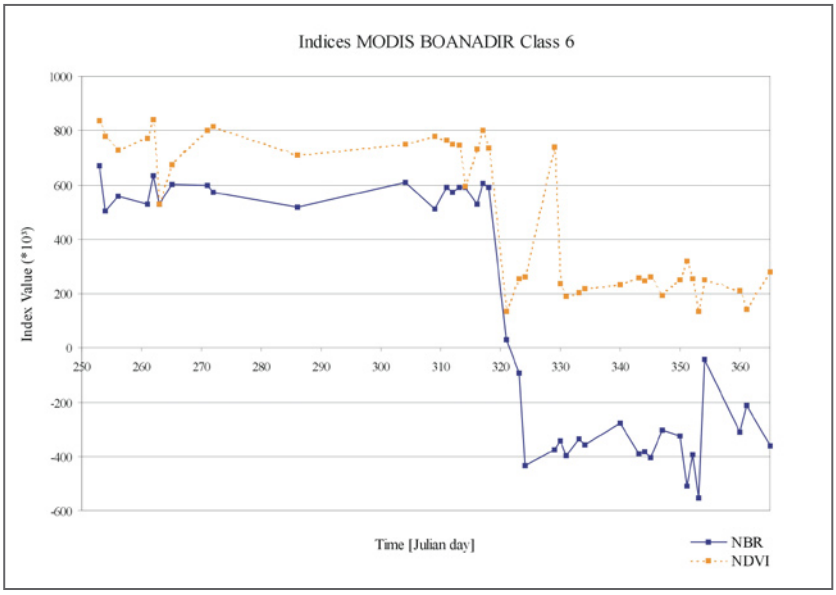

Figure A4-6: The trend of the NBR and NDVI through time in class 6, derived from MODIS bottom of atmosphere and BRDF corrected (BOANADIR) reflectance.

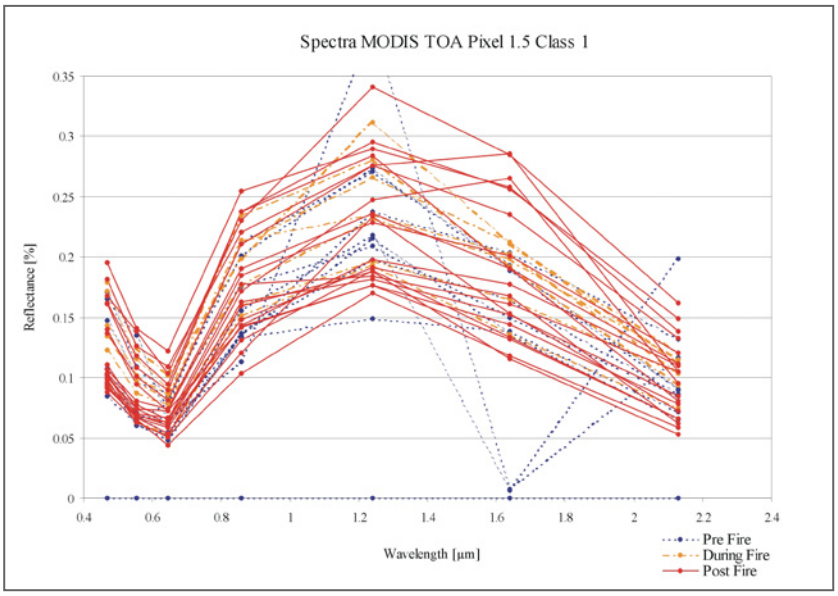

Figure A5-1: Spectral properties detected from bands 1 to 7 of MODIS top of atmosphere (TOA) reflectance within one pixel (1.5) selected in class 1.

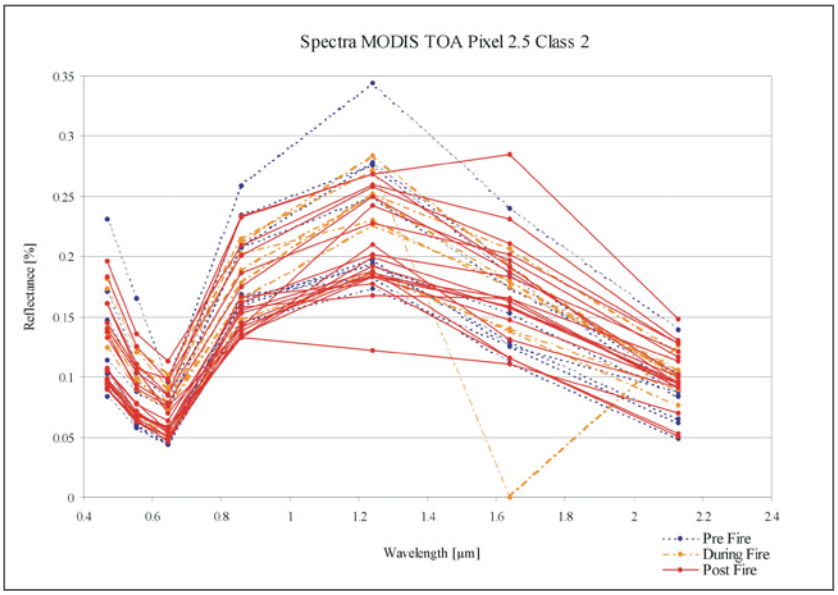

Figure A5-2: Spectral properties detected from bands 1 to 7 of MODIS top of atmosphere (TOA) reflectance within one pixel (2.5) selected in class 2.

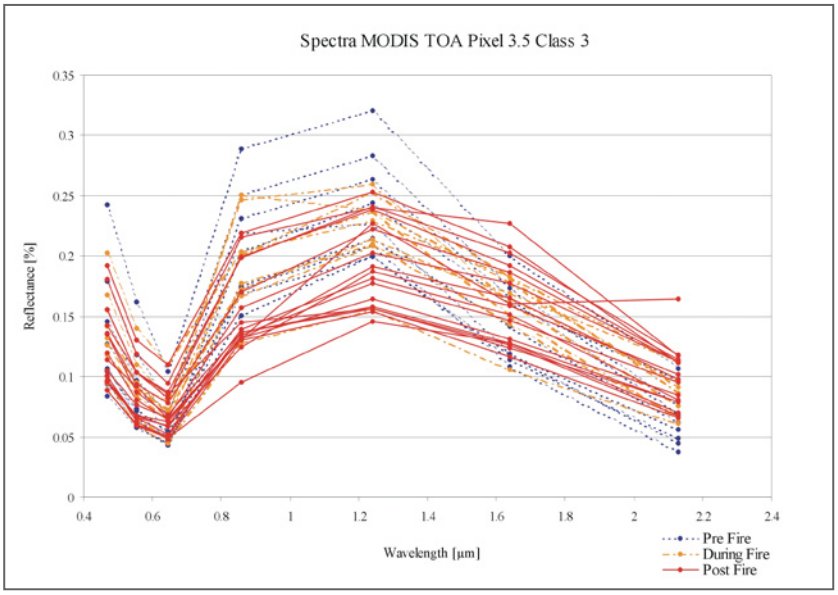

Figure A5-3: Spectral properties detected from bands 1 to 7 of MODIS top of atmosphere (TOA) reflectance within one pixel (3.5) selected in class 3.

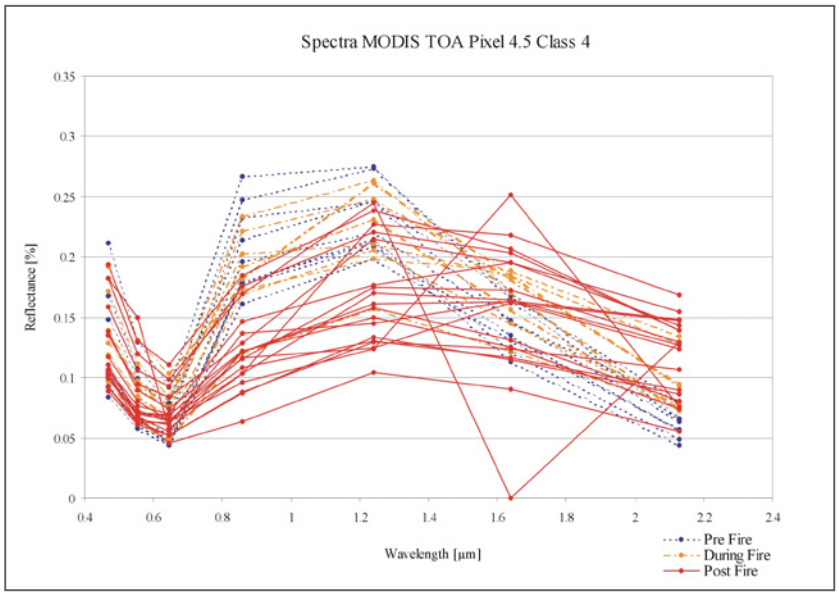

Figure A5-4: Spectral properties detected from bands 1 to 7 of MODIS top of atmosphere (TOA) reflectance within one pixel (4.5) selected in class 4.

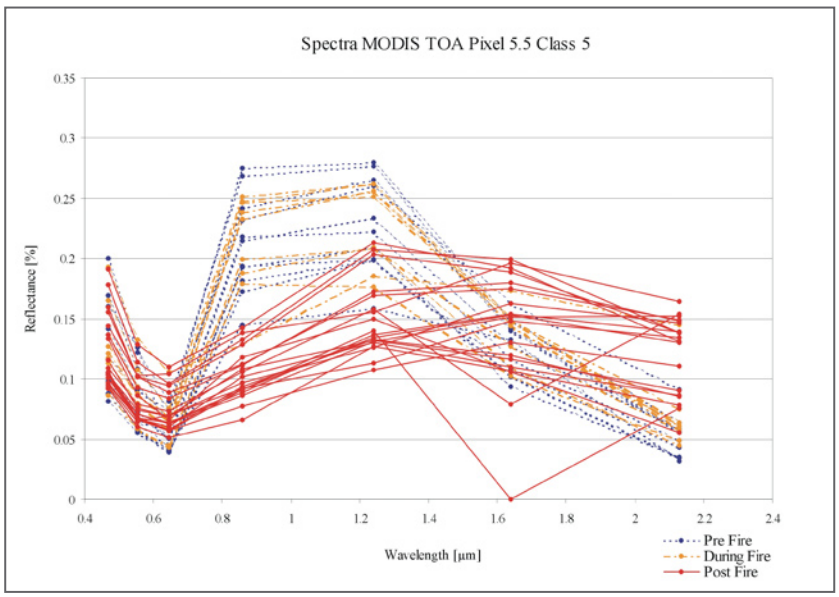

Figure A5-5: Spectral properties detected from bands 1 to 7 of MODIS top of atmosphere (TOA) reflectance within one pixel (5.5) selected in class 5.

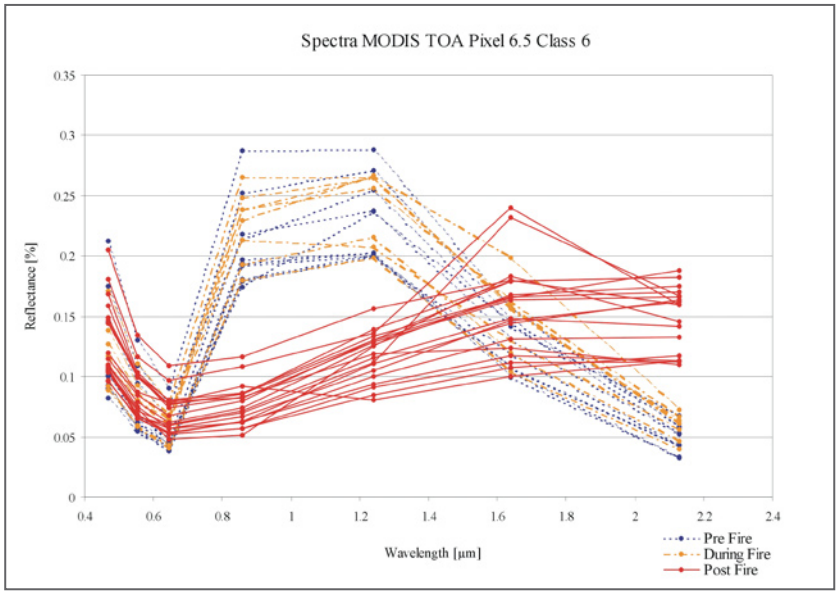

Figure A5-6: Spectral properties detected from bands 1 to 7 of MODIS top of atmosphere (TOA) reflectance within one pixel (6.5) selected in class 6.

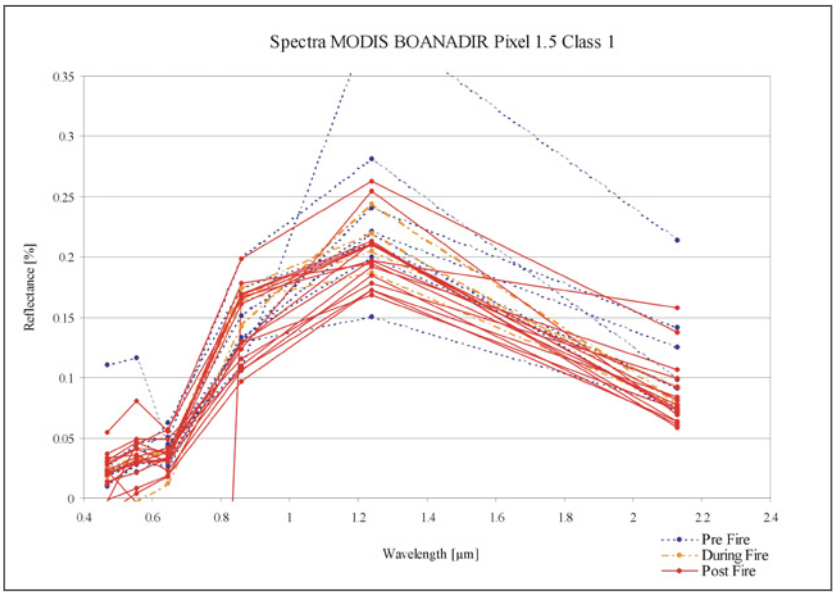

Figure A6-1: Spectral properties detected from bands 1 to 5 and 7 of MODIS bottom of atmosphere and BRDF corrected (BOANADIR) reflectance within one pixel (1.5) selected in class 1.

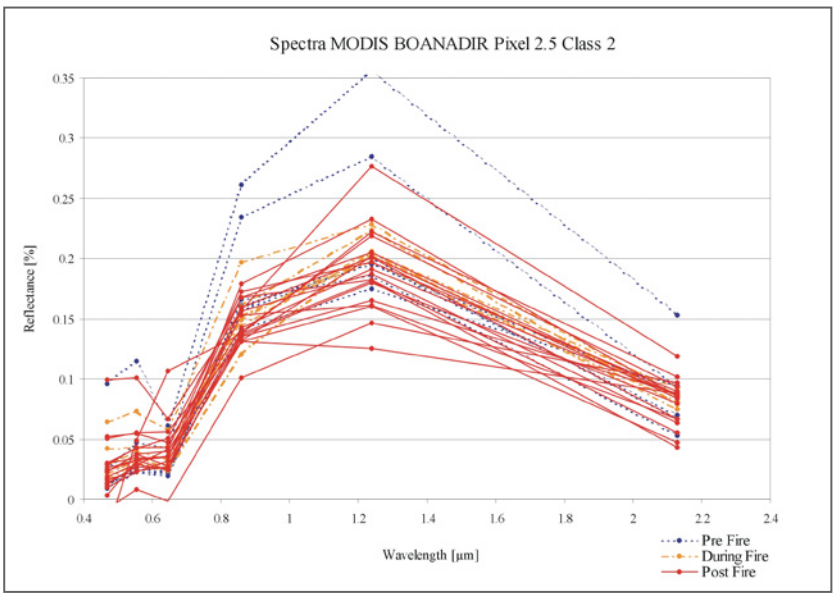

Figure A6-2: Spectral properties detected from bands 1 to 5 and 7 of MODIS bottom of atmosphere and BRDF corrected (BOANADIR) reflectance within one pixel (2.5) selected in class 2.

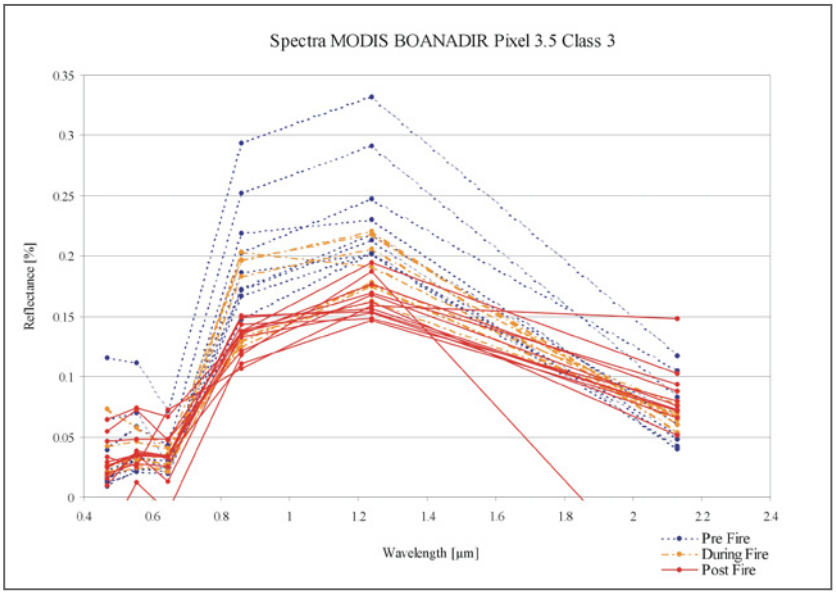

Figure A6-3: Spectral properties detected from bands 1 to 5 and 7 of MODIS bottom of atmosphere and BRDF corrected (BOANADIR) reflectance within one pixel (3.5) selected in class 3.

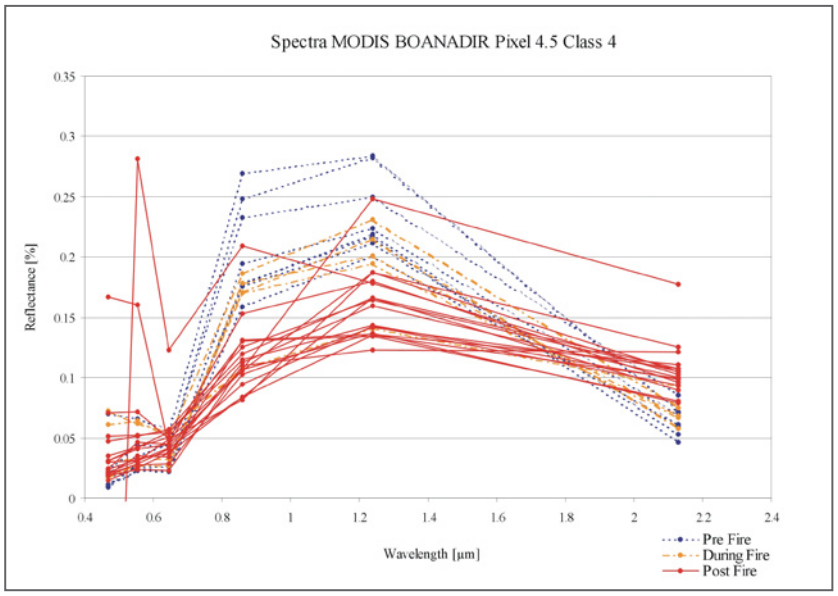

Figure A6-4: Spectral properties detected from bands 1 to 5 and 7 of MODIS bottom of atmosphere and BRDF corrected (BOANADIR) reflectance within one pixel (4.5) selected in class 4.

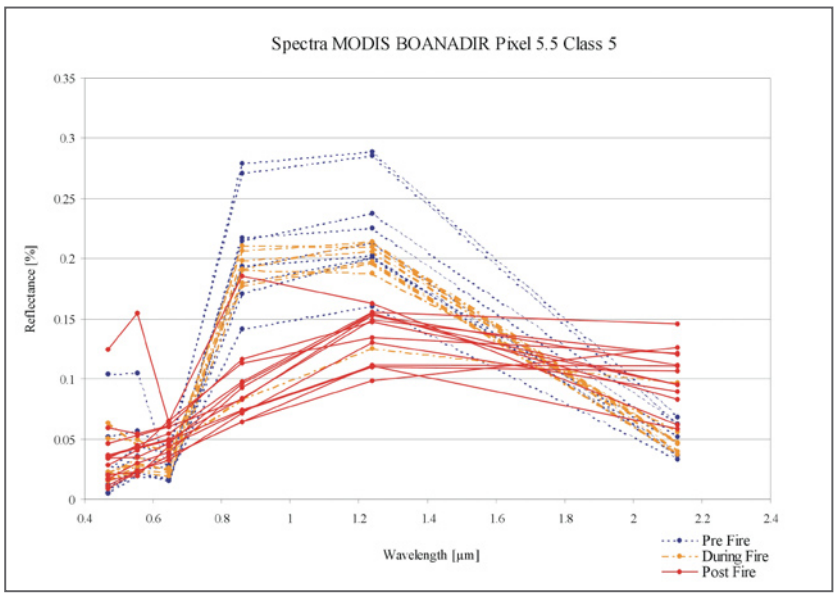

Figure A6-5: Spectral properties detected from bands 1 to 5 and 7 of MODIS bottom of atmosphere and BRDF corrected (BOANADIR) reflectance within one pixel (5.5) selected in class 5.

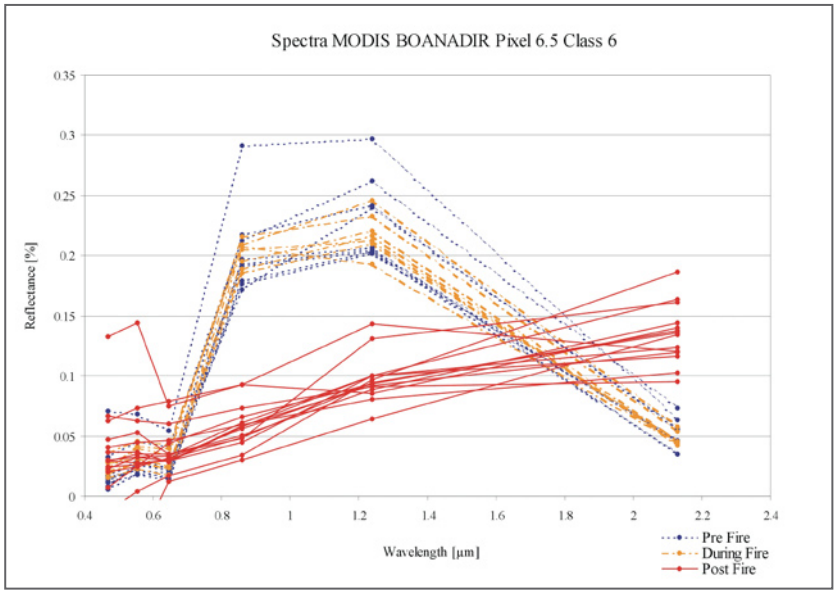

Figure A6-6: Spectral properties detected from bands 1 to 5 and 7 of MODIS bottom of atmosphere and BRDF corrected (BOANADIR) reflectance within one pixel (6.5) selected in class 6.

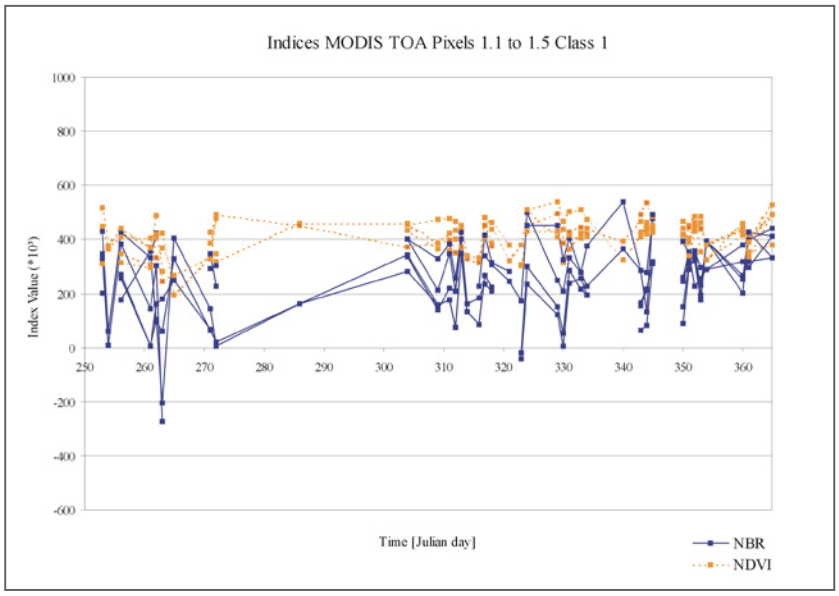

Figure A7-1: The trend of the NBR and NDVI through time within 5 pixels (1.1 to 1.5) selected in class 1, derived from MODIS top of atmosphere (TOA) reflectance.

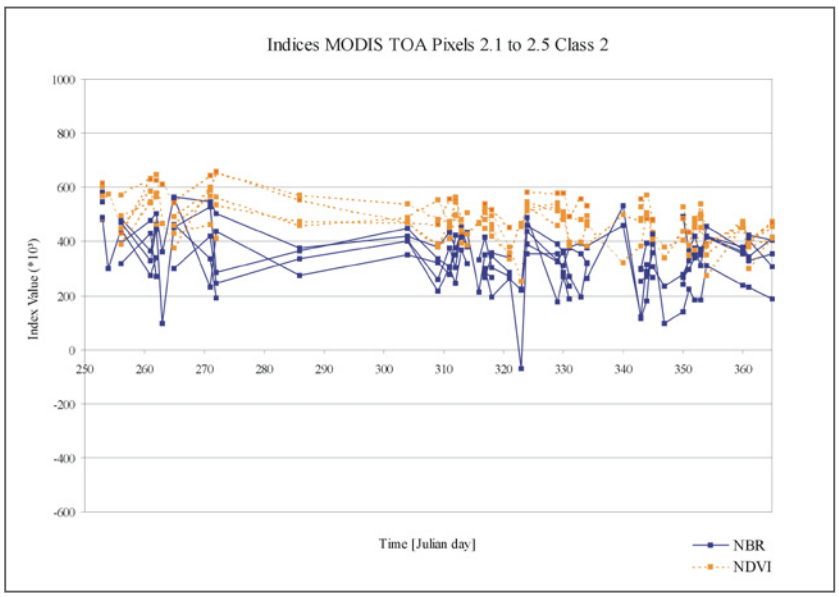

Figure A7-2: The trend of the NBR and NDVI through time within 5 pixels (2.1 to 2.5) selected in class 2, derived from MODIS top of atmosphere (TOA) reflectance.

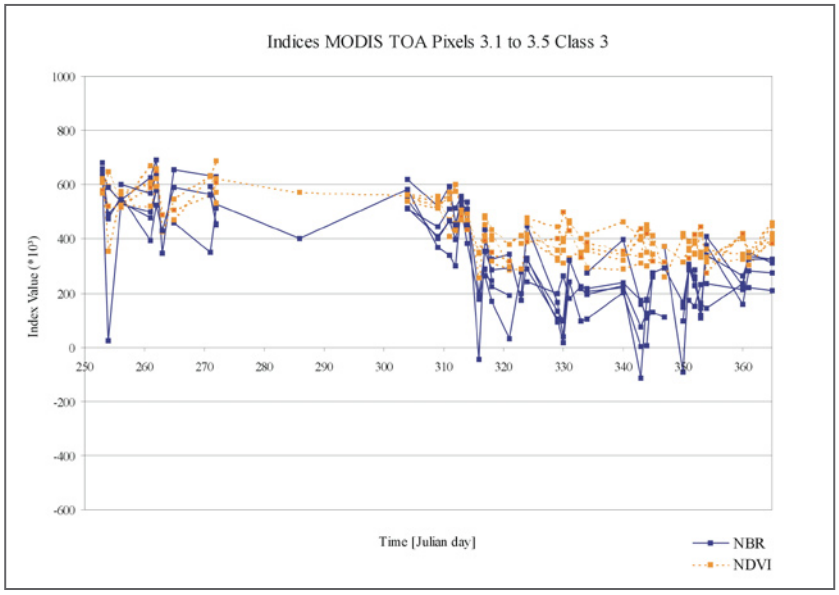

Figure A7-3: The trend of the NBR and NDVI through time within 5 pixels (3.1 to 3.5) selected in class 3, derived from MODIS top of atmosphere (TOA) reflectance.

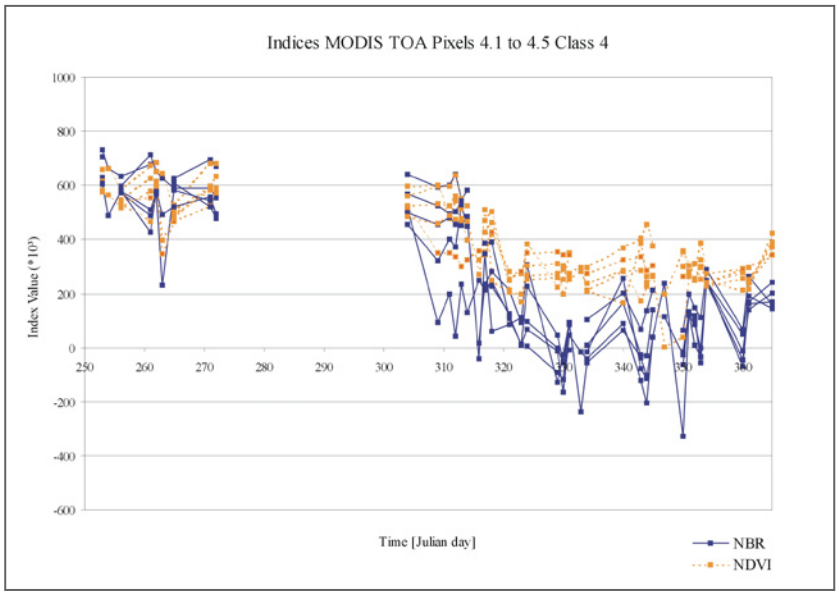

Figure A7-4: The trend of the NBR and NDVI through time within 5 pixels (4.1 to 4.5) selected in class 4, derived from MODIS top of atmosphere (TOA) reflectance.

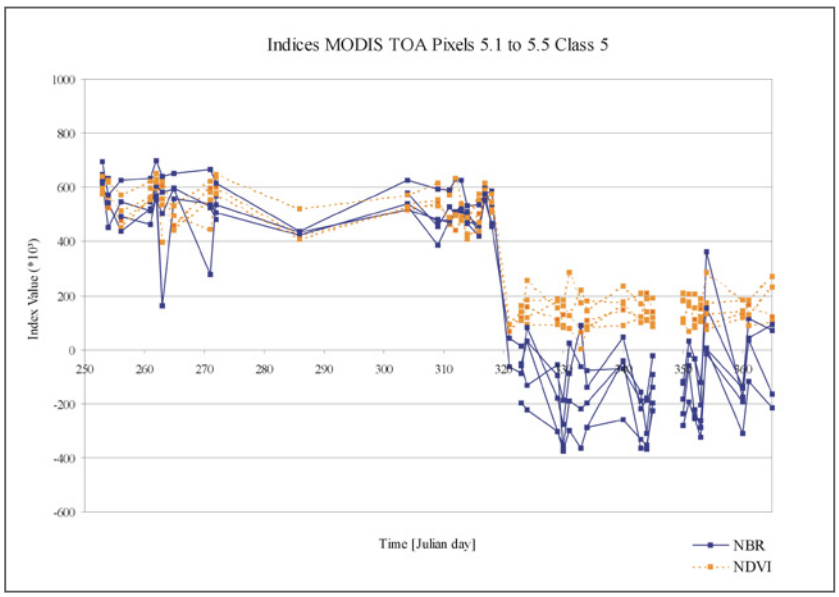

Figure A7-5: The trend of the NBR and NDVI through time within 5 pixels (5.1 to 5.5) selected in class 5, derived from MODIS top of atmosphere (TOA) reflectance.

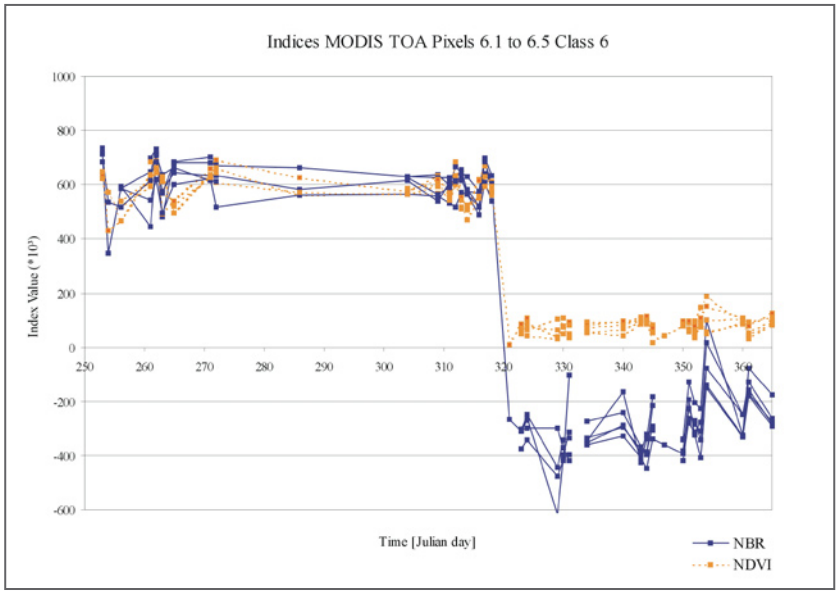

Figure A7-6: The trend of the NBR and NDVI through time within 5 pixels (6.1 to 6.5) selected in class 6, derived from MODIS top of atmosphere (TOA) reflectance.

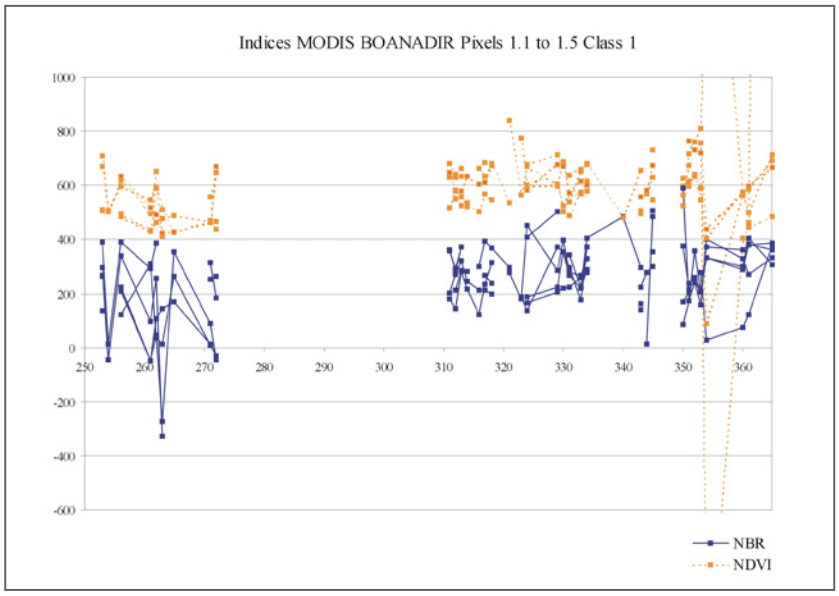

Figure A8-1: The trend of the NBR and NDVI through time within 5 pixels (1.1 to 1.5) selected in class 1, derived from MODIS bottom of atmosphere and BRDF corrected (BOANADIR) reflectance.

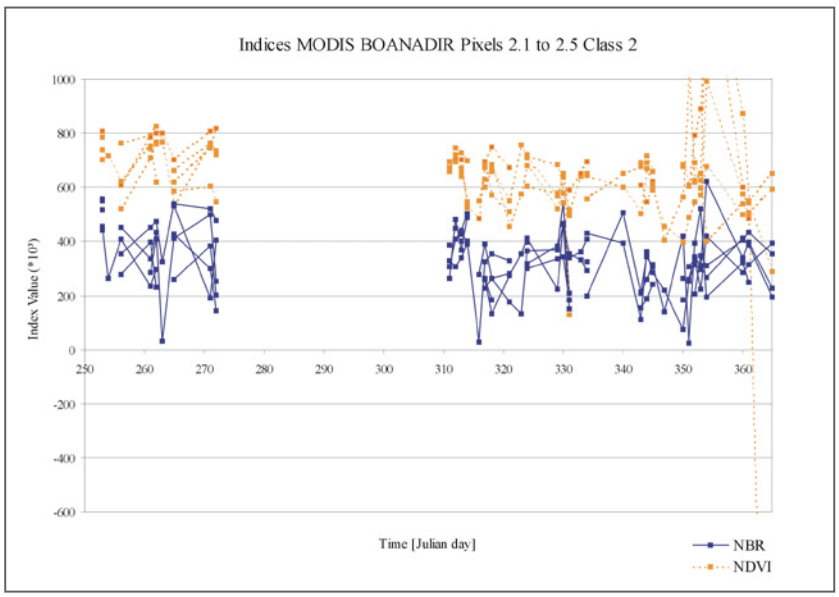

Figure A8-2: The trend of the NBR and NDVI through time within 5 pixels (2.1 to 2.5) selected in class 2, derived from MODIS bottom of atmosphere and BRDF corrected (BOANADIR) reflectance.

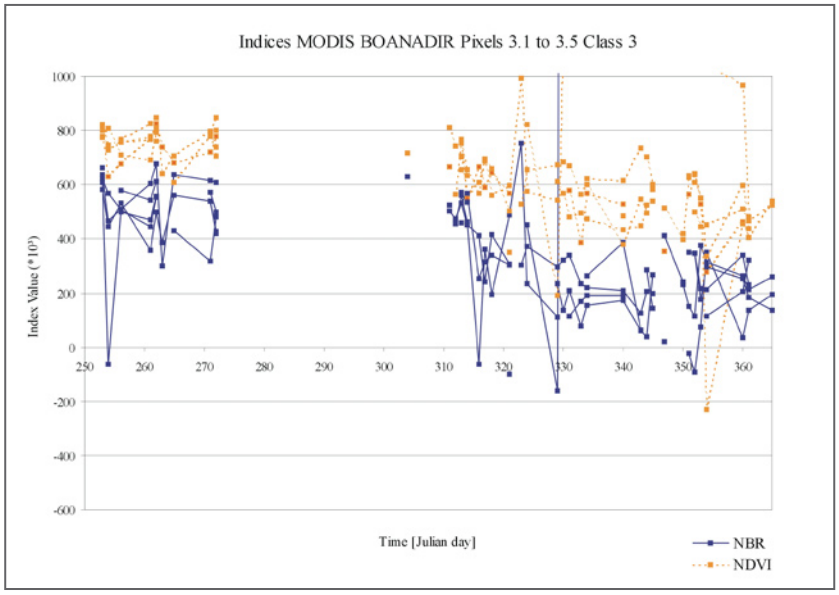

Figure A8-3: The trend of the NBR and NDVI through time within 5 pixels (3.1 to 3.5) selected in class 3, derived from MODIS bottom of atmosphere and BRDF corrected (BOANADIR) reflectance.

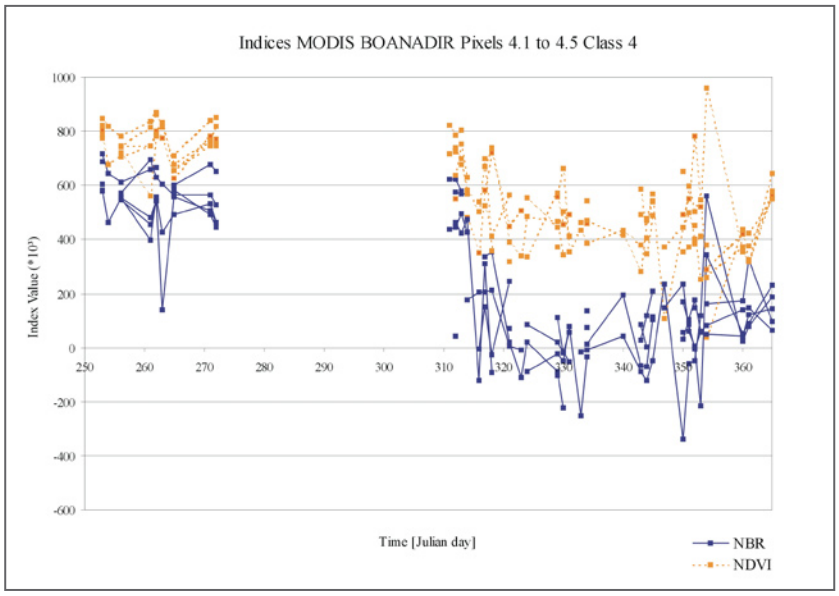

Figure A8-4: The trend of the NBR and NDVI through time within 5 pixels (4.1 to 4.5) selected in class 4, derived from MODIS bottom of atmosphere and BRDF corrected (BOANADIR) reflectance.

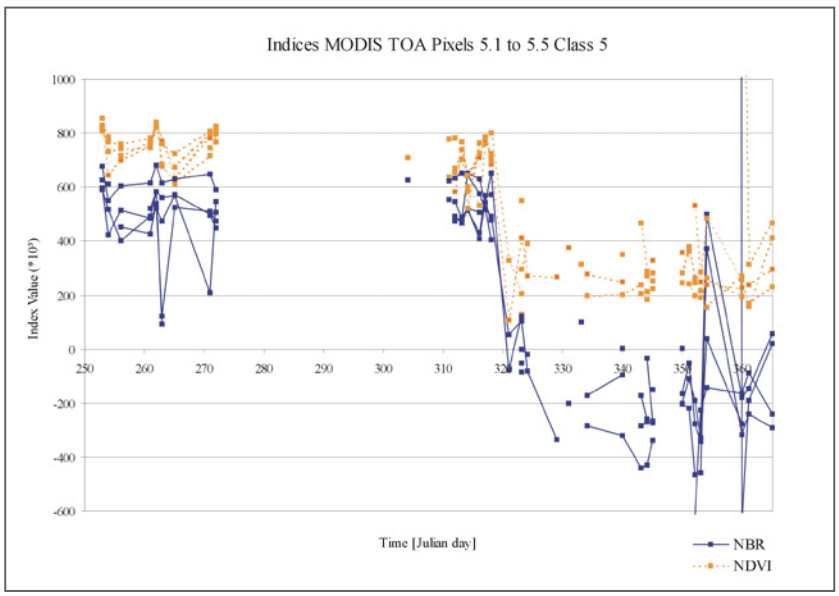

Figure A8-5: The trend of the NBR and NDVI through time within 5 pixels (5.1 to 5.5) selected in class 5, derived from MODIS bottom of atmosphere and BRDF corrected (BOANADIR) reflectance.

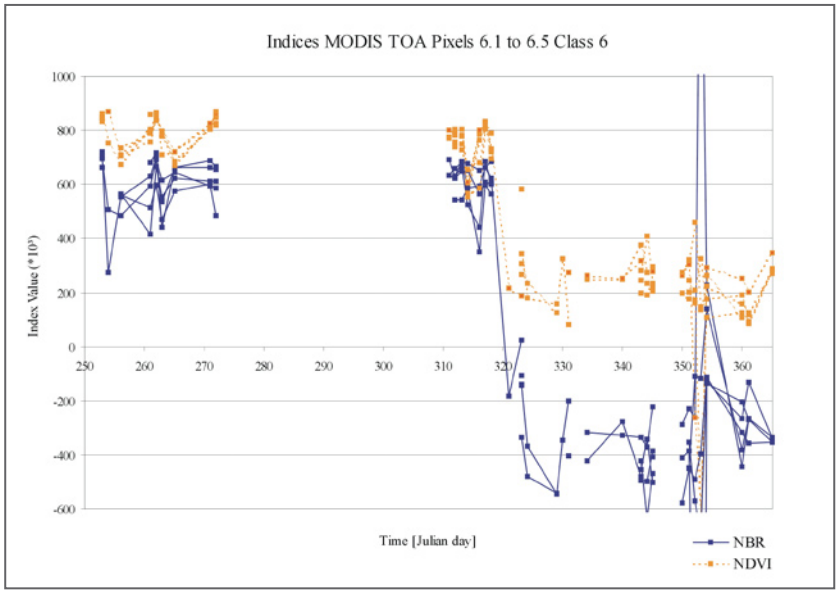

Figure A8-6: The trend of the NBR and NDVI through time within 5 pixels (6.1 to 6.5) selected in class 6, derived from MODIS bottom of atmosphere and BRDF corrected (BOANADIR) reflectance.

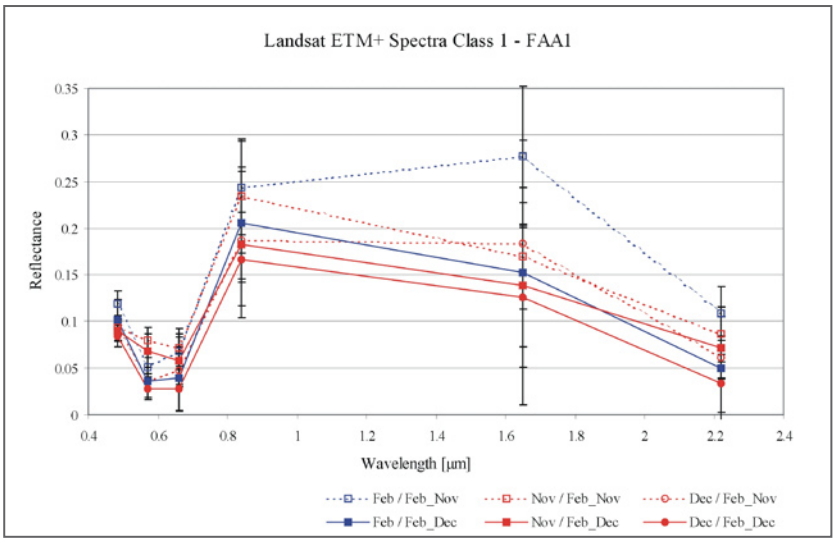

Figure A9-1: Spectral properties detected from bands 1 to 5 and 7 of Landsat ETM+ in class 1 of FAA1.

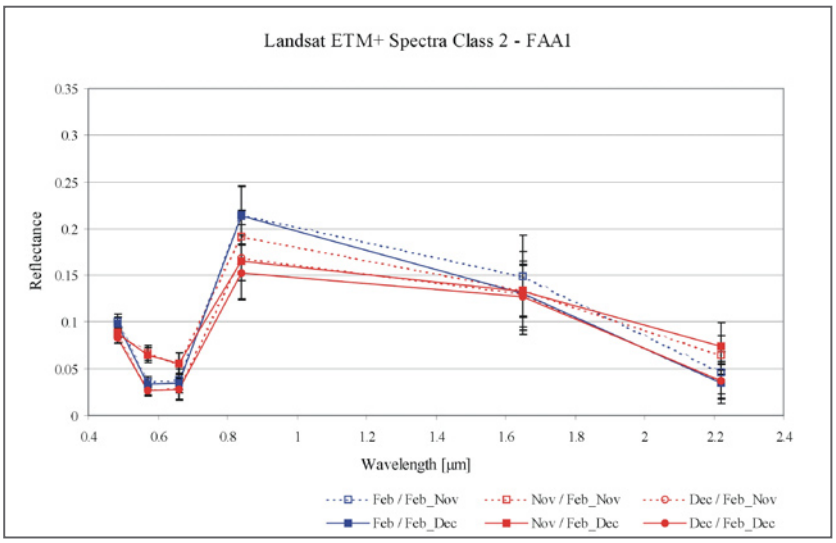

Figure A9-2: Spectral properties detected from bands 1 to 5 and 7 of Landsat ETM+ in class 2 of FAA1.

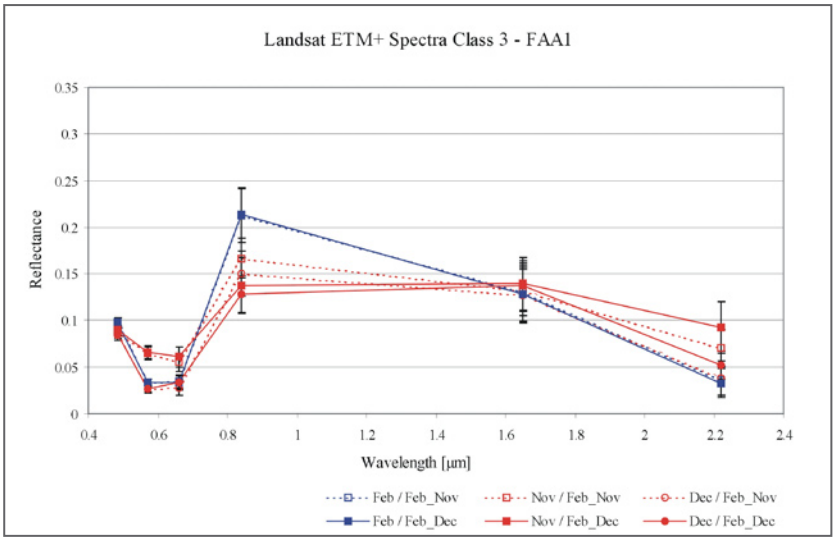

Figure A9-3: Spectral properties detected from bands 1 to 5 and 7 of Landsat ETM+ in class 3 of FAA1.

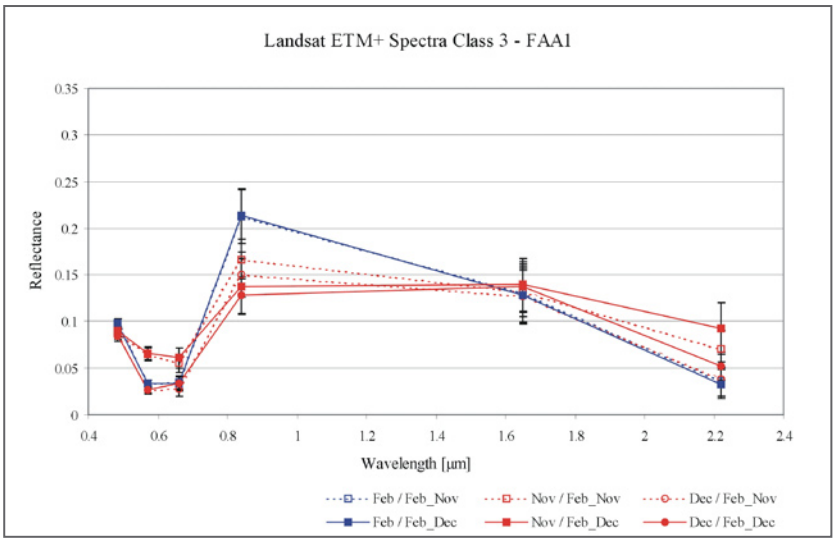

Figure A9-4: Spectral properties detected from bands 1 to 5 and 7 of Landsat ETM+ in class 4 of FAA1.

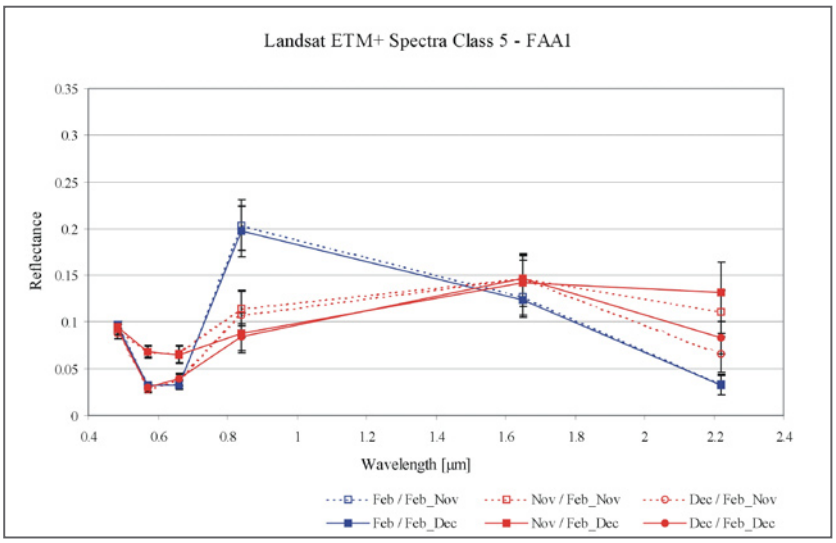

Figure A9-5: Spectral properties detected from bands 1 to 5 and 7 of Landsat ETM+ in class 5 of FAA1.

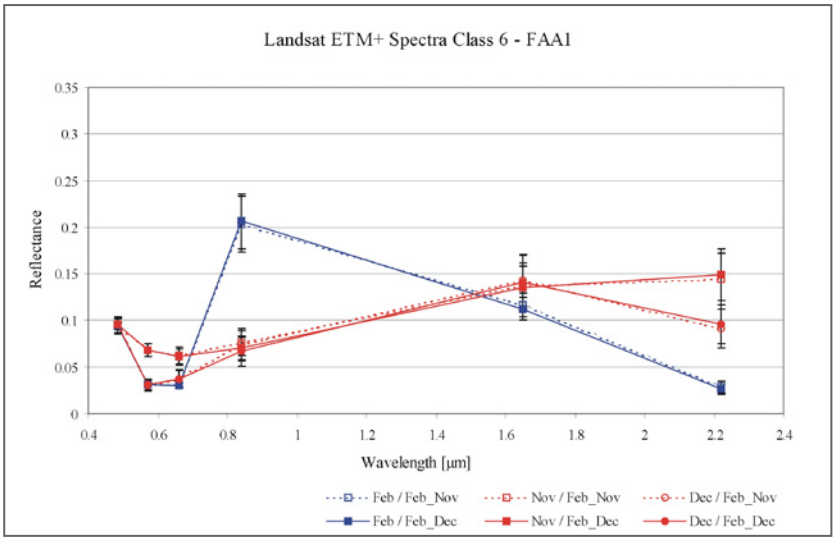

Figure A9-6: Spectral properties detected from bands 1 to 5 and 7 of Landsat ETM+ in class 6 of FAA1.

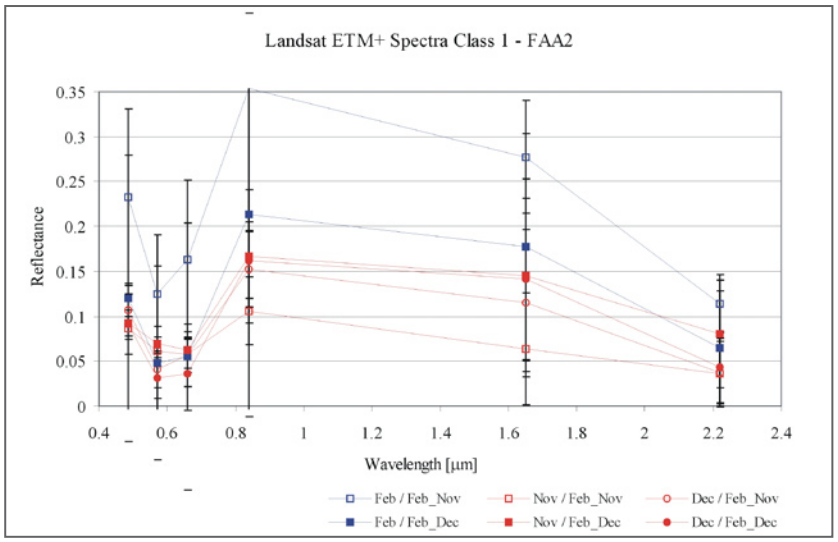

Figure A10-1: Spectral properties detected from bands 1 to 5 and 7 of Landsat ETM+ in class 1 of FAA2.

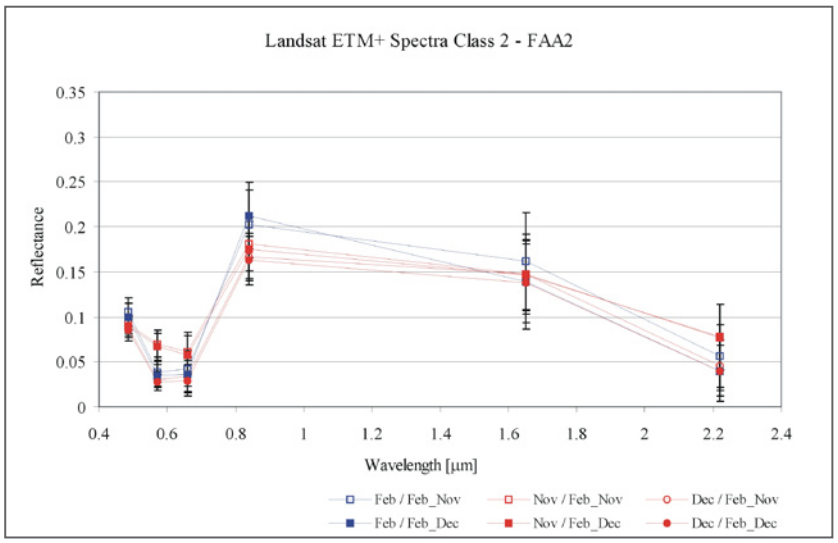

Figure A10-2: Spectral properties detected from bands 1 to 5 and 7 of Landsat ETM+ in class 2 of FAA2.

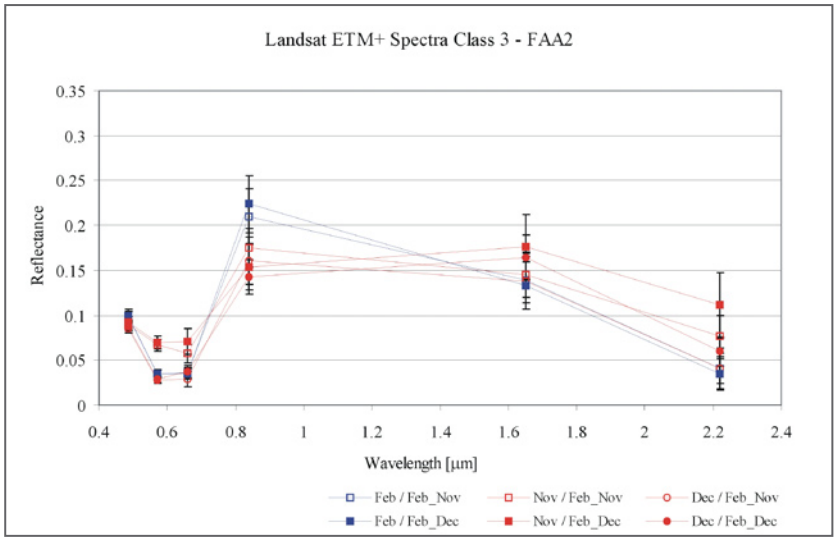

Figure A10-3: Spectral properties detected from bands 1 to 5 and 7 of Landsat ETM+ in class 3 of FAA2.

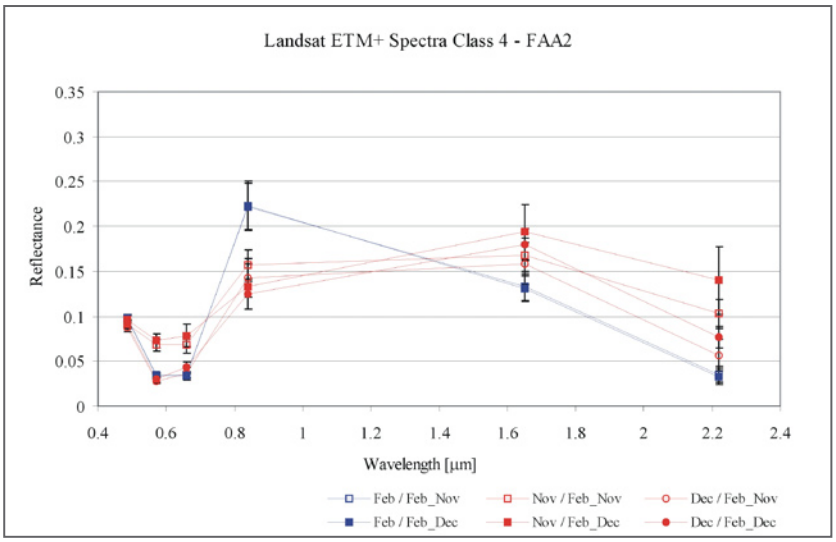

Figure A10-4: Spectral properties detected from bands 1 to 5 and 7 of Landsat ETM+ in class 4 of FAA2.

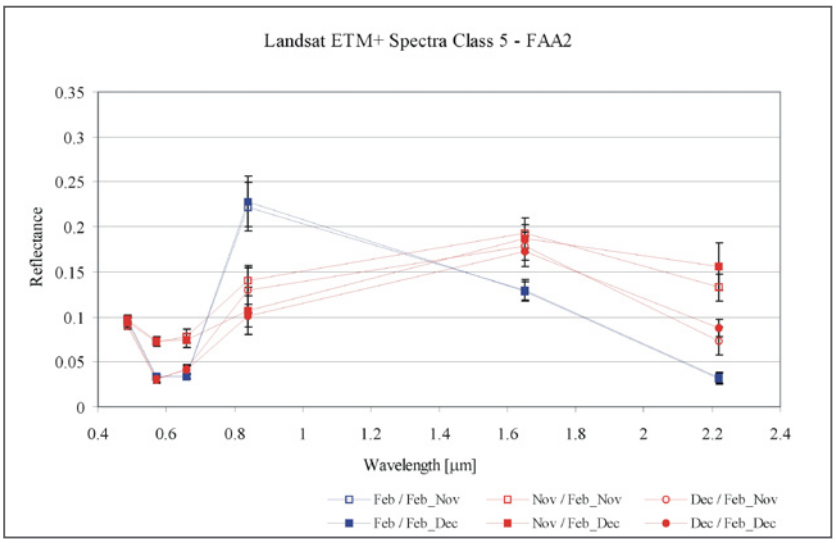

Figure A10-5: Spectral properties detected from bands 1 to 5 and 7 of Landsat ETM+ in class 5 of FAA2.

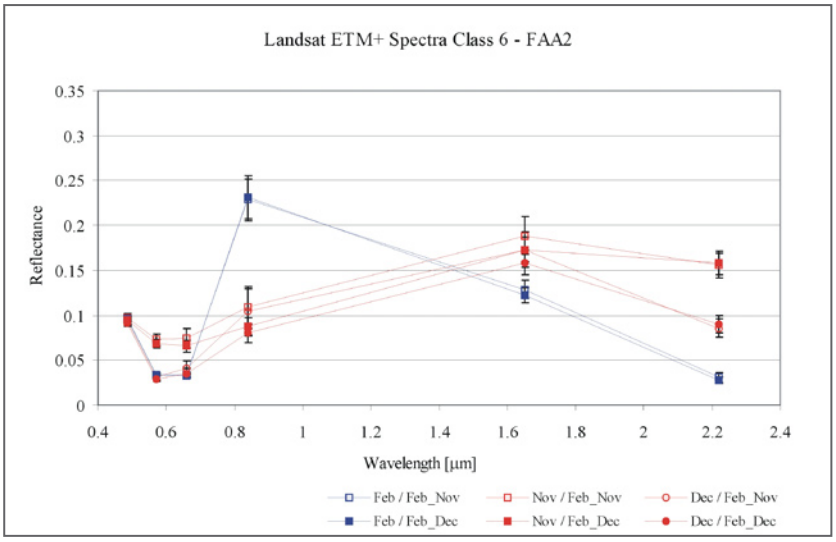

Figure A10-6: Spectral properties detected from bands 1 to 5 and 7 of Landsat ETM+ in class 6 of FAA2.

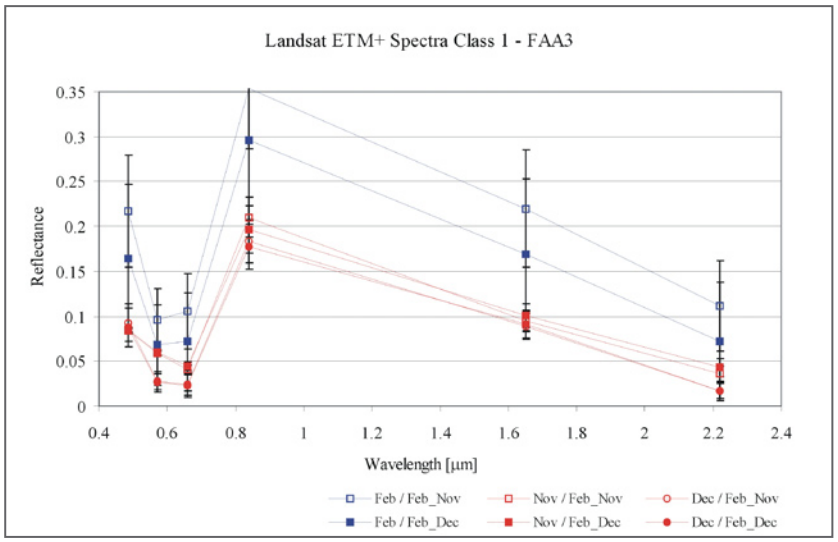

Figure A11-1: Spectral properties detected from bands 1 to 5 and 7 of Landsat ETM+ in class 1 of FAA3.

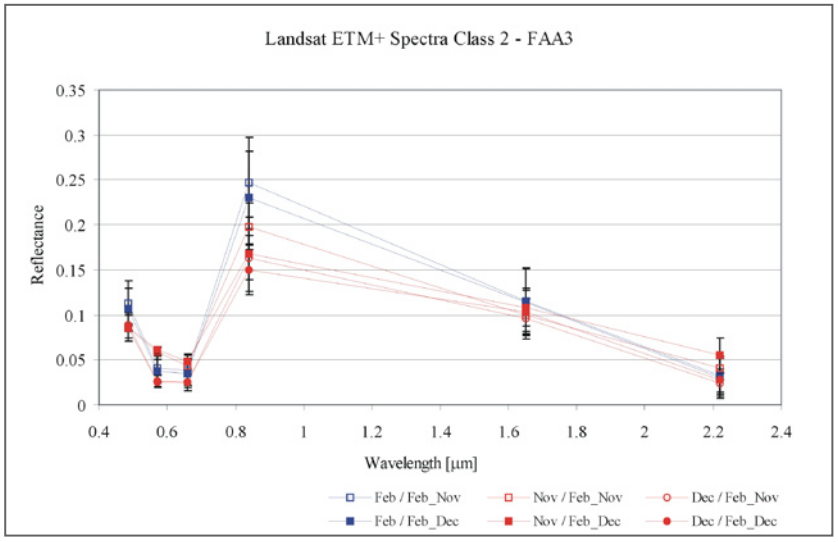

Figure A11-2: Spectral properties detected from bands 1 to 5 and 7 of Landsat ETM+ in class 2 of FAA3.

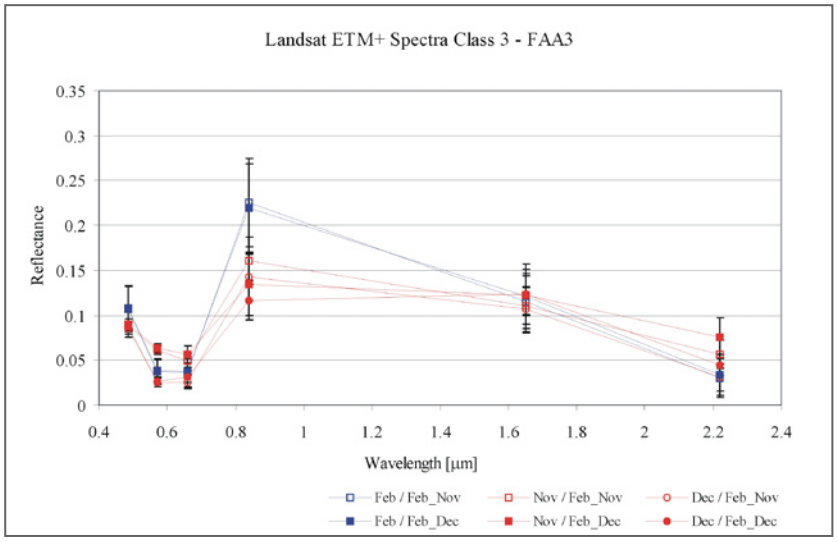

Figure A11-3: Spectral properties detected from bands 1 to 5 and 7 of Landsat ETM+ in class 3 of FAA3.

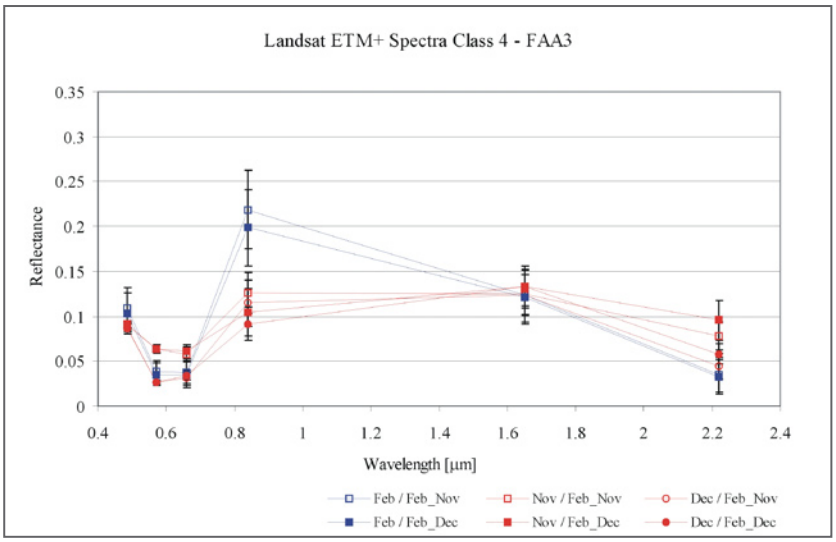

Figure A11-4: Spectral properties detected from bands 1 to 5 and 7 of Landsat ETM+ in class 4 of FAA3.

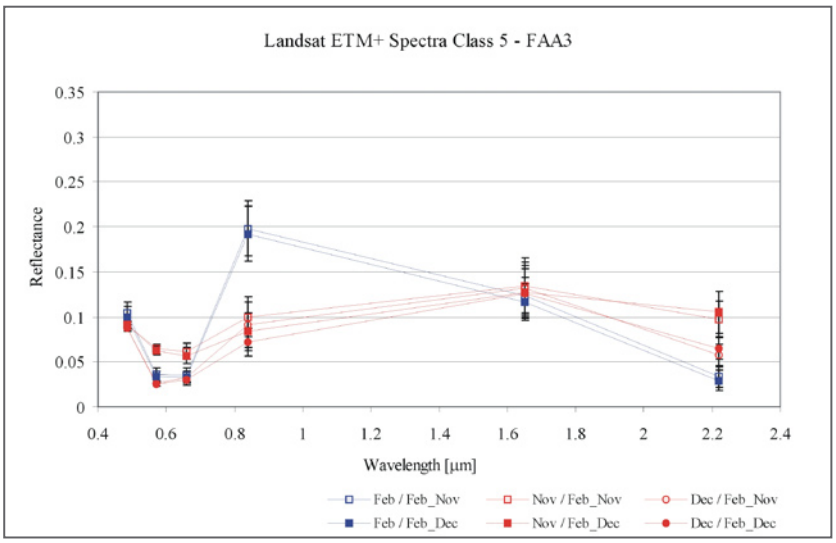

Figure A11-5: Spectral properties detected from bands 1 to 5 and 7 of Landsat ETM+ in class 5 of FAA3.

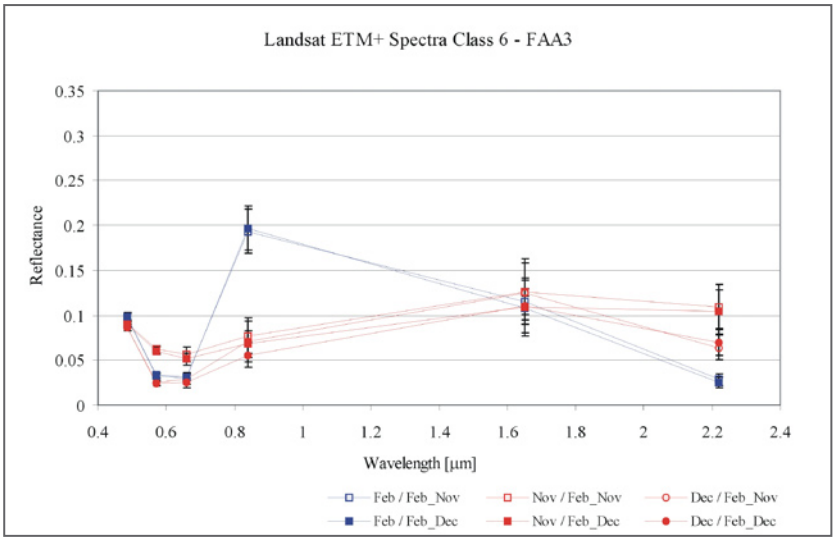

Figure A11-6: Spectral properties detected from bands 1 to 5 and 7 of Landsat ETM+ in class 6 of FAA3.

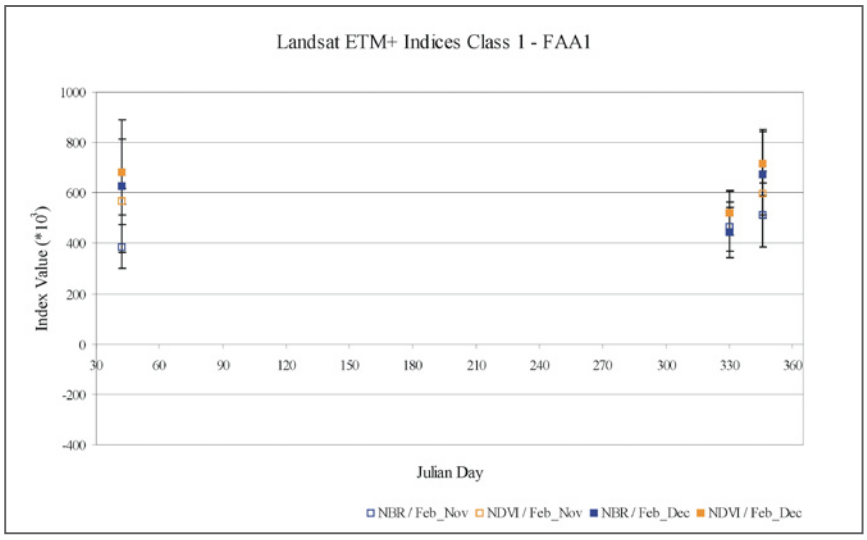

Figure A12-1: NBR and NDVI values derived from Landsat ETM+ data within class 1 of FAA1. The results are derived within class 1 from both the ΔNBR_{Nov} image and the ΔNBR_{Dec} image.

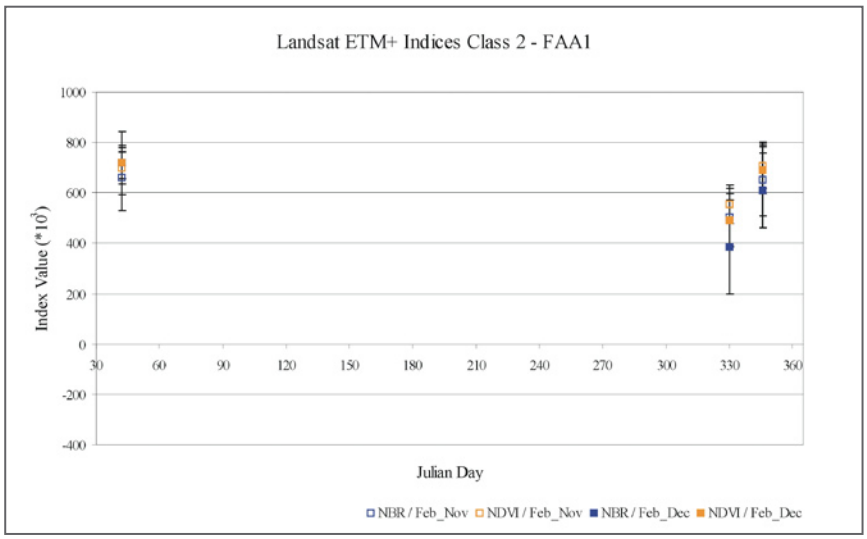

Figure A12-2: NBR and NDVI values derived from Landsat ETM+ data within class 2 of FAA1. The results are derived within class 2 from both the ΔNBR_{Nov} image and the ΔNBR_{Dec} image.

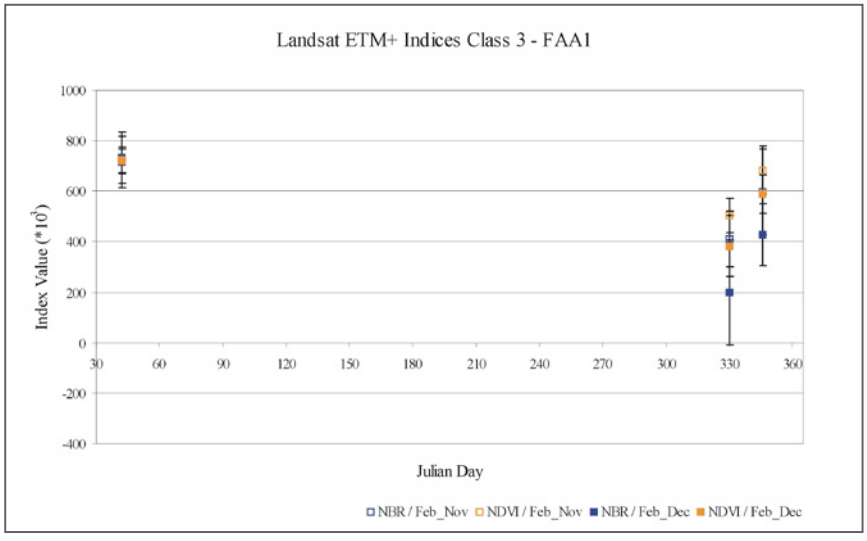

Figure A12-3: NBR and NDVI values derived from Landsat ETM+ data within class 3 of FAA1. The results are derived within class 3 from both the ΔNBR_{Nov} image and the ΔNBR_{Dec} image.

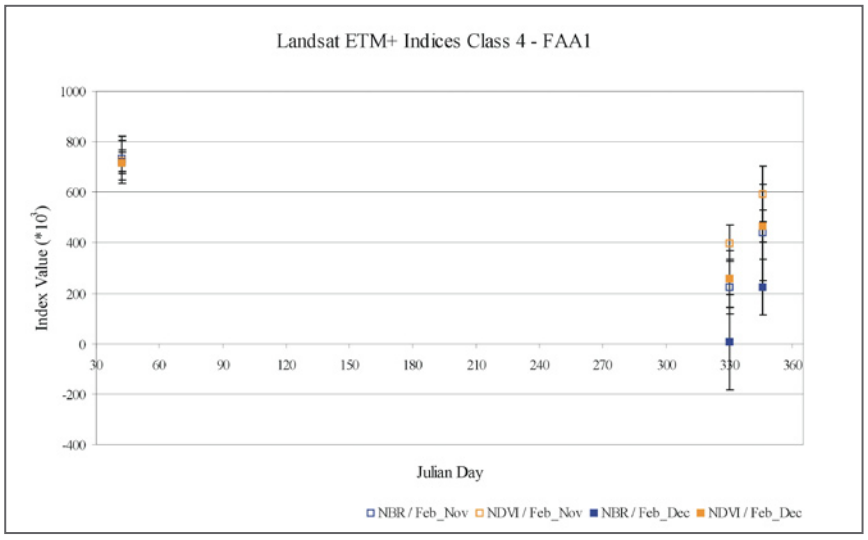

Figure A12-4: NBR and NDVI values derived from Landsat ETM+ data within class 4 of FAA1. The results are derived within class 4 from both the ΔNBR_{Nov} image and the ΔNBR_{Dec} image.

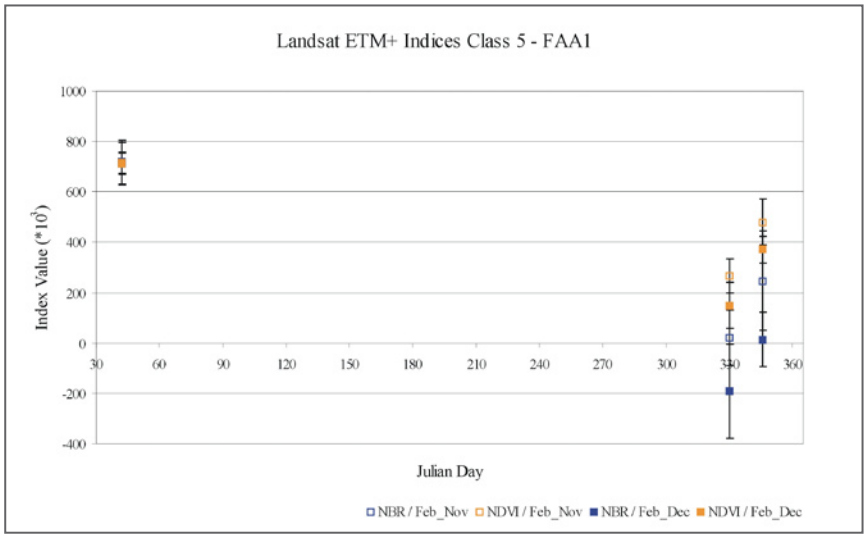

Figure A12-5: NBR and NDVI values derived from Landsat ETM+ data within class 5 of FAA1. The results are derived within class 5 from both the ΔNBR_{Nov} image and the ΔNBR_{Dec} image.

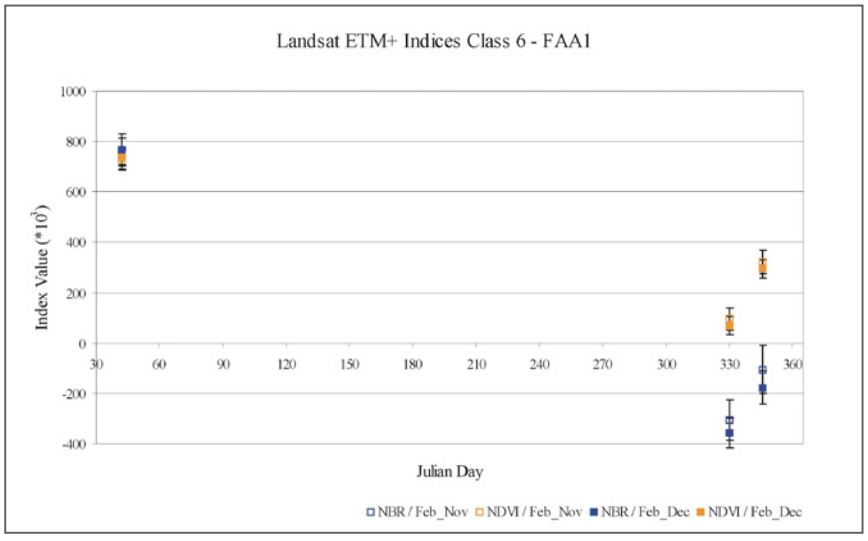

Figure A12-6: NBR and NDVI values derived from Landsat ETM+ data within class 6 of FAA1. The results are derived within class 6 from both the ΔNBR_{Nov} image and the ΔNBR_{Dec} image.

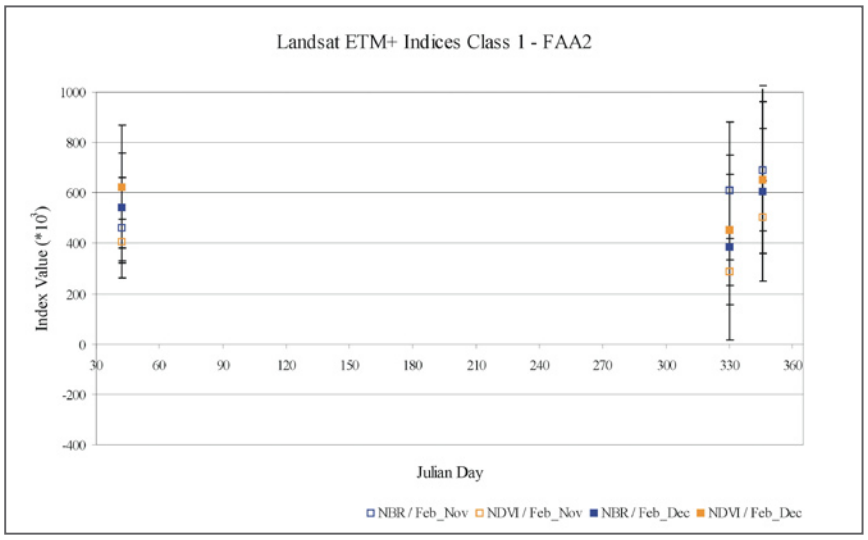

Figure A13-1: NBR and NDVI values derived from Landsat ETM+ data within class 1 of FAA2. The results are derived within class 1 from both the ΔNBR_{Nov} image and the ΔNBR_{Dec} image.

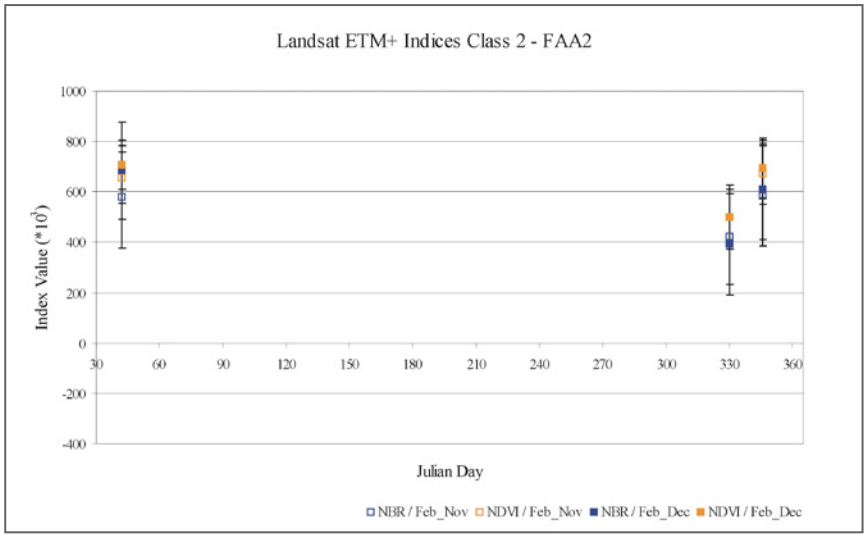

Figure A13-2: NBR and NDVI values derived from Landsat ETM+ data within class 2 of FAA2. The results are derived within class 2 from both the ΔNBR_{Nov} image and the ΔNBR_{Dec} image.

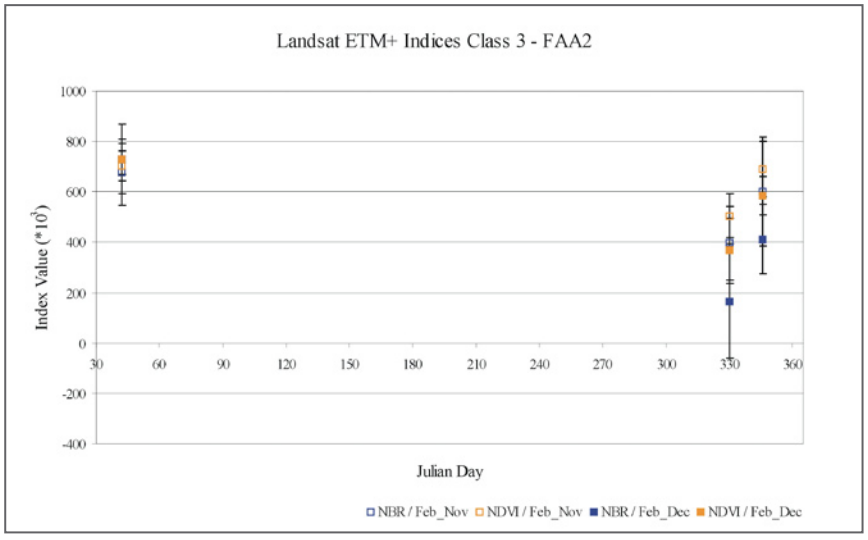

Figure A13-3: NBR and NDVI values derived from Landsat ETM+ data within class 3 of FAA2. The results are derived within class 3 from both the ΔNBR_{Nov} image and the ΔNBR_{Dec} image.

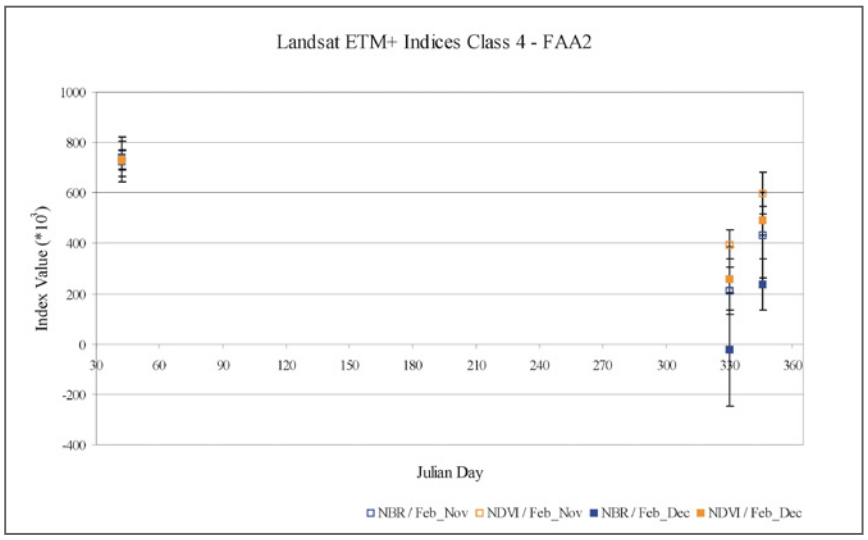

Figure A13-4: NBR and NDVI values derived from Landsat ETM+ data within class 4 of FAA2. The results are derived within class 4 from both the ΔNBR_{Nov} image and the ΔNBR_{Dec} image.

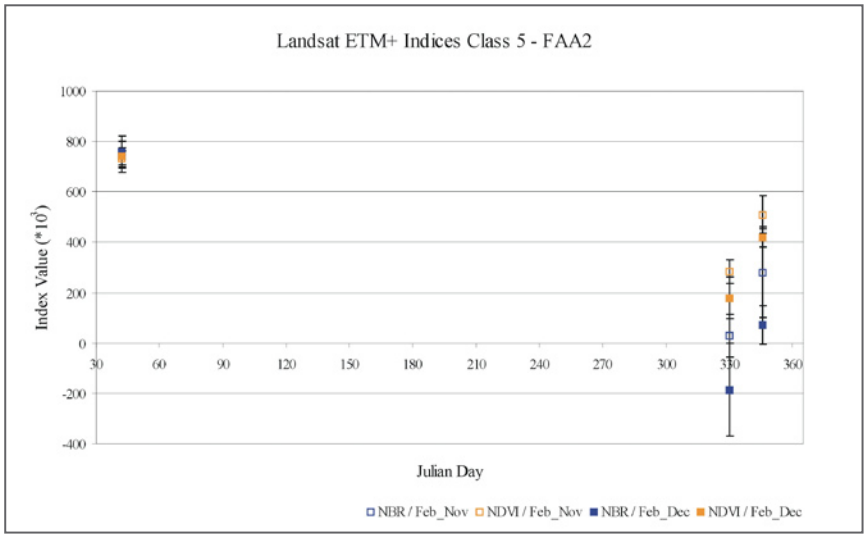

Figure A13-5: NBR and NDVI values derived from Landsat ETM+ data within class 5 of FAA2. The results are derived within class 5 from both the ΔNBR_{Nov} image and the ΔNBR_{Dec} image.

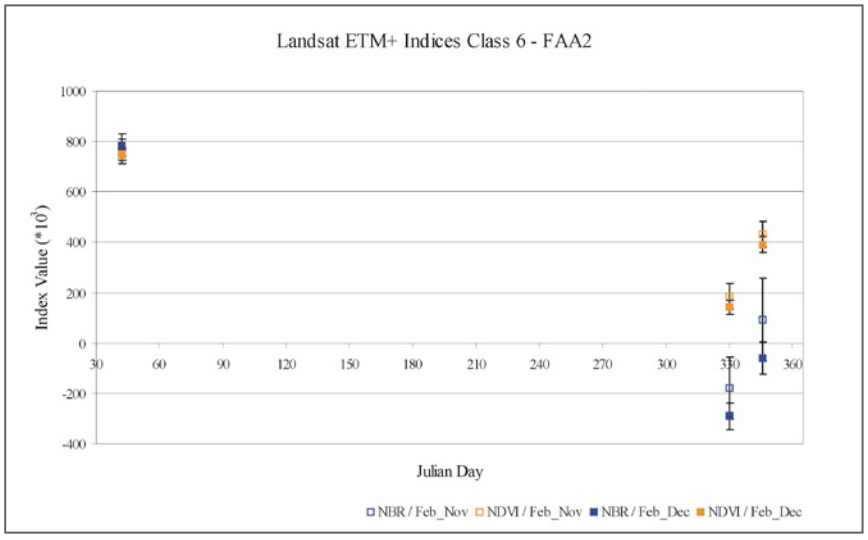

Figure A13-6: NBR and NDVI values derived from Landsat ETM+ data within class 6 of FAA2. The results are derived within class 6 from both the ΔNBR_{Nov} image and the ΔNBR_{Dec} image.

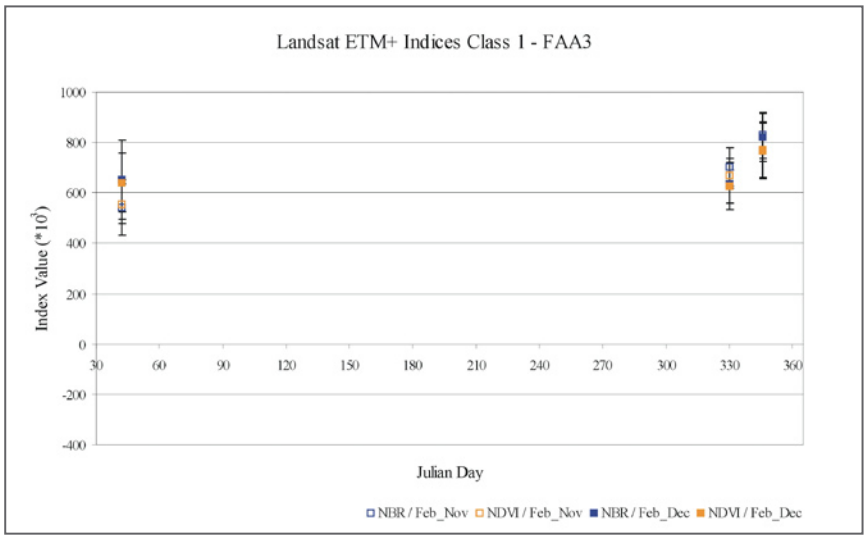

Figure A14-1: NBR and NDVI values derived from Landsat ETM+ data within class 1 of FAA3. The results are derived within class 1 from both the ΔNBR_{Nov} image and the ΔNBR_{Dec} image.

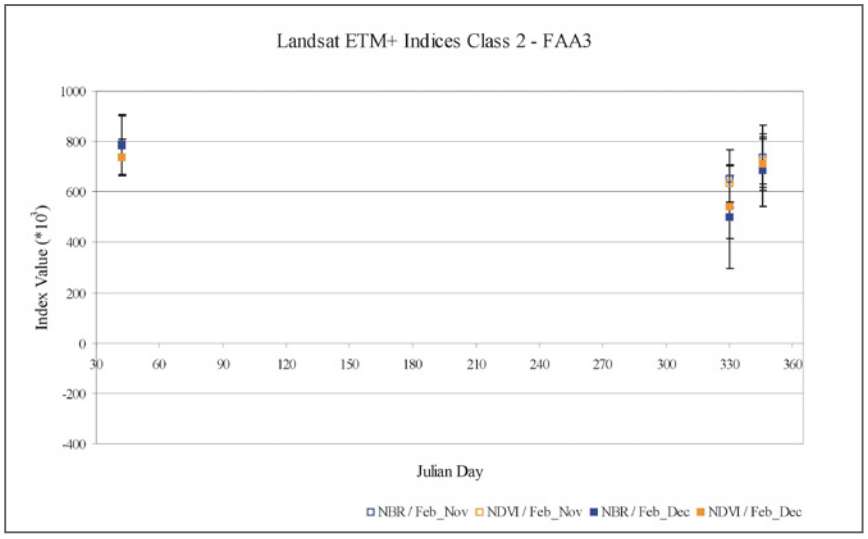

Figure A14-2: NBR and NDVI values derived from Landsat ETM+ data within class 2 of FAA3. The results are derived within class 2 from both the ΔNBR_{Nov} image and the ΔNBR_{Dec} image.

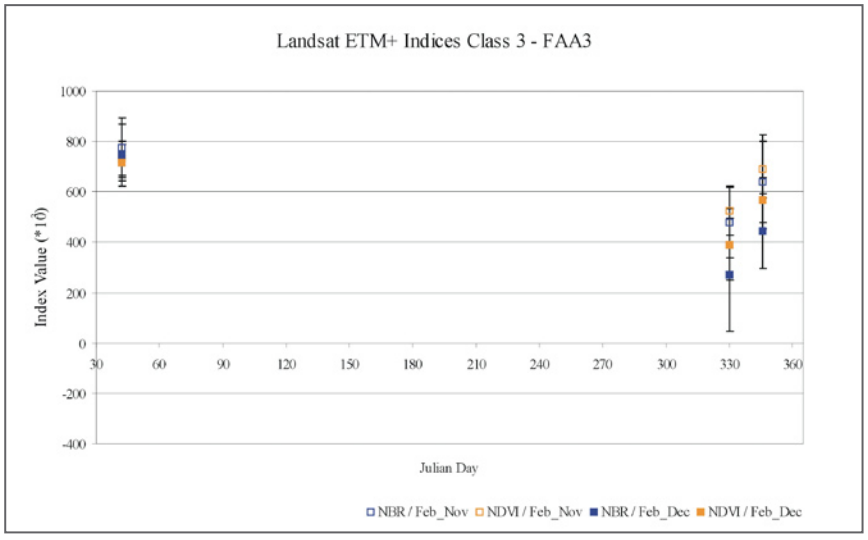

Figure A14-3: NBR and NDVI values derived from Landsat ETM+ data within class 3 of FAA3. The results are derived within class 3 from both the ΔNBR_{Nov} image and the ΔNBR_{Dec} image.

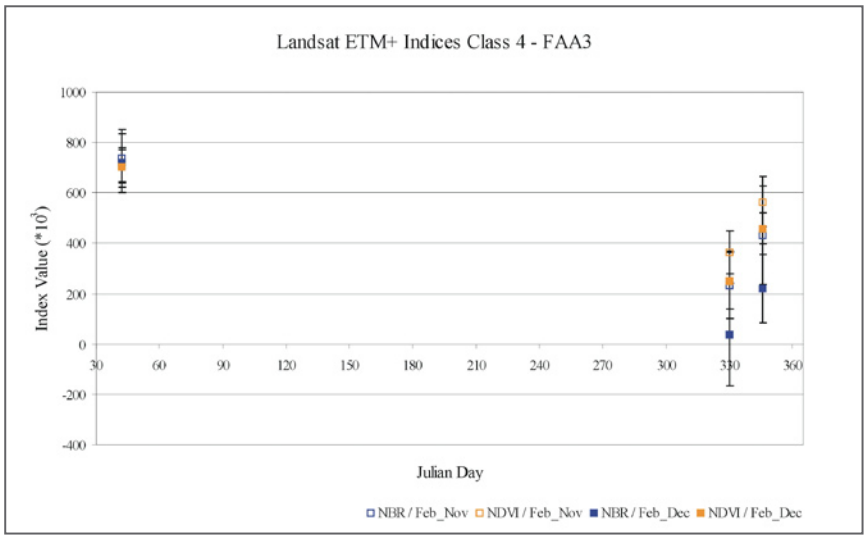

Figure A14-4: NBR and NDVI values derived from Landsat ETM+ data within class 4 of FAA3. The results are derived within class 4 from both the ΔNBR_{Nov} image and the ΔNBR_{Dec} image.

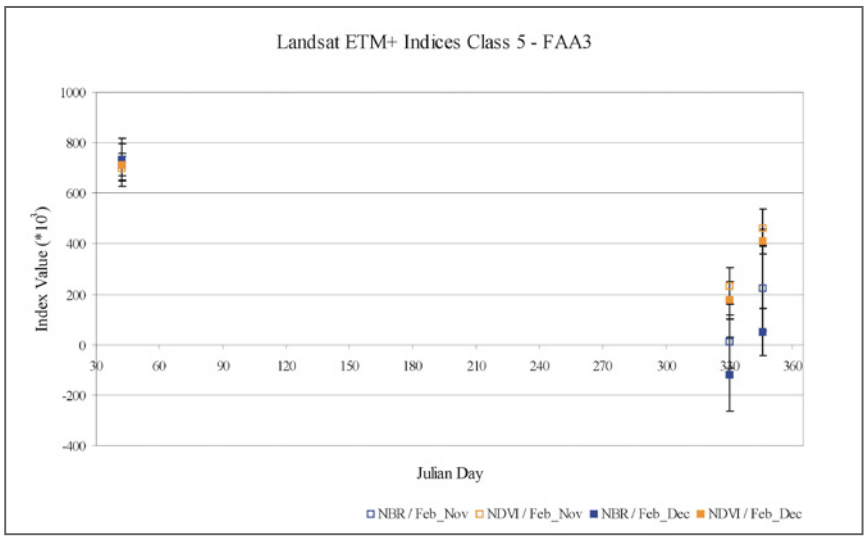

Figure A14-5: NBR and NDVI values derived from Landsat ETM+ data within class 5 of FAA3. The results are derived within class 5 from both the ΔNBR_{Nov} image and the ΔNBR_{Dec} image.

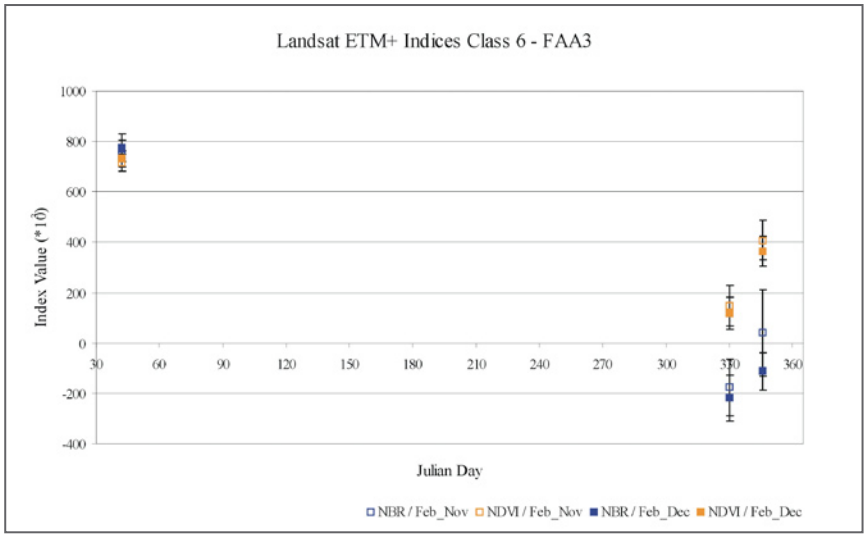

Figure A14-6: NBR and NDVI values derived from Landsat ETM+ data within class 6 of FAA3. The results are derived within class 6 from both the ΔNBR_{Nov} image and the ΔNBR_{Dec} image.

GCP 6	NBR	NDVI	ΔNBR	ΔNDVI
Pre Fire	557	564		
Post Fire	575	476	-19	88

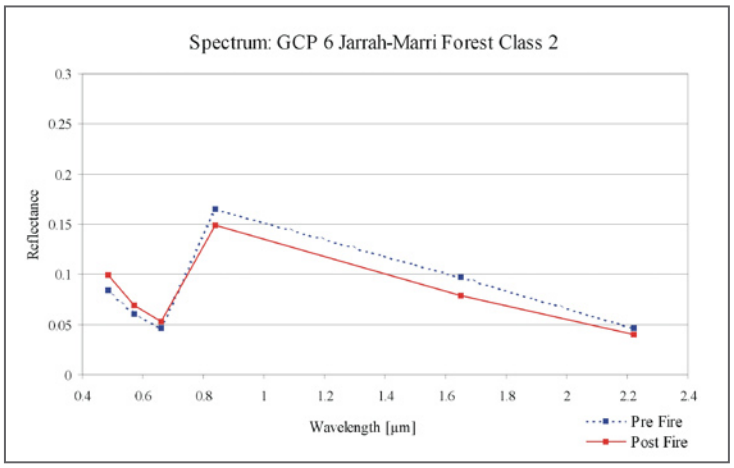

▲ *Figure A15-1: GCP 6 sampled in jarrah-marri forest, where burn severity was measured as low in class 2. The spectral properties and index values within the Landsat pixel of the GCP are compared with the field measurement of burn severity.*

▼ *Figure A15-2: GCP 7 sampled in jarrah-marri forest, where burn severity was measured as moderate in class 3. The spectral properties and index values within the Landsat pixel of the GCP are compared with the field measurement of burn severity.*

GCP 7	NBR	NDVI	ΔNBR	ΔNDVI
Pre Fire	513	544		
Post Fire	443	440	70	105

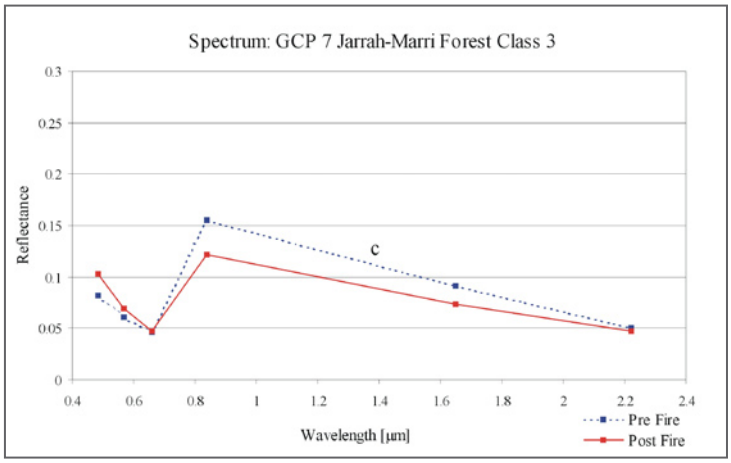

GCP 8	NBR	NDVI	ΔNBR	ΔNDVI
Pre Fire	511	546		
Post Fire	235	237	276	310

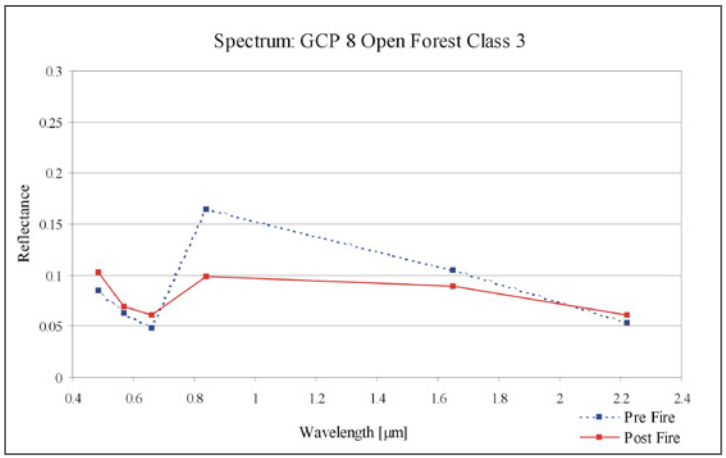

◄ *Figure A15-3: GCP 8 sampled in open forest, where burn severity was measured as moderate in class 3. The spectral properties and index values within the Landsat pixel of the GCP are compared with the field measurement of burn severity.*

GCP 9	NBR	NDVI	ΔNBR	ΔNDVI
Pre Fire	344	471		
Post Fire	130	207	214	264

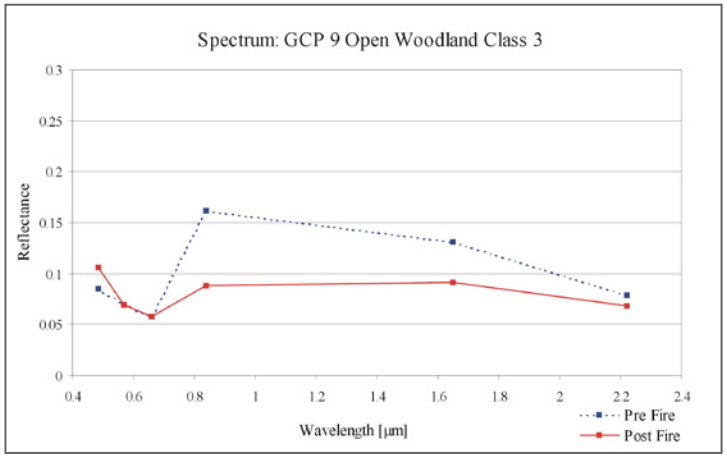

◄ *Figure A15-4: GCP 9 sampled in open woodland, where burn severity was measured as moderate in class 3. The spectral properties and index values within the Landsat pixel of the GCP are compared with the field measurement of burn severity.*

GCP 10	NBR	NDVI	ΔNBR	ΔNDVI
Pre Fire	310	440		
Post Fire	92	169	218	271

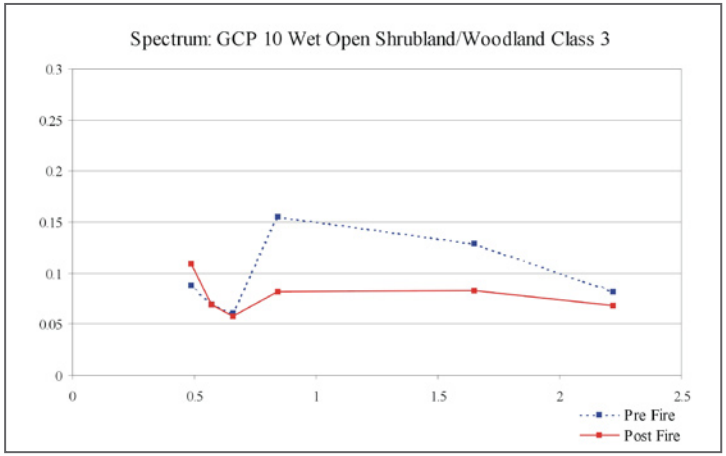

◄ *Figure A15-5: GCP 10 sampled in wet open shrubland/ woodland, where burn severity was measured as moderate in class 3. The spectral properties and index values within the Landsat pixel of the GCP are compared with the field measurement of burn severity.*

GCP 11	NBR	NDVI	ΔNBR	ΔNDVI
Pre Fire	248	425		
Post Fire	43	216	204	208

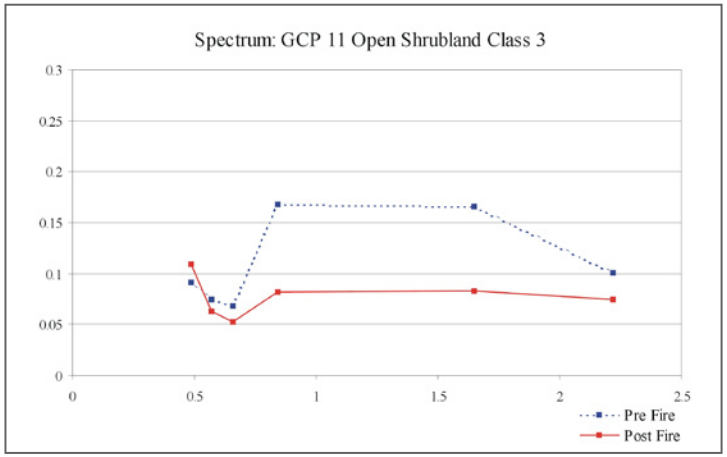

◄ *Figure A15-6: GCP 11 sampled in open shrubland, where burn severity was measured as moderate in class 3. The spectral properties and index values within the Landsat pixel of the GCP are compared with the field measurement of burn severity.*

GCP 12	NBR	NDVI	ΔNBR	ΔNDVI
Pre Fire	360	450		
Post Fire	125	196	235	254

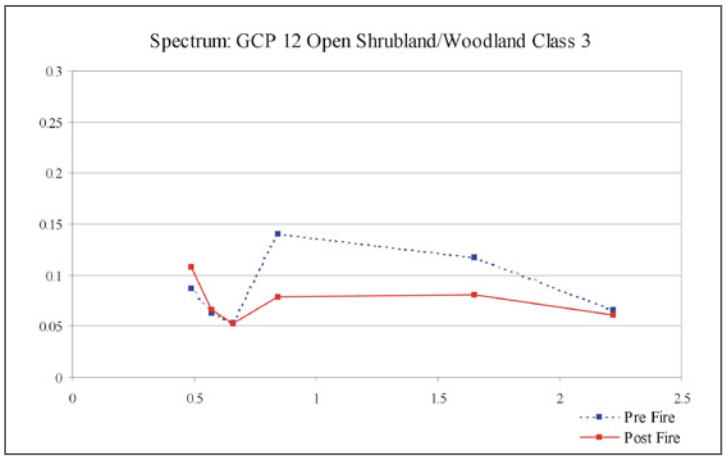

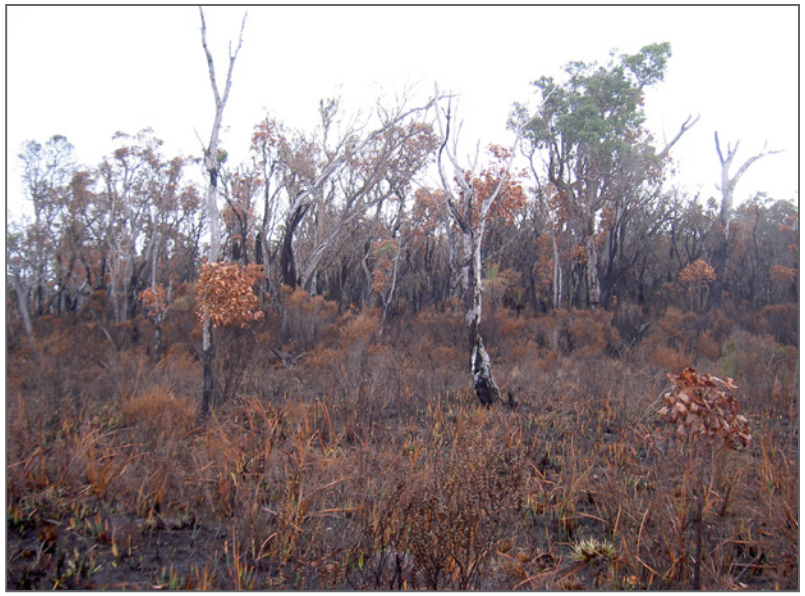

◄ *Figure A15-7: GCP 12 sampled in open shrubland/ woodland, where burn severity was measured as moderate in class 3. The spectral properties and index values within the Landsat pixel of the GCP are compared with the field measurement of burn severity.*

GCP 13	NBR	NDVI	ΔNBR	ΔNDVI
Pre Fire	382	488		
Post Fire	466	476	-85	12

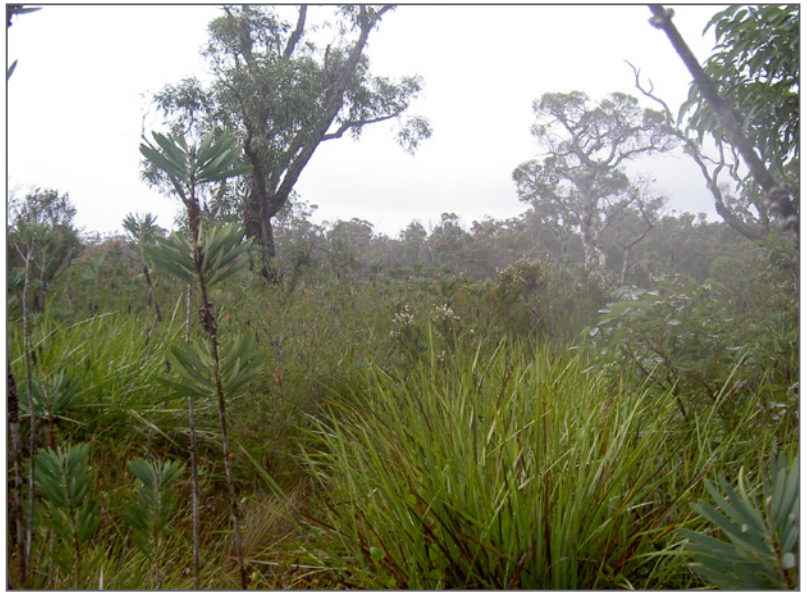

◄ *Figure A15-8: GCP 13 sampled in open shrubland/ woodland, which was not affected by fire. An unburnt pixel in pre-fire and post-fire data demonstrates reflectance change between Landsat data recorded in December 2003 and May 2004.*

GCP 14	NBR	NDVI	ΔNBR	ΔNDVI
Pre Fire	433	474		
Post Fire	513	459	-79	15

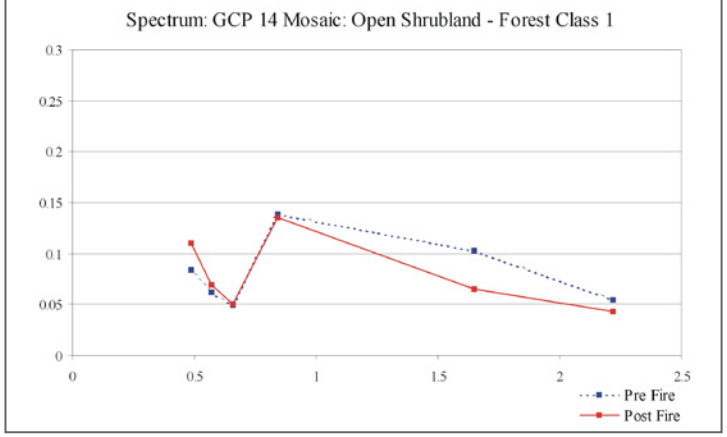

◄ *Figure A15-9: GCP 14 sampled in a mosaic of open shrubland and forest, which was not affected by fire. An unburnt pixel in pre-fire and post-fire data demonstrates reflectance change between Landsat data recorded in December 2003 and May 2004.*

Wahrheitsgemäße Erklärung

Ich erkläre hiermit wahrheitsgemäß, dass ich vorliegende Arbeit selbständig und ohne unerlaubte Hilfe angefertigt habe.
Alle verwendeten Quellen sind im Literaturverzeichnis angegeben.
Personen und Institutionen, die mir bei der Erstellung und Durchführung der Arbeit geholfen haben, sind im Dank (Acknowledgements) genannt.

Perth, 26. November 2004

Yvonne Walz